



HAL
open science

Thermoplastic composite filaments formulation and 3D-printing of a lithium-ion battery via fused deposition modeling

Alexis Maurel

► **To cite this version:**

Alexis Maurel. Thermoplastic composite filaments formulation and 3D-printing of a lithium-ion battery via fused deposition modeling. Other. Université de Picardie Jules Verne, 2020. English. NNT : 2020AMIE0049 . tel-03626274

HAL Id: tel-03626274

<https://theses.hal.science/tel-03626274>

Submitted on 31 Mar 2022

HAL is a multi-disciplinary open access archive for the deposit and dissemination of scientific research documents, whether they are published or not. The documents may come from teaching and research institutions in France or abroad, or from public or private research centers.

L'archive ouverte pluridisciplinaire **HAL**, est destinée au dépôt et à la diffusion de documents scientifiques de niveau recherche, publiés ou non, émanant des établissements d'enseignement et de recherche français ou étrangers, des laboratoires publics ou privés.



Thèse de Doctorat

*Mention Chimie
Spécialité Chimie et Électrochimie des Solides*

présentée à l'Ecole Doctorale en Sciences Technologie et Santé (ED 585)

de l'Université de Picardie Jules Verne

par

Alexis MAUREL

pour obtenir le grade de Docteur de l'Université de Picardie Jules Verne

*Thermoplastic composite filaments formulation and
3D-printing of a lithium-ion battery via fused deposition
modeling*

Soutenue le 25 Septembre 2020, après avis des rapporteurs, devant le jury d'examen :

Mme Christine CAMPAGNE, Professeur, ENSAIT Roubaix	Président
Mme Diana GOLODNITSKY, Professeur, TEL AVIV University	Rapporteur
M. Colm O'DWYER, Professeur, University College Cork	Rapporteur
M. Eric MACDONALD, Professeur, Youngstown State University	Examineur
M. Michel ARMAND, Directeur de recherche Emérite CNRS, UPJV Amiens	Examineur
Mme Sylvie GRUGEON, Ingénieur de Recherche, UPJV Amiens	Examineur
M. Loïc DUPONT, Professeur, UPJV Amiens	Co-Directeur de thèse
M. Stéphane PANIER, Professeur, UPJV Amiens	Co-Directeur de thèse



What we know is a drop, what we don't know is an ocean

Isaac Newton

Acknowledgments

2017-2020. Undoubtedly, these last 3 years, dedicated to the preparation of my PhD thesis, have been the most unforgettable of my life so far. Along this journey, I learnt a lot on a wide range of topics: materials chemistry, energy storage, electrochemistry, 3D-printing, engineering, but also communication, management, humility, respect and love from a human standpoint. This would not have been possible without the endless support of the following people:

Firstly, I would like to express my sincere gratitude to my advisors Prof. Stéphane PANIER, Prof. Loïc DUPONT and Dr. Sylvie GRUGEON. Your continuous and daily support, your motivation, and immense knowledge guided me in my researches and writing. You greatly contributed to be the scientist I have become. Stéphane, thank you for your positive encouragements, optimism, and open-mindedness. I owe you a lot, particularly regarding my knowledge on additive manufacturing and my aspiration to initiate/pursue great international research collaboration. I will never forget that you were there for my first talk in an international conference (October 2nd 2018 - Cancún, Mexico). Loïc, thank you so much for your kind words, for your unbeatable SEM images quality, and for my new nickname “le chat noir / the black cat” that is particularly consistent with the sanitary context of this PhD thesis. Sylvie, thank you for your help in my scientific researches, our day-to-day talks and for your involvement in this project. I learnt a lot from your articles/manuscript/ppt corrections and from your strong knowledge on energy storage. To all, I am really glad we will be able to pursue our collaboration during the next coming years.

Besides my advisors, I would like to thank the distinguished Jury members for accepting evaluating this thesis, for their insightful comments and encouragement: Prof. C. CAMPAGNE, Prof. D. GOLODNITSKY, Prof. C. O’DWYER, Prof. E. MACDONALD and Prof. M. ARMAND for their insightful comments and encouragement. My sincere thanks also goes to Prof. M. MORCLETTE, director of the LRCS and Prof. M. GUESSASMA, director of the MIM thematic from the LTI, who provided me access to their respective laboratory and research facilities. Without their precious support it would not be possible to conduct this research. I also would like to deeply thank the collaborators that were involved in this project supported by the European Union, the Fonds Européen de Développement Régional (FEDER), the Région Hauts-de-France and the

Université de Picardie Jules Verne (UPJV): Prof. M. ARMAND, H. TORTAJADA (LTI), Prof. K. PRASHANTHA (IMT Lille Douai), Dr. B. FLEUTOT (LRCS), Dr. M. COURTY (LRCS), Dr. C. DAVOISNE (LRCS), Dr. A. JAMALI (PME UPJV), Pr. A. CAYLA (ENSAIT Roubaix), H. KIM (LRCS), Prof. M. HAUKKA (University of Jyväskylä), Dr. L. KIVIJARVI (University of Jyväskylä), and Dr. E. LAHTINEN (University of Jyväskylä). It was my pleasure to work with such excellent and helpful people. Thank you also to my fellow LRCS and LTI colleagues and friends for all the stimulating discussions, lab-work together, and for all the fun we have had in the last years. Special thanks to my officemates: Gaspard, Simon, Anurag, Sylvain, Waad, Neelam and Roberto. I would like to thank as well my great friends from the MESC family: Ronan, Laura, Abbos, Scott, Cris, Khrysllyn, Raulito, Ghulam and others MESC12.

Merci to Grégoire BG95, Mathieu and Virgile, my longstanding friends who came regularly, from my hometown, beautiful and sunny city of Toulouse, to see me in the rainy Amiens. Merci pour votre amitié les amigos et allez les verts (l'histoire retiendra qu'on était 1^{er} et toujours invaincus le jour de la soutenance de ma thèse...CQFD). Gracias to my Mexican family, - Othoniel, Diana and Teresa -, and friends - Luis Konrado, Aurora, Mari, Julio LOL, Adrián, Estefi, Porfi y Jimmy, who me apoyaron muchísimo during this PhD thesis, Viva Mexico! This thesis is also dedicated to all of my family relatives and particularly my grandmother. Merci aux familles MAUREL / GIMENEZ / REY / COLOMBAN d'avoir fait le déplacement pour ma soutenance. Enfin, merci à ceux qui ont assisté à ma soutenance en broadcast.

Finally, I am thankful to my beloved family: my parents Rose and Patrick as well as my brother Maxime. Cette thèse est pour vous. Thank you for always being here. Je vous aime très fort, I love you with all my heart. Une pensée pour mon petit Punky.

Last but not least, I would like to especially thank my lovely fiancée and soon to be wife Ana who always encouraged and stood by me throughout this PhD journey. Te debo muchísimo, todo esto no hubiera sido posible sin tu apoyo. Este fin de año 2020 / inicio de 2021 será un momento particular en nuestras vidas que siempre vamos a recordar. Es el final de una importante etapa de nuestras vidas, pero también el inicio de otra aún más grande y muy exitosa. En los próximos meses, será también tu turno defender tu PhD. Serás una Doctora brillante. Nunca olvidas que siempre vamos a ser los mejores. Je t'aime énormément.

Preface

This PhD thesis is based on the following articles. They are referred within the text by their corresponding Roman numbers.

I A. Maurel, M. Courty, B. Fleutot, H. Tortajada, K. Prashantha, M. Armand, S. Grugeon, S. Panier and L. Dupont. Highly Loaded Graphite–Polylactic Acid Composite-Based Filaments for Lithium-Ion Battery Three-Dimensional Printing, *Chemistry of Materials*, **30**, 7484 (2018).

II A. Maurel, S. Grugeon, B. Fleutot, M. Courty, K. Prashantha, H. Tortajada, M. Armand, S. Panier and L. Dupont. Three-Dimensional Printing of a LiFePO₄/Graphite Battery Cell via Fused Deposition Modeling, *Scientific Reports*, **9**, 18031 (2019).

III A. Maurel, M. Armand, S. Grugeon, B. Fleutot, C. Davoisne, H. Tortajada, M. Courty, S. Panier and L. Dupont. Poly(Ethylene Oxide)–LiTFSI Solid Polymer Electrolyte Filaments for Fused Deposition Modeling Three-Dimensional Printing, *Journal of The Electrochemical Society*, **167**, 070536 (2020).

IV A. Maurel, M. Haukka, E. MacDonald, L. Kivijärvi, E. Lahtinen, H. Kim, M. Armand, A. Cayla, A. Jamali, S. Grugeon, L. Dupont and S. Panier. Considering Lithium-ion Battery 3D-printing via Thermoplastic Material Extrusion and Polymer Powder Bed Fusion, *Additive Manufacturing*, 101651 (2020).

V A. Maurel, H. Kim, S. Grugeon, A. Jamali, M. Armand, M. Courty, H. Tortajada, S. Panier and L. Dupont. Ag-Cu/Polylactic Acid Composite Filament for Lithium-Ion Battery Current Collector Three-Dimensional Printing (*in preparation*).

VI A. Maurel, S. Grugeon, M. Armand, B. Fleutot, M. Courty, K. Prashantha, C. Davoisne, H. Tortajada, S. Panier, and L. Dupont. Overview on Lithium-Ion Battery 3D-Printing By Means of Material Extrusion, *ECS Transactions*, **98**, 13 (2020).

Reprints were made with permission from the respective publishers.

Table of contents

General introduction	1
Chapter 1. State of the art on lithium-ion battery 3D-printing	5
1.1. Lithium-ion battery	7
1.1.1. Working principle	8
1.1.2. Components.....	9
1.1.2.1. Electrodes	9
1.1.2.1.1. Active material for the positive electrode	10
1.1.2.1.2. Active material for the negative electrode	12
1.1.2.1.3. Binder	13
1.1.2.2. Separator	13
1.1.2.3. Electrolyte	15
1.1.2.3.1. Liquid electrolyte	15
1.1.2.3.2. Solid electrolyte and gel electrolyte	17
1.1.2.4. Current collectors	18
1.1.3. From 2D to 3D architectures	19
1.2. Additive manufacturing	21
1.2.1. Working principle	24
1.2.2. Lithium-ion battery 3D-printing	25
1.2.2.1. Material extrusion	26
1.2.2.1.1. Liquid deposition modeling/Direct ink writing	26
1.2.2.1.2. Fused deposition modeling	31
1.2.2.2. Vat photopolymerization	32
1.2.2.3. Powder bed fusion	36
Conclusions and scope of this thesis	39
References	41

Chapter 2. Composite filaments elaboration for LIB 3D-printing via fused deposition modeling	53
2.1. Introduction.....	54
2.1.1. Elaboration process.....	54
2.1.2. Polymer choice.....	56
2.1.3. Selection of a suitable solvent.....	58
2.2. Highly-loaded electrodes filaments formulation.....	60
2.2.1. Negative electrode.....	60
2.2.1.1. Preliminary tests.....	60
2.2.1.2. Influence of various plasticizers.....	61
2.2.1.3. Optimization of plasticizer content.....	64
2.2.1.3.1. Mechanical characterization and printability.....	65
2.2.1.3.2. Optimized filament homogeneity.....	67
2.2.1.3.3. Thermal characterization.....	69
2.2.1.4. Optimization of conductive additives content.....	73
2.2.1.4.1. Electrical conductivity.....	73
2.2.1.4.2. Electrochemical characterization.....	76
2.2.2. Positive electrode.....	82
2.2.2.1. Optimization of plasticizer content.....	82
2.2.2.2. Optimization of conductive additives content.....	82
2.2.2.2.1. Electrical conductivity.....	83
2.2.2.2.2. Printability and mechanical characterization.....	85
2.2.2.2.3. Thermal characterization.....	87
2.2.2.2.4. Electrochemical characterization.....	90
2.2.3. Comparison with contemporary studies.....	93
2.3. Separator filament formulation.....	96
2.3.1. Preparation.....	96
2.3.2. Optimization of the ceramic content.....	98
2.4. Current collector filament formulation.....	103
2.4.1. Silver coated copper powder.....	103
2.4.2. Composite film and filament.....	106
Conclusions.....	110
References	112

Chapter 3. 3D-Printing of a complete LIB cell via fused deposition modeling	117
3.1. Introduction.....	118
3.2. Overview of the faced printability issues.....	119
3.2.1. Composite filament-related issues.....	119
3.2.2. Classical FDM issues.....	121
3.2.2.1. Temperature issues.....	121
3.2.2.2. Build platform level calibration related issues.....	124
3.2.3. 3D-printers related issues and optimization.....	125
3.3. Complete LiFePO ₄ /graphite LIB 3D-printing.....	127
3.3.1. Cell assembly from independent 3D-printed components.....	127
3.3.1.1. Preliminary tests.....	127
3.3.1.2. Separator infill pattern.....	128
3.3.2. Cell 3D-printing in one-shot.....	132
3.3.2.1. Experimental procedure.....	132
3.3.2.2. Preliminary tests.....	133
3.3.2.3. Separator infill pattern.....	134
3.4. Towards the printability of complex 3D LIB architectures.....	140
3.4.1. 3D architectures impact on electrochemical performances.....	140
3.4.1.1. Introduction to the tested 3D architectures.....	140
3.4.1.2. Theoretical models and assumptions.....	144
3.4.1.3. Finite element model.....	146
3.4.1.4. Results and discussion.....	148
3.4.2. Multi-materials FDM printing.....	152
3.4.2.1. Commercially available options comparison.....	152
3.4.2.2. First tests.....	154
Conclusions.....	157
References	159

Chapter 4. Solid polymer electrolyte filament elaboration for LIB 3D-printing via fused deposition modeling	162
4.1. Introduction.....	163
4.1.1. Materials choice.....	163
4.1.2. Elaboration process.....	164
4.2. Determination of the optimized composition.....	164
4.2.1. Infrared analysis.....	165
4.2.2. Correlation between electrical and thermal characterization.....	166
4.3. Influence of the sample holder on conductivity values	173
4.3.1. Introduction to the various sample holders.....	173
4.3.1.1. Lateral sample holder.....	174
4.3.1.2. Sandwich sample holder.....	174
4.3.1.3. Interdigitated-comb sample holder.....	174
4.3.2. Distinct ionic conductivity values for a same sample.....	175
4.4. PEO/LiTFSI solid polymer electrolyte extrusion and 3D-printing.....	177
4.4.1. Filament extrusion.....	177
4.4.2. Mechanical properties deduced via nano-indentation.....	181
4.4.3. FDM 3D-printing.....	185
4.4.3.1. Classical 3D-printer.....	185
4.4.3.2. Modified 3D-printer.....	187
4.4.4. Comparison with contemporary studies.....	189
Conclusions.....	192
References	193

Chapter 5. PP-based LIB 3D-printing via FDM and SLS	197
5.1. Introduction.....	198
5.2. Polymer matrix: PLA vs. PP.....	199
5.3. PP-based positive electrode via SLS and FDM.....	199
5.3.1. Elaboration process.....	200
5.3.2. Printing of positive electrodes of the same composition.....	202
5.3.2.1. Electrical conductivity characterization	203
5.3.2.2. Electron microscopy	204
5.3.2.3. Electrochemical characterization	207
5.3.2.4. Mechanical characterization	209
5.3.3. Higher charge loading via FDM	210
5.3.3.1. Mechanical characterization	211
5.3.3.2. Electrical conductivity characterization	212
5.3.3.3. Electrochemical characterization	214
5.3.4. Future SLS and FDM independent electrodes optimization	215
5.3.4.1. SLS electrodes	215
5.3.4.2. FDM electrodes	216
5.3.5. Considering the complete LIB printability	218
Conclusions.....	219
References	221
General conclusions and perspectives	222
Abbreviations	226
Résumé développé de la thèse en Français (Summary in French)	230

General introduction

General introduction

Current world population being estimated to have reached 7.8 billion people at the time this thesis is written, the supply of clean and sustainable energy sources and storage systems, to meet the endless energy demand, is more than ever a major contemporary concern. Besides the expansion of renewable energy sources such as solar, wind or also hydro-electricity to replace traditional fossil fuels raising environmental concerns, energy storage devices have lately appeared as a decisive obstacle to address. Capable of capturing the energy produced at one time to deliver it at a later time when it is needed, the most widespread technology among the current various energy storage options is the lithium-ion battery. Nowadays, due to its promising performances regarding energy density, power and cycle life, it is a component found at the heart of all modern-day electronics: smartphones, laptops, electric scooters and electric vehicles. As they undeniably became imperative in our everyday life, these small devices have done the headlines recently as the Nobel Prize in Chemistry 2019 was awarded on October 9, 2019 to three researchers (Goodenough-Whittingham-Yoshino) for their pioneering work on this particular technology of batteries. While current commercial lithium-ion batteries consist of stacked leaflets (2D planar design), innovative approaches are now required to enable the development of 3D complex architectures reported to significantly improve the electrochemical performances in term of power. Furthermore, the request to build flexible, wearable and customizable batteries of any shape while maximizing the energy storage as well as diminishing volume and weight must be addressed.

Additive manufacturing, also called 3D-printing, appears as a cutting-edge revolutionary discipline based on the 3D items preparation by addition of material layer-upon-layer. This innovative technology precisely enables to implement topological optimization of energy-storage devices. Indeed, battery components such as electrodes, separator, electrolyte and current collectors can be tailored with any shape, therefore allowing the future direct incorporation of batteries and all electronics within the final three-dimensional object. Moreover, the ability of this technique to build promising complex three-dimensional (3D) electrode architectures reported to theoretically enhance significantly the lithium-ion battery performances in terms of power and capacity make it appealing. Among the various additive manufacturing processes, Fused Deposition Modeling

emerges as a promising option in order to achieve complete lithium-ion battery without the necessity to perform any post-processes.

In this context, this PhD thesis was done under the joint supervision of two laboratories, respectively specialized on the formulation and characterization of materials for lithium-ion batteries and on 3D-printing and mechanical engineering:

- the Laboratoire de Réactivité et Chimie des Solides (LRCS), located at Picardie Jules Verne University in Amiens, France;
- the Laboratoire des Technologies Innovantes (LTI) located at Picardie Jules Verne University in Amiens, France.

Joining both laboratories expertise, this PhD thesis was focused on the development of Lithium-ion Battery 3D-Printing using Fused Deposition Modeling.

Chapter 1: The first chapter of this thesis consists of a literature review introducing the lithium-ion battery and additive manufacturing working principles. The advantages of moving from a 2D design to a 3D battery design as well as an overview of the recent advances in 3D-printed lithium-ion batteries are presented.

Chapter 2: In the second chapter, in order to feed a Fused Deposition Modeling 3D-printer, the formulation process of composite filaments corresponding to the positive and negative electrodes but also the separator and current collector of a lithium-ion battery operating with a liquid electrolyte is portrayed. The impact of plasticizer addition on mechanical properties and printability is thoroughly depicted. Considering the optimized plasticizer composition for the electrodes, an exhaustive study is carried out to identify the electrical and electrochemical impact of conductive additives. The incorporation of ceramic particles within the separator in order to favor the liquid electrolyte impregnation is described.

Chapter 3: Starting from the optimized filaments composition, the third chapter is dedicated to the assembly from independent 3D-printed components (stacking), and direct printing of the complete LIB in a single step (one-shot). The printing difficulties faced are here detailed. Taking advantage of the new design capabilities conferred by Fused Deposition Modeling, separator patterns and infill density are examined to improve the liquid electrolyte impregnation and avoid short-circuits. Electrochemical performances of the complete cells are evaluated by performing galvanostatic tests and interpretation of the results is revealed. Finally, a modeling study enabling the comparison of various 3D batteries architectures is introduced and an overview of the commercially available multi-materials options offered to print such complex designs is given.

Chapter 4: The fourth chapter of this thesis is a preliminary study devoted to the future printability of an all-solid-state lithium-ion battery through Fused Deposition Modeling. The advantage of such a technology in comparison with a battery using a more standard liquid electrolyte is depicted. In this part, a development and optimization of a solid polymer electrolyte filament is described in order to enhance the ionic conductivity and modifications of a Fused Deposition modeling 3D-printer to facilitate its printability are introduced. The impact of three different electrochemical impedance spectroscopy sample holders (lateral, sandwich and interdigitated-comb) on the final ionic conductivity value is presented.

Chapter 5: Finally, acting as a perspective study, fifth chapter is focused on the elaboration of a polypropylene (PP)-based positive electrode for a lithium-ion battery using a liquid electrolyte. In parallel with the fused deposition modeling additive manufacturing process, the ability of the selective laser sintering process is also examined to 3D-print PP-based LIB components for purposes of comparison. Requirements for printing materials, resolution, advantages and drawbacks of each technique to print PP electrodes and complete lithium-ion battery are discussed.

Chapter 1.

State of the art on lithium-ion battery 3D-printing

Chapter 1. State of the art on lithium-ion battery 3D-printing

1.1. Lithium-ion battery	7
1.1.1. Working principle	8
1.1.2. Components.....	9
1.1.2.1. Electrodes	9
1.1.2.1.1. Active material for the positive electrode	10
1.1.2.1.2. Active material for the negative electrode	12
1.1.2.1.3. Binder	13
1.1.2.2. Separator	13
1.1.2.3. Electrolyte	15
1.1.2.3.1. Liquid electrolyte	15
1.1.2.3.2. Solid electrolyte and gel electrolyte	17
1.1.2.4. Current collectors	18
1.1.3. From 2D to 3D architectures	19
1.2. Additive manufacturing	21
1.2.1. Working principle	24
1.2.2. Lithium-ion battery 3D-printing	25
1.2.2.1. Material extrusion	26
1.2.2.1.1. Liquid deposition modeling/Direct ink writing	26
1.2.2.1.2. Fused deposition modeling	31
1.2.2.2. Vat photopolymerization	32
1.2.2.3. Powder bed fusion	36
Conclusions and scope of this thesis	39
References	41

1.1. Lithium-ion battery

Encouraged by the high demand on portable electronic devices and the anticipated commercialization of electric vehicles, last decades have witnessed the elaboration and expansion of new energy storage systems.^{1,2} Among them, lithium-ion batteries (LIB) appeared as the system of choice due to their promising electrochemical performances (**Figure 1.1**) offering high energy density, power density, efficiency and long cycle life.³⁻⁵ Despite the impressive growth in sales of LIB worldwide, research strategies and challenges still remain on the synthesis, characterization, electrochemical performance and safety improvements.

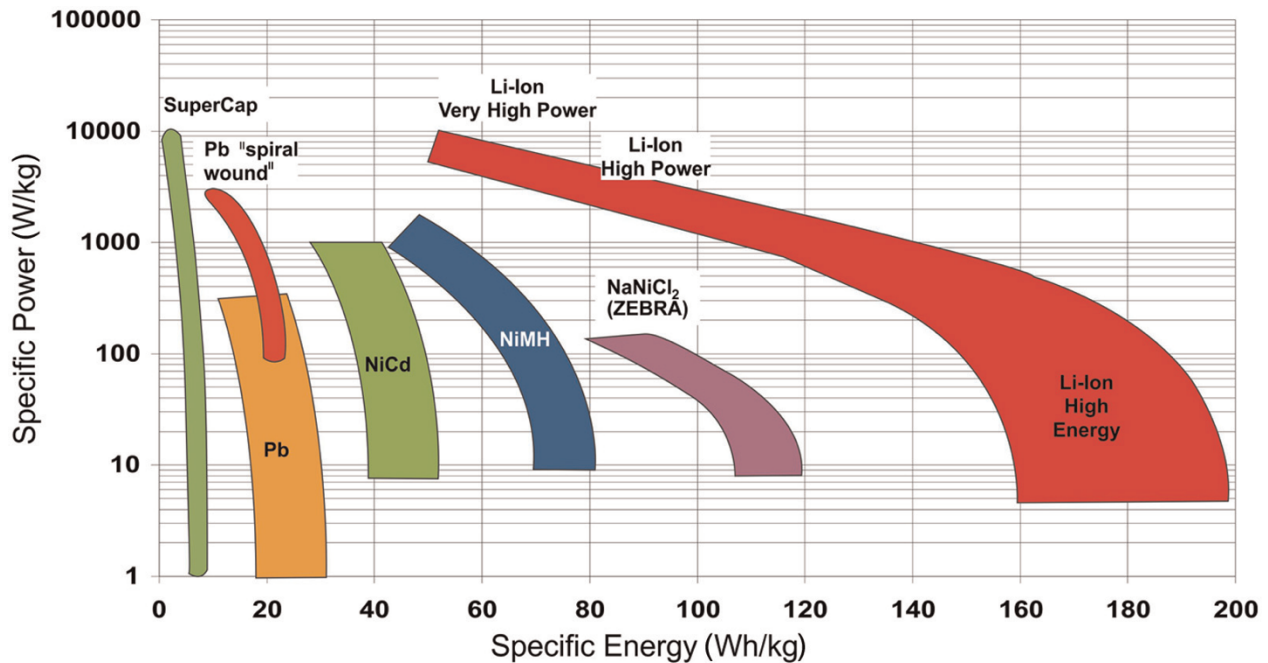


Figure 1. 1. Comparison of various energy storage systems technologies in terms of power and gravimetric energy density. (SuperCap: supercapacitor; Pb: lead; Li-ion: lithium-ion; NiCd: nickel–cadmium; NiMH: nickel–metal hydride; NaNiCl₂: sodium–nickel chloride; ZEBRA: Zero Emission Battery Research Activities). Reproduced with permission from ⁵. Copyright 2013 Sage publications.

1.1.1. Working principle

Operating as an electrochemical generator, commercial lithium-ion battery (**Figure 1.2**) consists of two electrodes which are isolated electronically by a separator membrane impregnated within a liquid electrolyte in charge of ensuring the good Li^+ ionic conductivity. Through oxidation-reduction reactions, the stored chemical energy is thus converted into electrical energy. During the discharge, lithium ions (Li^+) migrate from the negative electrode to the positive electrode through the electrolyte while electrons are released (oxidation) from the negative electrode and reach the positive electrode (reduction) through the external circuit. The opposite reactions occur during the battery charge. The negative and positive electrodes are usually respectively designated as anode and cathode with respect to the reactions happening during discharge. The total Gibbs free energy change due to the electrochemical reactions on both electrodes is directly linked to the selected electrode materials. Given the overall electrochemical reaction and charges transferred, the theoretical cell voltage ($\Delta E = -\Delta G/nF$) can be calculated.⁴

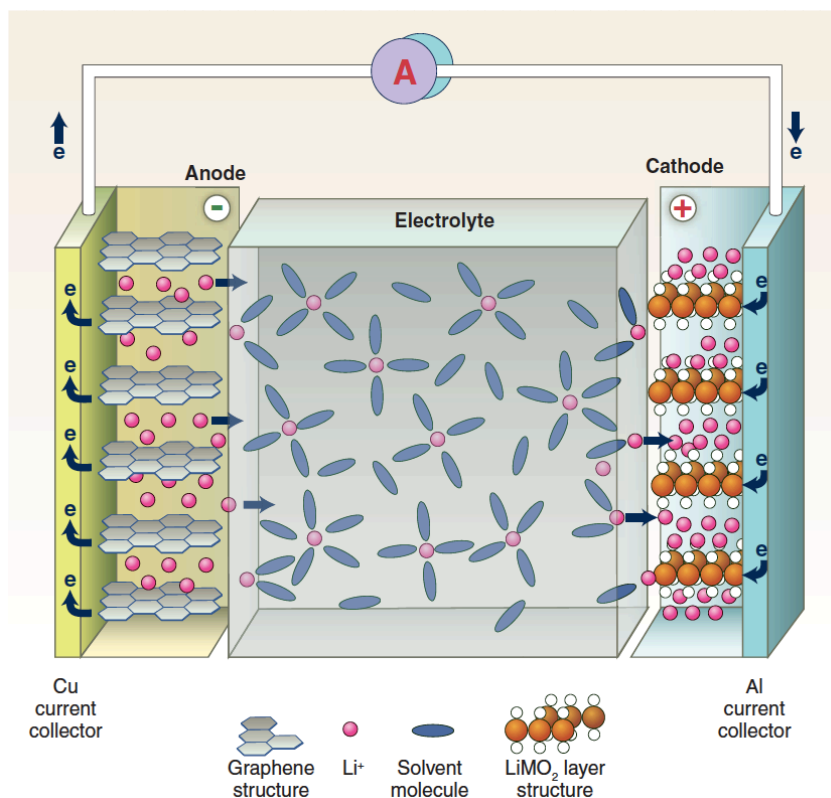


Figure 1. 2. Schematic of a lithium-ion battery. Reproduced with permission from ¹. Copyright 2011 Science.

From the electrochemical point of view, battery performances are generally given by parameters such as the capacity, the energy, the power and the cyclability. The battery capacity describes the total electric charges provided by the cell. This parameter, generally expressed in Ah kg⁻¹ of active material, is constantly reported at a particular current density (or cycling rate) defined as the amount of charge flowing per time unit. On the other hand, the specific energy of a battery indicates how much energy a battery can hold which is generally expressed in Wh kg⁻¹ or Wh L⁻¹, while the power density expressed in W kg⁻¹ or W L⁻¹ depicts the speed at which the energy is released. Finally, the cyclability parameter corresponds to the reversibility of the Li⁺ insertion and extraction processes, in terms of the number of charge and discharge cycles before the battery loses efficiency.⁴

1.1.2. Components

1.1.2.1. Electrodes

Nowadays, most of positive and negative electrodes consist in composites materials. These latter comprise an active material (**Figure 1.3**) conferring adequate electrochemical performances, conductive additives allowing the good electronic conductivity and also a binder/polymer-matrix contributing to improve the cohesion between these different particles.

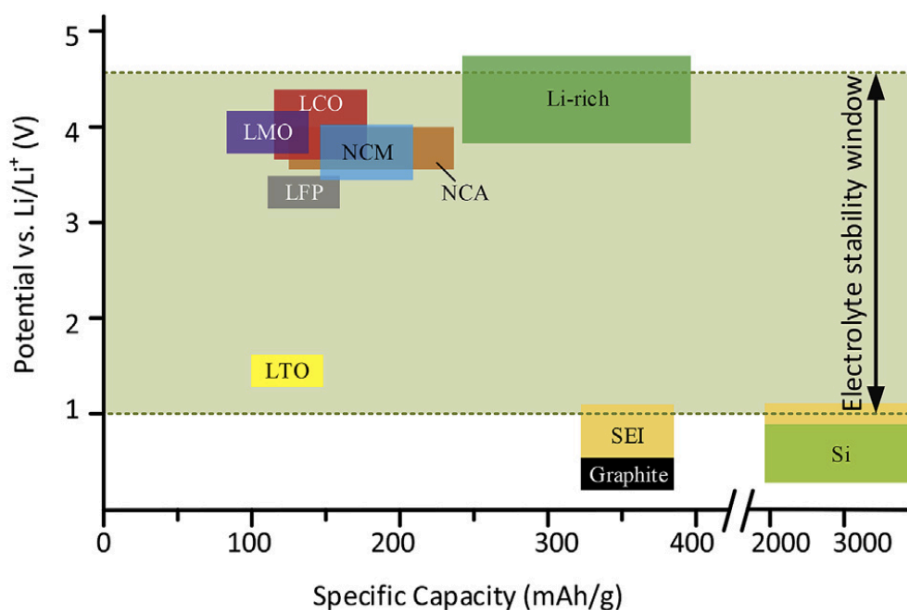


Figure 1. 3. Potential and specific capacity of commonly used active materials in lithium-ion batteries. Reproduced with permission from ⁶. Copyright 2019 Elsevier.

1.1.2.1.1. Active material for the positive electrode

Most of the positive electrodes used in commercial lithium-ion batteries involve the use of transition metal oxides as active material (**Figure 1.4**). These materials are capable of reversibly insert lithium ions within their respective structure without causing any major structural damage.⁷⁻

9

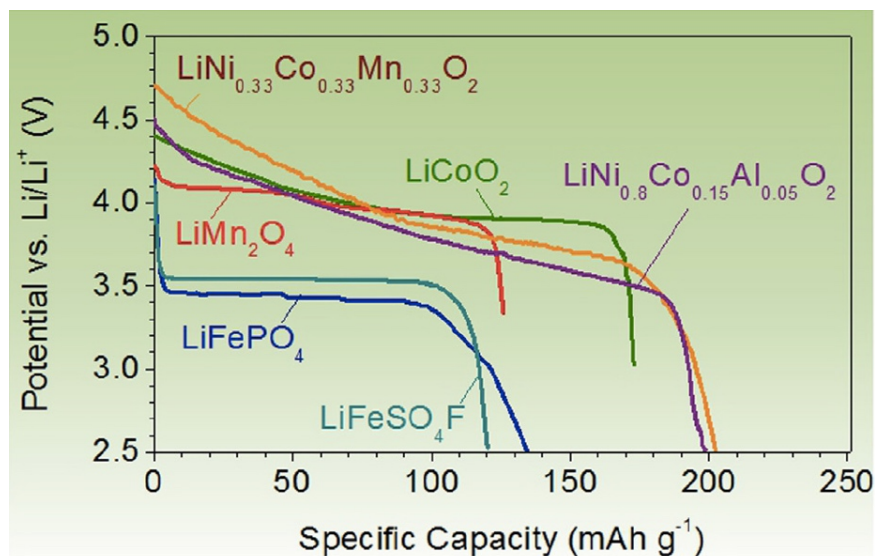


Figure 1. 4. Discharge profiles of representative intercalation cathode materials. Reproduced with permission from ⁸. Copyright 2015 Elsevier.

Among them, the lamellar structure oxide LiCoO_2 (LCO), discovered by Goodenough¹⁰ in the 1980s and first commercialized by SONY under the guidance of Yoshino¹¹, still remains a compound of choice for portable electronics applications. Presenting a theoretical capacity of 274 mAh g^{-1} , its operating potential is nonetheless limited to 4.2 V with a view to preserve its structure. Indeed, after 50% of the lithium is extracted from the structure, a transformation from hexagonal to monoclinic phase is observed, thus having a detrimental effect upon cycling. Hence, its structural instability reduces the practical electrochemical capacity to a lower capacity value of 140 mAh g^{-1} . Owing to the limited capacity, its high cost and toxicity, its use for large scale applications has been prevented.¹²

On the other hand, introduced by Ohzuku¹³ in 2001 and enabling to reach higher energy density due to the presence of nickel, the oxide material $\text{LiNi}_x\text{Mn}_y\text{Co}_z\text{O}_2$ (NMC) is nowadays a

promising material employed in hybrid and electric cars. Considering the composition $\text{LiNi}_{1/3}\text{Mn}_{1/3}\text{Co}_{1/3}\text{O}_2$, high practical reversible capacity is described in literature¹², reaching up to 200 mAh g^{-1} in the cut-off voltage range 2.8-4.6 V and 160 mAh g^{-1} in 2.5-4.4 V making it indeed very appealing for high power and high energy lithium-ion batteries. With a view to increase even further the energy density and reduce the cost, cobalt which is used within the NMC to preserve the structure stability was substituted by more abundant and cheaper element such as nickel. This recently led to the commercialization by the car manufacturer Tesla of the $\text{LiNi}_{0.8}\text{Co}_{0.15}\text{Al}_{0.05}\text{O}_2$ (NCA) having a higher practical capacity of about 180 mAh g^{-1} in the cut-off voltage range 2.7-4.4 V.^{14, 15} Nonetheless, this material faced capacity loss upon cycling due to the appearance of particles cracks.¹⁶

Available at a lower cost, being safer and environmentally-friendly, the spinel oxide LiMn_2O_4 (LMO) appears as an alternative to the options enumerated previously. Nonetheless, while its unique MnO_2 framework creating a three-dimensional diffusion pathway for lithium ions, provides an admirable rate capability, it experiences an important capacity fading upon cycling at a temperature higher than 50°C which is due to the manganese dissolution (Jahn Teller effect). Hence, the practical capacity is about 120 mAh g^{-1} .^{8, 12, 17} Various strategies to avoid the manganese dissolution and minimize the capacity fading were introduced such as the doping of LiMn_2O_4 with Ni to obtain the composition $\text{LiMn}_{1.5}\text{Ni}_{0.5}\text{O}_4$ (LMNO). The latter depicts the most promising electrochemical performance (140 mAh g^{-1}), with high operating voltage (up to 4.7 V) and good rate capability.¹²

Olivine phosphate materials such as the LiFePO_4 (LFP) have also been considered as a promising active material to replace the traditional layered positive electrodes.¹⁸ Indeed, it offers the advantage of presenting low cost, low toxicity, good safety, high mechanical strength and low capacity fade under high current density making this material very promising for power applications.^{7, 19} Moreover, this compound depicts relatively high specific capacity reaching about 170 mAh g^{-1} theoretically (162 mAh g^{-1} practically in the 2.8 – 3.8 V potential range)²⁰. Nonetheless, it is considerably limited by its low electronic conductivity ($10^{-9} \text{ S cm}^{-1}$) and low discharge plateau appearing around 3.4 V. By achieving a simple carbon coating, electronic conductivity was reported to be able to increase up to $10^{-2} \text{ S cm}^{-1}$.²¹

1.1.2.1.2. Active material for the negative electrode

Due to its important electronegativity (-3.05 V vs. standard hydrogen electrode) and high theoretical specific capacity reaching 3800 mAh g⁻¹ thanks to its low weight (M = 6.94 g mol⁻¹ and density $\rho = 0.53$ g cm⁻³), lithium metal was first considered as negative electrode. Nonetheless, its use was particularly limited due to the formation of dendrites in contact with organic liquid electrolyte, leading to important safety issues such as the battery short-circuit upon cycling.²

For these reasons, the use of much safer composite carbonaceous negative electrodes was introduced.²² Nowadays, most common negative electrode material is centered on the well-established graphite (working voltage about 0.05 V).¹¹ This latter, able to insert one lithium ion within six carbon atoms, depicts a theoretical specific capacity of 372 mAh g⁻¹, making this material unfortunately limited in comparison with metallic lithium. Considering graphite as active material, a little volume expansion up to 10% can be observed during the lithium ions insertion between the graphene sheets. Unfortunately, this swelling phenomenon can lead to the undesired formation of cracks within the structure.^{23, 24}

To avoid this phenomenon, spinel structure material such as Li₄Ti₅O₁₂ (LTO) has also been considered as a promising active material to replace the traditional layered negative carbonaceous electrodes.^{25, 26} Indeed, while its theoretical capacity is much lower (only 175 mAh g⁻¹) than graphite, its very low volume expansion (0.2%) makes it a material of choice for power application.²⁷

On the other hand, silicon was thoroughly studied for its use in negative electrodes due to its high theoretical specific capacity reaching 4000 mAh g⁻¹ (working potential about 0.4 V).²⁸ Nonetheless, the use of pure silicon is not feasible because of its significant volume expansion of about 400% upon cycling.^{29, 30} Hence, recent studies investigate the addition of a small fraction of silicon within a carbonaceous material to reach high capacity and good cycling retention.^{31, 32}

Finally, it is worth mentioning that through the lithium-ion battery first charge, a passivation layer called solid electrolyte interphase (SEI) created from the liquid electrolyte reduction is deposited at the negative electrode surface that allows it to operate beyond its electrochemical

stability window. While the formation of a homogeneous layer is contributing to the battery good electrochemical performances, the formation of a non-homogeneous layer in combination with extreme cycling conditions is often responsible for the battery electrochemical performances degradation.^{33, 34}

1.1.2.1.3. Binder

Indispensable within both electrodes in order to confer adequate mechanical strength and facilitate their production, the binder serving as a polymer matrix represents usually only ~2wt% of the total weight of the composite electrode. In comparison, the active material represents ~95wt% and the conductive additives ~3wt%. Preferably electrochemically inert, the binder role is to join together homogeneously the active material and conductive additives particles but also to enable a good adhesion with the current collector.

Thanks to its good electrochemical stability, polyvinylidene fluoride (PVDF) was first used on both electrodes of commercial lithium-ion batteries. Nonetheless, as the use of this material implicates the handling of toxic solvents such as N-methyl-2-pyrrolidone (NMP) during the electrodes manufacturing, research led to other more environmentally-friendly binder that would rather dissolve within an aqueous solvent. Among them, styrene-butadiene rubber (SBR) and/or carboxymethyl cellulose (CMC) emerged as a better option especially with graphite negative electrode.³⁵ Nevertheless, it is important to emphasize that PVDF still remain highly used within commercial positive electrodes. Indeed, SBR contains double bonds in its backbone that are prone to be oxidized. Also, while it was demonstrated that CMC can be used for positive composite electrodes composed of NMC or LFP as active material,³⁶ degradation of the active material and aluminum current collector tends to occur because of the presence of the aqueous medium, thus resulting in cell impedance increase, capacity loss and gas generation.

1.1.2.2. Separator

Within a lithium-ion battery, the separator acts as a physical barrier placed between both electrodes. Electronically insulator and ionically conductive, these electrochemically inactive microporous membranes are usually made of polyolefin such as polyethylene (PE) and/or

polypropylene (PP). These separators are generally less than 30 μm thick with pores diameter between 0.03 et 0.1 μm .³⁷

Considering a monolayer separator composed either of PE or PP, upon extreme heat, due to the melting of the polymer, the pores are close. This phenomenon is expected to act as an internal safety and prevents from thermal runaway of the lithium-ion battery. In order to strengthen this safety measure, preventive actions such as the use of tri-layered separator (**Figure 1.5**) composed of PP/PE/PP, in which polyethylene is placed in between two layers of polypropylene, was established. Here, upon excessive heat, the PE presenting the lower melting temperature (130 °C) melts and its pores close, thus shutting-down the battery cell. The outer PP layer having a higher melting temperature ($\sim 150^\circ\text{C}$) remains in the solid state, thus making the physical barrier more efficient in comparison with a monolayer separator. Recently, additional enhancements were completed by adding a ceramic coating onto the separator. Upon extreme heat, ceramic particles do not melt and thus promotes a superior safety.³⁸

Finally, it is worth-mentioning that the separator should remain as thin as possible to minimize internal resistance. Also, the latter must be compatible with the electrolyte and enable good impregnation.

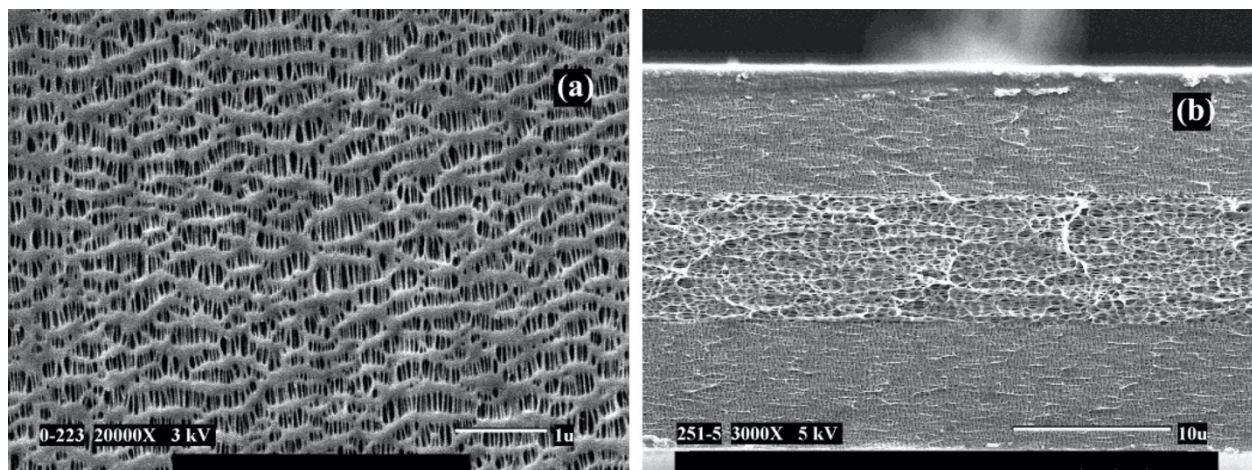


Figure 1. 5. Scanning electron micrographs of Celgard 2325 (PP/PE/PP) separator used in lithium-ion batteries: (a) surface SEM and (b) cross-section SEM. Reproduced with permission from ³⁷. Copyright 2004 American Chemical Society.

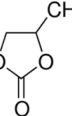
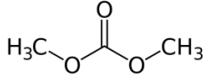
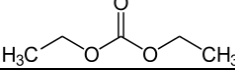
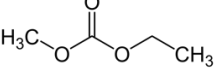
1.1.2.3. Electrolyte

As a key-component of lithium-ion batteries, the electrolyte has a critical responsibility concerning both electrochemical performance and safety of the final device. It should be electronically insulator but must exhibit ionic conductivity as high as possible. Last but not least, it must be chemically inert toward the electrode's components and electrochemically stable within the potential window. While commercial lithium-ion battery typically involves organic solvent-based liquid electrolytes, other technologies implicating the use of gel or solid electrolytes (ceramic or polymer-based) are being developed to overcome the concerns raised by the solvent's volatility and flammability.

1.1.2.3.1. Liquid Electrolyte

A liquid electrolyte is composed of a lithium salt dissolved in organic solvents mixture. As described by Marcinek et al.,³⁹ an ideal electrolyte solvent should be able to dissolve lithium salts to sufficient concentration, its viscosity should be low to enable fast ion transport, be inert with all cell components especially positive and negative electrode materials and the current collectors, have sufficient wettability towards the electrodes and separator, and remain liquid in a wide temperature range. Organic solvents usually used in batteries are based on a mixture of cyclic and linear carbonates (**Table 1.1**). They promote respectively the lithium salt dissociation (as cyclic carbonates such as ethylene carbonate (EC) and propylene carbonate (PC) have a high dielectric constant) and the lithium ion mobility in the electrolyte (due to the low viscosity of linear carbonates such as dimethyl carbonate (DMC) and diethyl carbonate (DEC) and ethyl methyl carbonate (EMC)). Nonetheless, main drawback of EC is its relatively high melting temperature limiting its use at low temperature. Also, PC was reported to regrettably exfoliate the graphite (active material for the negative electrode).⁴⁰

Table 1. 1. Physical properties of most common solvents employed in commercial LIB ⁴¹

Solvent	Structure	Density (g cm ⁻³)	Dielectric constant ϵ	Viscosity (cP at 25°C)	T _{melting} (°C)	T _{boiling} (°C)
EC		1.327	89.78	1.9 (40°C)	36.4	248
PC		1.200	64.92	2.53	-48.8	242
DMC		1.063	3.107	0.63	4.6	91
DEC		0.969	2.805	0.77	-74.3	126
EMC		1.006	2.958	0.65	-53.0	110

On the other hand, lithium salts must present high thermal and chemical stability, passivate the aluminum current collector from anodic dissolution, exhibit very high ionic conductivity within the solvent, be able to completely dissolve and dissociate in non-aqueous media and contribute to the homogeneous formation of the SEI at the negative electrode surface. Besides, solvated lithium ions must present high mobility (high transference number) in the media. Anion species must remain inert with the electrolyte solvents and present low toxicity. Nowadays, lithium hexafluorophosphate LiPF₆ is the most employed in commercial lithium-ion batteries as it exhibits high ionic conductivity within different solvents at ambient temperature (**Table 1.2**).

Table 1. 2. Ionic conductivity of most commonly used commercial liquid electrolytes.⁴¹

1 M LiPF ₆	EC : DMC (50 : 50 vol.%)	EC : DEC (50 : 50 vol.%)	EC : PC (50 : 50 vol.%)
Ionic conductivity at 20 °C (S cm ⁻¹)	1.05×10 ⁻²	7.5×10 ⁻³	6.5×10 ⁻³

1.1.2.3.2. Solid electrolyte and gel electrolyte

While concerns about the use of organic solvent-based liquid electrolytes are raised due to their volatility and flammability, all-solid-state devices represent a safer alternative enabling the use of lithium metal at the negative electrode. Hence, many studies focused their attention on the development of high-performance solid electrolytes (ceramic or polymer).³⁹

Typical materials used as inorganic ceramic solid electrolytes comprise Garnet-type oxides ($\text{Li}_5\text{La}_3\text{M}_2\text{O}_{12}$ with $\text{M} = \text{Zr}, \text{Ta}, \text{Hf}$ or Nb) and sulfides.^{42, 43} Amongst the several Garnet-type reported ceramic electrolytes, $\text{Li}_7\text{La}_3\text{Zr}_2\text{O}_{12}$ (LLZO) has been involved in many studies.⁴⁴⁻⁴⁶ The development of $\text{Li}_{6.75}\text{La}_3\text{Zr}_{1.75}\text{Ta}_{0.25}\text{O}_{12}$ cubic garnet with a conductivity value equals to $8.7 \times 10^{-4} \text{ S cm}^{-1}$ at 25°C was for example described by Allen et al.⁴⁷ Unfortunately, main drawbacks of these ceramic oxide solid electrolytes are their poor mechanical behavior and important charge transfer resistance conferred by the poor interface fit with the electrodes. In parallel, sulfide-based solid electrolytes were developed.⁴⁸ This includes for example $\text{Li}_{3.25}\text{Ge}_{0.25}\text{P}_{0.75}\text{S}_4$ which depicts a relatively high ionic conductivity ($2.2 \times 10^{-3} \text{ S cm}^{-1}$ at RT) and good electrochemical stability.⁴⁹ Also, much more conductive $\text{Li}_{10}\text{GeP}_2\text{S}_{12}$ (LGPS) ($1.2 \times 10^{-2} \text{ S cm}^{-1}$ at RT) and $\text{Li}_{9.54}\text{Si}_{1.74}\text{P}_{1.44}\text{S}_{11.7}\text{Cl}_{0.3}$ (LSPSC) ($2.5 \times 10^{-2} \text{ S cm}^{-1}$ at RT) are very promising.⁵⁰ Nevertheless, it is worth mentioning that both LGPS and LSPSC have poor chemical stability with lithium metal. Last but not least, LGPS is quite expensive because of the introduction of germanium.

Distinct from the inorganic ceramic solid electrolytes which are inherently rigid, the solid polymer electrolytes (SPE) represent an exciting alternative thanks to their good flexibility and safety behavior with lithium metal.³⁹ With a view to reach high conductivity values, several polymer matrix including the notorious poly(ethylene oxide) (PEO) or poly(vinylidene fluoride) (PVDF) were studied in details.^{51, 52} In particular, thanks to its faculty to solvate lithium cations through interaction of its ether oxygens, PEO has been investigated extensively.^{53, 54} Pioneering work was completed by Berthier and Armand who primary attributed the ionic conductivity to the amorphous phases of the PEO/lithium-salt system using NMR.⁵⁵ This significant understanding subsequently led further studies to increase these regions by eliminating crystallinity. Still, PEO-based SPE depicts generally low ionic conductivities (10^{-8} – $10^{-5} \text{ S cm}^{-1}$ at RT) compared to liquid electrolytes (10^{-3} – $10^{-2} \text{ S cm}^{-1}$ at RT) and thus have not been accepted broadly in commercial

batteries. With a view to attain enough ionic conductivity for battery application, the latter needs to be operating around 80 and 90°C.⁵³ In this temperature range, the solid-polymer electrolyte is in a viscous state, facilitating the lithium-ion displacement. Over the last decades, cutting-edge studies were reported in order to increase the SPE ionic conductivity by reducing crystallinity while enhancing the mechanical strength through the introduction of inorganic nanofillers such as SiO₂ or Al₂O₃ within the polymer matrix.⁵⁶⁻⁵⁸

These findings paved the way toward promising hybrid solid electrolytes based on the incorporation of inorganic ceramics solid electrolyte within classical polymer electrolyte matrix, thus combining the advantages of both types of electrolytes. Liu et al.⁵⁸ reported for example the introduction of Li_{0.33}La_{0.557}TiO₃ (LLTO) nanowires within a polyacrylonitrile (PAN) polymer matrix with LiClO₄. Remarkably, compared with random oriented nanowires, aligned nanowires induce one order of magnitude enhancement in ionic conductivity (6.05×10^{-5} S cm⁻¹ at 30°C). Recently, Yu et al.⁵⁹ reported a polymer/ceramic composite solid electrolyte for the operation of all-solid-state sodium batteries. The latter was obtained by dispersing Na₃Zr₂Si₂PO₁₂ into a PEO–sodium perchlorate (NaClO₄) matrix (EO:Na⁺ = 15:1). The resulting hybrid electrolyte depicted a conductivity of 5.6×10^{-4} S cm⁻¹ at 60°C and a long-term electrochemical stability.

Last but not least, with a view to take advantage of both liquid and solid electrolytes, gel polymer electrolytes (GPE) (semi-solid) operating at ambient temperature have appeared as a good option.^{60, 61} It consists of polymeric membranes acting as physical separator and being gelled when soaked within a liquid electrolyte due to the polymer/solvent interactions. When employed, a compromise between conductivity and mechanical properties must be found.

1.1.2.4. Current collectors

Current collectors being the direct connection between the electrode and the external circuit, they must exhibit electronical conductivity as high as possible. Hence, metal foils are usually employed in commercial LIB. Nonetheless, the metal selection for each current collector should be chosen in good agreement with their own electrochemical stability window.

Copper foil is generally employed as current collector at the negative electrode as it appears to be electrochemically stable between 0 and up to 3 V vs. Li/Li⁺. Above this value, it will then start oxidizing.⁶² On the other hand, aluminum foil current collector (cheaper and lighter) is used at the positive electrode as it is stable at higher potential due to the AlF₃ passivating layer created thanks to the presence of LiPF₆ salt,⁶³ thus blocking subsequent aluminum oxidation. Al is not used at the negative electrode as an Li–Al alloying process starts when potential is close to ~0.3 V vs. Li/Li⁺.⁶² Practically, extended corrosion of current collectors under cycling can lead to an increase of the cell overall resistance causing capacity fading. In extreme cases, it could even induce short-circuit, affecting the device safety.⁶²

Finally, it is important to mention that metallic foil current collectors, serving as support for the coated electrodes, can generate some adhesion issues due to their smooth surface. Indeed, metallic foils can unfortunately cause the active material particles detachment reported to be particularly problematic for flexible electrodes manufacturing. Hence, carbon-based materials or conducting polymers are potential candidates for flexible current collectors.⁶⁴

1.1.3. From 2D to 3D architectures

Commercial lithium-ion batteries involve two-dimensional (2D) parallel-plate arrangement in which the electrodes and separator films are usually stacked (pouch cell) or rolled (**Figure 1.6.a**).⁶⁵ In such a 2D battery planar design, the lithium ions diffusion is accomplished in one direction, thus reported to considerably limit the performances of the cell.^{66,67} In order to enhance performances, 3D lithium-ion battery designs (**Figure 1.6.b**) have been considered in the past. Long et al.⁶⁶ introduced different 3D architectures allowing more efficient Li⁺ diffusion path in two and three-dimensions. Moving from 2D electrodes to a 3D electrodes designs, an increased electrochemical active surface present on the same footprint area is achieved, thus leading theoretically to improve specific capacity and power performances⁶⁸ (cf. **3.4.1. 3D architectures impact on electrochemical performances** and cf. **Preface — IV**).

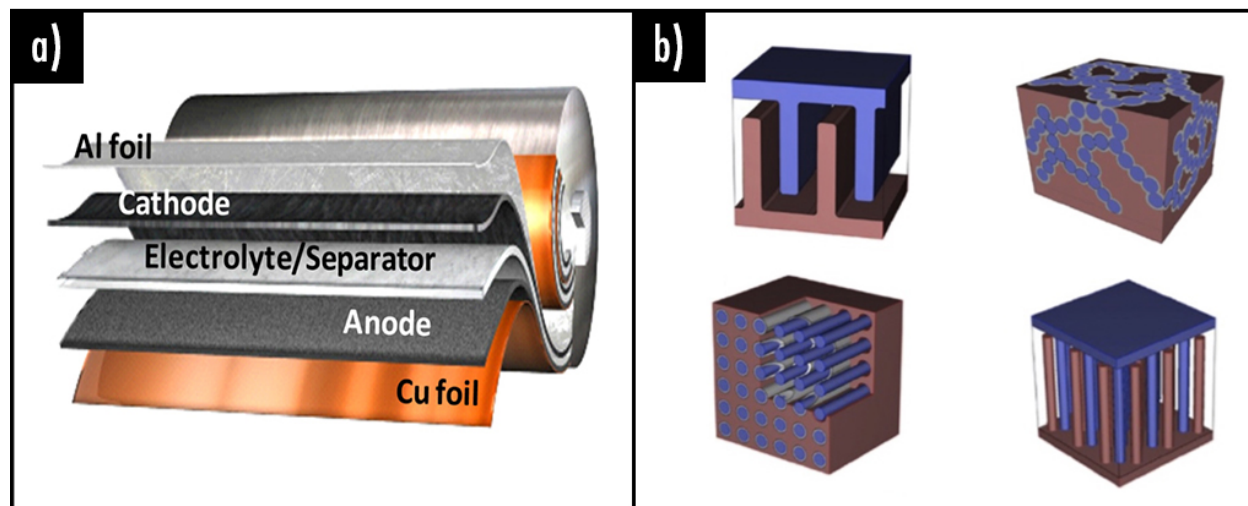


Figure 1. 6. (a) Scheme of a conventional cylindrical 2D Li-ion battery allowing Li^+ diffusion in one direction. Reproduced with permission from ⁶⁵. Copyright 2012 Scientific Reports; (b) Examples of potential 3D architectures for batteries: positive electrode (blue); negative electrode (red); electrolyte (grey/empty voids). Reproduced with permission from ⁶⁷. Copyright 2010 Elsevier.

From these promising theoretical results, the elaboration of independent 3D electrode pillars (negative or positive) and 3D micro-batteries assembly were investigated (**Figure 1.7**).⁶⁹⁻⁷³ An electrochemically assisted template growth of Cu nanorods onto a current collector followed by electrochemical plating of Fe_3O_4 was performed by Taberna et al.⁷¹ Similarly, Min et al.⁷⁰ reported the development of carbon posts arrangements interdigitated with dodecylbenzenesulfonate doped polypyrrole (PPYDBS) posts (**Figure 1.7.a-b**). Carbon electrode arrays and carbon current collectors were obtained by patterning the photoresist using photolithography and pyrolyzing the patterned photoresist. PPYDBS was then electrochemically polymerized on one set of the 3D carbon arrays.

While these architectures were reported to be very promising, the assembly of the final 3D apparatus by interpenetration of both electrodes still suffered from the electrodes surface irregularities (**Figure 1.7.c-e**) leading to short-circuit upon cycling. Hence, in this context, innovative manufacturing technologies allowing the 3D positive and negative electrodes perfect fitting, making sure to prevent any contact, are necessitated. These interpenetration concerns could be achieved for example through the cutting-edge Additive Manufacturing technologies.

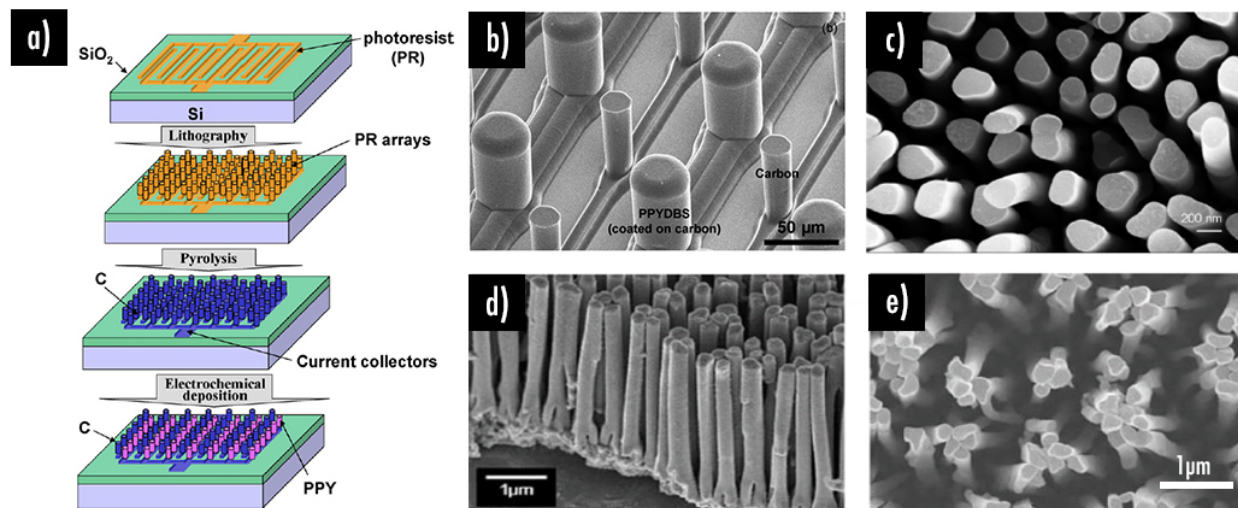


Figure 1. 7. (a) Preparation of the carbon/polypyrrole 3D battery; (b) SEM image of C/PPYDBS post arrays. Figures (a) and (b) were reproduced with permission from ⁷⁰. Copyright 2007 Elsevier; (c) SEM micrograph of electrodeposited aluminum nanorods. Reproduced with permission from ⁷². Copyright 2011 Elsevier; (d) SEM cross-sectional view of Cu-nanopillars grown in a Cu substrate; (e) SEM top view of Ni-nanopillars grown in a Ni substrate. Figures (d) and (e) were reproduced with permission from ⁷³. Copyright 2011 The Royal Society of Chemistry.

1.2. Additive manufacturing

Additive manufacturing (AM), also called 3D-printing, is a recent manufacturing technique employed to fabricate an extensive variety of structures and complex geometries from three-dimensional model data.⁷⁴⁻⁷⁸ Based on the printing of consecutive layers of materials deposited on top of each other, this innovative manufacturing technology, known originally as stereolithography (SLA), was first developed in 1986 by French (Alain Le Méhauté, Olivier de Witte and Jean Claude André) and American (Charles Hull) scientists.^{79, 80} Over the years, 3D-printing has been evolving through the introduction of new methods and materials. Hence, AM technology is now subdivided and categorized into seven categories according to the American Society for Testing and Materials (ASTM) in which SLA appears only as an offshoot (**Figure 1.8**). An explanation of the fast appearance rate of new AM branches is due to the expiry of former patents motivating manufacturers to create new 3D-printing machines.

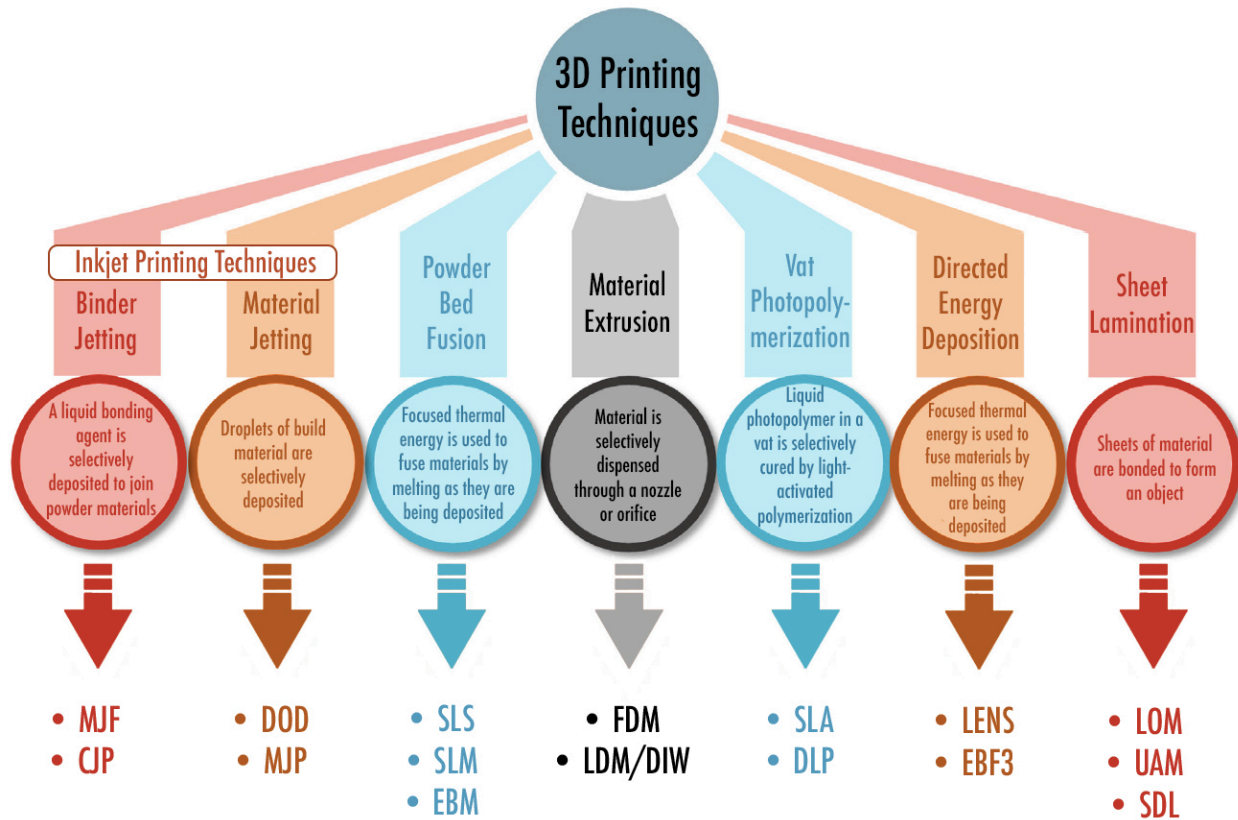


Figure 1. 8. Standard Terminology for Additive Manufacturing Technologies. This scheme was deeply modified and adapted with permission from ⁸¹. MJF: Multi-Jet Fusion; CJP: Color Jet Printing; DOD: Drop On Demand; MJP: Multi-Jet Printing; SLS: Selective Laser Sintering; SLM: Selective Laser Melting; EBM: Electron Beam Melting; FDM: Fused Deposition Modeling; LDM: Liquid Deposition Modeling; DIW: Direct Ink Writing; SLA: Stereolithography; DLP: Digital Light Processing; LENS: Laser Engineered Net Shaping; EBF3: Electron Beam Freeform Fabrication; LOM: Laminated Object Manufacturing; UAM: Ultrasonic Additive Manufacturing; SDL: Selective Deposition Lamination.

This technology is now widely used in numerous applications including footwear,⁸² healthcare,⁸³ construction,⁸⁴ automotive,⁸⁵ aerospace,⁸⁶ electronics⁸⁷ and energy storage⁸⁸ fields due to its ability to stand as a prototyping solution to accelerate a product development and also its capability to produce customized parts with fewer design restrictions. AM is particularly attractive to produce complex structures such as lattices where the use of manufacturing traditional methods such as molding, casting, machining and joining remains somewhat limited.

In 2019, according to the yearly report on AM published by the Dutch company 3D Hubs⁸⁹ and based on the summarized data provided from ten trustworthy market analysts, the total 3D-

printing market (including machines, materials, software and services) was estimated to represent \$12.1B on average, exhibiting a yearly 25% growth since 2014. The AM market, actually doubling every 3 years, is expected to reach \$34.9B in average by 2024 (Figure 1.9).

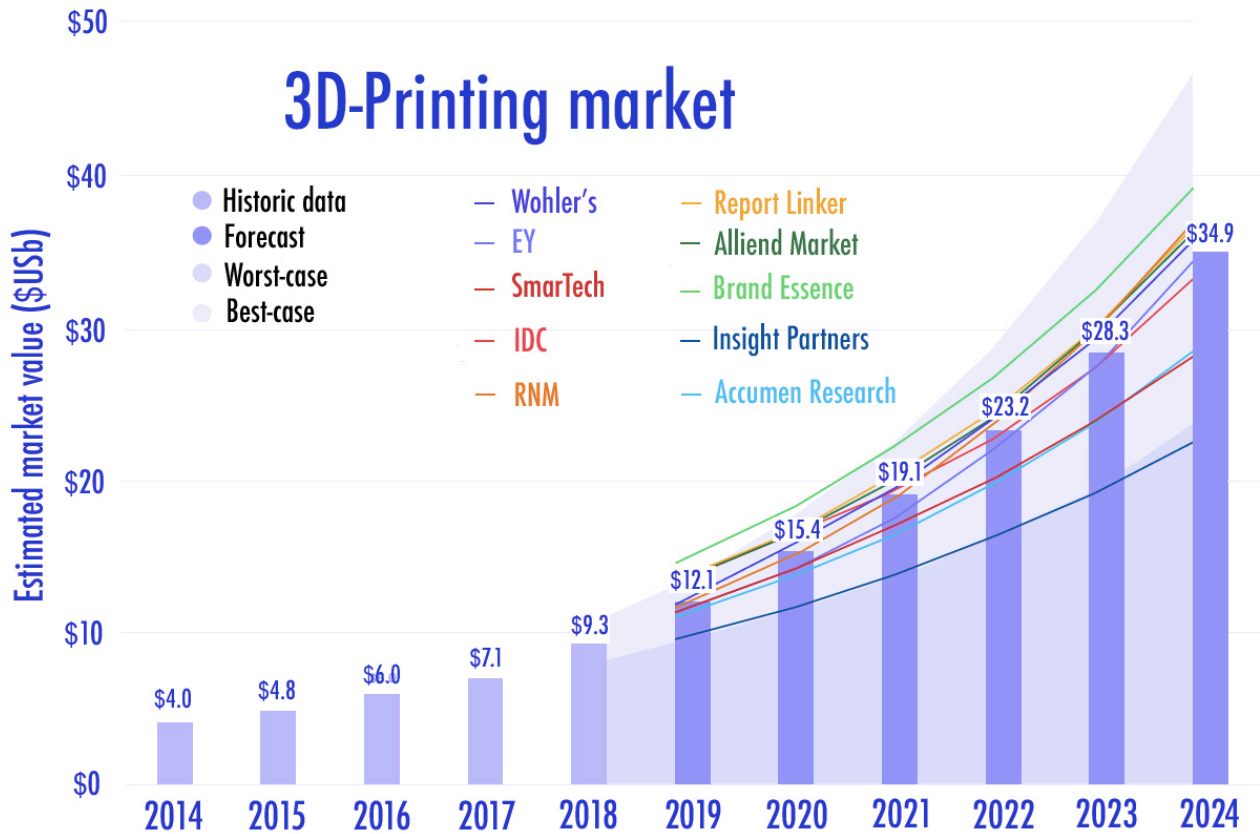


Figure 1. 9. Additive manufacturing market and forecast. This scheme was modified and adapted with permission from⁸⁹. Copyright 2020 3D-Hubs Manufacturing LLC. The historic market size was calculated by averaging the market size reported by Wohler's associates, EY, and SmarTech; The forecasted market size was calculated by averaging values estimated by all market analysts; The worst-case and best-case scenarios were calculated starting at $\pm 15\%$ of the market size in 2018 and by applying 20% and 28% compound annual growth rate respectively.

1.2.1. Working principle

3D-printing consists in building a three-dimensional solid object from a digital file (**Figure 1.10**).^{74, 75, 77, 78} Hence, first step resides in drawing the desired object architecture by using computer-aided design (CAD) software. Object design is saved into a digital .stl file format describing the surface geometry of the three-dimensional object without including any representation of color, texture or other common CAD model attributes. The second step involves the importation of the .stl file in a slicer software enabling to define many printing parameters including printing temperature, speed, layer thickness, perimeters, cooling parameters, infill pattern and density. The object digital file is cut into horizontal slices (layers) and a .gcode file format is generated. Last step corresponds to the importation of the .gcode file to the 3D-printer via USB, SD card or LAN, so it starts building the desired structure by stacking up materials in a layer-upon-layer approach.

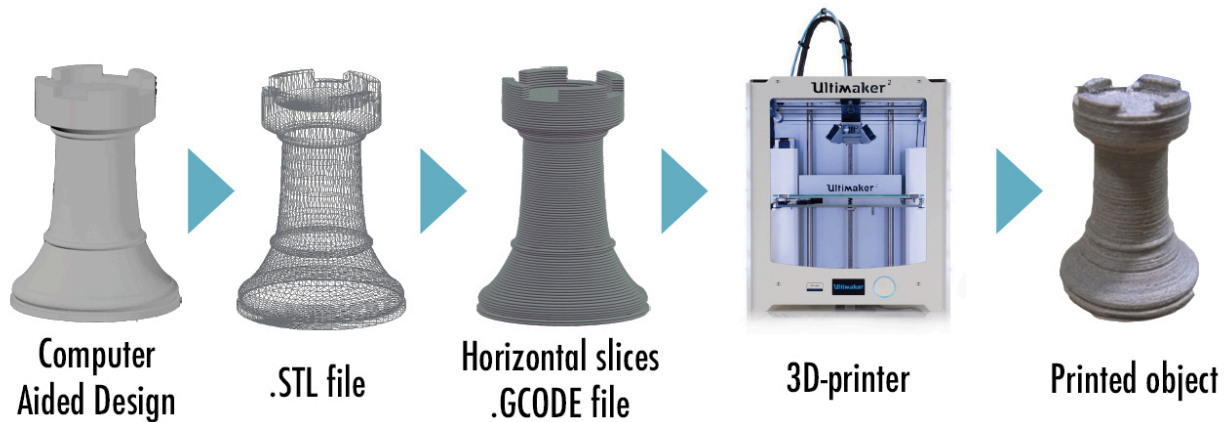


Figure 1. 10. 3D-printing process. This scheme was modified and adapted with permission from ⁹⁰. Copyright 2018 Association for Computing Machinery.

1.2.2. Lithium-ion battery 3D-printing

Due to its theoretical ability to maximize energy storage within the final object, but also to overcome short-circuits usually observed while performing the interpenetration of 3D-electrodes by using conventional manufacturing techniques (cf. **1.1.3. From 2D to 3D architectures**), the literature on lithium-ion battery 3D-printing has grown exponentially over the last years as depicted in **Figure 1.11**.

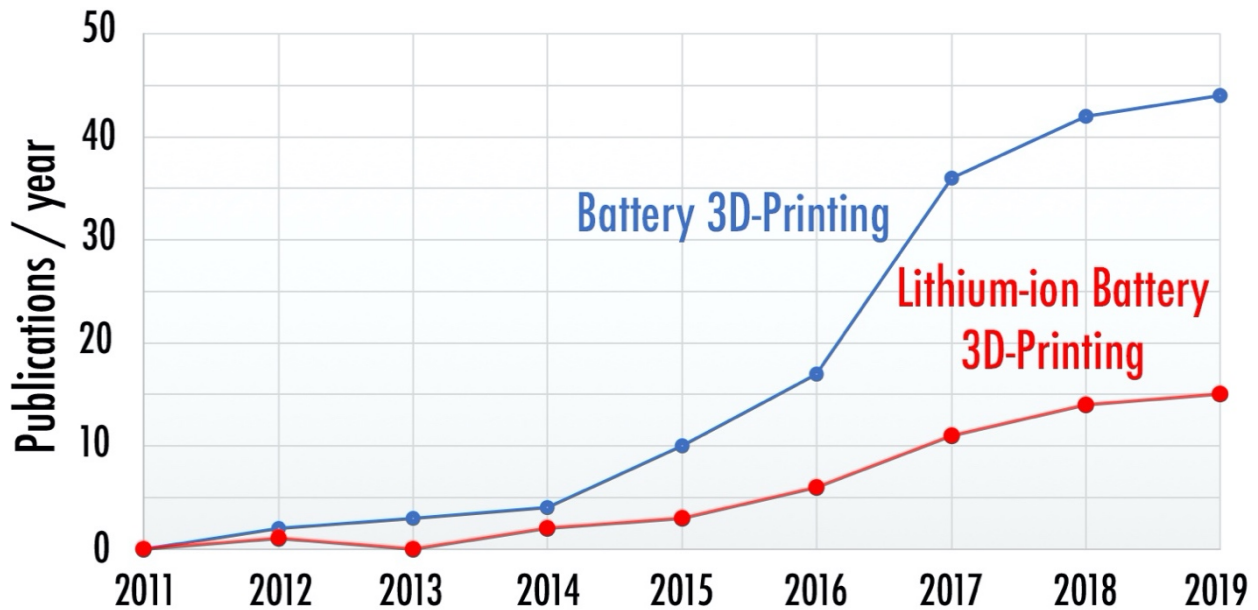


Figure 1. 11. Overview of the number of publications containing the following keywords on both title and abstract: “battery 3D-printing” (blue) and “lithium-ion battery 3D-Printing” (red). Data were extracted from Dimensions App website: <https://app.dimensions.ai/>.

Before presenting an overview of the recent advances and progress on that particular topic, it is worth-mentioning that while material jetting is officially recognized as a direct ramification of AM (**Figure 1.8**), this process was considered out of the scope of this PhD thesis. Indeed, so far, this technique consisting on the deposition of material droplets onto a substrate, has been extensively used to print only planar two-dimensional (2D) lithium-ion batteries since 2006.⁹¹⁻⁹⁷ This process is for now not suitable to print thick electrodes and 3D architectures (non-planar).

1.2.2.1. Material extrusion

According to the ASTM, material extrusion, appearing as a branch of AM (**Figure 1.8**), consists of a material deposition selectively dispensed through a nozzle or orifice. This technology is usually divided into two main sub-categories called Fused Deposition Modeling (FDM) and Liquid Deposition Modeling (LDM) which is also commonly known as Direct Ink Writing (DIW).

Material extrusion, originally invented by Scott Crump, co-founder of the American company Stratasys, has nowadays become the most popular AM technology thanks to the introduction of the RepRap mission by Adrian Bowyer (Bath University) in 2005. This project, based on patents expiry, was to create an open-source 3D-printer capable of “replicating rapidly” (RepRap) itself. Disclosed for the first time in 2008, it contributed actively to the general public awareness but also to the emergence of many companies around the world such as Makerbot or Prusa who create and release their own 3D-printer version.

Mechanically relatively simple, both FDM and LDM technologies are easily scalable thanks to the open-source designs disposal and are thus only limited by their nozzle size and 3D-printer architecture (cartesian, delta or robot arm configuration).

Moreover, recent years have witnessed the emergence of multi-material printing configurations paving the way toward new applications such as energy storage. In this context, LDM and FDM were seriously investigated in order to 3D-print electrochemical storage systems such as lithium-ion batteries.

1.2.2.1.1. Liquid deposition modeling/Direct ink writing

Liquid Deposition Modeling (LDM), also identified as Direct Ink Writing (DIW), is based on the extrusion, by applying a pressure, of a semi-liquid material known as paste or ink which is deposited layer after layer through a syringe needle (**Figure 1.12.a**). The structural strength of the object is strongly dependent on the printing ink viscoelasticity. Extruded materials include ceramic pastes, composites inks, blended food, biocompatible organic cellular gel, cement or even chocolate. Nowadays, it is the most popular reported technique for lithium-ion battery 3D-printing

due to its ability to build inexpensive 3D complex structures of any shape at ambient temperature. After printing, inks solidify to form the final object mostly through solvent evaporation. Considering the lithium-ion battery DIW, additional post-processes steps such as freeze-drying or thermal annealing are usually required. Here, a chronological overview of LIB 3D-printing through LDM is described.

Everything started in 2013, when Sun et al.⁸⁸ reported for the first time a LDM 3D-printed Li-ion microbattery (**Figure 1.12.b**). Authors prepared cellulose-based inks of $\text{Li}_4\text{Ti}_5\text{O}_{12}$ (LTO) and LiFePO_4 (LFP) nanoparticles by suspending these active materials in aqueous solutions for the formulation of negative and positive electrodes respectively. After printing, inks were successively dried and sintered at 600 °C during 2 h under an inert atmosphere to remove the organic additives and promote nanoparticle sintering. Electrochemical measurements for the half-cell of LFP upon discharge led to specific capacity of 160 mAh g⁻¹ of active material at current density of 170 mA g⁻¹ (1 C), equivalent to areal capacity of 1.6 mAh cm⁻² at 1.7 mA cm⁻². Half-cell of LTO exhibited a specific capacity of 131 mAh g⁻¹ of active material at current density of 175 mA g⁻¹ (1 C), corresponding to areal capacity of 1.4 mAh cm⁻² at 1.87 mA cm⁻².

To enhance the electrical conductivity of the electrodes and reach suitable viscosity for LDM, Fu et al.⁹⁸ developed aqueous inks based on LTO/graphene oxide (GO) and LFP/GO (**Figure 1.12.c**). Printed electrodes were then freeze-dried to remove water solvent and harden the 3D structures. Sintering under Ar/H₂ (600 °C for 2 h) was also employed to create reduced graphene oxide (rGO). Lastly, LFP/rGO and LTO/rGO half cells were electrochemically tested after depositing a polyvinylidene fluoride-co-hexafluoropropylene (PVDF-co-HFP) with Al₂O₃ ink. After drying, the 3D-printed separator was soaked with a classical liquid electrolyte (1 M LiPF₆ in ethylene carbonate and diethyl carbonate) to reach a gel electrolyte. At current density of 10 mA g⁻¹ (C/17), specific capacities of 164 and 185 mAh g⁻¹ of active material were respectively determined. These electrodes were then assembled and full battery depicted a capacity about 100 mAh g⁻¹ at current density of 50 mA g⁻¹.

In 2017, Blake et al.⁹⁹ confirmed the LDM printability of several PVDF-based separator membranes. PVDF was dissolved in a N-methyl-2-pyrrolidone (NMP) solution while glycerol was added to act as a weak nonsolvent with higher boiling point. This dual-solvent method was reported

to create important porosity within the polymer matrix after drying because of the phase separation phenomenon. Ceramic filler such as alumina (Al_2O_3) was introduced within the mixture to govern the pore arrangement after drying. Finally, the membrane was soaked in a liquid carbonate-based electrolyte solution to form a gel. An enhanced wettability and thermal stability were reported by the authors in comparison with a commercial polyolefin separator.

Similarly, Liu et al.¹⁰⁰ reported the preparation of a PVDF-co-HFP/boron-nitride (BN) ink using dimethyl formamide as solvent to print a separator via LDM. Once deposited, the ink was then dried at room temperature. BN-separator was shown to allow fast heat dispersion and uniform thermal distribution at the interface during the lithium plating process increasing electrochemical performance of the lithium-ion battery.

A year later, Cheng et al.¹⁰¹ related the preparation of an electrolyte ink consisting of PVDF-co-HFP and TiO_2 nanofillers dispersed in an ionic-liquid composed of N-Propyl-N-methyl pyrrolidinium bis (trifluoromethane sulfonyl)imide (Pyr13TFSI) and lithium bis(trifluoromethanesulfonyl)imide (LiTFSI) salt. Thus, an ionic conductivity of $7.8 \times 10^{-4} \text{ S cm}^{-1}$ was reported. Printability of a complex 3D Hilbert electrolyte structure on a polydimethylsiloxane (PDMS) substrate was completed.

LDM studies also included the printability of inorganic ceramic electrolyte such as the garnet-type $\text{Li}_7\text{La}_3\text{Zr}_2\text{O}_{12}$ (LLZO). In that regard, McOwen et al.¹⁰² 3D-printed texanol-LLZO and polyvinyl butyral-benzyl butyl phthalate-LLZO inks. Once the desired 3D pattern was printed on both sides of a LLZO substrate, the structure was subsequently located in an oven to remove the binder and achieve sintering. The resulting 3D-printed LLZO framework was then disposed for the further electrodes infiltration to assemble the complete battery.

Focused on the positive electrode formulation, Li et al.¹⁰³ described preparation of a LiMn_2O_4 /carbon black/PVDF ink (wt.% LMO/CB/PVDF 85.5/6.5/8) dispersed in N-methyl-2-pyrrolidone solvent (NMP). Once printed, voltage (10 kV) was applied at a distance of 1.25 cm for 10 minutes. A hot plate (at 120°C) was then used to remove the solvent. The applied electric field was reported to control the microstructure of manganese-based electrode, while AM controls

macro-3D structure. In comparison with a conventional laminated structure (1.8 mAh cm⁻² at C/10), the macro-micro controlled structure exhibited enhanced performances (3.5 mAh cm⁻²).

That same year, in 2018, a significant milestone was reported by Wei et al.¹⁰⁴ who related 3D-printing of an entirely packaged LIB (**Figure 1.12.d**). Authors developed positive (LFP) and negative (LTO) electrode inks, as well as UV curable packaging and separator inks. Electrodes ink were prepared by adding 30 vol% LFP with 1.25 vol% Ketjen black (KB) conductive particles and 30 vol% LTO with 1.35 vol% KB in 1 M LiTFSI/propylene carbonate with 1 wt.% polyvinylpyrrolidone (with respect to LFP or LTO) for the cathode and anode, respectively. The separator ink was a mixture of PC/Al₂O₃/Triton X-100 surfactant. Inks being contained in various syringes, LDM printing was completed by means of an Ar-powered fluid dispenser to control the flow rate. After a post-processing step of UV-curing (cf. **1.2.2.2. Vat photopolymerization**), the fully printed LIB was encased between two glassy carbon current collectors and delivered an aerial capacity of 4.45 mAh cm⁻² (corresponding to 17.3 mAh cm⁻³) at a current density of 0.14 mA cm⁻².

Finally, in 2019, Liu et al.¹⁰⁵ demonstrated the interest of performing LDM printing at low temperature (LT-LDM). In that respect, positive electrode inks composed of various solid content of LFP, carbon black and CMC were dispersed in water and 1,4-dioxane. To perform LT-LDM, a machine was customized to store the inks at -30 °C. After printing, freeze-drying process was performed at -60 °C during 6 h. In comparison with conventional LDM performed at ambient temperature, LT-LDM presents the advantage to precisely control the deposited line width. Hence, in comparison with traditional processes of roller coating and room temperature LDM, LT-LDM samples were reported to exhibit a different microstructure in terms of porosity, pore size and distribution. For ink with a solid content of 0.467 g mL⁻¹, LT-LDM printed electrode was reported to depict the highest specific capacity reaching up to 82 mAh g⁻¹ at high current density of 1700 mA g⁻¹ (10C).

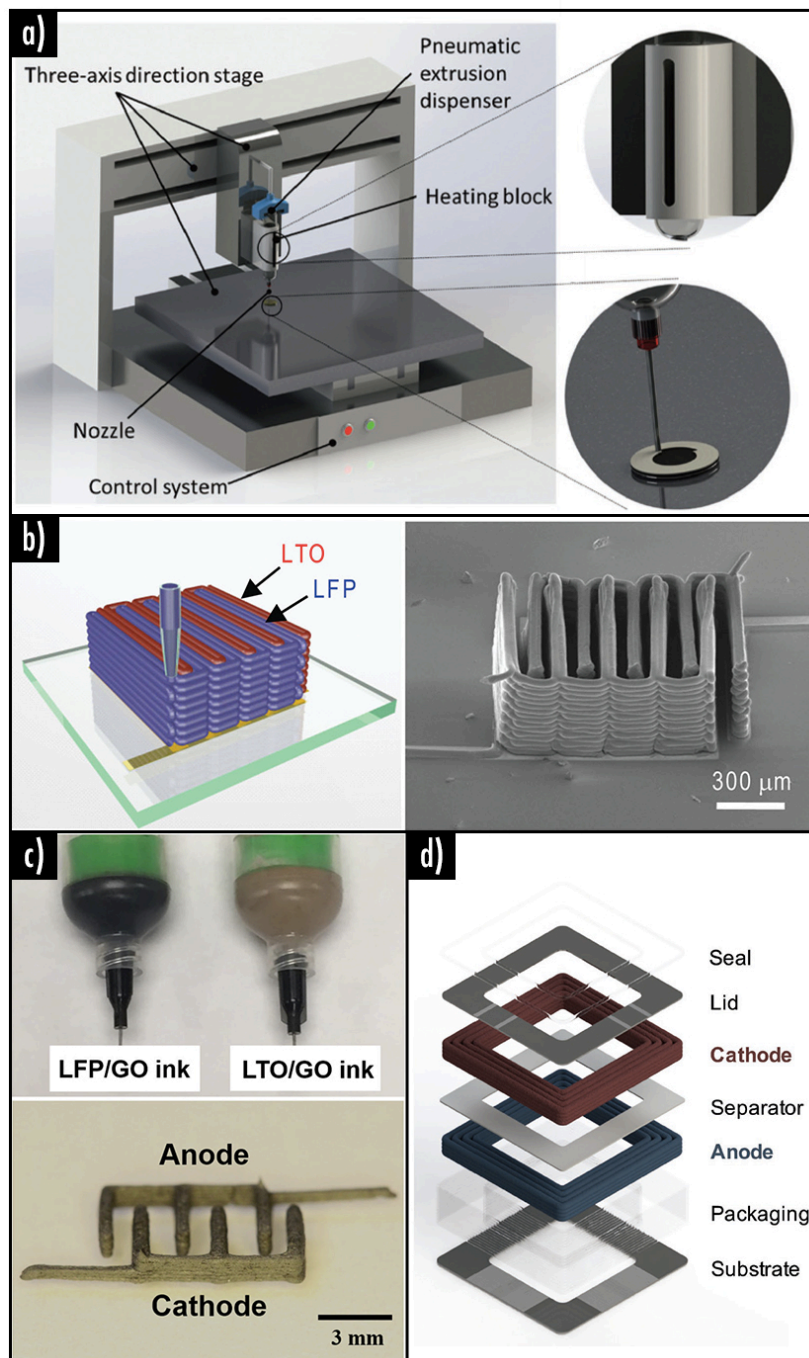


Figure 1. 12. (a) LDM 3D-printing process. Reproduced and adapted with permission from ¹⁰¹. Copyright 2018 Wiley; (b) 3D interdigitated microbattery architectures design (left) and SEM image after printing and annealing (right). Reproduced with permission from ⁸⁸. Copyright 2013 Wiley; (c) Inks loaded in syringes (top) and digital image of the interdigitated electrodes (bottom). Reproduced with permission from ⁹⁸. Copyright 2016 Wiley; (d) Schematic representation of fully 3D printed Li-ion square cell battery. Reproduced with permission from ¹⁰⁴. Copyright 2018 Wiley.

1.2.2.1.2. Fused deposition modeling

Fused deposition modeling (FDM) process involves the deposition of thin layers of melted thermoplastic material through a computer-controlled heated nozzle with a view to build the final 3D-object (**Figure 1.13.a**). Used as material source for the FDM printer, the thermoplastic material consists most of the time of a 1.75 mm diameter filament. Heated few degrees above its melting temperature to be deposited, it immediately cools down and solidifies after extrusion. Most common thermoplastic polymers for FDM application involve polylactic acid (PLA), acrylonitrile-butadiene-styrene (ABS), polycarbonate (PolyC), polypropylene (PP) or polyethylene terephthalate glycol (PETG). Typical layer thickness resolution of current commercial FDM 3D-printers is about 150-200 μm for the first layer and down to 50 μm for the successive layers. For advanced applications, resolution can be enhanced through machine modifications and settings adjustments.

For conductivity or mechanical purposes, different groups first focused their work on the development of composite thermoplastic FDM filaments.^{106, 107} In particular, several studies reported the introduction, within the polymer matrix, of small amount of carbonaceous materials, similar to what is traditionally employed at the LIB negative electrode. In 2012, Leigh et al.¹⁰⁶ reported the preparation of a polycaprolactone-based (PCL) filament containing carbon black (15 wt%) conductive additives for the fabrication of electronic sensors (**Figure 1.13.b**). Wei et al.¹⁰⁸ reported in 2015 the formulation and characterization of PLA/graphene and ABS/graphene (loading up to 5.6 wt %) filaments (**Figure 1.13.c**). In 2016, to enhance the mechanical strength of the filament, Dul et al.¹⁰⁷ reported the preparation of a conductive ABS-based filament loaded with 4 wt% graphene nanoplatelets (GnP) to feed a FDM printer.

Finally, in March 2017, few months before the beginning of this PhD project, FDM just started to be considered for LIB 3D-printing. Foster et al.¹⁰⁹ employed a commercially available graphene-based polylactic acid filament (graphene/PLA) to fabricate a 1 mm-thick 3D printed electrode disc. The latter was then characterized both electrochemically and physico-chemically to be used as negative electrode in LIB. Due to the low ratio of active material (8 wt % graphene and 92 wt % PLA) into the filament (103 mg of active material per cm^3 of composite), relatively low

discharge specific capacities of 15.8, 6.2, 2.6, 1.1, and 0.6 mAh g⁻¹ of active material were reached at current densities of 10, 50, 70, 100, and 200 mA g⁻¹ (C/37, C/7, C/5, C/4, and C/2) respectively.

To conclude on this particular AM process, no homemade composite filament specifically elaborated for its use in a LIB was reported at the time this PhD thesis was started (October 2017).

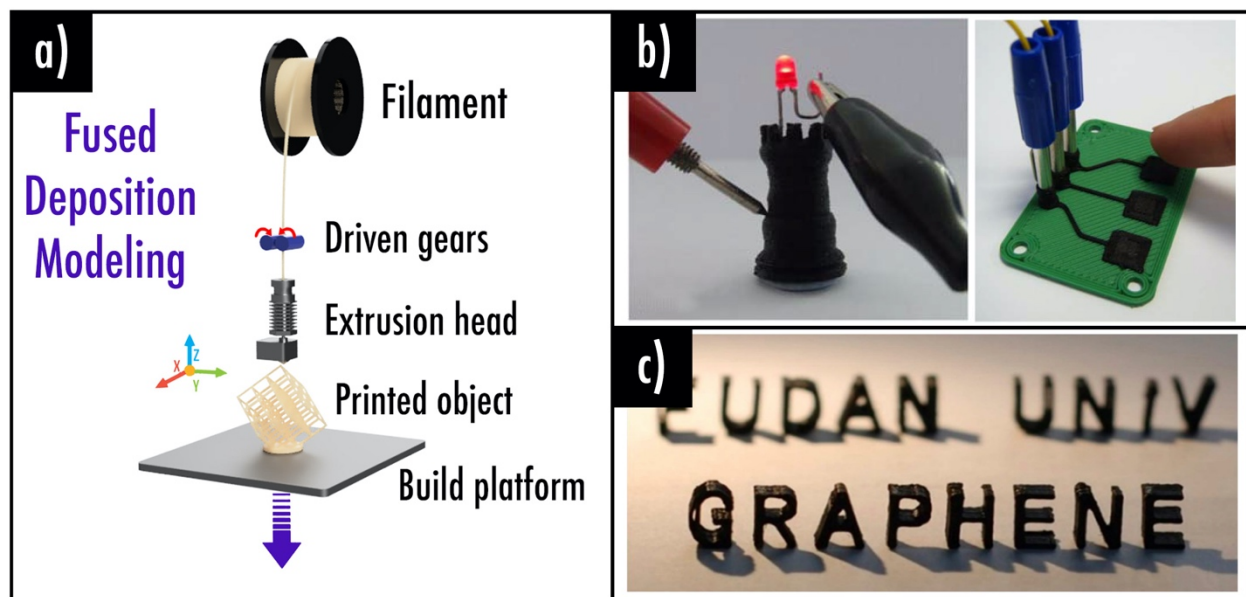


Figure 1. 13. (a) FDM 3D-printing process. Reproduced and adapted with permission from III. Copyright 2020 JES; (b) 3D printed conductive PCL/carbon black chess rook (left) and capacitive interface device (right). Reproduced with permission from ¹⁰⁶. Copyright 2012 Plos One; (c) ABS/graphene 3D-printed model. Reproduced with permission from ¹⁰⁸. Copyright 2012 Scientific Reports.

1.2.2.2. Vat photopolymerization

According to the ASTM, vat photopolymerization appears as a direct ramification of 3D-printing (**Figure 1.8**). This technology involves a liquid photosensitive polymer resin located in a tank (also called “vat”) that is selectively cured by light-activated polymerization. After curing of the first layer, the build platform is risen, thus leaving the solidified part at the exact surface of the liquid resin so the process can be repeated to produce the next layer.

This technology is named differently depending on the light type. The most widespread process is undoubtedly the process involving a Stereolithography Apparatus (SLA) using an

ultraviolet light (**Figure 1.14.a**). Typically, the LASER beam coming from the bottom of the tank, is driven thanks to mirrors so the resin is cured in a “point after point” procedure. Working on a very similar approach, another process called digital light processing (DLP) involves a digital light projector screen as light source (**Figure 1.14.b**). The projector displays the whole image of the layer that will be printed within the resin. Hence, all points of a same layer are cured at the same time. The print speed is thus enhanced in comparison with SLA since it takes less time to cure each single layer.

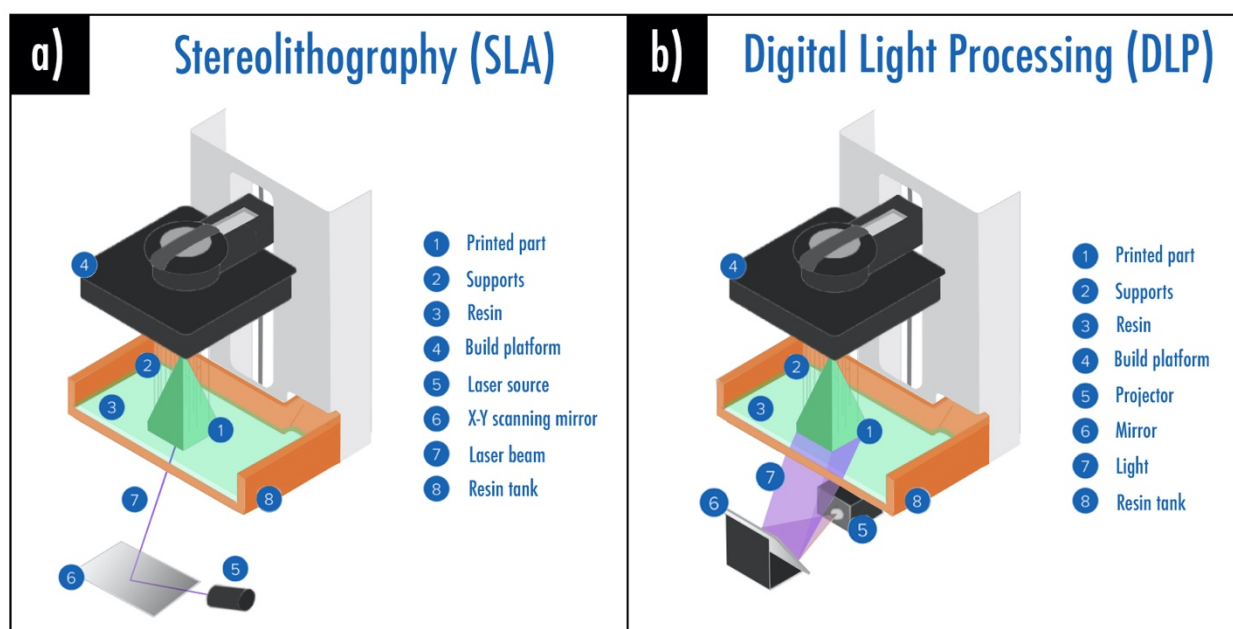


Figure 1. 14. Vat photopolymerization 3D-printing processes: (a) Stereolithography; (b) Digital light processing.

Using vat photopolymerization, some groups focused their work on the preparation of electrolytes. In 2017, by means of SLA, Chen et al.¹¹⁰ reported the elaboration of a gel electrolyte (GPE) by printing a mixture of UV-curable resin and 1M LiClO₄ in an EC/PC (v/v 1/1) liquid electrolyte. A zig-zag shape was obtained. Then, the complete battery was assembled by filling both sides with electrode slurries (GPE-LFP and GPE-LTO) and adding an Al foil as current collectors.

A year later, Zekoll et al.¹¹¹ prepared a hybrid electrolyte composed of 3D microchannels of $\text{Li}_{1.4}\text{Al}_{0.4}\text{Ge}_{1.6}(\text{PO}_4)_3$ (LAGP) ceramic solid electrolyte and non-conducting polymer (epoxy polymer, polypropylene). The porous polymer framework (**Figure 1.15.a**) was primarily achieved via SLA whereas the remained empty space was filled with the LAGP ceramic powder. Lastly, the structure was placed in an oven to eliminate the polymer matrix and sinter the LAGP 3D arrangement. Cubic, diamond-shaped or also gyroidal microarchitectures were produced. Higher performances were found with the gyroid LAGP structure depicting an ionic conductivity of $1.6 \times 10^{-4} \text{ S cm}^{-1}$ at ambient temperature.

That same year, in 2018, as described beforehand, Wei et al.¹⁰⁴ prepared classical electrodes inks for LDM printing (cf. **1.2.2.1.1. Liquid deposition modeling/Direct ink writing**). At the same time, authors also developed LDM printable UV-curable packaging and separator inks. The packaging ink was prepared by adding SiO_2 within a UV-curable epoxy resin. The separator ink was composed of UV-curable ethoxylated trimethylolpropane triacrylate (ETPTA), Al_2O_3 particles, Triton X-100 surfactant in 1 M LiTFSI/propylene carbonate. During the complete LIB preparation, packaging and separator inks were first deposited through LDM printing before undergoing UV-curing post-process similar to what is performed during SLA.

Another methodology was introduced by Cohen et al.¹¹² who used SLA to prepare complex 3D structures. After thermal annealing, these complex architectures were used as substrate for performing an electrophoretic-deposition of the battery components. Tri-layered structure consisting of the LFP (positive electrode), LiAlO_2 -PEO or $\text{Li}_{1.5}\text{Al}_{0.5}\text{Ge}_{1.5}\text{P}_3\text{O}_{12}$ -polyethyleneimine separator, and LTO-based negative electrode were thus deposited on top of an electronically conductor substrate without the need of an additional metallic current collector (**Figure 1.15.b**).

So far, no studies reported the direct preparation of composite electrodes for LIB via vat photopolymerization techniques. However, it is worth-mentioning that such a work had been considered lately for the preparation of supercapacitors and capacitors. Indeed, Park et al.¹¹³ reported recently the preparation of a photocurable composite resin with silver nanowires. Thus, using DLP, authors were able to print 3D hierarchical octet truss structure (**Figure 1.15.c**). After performing pyrolysis of the structure, a silver 3D array was obtained and used as supercapacitor.

Likewise, Yang et al.¹¹⁴ reported the elaboration of 3D-printed capacitors via DLP based on the incorporation of $\text{Ag/Pb}(\text{Zr,Ti})\text{O}_3$ filler particles into the photo-curable polymer resin.

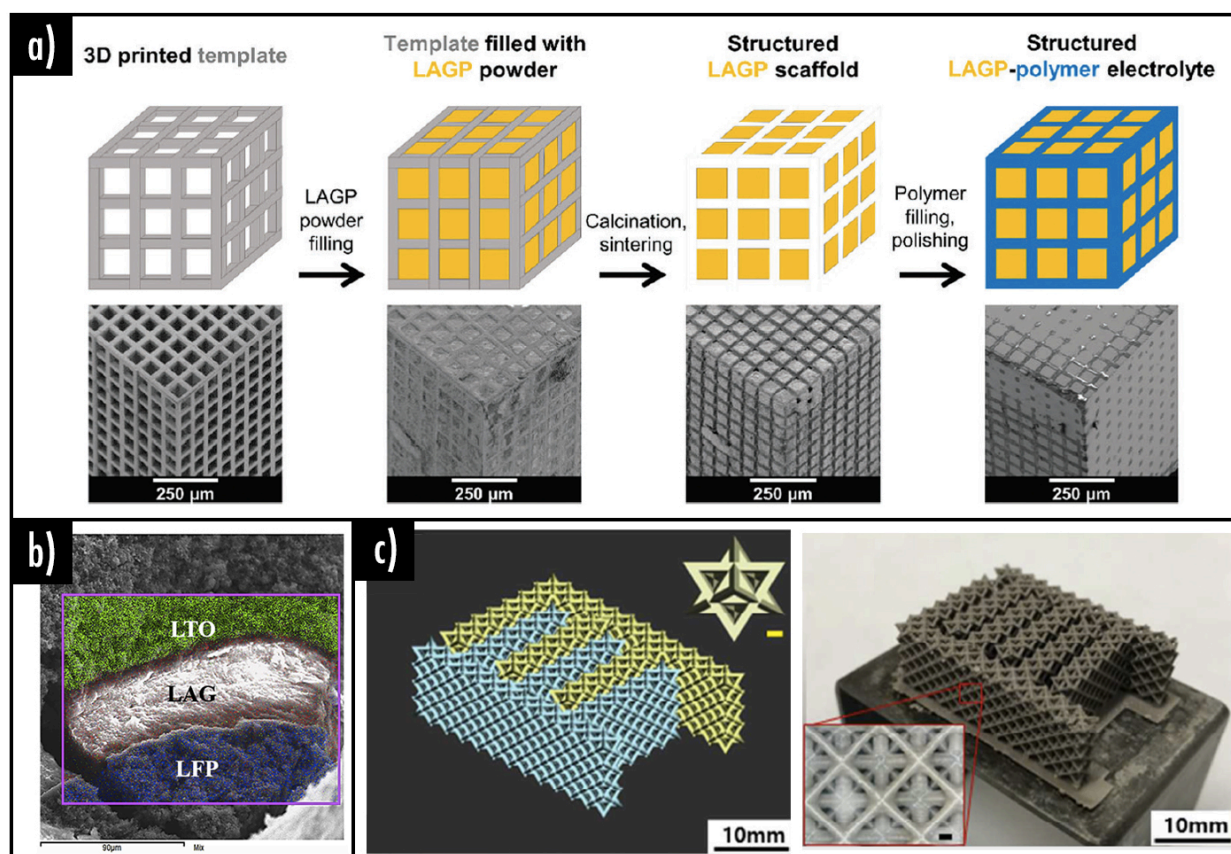


Figure 1. 15. (a) Templating procedure used for the synthesis of structured hybrid electrolytes and corresponding SEM images. Reproduced with permission from ¹¹¹. Copyright 2018 The Royal Society of Chemistry; (b) Cross-sectional EDS mapping of tri-layer battery structures deposited on a 3D-printed substrate. Reproduced with permission from ¹¹². Copyright 2018 Elsevier; (c) 3D model images of interdigitated electrode (left) and the corresponding DLP printed structure (right). Reproduced with permission from ¹¹³. Copyright 2018 ACS.

1.2.2.3. Powder bed fusion

According to the ASTM, powder bed fusion appears as a direct branch of AM (**Figure 1.8**). This technology was originally created in the 1980s by a group from the University of Texas at Austin. This technique primarily involves the spreading of a thin and homogeneous powder over the build platform thanks to a leveling blade. Afterwards, either a LASER or an electron beam is applied selectively in order to partially melt (sintering) or completely melt the powder according to the pre-designed pattern. The build platform is subsequently lowered and a thin layer of powder is spread again homogeneously upon the platform. The process is thus repeated layer after layer until the final 3D object is finished (**Figure 1.16.a**).

Powder bed fusion is usually divided into various sub-categories which names are given depending on the heat source, the environment and the degree to which powders are melted. Both selective laser sintering (SLS) and selective laser melting (SLM) use a LASER as energy source. Nonetheless, SLS is usually performed under air to partially melt together polymer or ceramic particles while SLM is rather employed to completely melt metal powders together. Because of the reactivity of some powder metals with oxygen, SLM is generally performed under inert atmosphere. Another process called electron beam melting (EBM), achieved under vacuum, consists of an electron beam which is employed to fully melt metals, ceramics or polymers particles. Because of the process itself, EBM and SLM processes result in very dense 3D objects in opposite with SLS where a porosity can be created.

So far, using this particular technology, very few studies have been reported on the topic. Among the powder bed fusion technologies, SLS process had been the most employed for LIB applications thanks to its ability to partially sinter polymer particles in such a way that only their surfaces are fused together. Hence, in 2019, Lahtinen et al.¹¹⁵ demonstrated, that highly porous structures can be obtained by controlling thoroughly the printing parameters (LASER exposition time and power), thus making it quite appealing to print LIB electrodes (**Figure 1.16.b**). When polymer particles are only partially sintered, the charges (active material and conductive additives) are distributed on the surface of these particles and are therefore reachable by the liquid electrolyte flowing through the printed electrode. Authors reported the fabrication via SLS of highly porous carbonaceous polyamide 12/graphite, polystyrene/graphite and polyurethane/graphite negative

electrodes. Unfortunately, with such a high porosity, relatively low amount of charges (active material) was introduced to get electrodes with suitable mechanical strength. The active material (graphite) concentration, polymer matrix, and printing conditions all had an impact on the final mechanical strength, porosity, conductivity, and thus future electrochemical performances.

In order to reach higher loading of charges within the electrodes, an alternative was proposed by Sha et al.¹¹⁶ who added a post-processing step. Authors used SLS to sinter a Ni/sucrose powder mixture. During printing, the sucrose was turned into graphene such creating a 3D graphene foam structure. After printing, Ni particles originally employed as catalyst, were then removed via etching post-process.

In parallel, so far, SLM process has been mostly used to prepare supercapacitors or capacitors. In 2018, Lu et al.¹¹⁷ first printed via this method a porous Ni-Fe alloy 3D complex structure. The resulting architecture was then corroded using diluted hydrochloric acid for 12 h to eliminate the impurities in the pores. Polyaniline (PANI) was finally electrodeposited onto the ordered porous architecture via anodic electrochemical polymerization of aniline monomer. A Ni-Fe/PANI nanocage supercapacitor was thus obtained. Thanks to 3D-printing, the specific surface area was increased thus leading to enhanced specific capacitance. Likewise, Zhao et al.¹¹⁸ employed SLM to create titanium interdigitated pillar electrodes structures (**Figure 1.16.c**). These latter were subsequently subjected to electrodeposition of polypyrrole as the electroactive material. Both electrodes were then assembled and the resulting supercapacitor was soaked in poly(vinyl alcohol)–H₃PO₄ electrolyte solution.

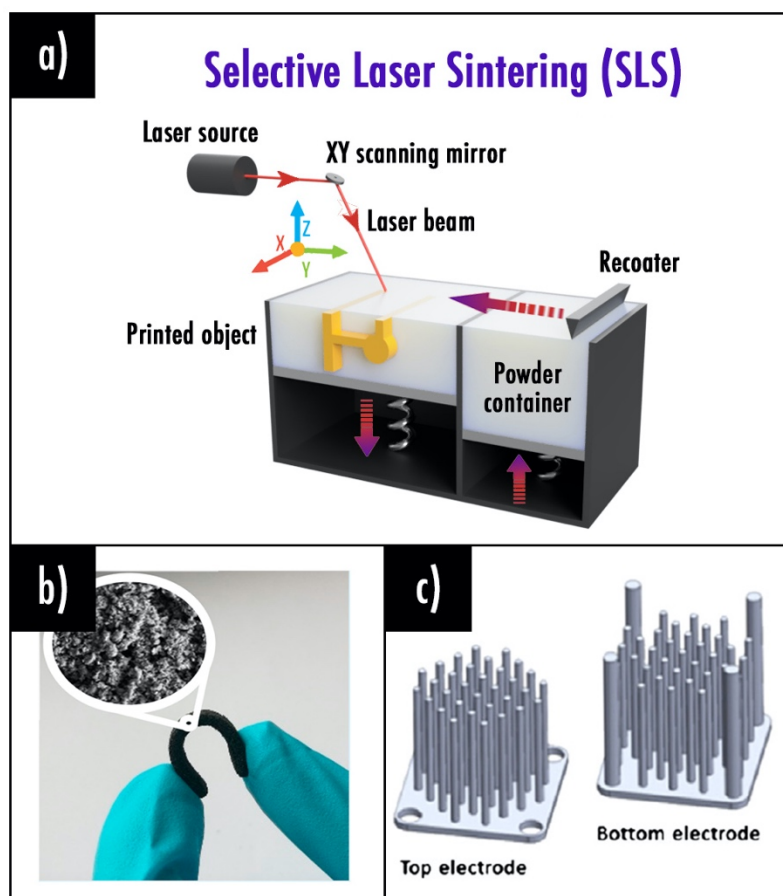


Figure 1. 16. (a) Selective laser sintering 3D-printing process^{IV}; (b) Highly porous carbonaceous negative electrodes obtained via SLS. Reproduced with permission from ¹¹⁵. Copyright 2019 ACS; (c) Schematic representation of the interdigitated Ti electrodes design prepared by means of SLM to fabricate solid state supercapacitors. Reproduced with permission from ¹¹⁸. Copyright 2014 Elsevier.

Conclusions and scope of this thesis

To conclude, over the last few years, both LIB and 3D-printing had been revolutionizing their own respective disciplines. Thanks to their respectable electrochemical performances, LIB appears nowadays as a technology of choice that undeniably became imperative in our everyday life to power an extensive variety of devices. On the other hand, in comparison with traditional manufacturing methods, AM recently emerges as a cutting-edge revolutionary discipline impacting progressively a wide range of applications including energy storage and more specifically LIB.

In that respect, 3D-printing of LIB appears as a promising route to implement topological optimization of energy-storage devices and to build electrochemically-promising complex 3D electrode architectures. So far, many AM technologies had been employed, mostly including the following sub-categories: material jetting, material extrusion, vat photopolymerization and powder bed fusion. As explained previously (cf. **1.2.2. Lithium-ion battery 3D-printing**), material jetting, direct branch of material jetting technique, was ruled out of the scope of this PhD thesis as it consists of the deposition of material droplets onto a substrate leading mostly to 2D patterns. While this method has been significantly used to print LIB, it is not suitable to print thick electrodes and non-planar 3D architectures (non-planar). In parallel, while LDM was extensively explored recently (cf. **1.2.2.1.1. Liquid deposition modeling/Direct ink writing**) due to its significant advantage to achieve high active mass loading within the electrodes, the main drawback of this technique is the requirement to perform post-processes such as freeze-drying and sintering prior to its use. Besides, ink viscosity is a key-factor to contemplate as it limits the height of the resulting 3D-printed object. Hence, many parameters must be studied thoroughly such as the introduction of a surfactant. On the other hand, while vat photopolymerization (cf. **1.2.2.2. Vat photopolymerization**) and powder bed fusion (cf. **1.2.2.3. Powder bed fusion**) are suitable options requiring further investigations, both techniques are strictly limited for now to the printing of a single-material. So far, printability of multi-material structures is not widely established for these techniques.

Finally, the ultimate goal of this project being the development of a complete LIB in one-single step through 3D-printing without the necessity to perform any post-processes, FDM (cf. **1.2.2.1.2. Fused deposition modeling**) was therefore chosen among the various AM processes

considered. In October 2017, at the time this PhD thesis was started, FDM just started to be considered for LIB 3D-printing. Hence, this project was logically oriented towards a proof of concept demonstration. The FDM process requiring a filament-shape thermoplastic material to feed the printer, a thorough formulation and optimization of composite filaments for each component of the battery (electrodes, separator, electrolyte, current collectors) was thus started.

References

1. Dunn, B.; Kamath, H.; Tarascon, J. M., Electrical Energy Storage for the Grid: A Battery of Choices. *Science* **2011**, 334, (6058), 928-935.
2. Tarascon, J. M.; Armand, M., Issues and challenges facing rechargeable lithium batteries. *Nature* **2001**, 414, (6861), 359-367.
3. Scrosati, B.; Garche, J., Lithium batteries: Status, prospects and future. *Journal of Power Sources* **2010**, 195, (9), 2419-2430.
4. Deng, D., Li-ion batteries: basics, progress, and challenges. *Energy Science & Engineering* **2015**, 3, (5), 385-418.
5. Budde-Meiwes, H.; Drillkens, J.; Lunz, B.; Muennix, J.; Rothgang, S.; Kowal, J.; Sauer, D. U., A review of current automotive battery technology and future prospects. *Proceedings of the Institution of Mechanical Engineers Part D-Journal of Automobile Engineering* **2013**, 227, (5), 761-776.
6. Han, X.; Lu, L.; Zheng, Y.; Feng, X.; Li, Z.; Li, J.; Ouyang, M., A review on the key issues of the lithium ion battery degradation among the whole life cycle. *eTransportation* **2019**, 1, 100005.
7. Whittingham, M. S., Lithium batteries and cathode materials. *Chemical Reviews* **2004**, 104, (10), 4271-4301.
8. Nitta, N.; Wu, F. X.; Lee, J. T.; Yushin, G., Li-ion battery materials: present and future. *Materials Today* **2015**, 18, (5), 252-264.
9. Xu, J. T.; Dou, S. X.; Liu, H. K.; Dai, L. M., Cathode materials for next generation lithium ion batteries. *Nano Energy* **2013**, 2, (4), 439-442.
10. Mizushima, K.; Jones, P. C.; Wiseman, P. J.; Goodenough, J. B., Li_xCoO_2 ($0 < x < 1$): A new cathode material for batteries of high energy density. *Materials Research Bulletin* **1980**, 15, (6), 783-789.
11. Yoshino, A.; Sanechika, K.; Nakajima, T. Secondary Battery US 4668595. 1986.
12. Daniel, C.; Mohanty, D.; Li, J. L.; Wood, D. L. In *Cathode Materials Review*, 1st International Freiberg Conference on Electrochemical Storage Materials, TU Bergakademie Freiberg, Freiberg, Germany, Jun 03-04, 2013; pp 26-43.
13. Ohzuku, T.; Makimura, Y., Layered lithium insertion material of $\text{LiNi}_{1/2}\text{Mn}_{1/2}\text{O}_2$: A possible alternative to LiCoO_2 for advanced lithium-ion batteries. *Chemistry Letters* **2001**, (8), 744-745.

14. Lai, Y. Q.; Xu, M.; Zhang, Z. A.; Gao, C. H.; Wang, P.; Yu, Z. Y., Optimized structure stability and electrochemical performance of $\text{LiNi}_{0.8}\text{Co}_{0.15}\text{Al}_{0.05}\text{O}_2$ by sputtering nanoscale ZnO film. *Journal of Power Sources* **2016**, 309, 20-26.
15. Yoon, W. S.; Chung, K. Y.; McBreen, J.; Yang, X. Q., A comparative study on structural changes of $\text{LiCo}_{1/3}\text{Ni}_{1/3}\text{Mn}_{1/3}\text{O}_2$ and $\text{LiNi}_{0.8}\text{Co}_{0.15}\text{Al}_{0.05}\text{O}_2$ during first charge using in situ XRD. *Electrochemistry Communications* **2006**, 8, (8), 1257-1262.
16. Lang, M.; Darma, M. S. D.; Kleiner, K.; Riekehr, L.; Mereacre, L.; Perez, M. A.; Liebau, V.; Ehrenberg, H., Post mortem analysis of fatigue mechanisms in $\text{LiNi}_{0.8}\text{Co}_{0.15}\text{Al}_{0.05}\text{O}_2$ - $\text{LiNi}_{0.5}\text{Co}_{0.2}\text{Mn}_{0.3}\text{O}_2$ - LiMn_2O_4 /graphite lithium ion batteries. *Journal of Power Sources* **2016**, 326, 397-409.
17. Lee, M. J.; Lee, S.; Oh, P.; Kim, Y.; Cho, J., High Performance LiMn_2O_4 Cathode Materials Grown with Epitaxial Layered Nanostructure for Li-Ion Batteries. *Nano Letters* **2014**, 14, (2), 993-999.
18. Padhi, A. K.; Nanjundaswamy, K. S.; Goodenough, J. B., Phospho-olivines as positive-electrode materials for rechargeable lithium batteries. *Journal of the Electrochemical Society* **1997**, 144, (4), 1188-1194.
19. Chung, S. Y.; Bloking, J. T.; Chiang, Y. M., Electronically conductive phospho-olivines as lithium storage electrodes. *Nature Materials* **2002**, 1, (2), 123-128.
20. Yamada, A.; Chung, S. C.; Hinokuma, K., Optimized LiFePO_4 for lithium battery cathodes. *Journal of the Electrochemical Society* **2001**, 148, (3), A224-A229.
21. Ge, Y. C.; Yan, X. D.; Liu, J.; Zhang, X. F.; Wang, J. W.; He, X. G.; Wang, R. S.; Xie, H. M., An optimized Ni doped LiFePO_4/C nanocomposite with excellent rate performance. *Electrochimica Acta* **2010**, 55, (20), 5886-5890.
22. Mohri, M.; Yanagisawa, N.; Tajima, Y.; Tanaka, H.; Mitate, T.; Nakajima, S.; Yoshida, M.; Yoshimoto, Y.; Suzuki, T.; Wada, H., Rechargeable lithium battery based on pyrolytic carbon as a negative electrode. *Journal of Power Sources* **1989**, 26, (3-4), 545-551.
23. Sethuraman, V. A.; Hardwick, L. J.; Srinivasan, V.; Kostecki, R., Surface structural disordering in graphite upon lithium intercalation/deintercalation. *Journal of Power Sources* **2010**, 195, (11), 3655-3660.
24. Aurbach, D.; Markovsky, B.; Weissman, I.; Levi, E.; Ein-Eli, Y., On the correlation between surface chemistry and performance of graphite negative electrodes for Li ion batteries. *Electrochimica Acta* **1999**, 45, (1-2), 67-86.

25. Takami, N.; Inagaki, H.; Tatebayashi, Y.; Saruwatari, H.; Honda, K.; Egusa, S., High-power and long-life lithium-ion batteries using lithium titanium oxide anode for automotive and stationary power applications. *Journal of Power Sources* **2013**, 244, 469-475.
26. Li, M.; Lu, J.; Chen, Z. W.; Amine, K., 30 Years of Lithium-Ion Batteries. *Advanced Materials* **2018**, 30, (33).
27. Zaghbi, K.; Dontigny, M.; Guerfi, A.; Charest, P.; Rodrigues, I.; Mauger, A.; Julien, C. M., Safe and fast-charging Li-ion battery with long shelf life for power applications. *Journal of Power Sources* **2011**, 196, (8), 3949-3954.
28. Ashuri, M.; He, Q. R.; Shaw, L. L., Silicon as a potential anode material for Li-ion batteries: where size, geometry and structure matter. *Nanoscale* **2016**, 8, (1), 74-103.
29. Kasavajjula, U.; Wang, C. S.; Appleby, A. J., Nano- and bulk-silicon-based insertion anodes for lithium-ion secondary cells. *Journal of Power Sources* **2007**, 163, (2), 1003-1039.
30. Jerliu, B.; Huger, E.; Dorrer, L.; Seidlhofer, B. K.; Steitz, R.; Oberst, V.; Geckle, U.; Bruns, M.; Schmidt, H., Volume Expansion during Lithiation of Amorphous Silicon Thin Film Electrodes Studied by In-Operando Neutron Reflectometry. *Journal of Physical Chemistry C* **2014**, 118, (18), 9395-9399.
31. Cui, L. F.; Yang, Y.; Hsu, C. M.; Cui, Y., Carbon-Silicon Core-Shell Nanowires as High Capacity Electrode for Lithium Ion Batteries. *Nano Letters* **2009**, 9, (9), 3370-3374.
32. Kim, I. S.; Kumta, P. N., High capacity Si/C nanocomposite anodes for Li-ion batteries. *Journal of Power Sources* **2004**, 136, (1), 145-149.
33. Eshkenazi, V.; Peled, E.; Burstein, L.; Golodnitsky, D., XPS analysis of the SEI formed on carbonaceous materials. *Solid State Ionics* **2004**, 170, (1-2), 83-91.
34. Forestier, C.; Jankowski, P.; Coser, L.; Gachot, G.; Sannier, L.; Johansson, P.; Armand, M.; Grugeon, S.; Laruelle, S., Facile reduction of pseudo-carbonates: Promoting solid electrolyte interphases with dicyanoketene alkylene acetals in lithium-ion batteries. *Journal of Power Sources* **2016**, 303, 1-9.
35. Buqa, H.; Holzapfel, M.; Krumeich, F.; Veit, C.; Novak, P., Study of styrene butadiene rubber and sodium methyl cellulose as binder for negative electrodes in lithium-ion batteries. *Journal of Power Sources* **2006**, 161, (1), 617-622.
36. Xu, J. T.; Chou, S. L.; Gu, Q. F.; Liu, H. K.; Dou, S. X., The effect of different binders on electrochemical properties of $\text{LiNi}_{1/3}\text{Mn}_{1/3}\text{C}_{1/3}\text{O}_2$ cathode material in lithium ion batteries. *Journal of Power Sources* **2013**, 225, 172-178.

37. Arora, P.; Zhang, Z. M., Battery separators. *Chemical Reviews* **2004**, 104, (10), 4419-4462.
38. Guan, H. Y.; Lian, F.; Ren, Y.; Wen, Y.; Pan, X. R.; Sun, J. L., Comparative study of different membranes as separators for rechargeable lithium-ion batteries. *International Journal of Minerals Metallurgy and Materials* **2013**, 20, (6), 598-603.
39. Marcinek, M.; Syzdek, J.; Marczewski, M.; Piszcz, M.; Niedzicki, L.; Kalita, M.; Plewa-Marczewska, A.; Bitner, A.; Wieczorek, P.; Trzeciak, T.; Kasprzyk, M.; Lezak, P.; Zukowska, Z.; Zalewska, A.; Wieczorek, W., Electrolytes for Li-ion transport - Review (vol 276, pg 107, 2015). *Solid State Ionics* **2015**, 282, 95-95.
40. Zhao, H.; Park, S. J.; Shi, F. F.; Fu, Y. B.; Battaglia, V.; Ross, P. N.; Liu, G., Propylene Carbonate (PC)-Based Electrolytes with High Coulombic Efficiency for Lithium-Ion Batteries. *Journal of the Electrochemical Society* **2014**, 161, (1), A194-A200.
41. Forestier, C. Influence of the electrolyte on the safety of Li-ion batteries: role of additives and lithium salt. University Picardie Jules Verne, Amiens, France, 2017.
42. Fergus, J. W., Ceramic and polymeric solid electrolytes for lithium-ion batteries. *Journal of Power Sources* **2010**, 195, (15), 4554-4569.
43. Famprikis, T.; Canepa, P.; Dawson, J. A.; Islam, M. S.; Masquelier, C., Fundamentals of inorganic solid-state electrolytes for batteries. *Nature materials* **2019**, 18, (12), 1278-1291.
44. Murugan, R.; Thangadurai, V.; Weppner, W., Fast lithium ion conduction in garnet-type $\text{Li}_7\text{La}_3\text{Zr}_2\text{O}_{12}$. *Angewandte Chemie-International Edition* **2007**, 46, (41), 7778-7781.
45. Thangadurai, V.; Narayanan, S.; Pinzaru, D., Garnet-type solid-state fast Li ion conductors for Li batteries: critical review. *Chemical Society Reviews* **2014**, 43, (13), 4714-4727.
46. Awaka, J.; Kijima, N.; Hayakawa, H.; Akimoto, J., Synthesis and structure analysis of tetragonal $\text{Li}_7\text{La}_3\text{Zr}_2\text{O}_{12}$ with the garnet-related type structure. *Journal of Solid State Chemistry* **2009**, 182, (8), 2046-2052.
47. Allen, J. L.; Wolfenstine, J.; Rangasamy, E.; Sakamoto, J., Effect of substitution (Ta, Al, Ga) on the conductivity of $\text{Li}_7\text{La}_3\text{Zr}_2\text{O}_{12}$. *Journal of Power Sources* **2012**, 206, 315-319.
48. Kanno, R.; Hata, T.; Kawamoto, Y.; Irie, M., Synthesis of a new lithium ionic conductor, thio-LISICON-lithium germanium sulfide system. *Solid State Ionics* **2000**, 130, (1-2), 97-104.
49. Kanno, R.; Maruyama, M., Lithium ionic conductor thio-LISICON - The $\text{Li}_2\text{S-GeS}_2\text{-P}_2\text{S}_5$ system. *Journal of the Electrochemical Society* **2001**, 148, (7), A742-A746.

50. Kato, Y.; Hori, S.; Saito, T.; Suzuki, K.; Hirayama, M.; Mitsui, A.; Yonemura, M.; Iba, H.; Kanno, R., High-power all-solid-state batteries using sulfide superionic conductors. *Nature Energy* **2016**, 1.
51. Wang, F.; Li, L.; Yang, X.; You, J.; Xu, Y.; Wang, H.; Ma, Y.; Gao, G., Influence of additives in a PVDF-based solid polymer electrolyte on conductivity and Li-ion battery performance. *Sustainable Energy & Fuels* **2018**, 2, (2), 492-498.
52. Abraham, K. M.; Jiang, Z.; Carroll, B., Highly conductive PEO-like polymer electrolytes. *Chemistry of Materials* **1997**, 9, (9), 1978-1988.
53. Gauthier, M.; Fauteux, D.; Vassort, G.; Belanger, A.; Duval, M.; Ricoux, P.; Chabagno, J. M.; Muller, D.; Rigaud, P.; Armand, M. B.; Deroo, D., Behavior of polymer electrolyte batteries at 80-100 degrees-C and near room-temperature. *Journal of Power Sources* **1985**, 14, (1-3), 23-26.
54. Mindemark, J.; Lacey, M. J.; Bowden, T.; Brandell, D., Beyond PEO-Alternative host materials for Li⁺-conducting solid polymer electrolytes. *Progress in Polymer Science* **2018**, 81, 114-143.
55. Berthier, C.; Gorecki, W.; Minier, M.; Armand, M. B.; Chabagno, J. M.; Rigaud, P., Microscopic investigation of ionic-conductivity in alkali-metal salts poly(ethylene oxide) adducts. *Solid State Ionics* **1983**, 11, (1), 91-95.
56. Croce, F.; Persi, L.; Scrosati, B.; Serraino-Fiory, F.; Plichta, E.; Hendrickson, M. A., Role of the ceramic fillers in enhancing the transport properties of composite polymer electrolytes. *Electrochimica Acta* **2001**, 46, (16), 2457-2461.
57. Croce, F.; Curini, R.; Martinelli, A.; Persi, L.; Ronci, F.; Scrosati, B.; Caminiti, R., Physical and chemical properties of nanocomposite polymer electrolytes. *Journal of Physical Chemistry B* **1999**, 103, (48), 10632-10638.
58. Liu, W.; Lee, S. W.; Lin, D. C.; Shi, F. F.; Wang, S.; Sendek, A. D.; Cui, Y., Enhancing ionic conductivity in composite polymer electrolytes with well-aligned ceramic nanowires. *Nature Energy* **2017**, 2, (5).
59. Yu, X.; Xue, L.; Goodenough, J. B.; Manthiram, A., A High-Performance All-Solid-State Sodium Battery with a Poly(ethylene oxide)-Na₃Zr₂Si₂PO₁₂ Composite Electrolyte. *ACS Materials Letters* **2019**, 1, (1), 132-138.
60. Saunier, J.; Alloin, F.; Sanchez, J. Y.; Maniguet, L., Plasticized microporous poly(vinylidene fluoride) separators for lithium-ion batteries. III. Gel properties and irreversible

modifications of poly(vinylidene fluoride) membranes under swelling in liquid electrolytes. *Journal of Polymer Science Part B-Polymer Physics* **2004**, 42, (12), 2308-2317.

61. Sannier, L.; Bouchet, R.; Grugeon, S.; Naudin, E.; Vidal, E.; Tarascon, J. M., Room temperature lithium metal batteries based on a new Gel Polymer Electrolyte membrane. *Journal of Power Sources* **2005**, 144, (1), 231-237.

62. Myung, S. T.; Hitoshi, Y.; Sun, Y. K., Electrochemical behavior and passivation of current collectors in lithium-ion batteries. *Journal of Materials Chemistry* **2011**, 21, (27), 9891-9911.

63. Forestier, C.; Grugeon, S.; Davoisne, C.; Lecocq, A.; Marlair, G.; Armand, M.; Sannier, L.; Laruelle, S., Graphite electrode thermal behavior and solid electrolyte interphase investigations: Role of state-of-the-art binders, carbonate additives and lithium bis(fluorosulfonyl)imide salt. *Journal of Power Sources* **2016**, 330, 186-194.

64. Kim, S. W.; Cho, K. Y., Current Collectors for Flexible Lithium Ion Batteries: A Review of Materials. *Journal of Electrochemical Science and Technology* **2015**, 6, (1), 1-6.

65. Singh, N.; Galande, C.; Miranda, A.; Mathkar, A.; Gao, W.; Reddy, A. L. M.; Vlad, A.; Ajayan, P. M., Paintable Battery. *Scientific Reports* **2012**, 2.

66. Long, J. W.; Dunn, B.; Rolison, D. R.; White, H. S., Three-dimensional battery architectures. *Chemical Reviews* **2004**, 104, (10), 4463-4492.

67. Zadin, V.; Kasemagi, H.; Aabloo, A.; Brandell, D., Modelling electrode material utilization in the trench model 3D-microbattery by finite element analysis. *Journal of Power Sources* **2010**, 195, (18), 6218-6224.

68. Trembacki, B.; Duoss, E.; Oxberry, G.; Stadermann, M.; Murthy, J., Mesoscale Electrochemical Performance Simulation of 3D Interpenetrating Lithium-Ion Battery Electrodes. *Journal of the Electrochemical Society* **2019**, 166, (6), A923-A934.

69. Ferrari, S.; Loveridge, M.; Beattie, S. D.; Jahn, M.; Dashwood, R. J.; Bhagat, R., Latest advances in the manufacturing of 3D rechargeable lithium microbatteries. *Journal of Power Sources* **2015**, 286, 25-46.

70. Min, H. S.; Park, B. Y.; Taherabadi, L.; Wang, C. L.; Yeh, Y.; Zaouk, R.; Madou, M. J.; Dunn, B., Fabrication and properties of a carbon/polypyrrole three-dimensional microbattery. *Journal of Power Sources* **2008**, 178, (2), 795-800.

71. Taberna, L.; Mitra, S.; Poizot, P.; Simon, P.; Tarascon, J. M., High rate capabilities Fe₃O₄-based Cu nano-architected electrodes for lithium-ion battery applications. *Nature Materials* **2006**, 5, (7), 567-573.

72. Oltean, G.; Nyholm, L.; Edstrom, K., Galvanostatic electrodeposition of aluminium nano-rods for Li-ion three-dimensional micro-battery current collectors. *Electrochimica Acta* **2011**, *56*, (9), 3203-3208.
73. Roberts, M.; Johns, P.; Owen, J.; Brandell, D.; Edstrom, K.; El Enany, G.; Guery, C.; Golodnitsky, D.; Lacey, M.; Lecoœur, C.; Mazor, H.; Peled, E.; Perre, E.; Shaijumon, M. M.; Simon, P.; Taberna, P. L., 3D lithium ion batteries-from fundamentals to fabrication. *Journal of Materials Chemistry* **2011**, *21*, (27), 9876-9890.
74. Bikas, H.; Stavropoulos, P.; Chryssolouris, G., Additive manufacturing methods and modelling approaches: a critical review. *International Journal of Advanced Manufacturing Technology* **2016**, *83*, (1-4), 389-405.
75. Chen, L.; He, Y.; Yang, Y. X.; Niu, S. W.; Ren, H. T., The research status and development trend of additive manufacturing technology. *International Journal of Advanced Manufacturing Technology* **2017**, *89*, (9-12), 3651-3660.
76. Berman, B., 3-D printing: The new industrial revolution. *Business Horizons* **2012**, *55*, (2), 155-162.
77. Gao, W.; Zhang, Y. B.; Ramanujan, D.; Ramani, K.; Chen, Y.; Williams, C. B.; Wang, C. C. L.; Shin, Y. C.; Zhang, S.; Zavattieri, P. D., The status, challenges, and future of additive manufacturing in engineering. *Computer-Aided Design* **2015**, *69*, 65-89.
78. Ngo, T. D.; Kashani, A.; Imbalzano, G.; Nguyen, K. T. Q.; Hui, D., Additive manufacturing (3D printing): A review of materials, methods, applications and challenges. *Composites Part B-Engineering* **2018**, *143*, 172-196.
79. Hull, C. W. US4575330A Apparatus for production of three-dimensional objects by stereolithography. 1986.
80. André, J.-C.; Le Mehauté, A.; De Witte, O. FR 2567668 A1 Dispositif pour réaliser un modèle de pièce industrielle. 1986.
81. Yang, Y.; Yuan, W.; Zhang, X.; Yuan, Y.; Wang, C.; Ye, Y.; Huang, Y.; Qiu, Z.; Tang, Y., Overview on the applications of three-dimensional printing for rechargeable lithium-ion batteries. *Applied Energy* **2020**, *257*, 114002.
82. Savage, N., VOXEL8 3D printing mixes materials. *Nature* **2017**, *545*, (7654), S20-S20.
83. Dodziuk, H., Applications of 3D printing in healthcare. *Kardiochirurgia I Torakochirurgia Polska-Polish Journal of Thoracic and Cardiovascular Surgery* **2016**, *13*, (3), 283-293.

84. Krimi, I.; Lafhaj, Z.; Ducoulombier, L., Prospective study on the integration of additive manufacturing to building industry-Case of a French construction company. *Additive Manufacturing* **2017**, 16, 107-114.
85. Leal, R.; Barreiros, F. M.; Alves, L.; Romeiro, F.; Vasco, J. C.; Santos, M.; Marto, C., Additive manufacturing tooling for the automotive industry. *International Journal of Advanced Manufacturing Technology* **2017**, 92, (5-8), 1671-1676.
86. Martin, J. H.; Yahata, B. D.; Hundley, J. M.; Mayer, J. A.; Schaedler, T. A.; Pollock, T. M., 3D printing of high-strength aluminium alloys. *Nature* **2017**, 549, (7672), 365-+.
87. Espalin, D.; Muse, D. W.; MacDonald, E.; Wicker, R. B., 3D Printing multifunctionality: structures with electronics. *International Journal of Advanced Manufacturing Technology* **2014**, 72, (5-8), 963-978.
88. Sun, K.; Wei, T. S.; Ahn, B. Y.; Seo, J. Y.; Dillon, S. J.; Lewis, J. A., 3D Printing of Interdigitated Li-Ion Microbattery Architectures. *Advanced Materials* **2013**, 25, (33), 4539-4543.
89. *3D-Hubs Manufacturing LLC - Annual Report - 3D printing trends 2020 : Industry highlights and market trends*; 2020.
90. Gao, Y.; Li, B.; Wang, W.; Xu, W.; Zhou, C.; Jin, Z., Watching and Safeguarding Your 3D Printer: Online Process Monitoring Against Cyber-Physical Attacks. *Proc. ACM Interact. Mob. Wearable Ubiquitous Technol.* **2018**, 2, (3), 108.
91. Delannoy, P. E.; Riou, B.; Lestriez, B.; Guyomard, D.; Brousse, T.; Le Bideau, J., Toward fast and cost-effective ink-jet printing of solid electrolyte for lithium microbatteries. *Journal of Power Sources* **2015**, 274, 1085-1090.
92. Zhao, Y.; Zhou, Q.; Liu, L.; Xu, J.; Yan, M.; Jiang, Z., A novel and facile route of ink-jet printing to thin film SnO₂ anode for rechargeable lithium ion batteries. *Electrochimica Acta* **2006**, 51, (13), 2639-2645.
93. Zhao, Y. M.; Xu, J.; Liu, L.; Yang, J.; Jiang, Z. Y., Thin film LiCoO₂ Cathode prepared by using ink-jet printing technique and its electrochemical properties. *Chemical Journal of Chinese Universities-Chinese* **2007**, 28, (6), 1122-1125.
94. Huang, J.; Yang, J.; Li, W.; Cai, W.; Jiang, Z., Electrochemical properties of LiCoO₂ thin film electrode prepared by ink-jet printing technique. *Thin Solid Films* **2008**, 516, (10), 3314-3319.
95. Zhao, Y. M.; Liu, G. Q.; Liu, L.; Jiang, Z. Y., High-performance thin-film Li₄Ti₅O₁₂ electrodes fabricated by using ink-jet printing technique and their electrochemical properties. *Journal of Solid State Electrochemistry* **2009**, 13, (5), 705-711.

96. Lee, J. H.; Wee, S. B.; Kwon, M. S.; Kim, H. H.; Choi, J. M.; Song, M. S.; Park, H. B.; Kim, H.; Paik, U., Strategic dispersion of carbon black and its application to ink-jet-printed lithium cobalt oxide electrodes for lithium ion batteries. *Journal of Power Sources* **2011**, 196, (15), 6449-6455.
97. Gu, Y.; Wu, A.; Sohn, H.; Nicoletti, C.; Iqbal, Z.; Federici, J. F., Fabrication of rechargeable lithium ion batteries using water-based inkjet printed cathodes. *Journal of Manufacturing Processes* **2015**, 20, 198-205.
98. Fu, K.; Wang, Y. B.; Yan, C. Y.; Yao, Y. G.; Chen, Y. A.; Dai, J. Q.; Lacey, S.; Wan, J. Y.; Li, T.; Wang, Z. Y.; Xu, Y.; Hu, L. B., Graphene Oxide-Based Electrode Inks for 3D-Printed Lithium-Ion Batteries. *Advanced Materials* **2016**, 28, (13), 2587-+.
99. Blake, A. J.; Kohlmeyer, R. R.; Hardin, J. O.; Carmona, E. A.; Maruyama, B.; Berrigan, J. D.; Huang, H.; Durstock, M. F., 3D Printable Ceramic-Polymer Electrolytes for Flexible High-Performance Li-Ion Batteries with Enhanced Thermal Stability. *Advanced Energy Materials* **2017**, 7, (14).
100. Liu, Y.; Qiao, Y.; Zhang, Y.; Yang, Z.; Gao, T. T.; Kirsch, D.; Liu, B. Y.; Song, J. W.; Yang, B.; Hu, L. B., 3D printed separator for the thermal management of high-performance Li metal anodes. *Energy Storage Materials* **2018**, 12, 197-203.
101. Cheng, M.; Jiang, Y. Z.; Yao, W. T.; Yuan, Y. F.; Deivanayagam, R.; Foroozan, T.; Huang, Z. N.; Song, B.; Rojaee, R.; Shokuhfar, T.; Pan, Y. Y.; Lu, J.; Shahbazian-Yassar, R., Elevated-Temperature 3D Printing of Hybrid Solid-State Electrolyte for Li-Ion Batteries. *Advanced Materials* **2018**, 30, (39).
102. McOwen, D. W.; Xu, S. M.; Gong, Y. H.; Wen, Y.; Godbey, G. L.; Gritton, J. E.; Hamann, T. R.; Dai, J. Q.; Hitz, G. T.; Hu, L. B.; Wachsman, E. D., 3D-Printing Electrolytes for Solid-State Batteries. *Advanced Materials* **2018**, 30, (18).
103. Li, J.; Liang, X. H.; Liou, F.; Park, J., Macro-/Micro-Controlled 3D Lithium-Ion Batteries via Additive Manufacturing and Electric Field Processing. *Scientific Reports* **2018**, 8.
104. Wei, T. S.; Ahn, B. Y.; Grotto, J.; Lewis, J. A., 3D Printing of Customized Li-Ion Batteries with Thick Electrodes. *Advanced Materials* **2018**, 30, (16), 7.
105. Liu, C. Y.; Xu, F.; Cheng, X. X.; Tong, J. D.; Liu, Y. L.; Chen, Z. W.; Lao, C. S.; Ma, J., Comparative study on the electrochemical performance of LiFePO₄ cathodes fabricated by low temperature 3D printing, direct ink writing and conventional roller coating process. *Ceramics International* **2019**, 45, (11), 14188-14197.

106. Leigh, S. J.; Bradley, R. J.; Pursell, C. P.; Billson, D. R.; Hutchins, D. A., A Simple, Low-Cost Conductive Composite Material for 3D Printing of Electronic Sensors. *Plos One* **2012**, 7, (11).
107. Dul, S.; Fambri, L.; Pegoretti, A., Fused deposition modelling with ABS-graphene nanocomposites. *Composites Part a-Applied Science and Manufacturing* **2016**, 85, 181-191.
108. Wei, X. J.; Li, D.; Jiang, W.; Gu, Z. M.; Wang, X. J.; Zhang, Z. X.; Sun, Z. Z., 3D Printable Graphene Composite. *Scientific Reports* **2015**, 5.
109. Foster, C. W.; Down, M. P.; Zhang, Y.; Ji, X. B.; Rowley-Neale, S. J.; Smith, G. C.; Kelly, P. J.; Banks, C. E., 3D Printed Graphene Based Energy Storage Devices. *Scientific Reports* **2017**, 7, 11.
110. Chen, Q. M.; Xu, R.; He, Z. T.; Zhao, K. J.; Pan, L., Printing 3D Gel Polymer Electrolyte in Lithium-Ion Microbattery Using Stereolithography. *Journal of the Electrochemical Society* **2017**, 164, (9), A1852-A1857.
111. Zekoll, S.; Marriner-Edwards, C.; Hekselman, A. K. O.; Kasemchainan, J.; Kuss, C.; Armstrong, D. E. J.; Cai, D. Y.; Wallace, R. J.; Richter, F. H.; Thijssen, J. H. J.; Bruce, P. G., Hybrid electrolytes with 3D bicontinuous ordered ceramic and polymer microchannels for all-solid-state batteries. *Energy & Environmental Science* **2018**, 11, (1), 185-201.
112. Cohen, E.; Menkin, S.; Lifshits, M.; Kamir, Y.; Gladkikh, A.; Kosa, G.; Golodnitsky, D., Novel rechargeable 3D-Microbatteries on 3D-printed-polymer substrates: Feasibility study. *Electrochimica Acta* **2018**, 265, 690-701.
113. Park, S. H.; Kaur, M.; Yun, D.; Kim, W. S., Hierarchically Designed Electron Paths in 3D Printed Energy Storage Devices. *Langmuir* **2018**, 34, (37), 10897-10904.
114. Yang, Y.; Chen, Z. Y.; Song, X.; Zhu, B. P.; Hsiai, T.; Wu, P. I.; Xiong, R.; Shi, J.; Chen, Y.; Zhou, Q. F.; Shung, K. K., Three dimensional printing of high dielectric capacitor using projection based stereolithography method. *Nano Energy* **2016**, 22, 414-421.
115. Lahtinen, E.; Kukkonen, E.; Jokivartio, J.; Parkkonen, J.; Virkajarvi, J.; Kivijarvi, L.; Ahlskog, M.; Haukka, M., Preparation of Highly Porous Carbonous Electrodes by Selective Laser Sintering. *Acs Applied Energy Materials* **2019**, 2, (2), 1314-1318.
116. Sha, J. W.; Li, Y. L.; Salvatierra, R. V.; Wang, T.; Dong, P.; Ji, Y. S.; Lee, S. K.; Zhang, C. H.; Zhang, J. B.; Smith, R. H.; Ajayan, P. M.; Lou, J.; Zhao, N. Q.; Tour, J. M., Three-Dimensional Printed Graphene Foams. *Acs Nano* **2017**, 11, (7), 6860-6867.

117. Lu, X. F.; Zhao, T. K.; Ji, X. L.; Hu, J. T.; Li, T. H.; Lin, X.; Huang, W. D., 3D printing well organized porous iron-nickel/polyaniline nanocages multiscale supercapacitor. *Journal of Alloys and Compounds* **2018**, 760, 78-83.
118. Zhao, C.; Wang, C. Y.; Gorkin, R.; Beirne, S.; Shu, K. W.; Wallace, G. G., Three dimensional (3D) printed electrodes for interdigitated supercapacitors. *Electrochemistry Communications* **2014**, 41, 20-23.

Chapter 2.

Composite filaments elaboration for LIB 3D-printing via fused deposition modeling

Chapter 2. Composite filaments elaboration for LIB 3D-printing via fused deposition modeling

2.1. Introduction.....	54
2.1.1. Elaboration process.....	54
2.1.2. Polymer choice.....	56
2.1.3. Selection of a suitable solvent.....	58
2.2. Highly-loaded electrodes filaments formulation.....	60
2.2.1. Negative electrode.....	60
2.2.1.1. Preliminary tests.....	60
2.2.1.2. Influence of various plasticizers.....	61
2.2.1.3. Optimization of plasticizer content.....	64
2.2.1.3.1. Mechanical characterization and printability.....	65
2.2.1.3.2. Optimized filament homogeneity.....	67
2.2.1.3.3. Thermal characterization.....	69
2.2.1.4. Optimization of conductive additives content.....	73
2.2.1.4.1. Electrical conductivity.....	73
2.2.1.4.2. Electrochemical characterization.....	76
2.2.2. Positive electrode.....	82
2.2.2.1. Optimization of plasticizer content.....	82
2.2.2.2. Optimization of conductive additives content.....	82
2.2.2.2.1. Electrical conductivity.....	83
2.2.2.2.2. Printability and mechanical characterization.....	85
2.2.2.2.3. Thermal characterization.....	87
2.2.2.2.4. Electrochemical characterization.....	90
2.2.3. Comparison with contemporary studies.....	93
2.3. Separator filament formulation.....	96
2.3.1. Preparation.....	96
2.3.2. Optimization of the ceramic content.....	98
2.4. Current collector filament formulation.....	103
2.4.1. Silver coated copper powder.....	103
2.4.2. Composite film and filament.....	106
Conclusions.....	110
References	112

2.1. Introduction

Fused Deposition Modeling (FDM) involves the use of a thermoplastic polymer-based filament as material source for the 3D-printer. With the aim to print a liquid electrolyte-based LIB battery, the preparation and optimization of customized composite filaments for each component was addressed. Beforehand, the implementation of a suitable elaboration protocol and choice of materials was required.

2.1.1. Elaboration process

Figure 2.1 displays the main steps of the elaboration procedure that was established. In order to further ensure a good dispersion of the charges within the polymer matrix, this latter was first of all dissolved within a solvent at room temperature under magnetic stirring. Once the polymer particles complete dissolution was reached, the desired amount of plasticizer and charges (active material, conductive additives, or ceramic particles) was introduced. After applying a magnetic stirring for at least 30 minutes, the slurry was then tape-casted onto a glass substrate and solvent was evaporated. Resulting from this step, films with two different thicknesses were achieved. Obtained films about 60 μm thick were strictly reserved to endure further electrochemical characterization, while 1 mm thicker samples were rather used to undergo thermal, mechanical, microstructural, morphological and electrical characterization.

Films specimen were then cut into small pieces to feed homogeneously a laboratory-scale screw extruder (Filabot Original supplied by Filabot Triex LLC, USA) and produce standard $\sim 1.75\text{mm}$ diameter filaments. Typically used in the polymer industry, this machine consists of an electrically heated metal barrel, a hopper for feeding, a motor for rotating a screw, and a die where the polymer is melted and released. The combination of thermal energy generated by a heater and frictional heat due to friction between the polymer material and the screw and barrel provides heat allowing samples melting. Temperature of the extruder was fixed typically between 10°C and 35°C above the melting temperature of the polymer composite film deduced from differential scanning calorimetry (DSC) results. The filament coming out from the hot extruder nozzle was rolled manually around a beaker, and solidified immediately by contact with the cold surface.

Subsequently, the cooled composite filament was rolled around a standard spool using a Filabot spooler (Filabot Triex LLC, USA). Prior to extrusion of each sample with a different composition, the extruder was cleaned thoroughly with neat polymer. Finally, the afore-prepared composite filaments were then used to feed a FDM 3D-printer. The resulting printed samples were then characterized.

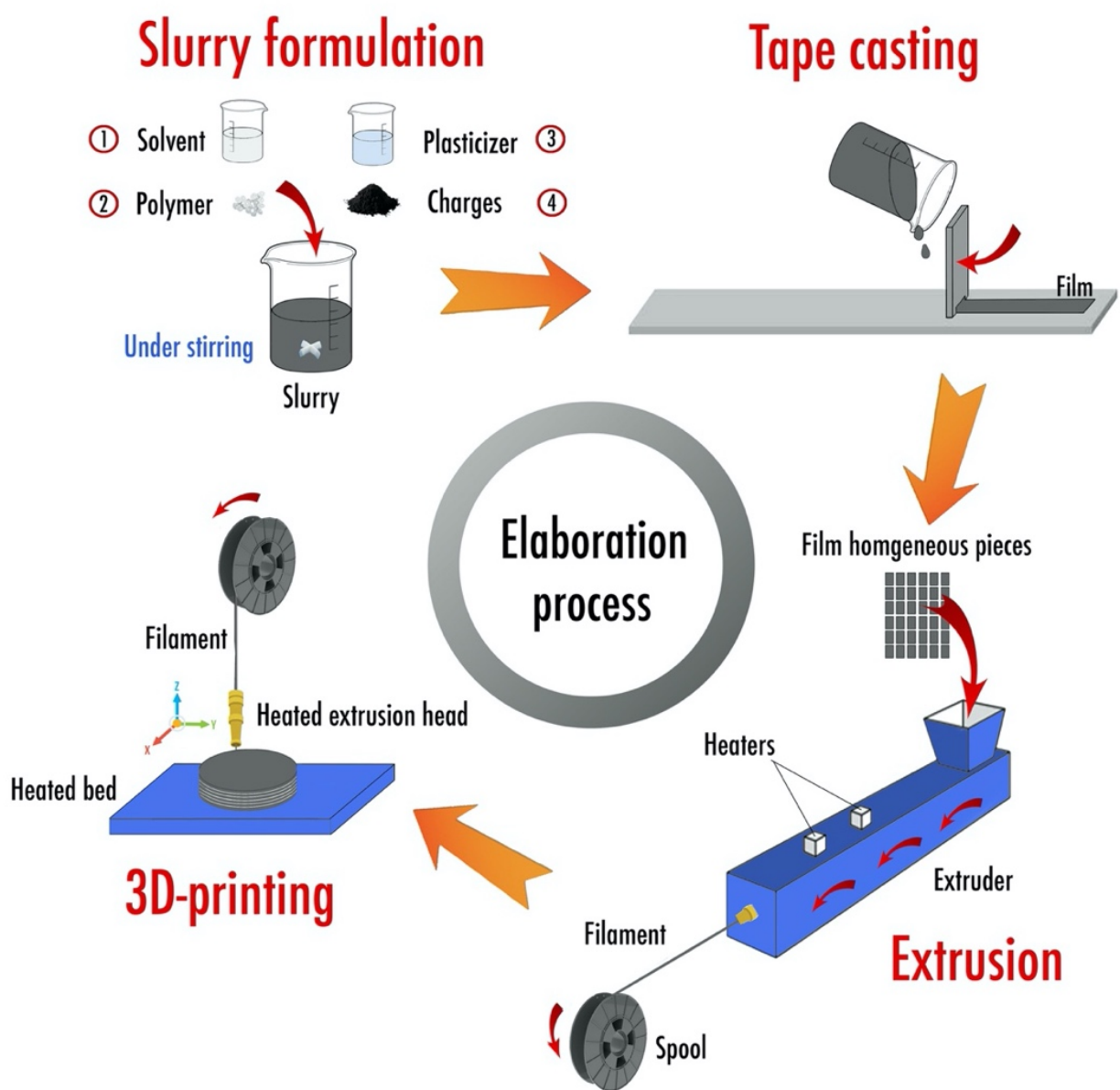


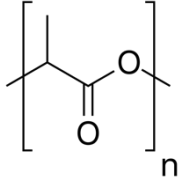
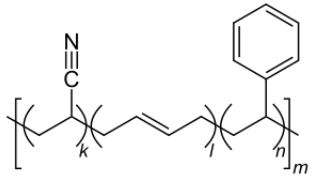
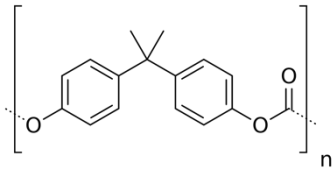
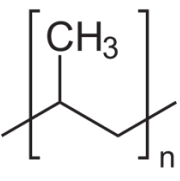
Figure 2.1. Principal stages of the elaboration process — cf. Preface – I.

2.1.2. Polymer choice

Directly linked to the filament mechanical properties and FDM printability, the polymer selection appears as a crucial step. Due to their ability to melt and be processed again, thermoplastics are compulsory for FDM printing application. When temperature increases, the intermolecular forces of the polymer chains decrease and lead to a viscous liquid. Upon cooling, it solidifies again. Thermoplastics are differentiated from thermosetting polymers, which rather create irreversible chemical bonds during the curing process and cannot be melted for reshaping.

As described beforehand (cf. **1.2.2.1.2. Fused deposition modeling**), most common thermoplastic polymers employed for FDM printing involve polylactic acid (PLA), acrylonitrile butadiene styrene (ABS), polycarbonate (PolyC) or polypropylene (PP). Among them, PLA, linear aliphatic polyester that can be prepared by both direct condensation of lactic acid and by ring-opening polymerization of the cyclic lactide dimer,¹ appears as an interesting option as it is a biodegradable polymer derived from renewable agricultural resources such as corn starch.^{2, 3} Unlike the hydrocarbon-based polymers, PLA absorbs greenhouse gases such as CO₂, main contributor of global warming, during its production.⁴ Due to its unique properties such as high mechanical strength, low toxicity and low melting/printing temperature in comparison with the other offered options (**Table 2.1**), PLA was chosen as polymer matrix for the subsequent composite filament formulation. PLA 4032D pellets, supplied by Natureworks, USA, were employed for this project and used as received.

Table 2.1. Compared characteristics of common polymers employed for FDM.

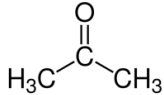
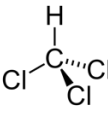
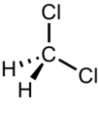
Polymer	PLA	ABS	PolyC	PP
Production	Corn-based	Oil-based	Oil-based	Oil-based
Printing temperature	~190 °C	~230 °C	~260°C	~240 °C
Toxicity	None	Harmful vapors emission		
Tensile strength (MPa)	~59	25 – 50	55 – 75	20 – 40
Young's modulus (GPa)	~3.5	1.1 – 2.9	2.0 – 2.4	1.1 – 1.6
Representation				

2.1.3. Selection of a suitable solvent

Allowing the charges to be incorporated homogeneously within the PLA polymer matrix, the solvent choice is essential. Sato et al.⁵ determined the impact of several liquid organic solvents on PLA, noticing that it is soluble in polar aprotic solvent but insoluble in polar protic and nonpolar solvents. Therefore, solubility experiments were accomplished at room temperature by testing various polar aprotic solvents from different chemical classes with a weight ratio PLA/solvent 1:10 under magnetic stirring. Total amount of PLA equals to 3 g was thus incorporated within dichloromethane ($\geq 99.5\%$, VWR Chemicals, USA), tetrahydrofuran ($\geq 99\%$, VWR Chemicals, USA), acetone ($\geq 99.5\%$, Sigma-Aldrich, USA) and chloroform ($\geq 99\%$, Sigma-Aldrich, USA). Toxicity, time of dissolution and boiling point criteria were taken into consideration to determine the best solvent to dissolve pure PLA pellets (**Table 2.2**). Finally, dichloromethane (DCM) was considered as the best option as it allows a quick dissolution of PLA, toxicity is less important than chloroform, and its relatively low boiling point results in a fast evaporation of the solvent after slurry tape-casting.

Chapter 2. Composite filaments elaboration for LIB 3D printing via fused deposition modeling

Table 2.2. Determination of the best solvent for pure PLA. Weight ratio PLA/solvent 1:10 under constant magnetic stirring and at room temperature.

Group	Solvent	Formula	Melting point (°C)	Boiling point (°C)	Density (g cm ⁻³)	Hazards (NFPA 704)	Dissolution time
Ketone	Acetone		-94.7	56.05	0.7845 (25 °C)		Insoluble (after 4 months of tests)
Ether	Tetrahydrofuran (THF)		-108.4	66	0.8892 (20 °C)		Long (6 hours)
Chloroalkane	Chloroform		-63.5	61.15	1.489 (25 °C)		Fast (1h30)
Chloroalkane	Dichloromethane (DCM)		-96.7	39.6	1.3266 (20 °C)		Very fast (45 minutes)

2.2. Highly-loaded electrodes filaments formulation

At the time this PhD thesis was started, as depicted earlier in the FDM literature overview (cf. **1.2.2.1.2. Fused deposition modeling**), only composite filaments containing a very limited amount of charges (ranging from 4 wt.% to 15wt.% of the total composite) were reported,⁶⁻⁹ thus prioritizing the good mechanical handling at the expense of the electrochemical performances. On the contrary, this PhD thesis was dedicated to increase as high as possible the introduction of charges with a view to favor the electrochemical performances while still maintaining just enough mechanical strength for handling and printing. Note that results presented in the following sections are already part of published articles (cf. **Preface — I and II**).

2.2.1. Negative electrode

2.2.1.1. Preliminary tests

Preliminary tests were focused on the introduction of a high amount of carbonaceous active material (graphite) usually employed at the negative electrode. Hence, after complete dissolution of the PLA polymer matrix into DCM (wt% PLA/DCM 1:10) at room temperature and under magnetic stirring for 1 hour, a significant amount of artificial graphite ($1.5 \text{ m}^2 \text{ g}^{-1}$, $d_{50}=14\mu\text{m}$, $d_{90}=26\mu\text{m}$) was introduced (wt% ratio PLA/Graphite 30:70). After slurry tape casting and complete evaporation of the solvent, a free-standing composite film was thus obtained.

Serving here as reference, as depicted in **Figure 2.2**, it was observed by performing Differential Scanning Calorimetry (DSC204F1 supplied by Netzsch-Gerätebau GmbH, heating rate of $10^\circ\text{C min}^{-1}$, between -60°C to 300°C in argon atmosphere 50 mL min^{-1} , using about 10 mg of sample, data from first heating operation) that neat PLA film displays an endothermic peak related to the melting temperature (T_m) at 146°C and a sharp peak corresponding to the glass transition (T_g) appearing at 63°C . Instead, through the introduction of such a high amount of graphite within the polymer matrix, the endothermic peak corresponding to the melting temperature was slightly shifted to lower temperature (141°C) while T_g was no longer distinctly visible. A minor endothermic peak corresponding to the water desorption was observed around 100°C .

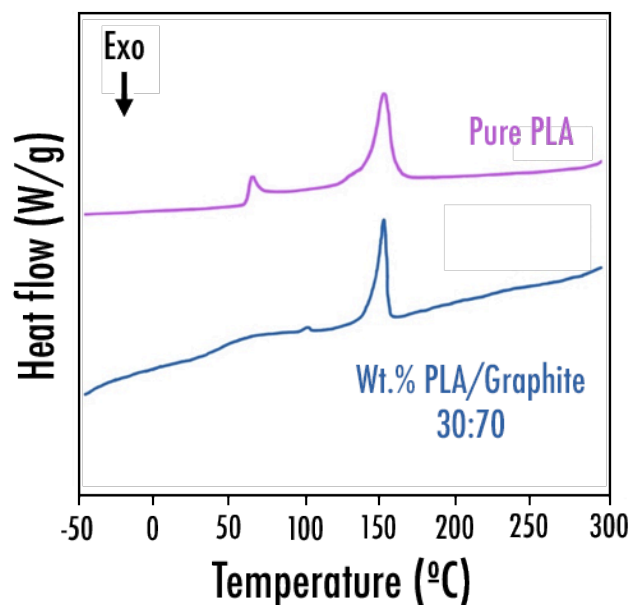


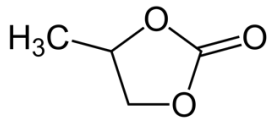
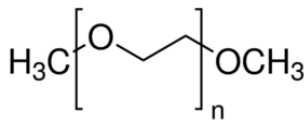
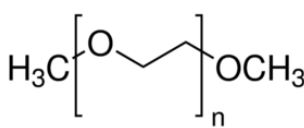
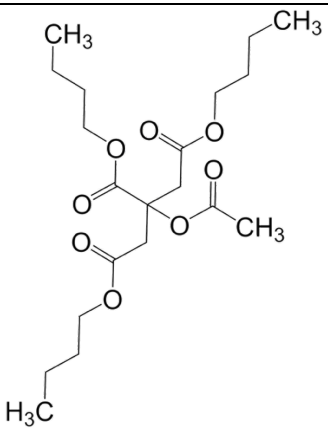
Figure 2.2. DSC curves of pure PLA and PLA/Graphite (wt% PLA/Graphite 30:70) films.

Besides, due to the very high amount of charges added to the polymer matrix, here, without necessity of performing any mechanical test, it was clearly perceived that the resulting composite film depicted a too important brittle behavior. From this composition (wt% ratio PLA/Graphite 30:70), the resulting highly loaded filament was impossible to handle and obviously not printable. Consequently, with the aim to improve the mechanical behavior while keeping such a high amount of charges, the introduction of a plasticizer to the composite was thoroughly investigated.

2.2.1.2. Influence of various plasticizers

The impact of a significant amount (wt.% PLA/plasticizer 100:60) of several plasticizers (**Table 2.3**) such as propylene carbonate (PC), acetyl tributyl citrate (ATBC), poly(ethylene glycol) dimethyl ether average Mn ~ 2000 (PEGDME2000) and poly(ethylene glycol) dimethyl ether average Mn ~ 500 (PEGDME500) was studied to underline their influence on the thermal behavior (**Figure 2.3**) and compatibility with the aforementioned composite film (wt.% PLA/graphite 30:70). Slurry formulation and DSC thermal characterization was thus achieved by following the experimental protocols described previously (cf. **2.1.1. Elaboration process** and cf. **2.2.1.1. Preliminary tests**).

Table 2.3. Comparison of plasticizers used during formulation.

Group	Plasticizer	Formula	Melting point (°C)	Boiling point (°C)	Density @25°C (g cm ⁻³)
Carbonate ester	Propylene carbonate (PC)		-48.8	242	1.205
Ether	PEGDME2000 Mn ~ 2000		53	>250	1.08
Ether	PEGDME500 Mn ~ 500		13	>250	1.05
Ester	Acetyl tributyl citrate (ATBC)		-80	331	1.046

In comparison with the sample (wt.% PLA/graphite 30:70) without any plasticizer (cf. **2.2.1.1. Preliminary tests**) which only depicts a sharp T_m peak, the addition of a plasticizer occasions an exothermal crystallization peak (T_c) (except for PC) around 70 °C. This phenomenon is characteristic of plasticized thermoplastics, where plasticizer's introduction may affect crystallinity due to enhanced chain mobility.¹⁰ Plasticized PLA/graphite films exhibit T_m lower than 0%plasticizer sample, decreasing from 146 °C to 130 °C.

Regarding the 60%PC film sample, a wide endothermal peak from 120 to 250 °C corresponding to the evaporation of PC was observed. Because of this feature, sample turns very brittle after being stored for few days under atmospheric conditions. Consequently, PC was ruled out of the available plasticizer possibilities, as the resulting filament is expected to exhibit very poor mechanical properties (not suitable for further FDM 3D-printing). Considered as other alternatives, 60%PEGDME2000 and 60%PEGDME500 film samples, both depicted a very similar thermal behavior. This can easily be explained by their lone difference of molecular chain length. Resulting film samples exhibit an analogous melting peak around 130 °C. Main distinction between these two samples remains on the first endothermal peak attributed to the plasticizer fusion at 45 and 4 °C for the PEGDME2000 and PEGDME500, respectively. Minor shift of about 10 °C between both crystallization peaks was observed. Films containing PEGDME2000 and ATBC, stored under atmospheric conditions and room temperature (20–25 °C), were found to exude the plasticizer and become fragile after few days. This phenomenon may be explained by an impossibility of these latter to fit into the PLA matrix. Consequently, samples containing PEGDME2000 and ATBC were excluded as well.

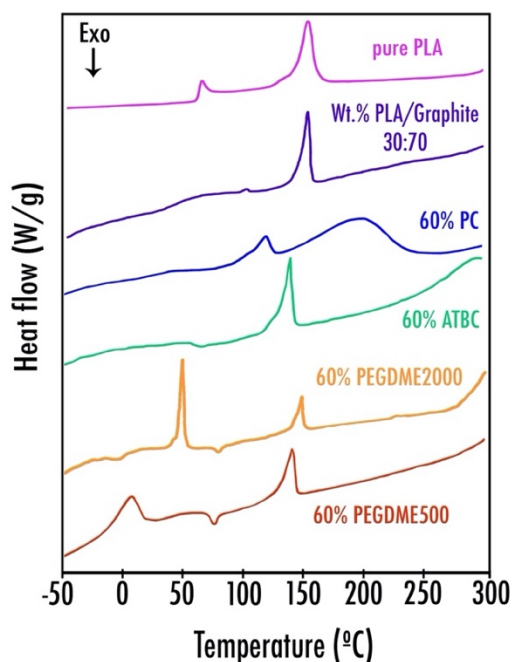


Figure 2.3. DSC curves (first heating process) exhibiting the impact of different plasticizers such as PC, ATBC, PEGDME2000 and PEGDME500. Pure PLA and 0%plasticizer sample (PLA/graphite wt % 30/70) are displayed for reference purposes — cf. **Preface – I**.

Hence, among the different plasticizers studied, PEGDME500 was chosen as it appears to be the only one that can be regarded as appropriate plasticizer for PLA. Nonetheless, the produced filament corresponding to the 60%PEGDME500 sample was too flexible and soft, thus resulting in a deformation of the filament due to the forces applied by the extruder gears during printing. Therefore, filament was then not able to enter properly the 1.75 mm diameter inlet nozzle. To overcome this undesired phenomenon, optimization of the plasticizer content within the composite to obtain a 3D-printable filament with adequate mechanical properties was required. It is worth mentioning that no phase separation of the PLA:PEGDME500 mix was highlighted visually. This should be confirmed in the future by performing in-depth by Infrared/Raman characterization experiments.

2.2.1.3. Optimization of plasticizer content

Slurry formulation at increasing plasticizer concentration was achieved by following the experimental protocol described previously (cf. 2.1.1. Elaboration process). Film samples containing $x\%$ of PEGDME500 (with x ranging from 10 to 60 wt.% plasticizer/PLA) were prepared (Table 2.4).

Table 2.4. Summary of the film compositions produced at increasing plasticizer content (PC, ATBC, PEGDME200, and PEGDME500) — cf. Preface – I.

Sample name	Weight ratio PLA:graphite	Weight ratio PLA:plasticizer	Wt.% total composite PLA/graphite/plasticizer
<i>0%plasticizer</i>	30:70	100:0	30/70/0
<i>10%plasticizer</i>	30:70	100:10	29/68/3
<i>20%plasticizer</i>	30:70	100:20	28/66/6
<i>30%plasticizer</i>	30:70	100:30	27/64/9
<i>40%plasticizer</i>	30:70	100:40	26/63/11
<i>50%plasticizer</i>	30:70	100:50	26/61/13
<i>60%plasticizer</i>	30:70	100:60	25/60/15

2.2.1.3.1. Mechanical characterization and printability

Regarding the handling and printing capabilities, samples with less than 20% of plasticizer (wt % PEGDME500/PLA) appeared to be too brittle to be tested. In the opposite, as depicted previously (cf. **2.2.1.2. Influence of various plasticizers**), sample containing a significant amount of plasticizer (60%PEGDME500) was too soft to be used as filament in an FDM printer. Hence, samples with only three weight ratios of plasticizer ($x = 30, 40,$ and 50) were mechanically tested to estimate the plasticizer effect on a highly loaded composite film. After tape casting, films were compression molded into 2 mm-thick plates using a Doloutes hydraulic press at 160 °C during 2 min before cooling to room temperature. Samples were subsequently cut into ISO 527 specimens with a punch to perform further mechanical characterization. Tensile mechanical experiments were achieved on a Llyod LR 50 K tensile machine set with a 1 KN load unit. Experiments were controlled by displacement with a speed of 10 mm min⁻¹. For each composition (dumbbell shaped), five samples were tested, and the average values of mechanical properties such as the Young's modulus, tensile strength, and elongation at break (**Table 2.5**) were finally determined from the stress–strain curves (**Figure 2.4.a**).

Table 2.5. Summary of the film compositions produced at increasing plasticizer content (PC, ATBC, PEGDME200, and PEGDME500) — cf. **Preface – I**.

Sample name	Young's modulus (MPa)	Tensile strength (MPa)	Elongation at break (%)
30%PEGDME500	844 ± 7	8.80 ± 0.50	4.33 ± 0.25
40%PEGDME500	780 ± 45	6.25 ± 0.43	3.70 ± 0.15
50%PEGDME500	655 ± 14	5.40 ± 0.40	3.00 ± 0.15

Unlike pure PLA mechanical properties (Young's modulus: 3.5 GPa, tensile strength: 59 MPa, elongation at break: 7%),¹¹ the obtained properties are very low due to the high loading of charges (up to 62.5 wt % of graphite), leading to a brittle behavior. Young's modulus was seen to decrease with higher content, thus meaning the material loses its stiffness and becomes more flexible with the addition of the plasticizer. Besides, the tensile strength decreases with the plasticizer content. Both behaviors are consistent with the general expectation for a plasticized

polymer depicted in literature.¹⁰ Nonetheless, a decrease of the elongation at break was witnessed, while the elongation is rather expected to be higher with the addition of plasticizer. Here, due to the significant graphite loading, the elongation property of the matrix (here PLA and plasticizer) has a small influence on the macroscopic behavior, the latter being driven by the properties of the interface between the charges and the matrix. By means of a FEI Quanta200F (Thermo Fisher Scientific, USA) operating at 2kV under high vacuum, the 40%PEGDME500 filament SEM image (**Figure 2.4.b**) showed that graphite grains are easily detached from the polymer matrix, demonstrating a very weak interaction between these materials that leads to low elongation property. As the idealized material for a filament is to be soft enough to follow the pipe linked with the printer-extruder and resistant enough to support the stress due to the mechanical components, overall tensile results suggest an optimum PEGDME500 plasticizer content of 40% (weight ratio PLA:PEGDME500 100:40). From these results, further experiments and characterization were thus concentrated exclusively on this particular composition.

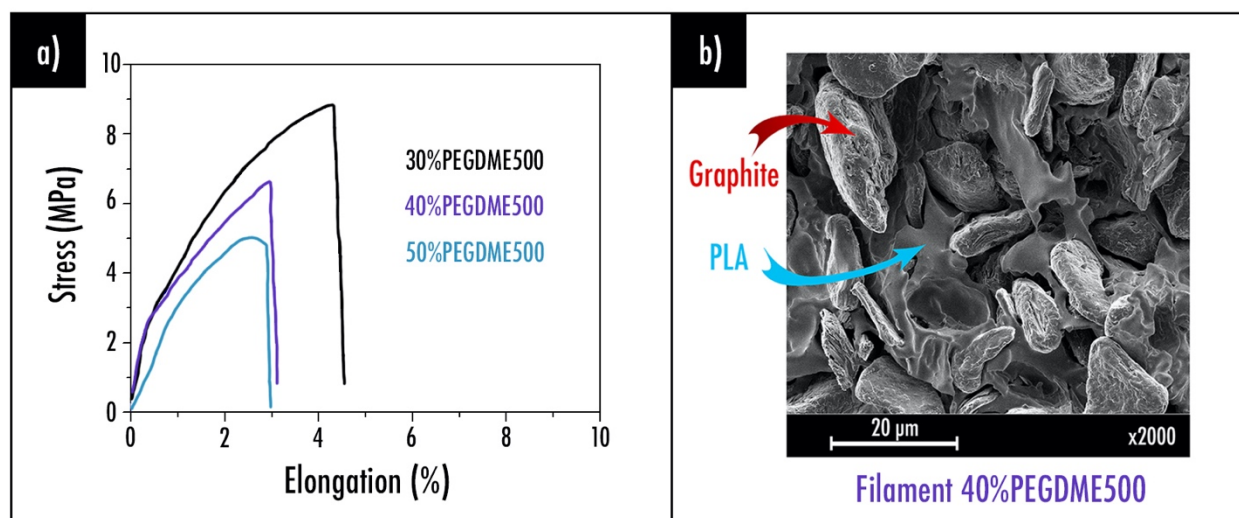


Figure 2.4. (a) Stress-strain curves of samples containing $x\%$ of PEGDME500 ($x = 30, 40, 50$); (b) SEM image of the 40%PEGDME500 homogeneous filament sample inner part — cf. **Preface – I**.

2.2.1.3.2. Optimized filament homogeneity

After extrusion, the proper homogeneity of the most printable filament *40%PEGDME500* was corroborated by performing Raman microscopy analysis (Raman DXR Microscope, with excitation LASER beam wavelength of 532 nm at 5 mW, fluorescence correction was applied, data processing using Omnic software, ThermoFisher Scientific) of the cross section, after impregnation in an epoxy resin. It is worth noting that a nonhomogeneous filament with pure cleaning PLA confined in its center can be obtained (**Figure 2.5.a**), indicating the PLA residual material used to purge the extruder is not completely removed. A significant quantity of ~100 g of material must be introduced within the extruder to further get a non-contaminated filament (**Figure 2.5.b**). Through purely qualitative Raman spectroscopy experiments, the good homogeneity of the composite filament was confirmed. Both characteristic peaks corresponding to graphite and PLA were obtained (**Figure 2.5.c**). Important features of the composite filament appear at 1582, 1350, 1620, and at about 2700 cm^{-1} and correspond respectively to the G, D, D', and G'-bands perceived conventionally for graphite in good agreement with the literature.^{12,13} Moreover, very intense peaks related to the PLA at 2949 and 875 cm^{-1} , corresponding respectively to the CH₃ symmetric stretching and the C-COO stretching, were witnessed.^{14, 15} From this optimized plasticizer composition (*40%PEGDME500*), printability behavior of the extruded composite filament was tested using a commercially available 3D printer. Planar electrode discs and high resolution complex three-dimensional structures such as a semi-cube lattice and a “3Dbenchy” boat were successfully 3D printed at a temperature of 150 °C (**Figure 2.5.d**).

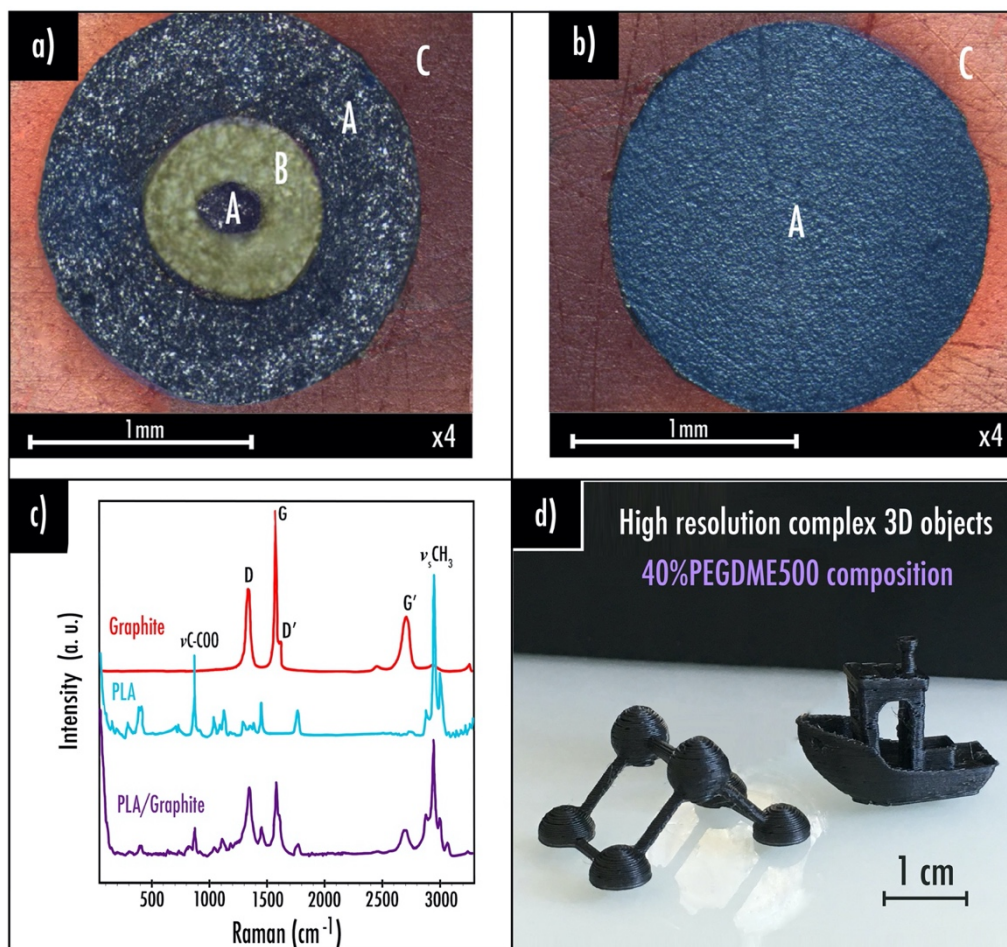


Figure 2.5. (a) Nonhomogeneous filament image obtained by optical microscopy (A: graphite, B: PLA, C: epoxy resin); (b) 40%PEGDME500 homogeneous filament image obtained by optical microscopy; (c) Raman curves obtained for pure graphite, pure PLA, and 40%PEGDME500; (d) High resolution 3D objects printed by using the 40% PEGDME500 filament as material source for the 3D printer — cf. **Preface – I**.

2.2.1.3.3. Thermal characterization

As expected for a plasticized polymer,¹⁰ by increasing the plasticizer content (**Figure 2.6**), melting temperature values slightly decreased, and crystallization temperature T_c was seen to decrease from 84 to 70 °C (DSC thermal characterization was here achieved by following the experimental protocol described previously — cf. **2.2.1.1. Preliminary tests**). Based on the work reported by Ragonés et al.¹⁶, the percentage of crystallinity of the polymer matrix was calculated using the **Equation 2.1**:

$$X_c = \frac{\Delta H_m - \Delta H_c}{w \cdot \Delta H_{100}} \cdot 100 \quad (\text{Equation 2.1})$$

where ΔH_m is the value of melting enthalpy, ΔH_c is the crystallization enthalpy, ΔH_{100} is the enthalpy of the completely crystalline PLA serving here as reference (93.6 J/g for PLA^{16, 17}), and w is the weight fraction of polymer in the sample. While from the DSC experiments, it was demonstrated that neat PLA pellet depicts a crystallinity of 42.0%, it seems that this latter is considerably decreased through the introduction of a significant amount of active material (X_c only equals to 32.1% for sample *0%PEGDME500*). As depicted in **Table 2.6**, at increasing PEGDME500 concentration within the composite film, it appears that X_c is increased (41.3% for the *60%PEGDME500* sample taking into account the plasticizer), in good agreement with literature.¹⁸ It is important to note that, as the weight fraction of PLA, w , is directly linked to the plasticizer evaporation (complicated to evaluate precisely), an estimation range of X_c was calculated rather than precise values.

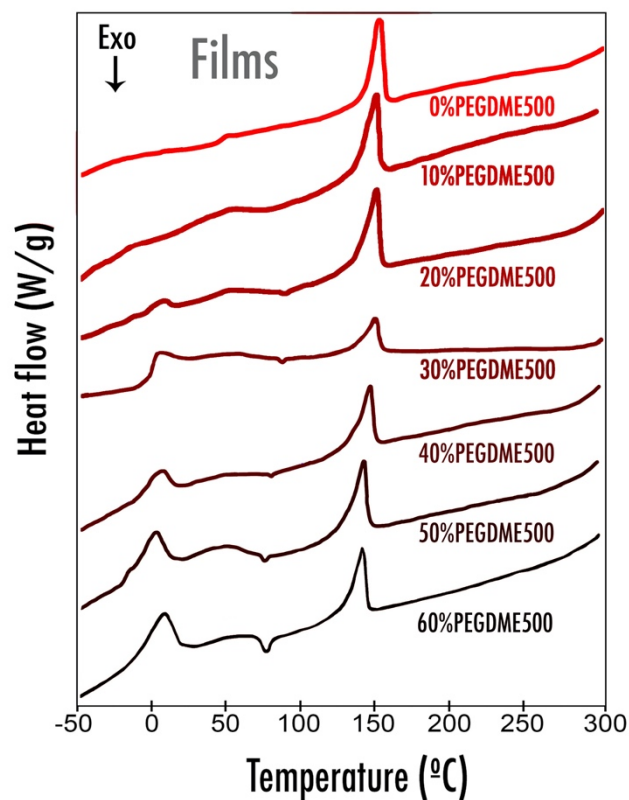


Figure 2.6. DSC curves of composites films at increasing PEGDME500 content (PEGDME500:PLA ratio from 0 to 60 wt%) — cf. **Preface – I**.

Table 2.6. Crystallinity percentage for composite films at increasing PEGDME500 plasticizer content. Pure PLA pellet was tested for reference.

Sample	Xc (considering complete plasticizer evaporation)	Xc (considering null plasticizer evaporation)
Pure PLA pellet	42.0% (no plasticizer in the composition)	
0%PEGDME500	32.1% (no plasticizer in the composition)	
10%PEGDME500	29.9%	34.6%
20%PEGDME500	35.3%	37.5%
30%PEGDME500	29.7%	33.5%
40%PEGDME500	36.1%	41.7%
50%PEGDME500	37.7%	43.3%
60%PEGDME500	35.1%	41.3%

Finally, the DSC curves obtained for the corresponding *40%PEGDME500* film, filament, and 3D printed disc (**Figure 2.7**) exhibit the same melting temperature value equals to 135 °C. However, endothermal broad peak corresponding to the fusion of the plasticizer around 6 °C tends to decrease after extrusion and 3D printing at 150 °C, meaning partial evaporation of the plasticizer takes place during both steps. Fortunately, the lower plasticizer content still provides enough flexibility to the filament to feed the 3D printer. On the other hand, after both extrusion and 3D printing, the exothermal peak of crystallization appearing at 80 °C becomes more intense. This behavior may be explained by a thermally induced rearrangement (chains elongation) of the polymer chains during both steps. X_c values for film, filament and 3D-printed disc (*40%PEGDME500* composition) are reported in **Table 2.7**. From the DSC experiments, it was shown that *40%PEGDME500* film depicts a crystallinity percentage between 36.1% and 41.7%. Surprisingly, after extrusion, lower crystallinity value of 21.8% was determined (considering complete plasticizer evaporation). In good agreement with literature,¹⁶ 3D-printing was shown to even more lower the composite crystallinity (down to 14.7% considering the complete plasticizer evaporation). According to Ragonés et al.¹⁶, such behavior may be explained by the formation, at high temperature under constraint, of a PLA mesophase, between amorphous and crystalline, that is prone to melt quickly upon printing, thus resulting in chain randomization and release of the constraints on the thermodynamic relaxation of the oriented amorphous chains.

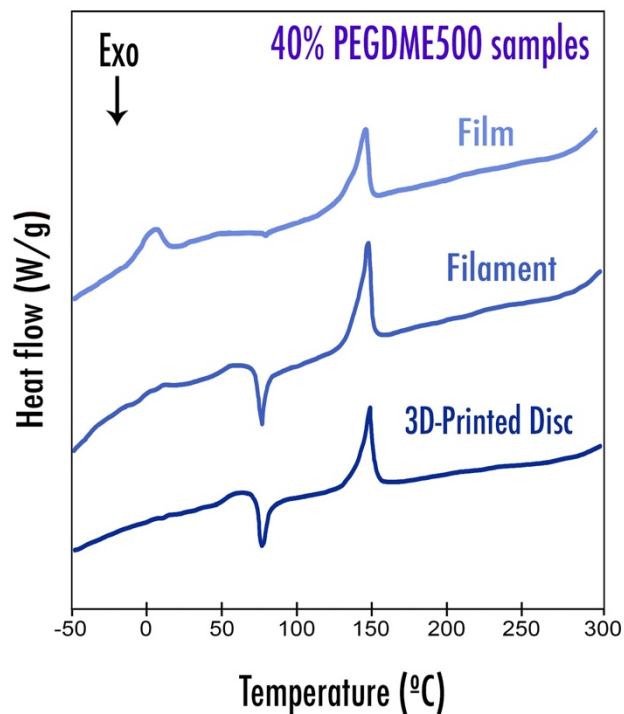


Figure 2.7. DSC curves comparison between film, filament, and 3D-printed disc for a same content of plasticizer 40%PEGDME500 — cf. **Preface – I.**

Table 2.7. Crystallinity percentage for 40%PEGDME500 film, filament and 3D-printed disc.

Sample	Xc (considering complete plasticizer evaporation)	Xc (considering null plasticizer evaporation)
Film	36.1%	41.7%
Filament	21.8%	25.1%
3D-printed disc	14.7%	17.0%

2.2.1.4. Optimization of conductive additives content

The influence of commonly used conductive additives, such as carbon black Super P (CSP) and carbon nanofibers (CNF), on the most relevant film sample *40%PEGDME500* was investigated. Slurry formulation (**Table 2.8**) was achieved by following the experimental protocol described previously (cf. **2.1.1. Elaboration process**). Here, carbon additives were premixed with graphite active material in a mortar prior to introduction into the slurry to ensure thorough mixing.

Table 2.8. Summary of the film compositions produced at increasing conductive additives content (CSP and/or CNF) while maintaining constant PLA/PEGDME500 (wt.% 100/40) — cf. **Preface – I**.

Sample name	Weight ratio PLA:Graphite	Weight ratio Graphite/ Conductive additive	Wt.% total composite PLA/ Graphite /Plasticizer/ Conductive additive
40%PEGDME500	30:70	100:0	26.8/ 62.5 /10.7/ 0
1%CSP	30:70	100:1	26.6/ 62.1 /10.7/ 0.6
2%CSP	30:70	100:2	26.5/ 61.7 /10.6/ 1.2
1%CNF	30:70	100:1	26.6/ 62.1 /10.7/ 0.6
2%CNF	30:70	100:2	26.5/ 61.7 /10.6/ 1.2
1%CSP+1%CNF	30:70	100:1 + 100:1	26.5/ 61.7 /10.6/ 1.2
10%CSP	40:60	100:10	32.8/ 49.2 /13.1/ 4.9

2.2.1.4.1. Electrical conductivity

For film samples described in **Table 2.8** obtained after slurry casting, with 1, 2, and 10% of conductive additives, characteristic complex impedance spectra were recorded at various temperatures from 20 to 50 °C (upon heating in steps of 10 °C). It is important to note that due to the high volume of charges (graphite and black carbon), it was necessary to slightly adjust the PLA/graphite ratio (wt % 40/60) for sample 10%CSP (weight ratio graphite/conductive additive 100:10). A MTZ-35 frequency response analyzer and an intermediate temperature system (ITS) developed by BioLogic, France, were used to perform the analysis. Inductive phenomenon from the cables were prevented by performing preliminarily the device calibration of the empty ITS with

cables. Hence, only sample signal was considered thereafter. Composite 200 μm -thick films were cut into 5.50 mm diameter discs by means of a punch. They were introduced into a controlled environment sample holder (CESH) to perform AC impedance measurements under air. A frequency range of 0.2 MHz to 1 Hz (20 points per decade and 10 measures per points) and an excitation voltage of 0.01 V were applied during the measurements. From the Nyquist and Phase-Bode plots of the complex impedance, the film electronic conductivities were obtained as well as the activation energy.

For each sample, the obtained Nyquist and Bode plots are consistent with an electronic conductor typical behavior as reported for the *40%PEGDME500* sample in **Figure 2.8.a,b**. Indeed, Nyquist plot depicts only Z' real part, while $|Z|$ magnitude is constant for all frequencies. For each sample, the electrical conductivity is increasing with temperature as shown in **Figure 2.8.c**, and homogeneous activation energy values ranging between 0.046 and 0.106 eV are calculated. Panabiere et al.¹⁹ showed that electrons transport mechanism in carbon/polymer mixtures used in battery field was tunneling with no temperature dependence (metal-like behavior). Nonetheless, such temperature dependence would be perceived when strong dipoles are adsorbed at the carbon particles surface. In this respect, it is not surprising to observe activation energy values increasing with higher conductive additives content. This behavior can be perceived through the Z' real part resistance drop (thickness and area remaining constants) in the Nyquist plot. Indeed, conductivities were calculated from **Equation 2.2**:

$$\sigma = \frac{1}{R} \times \frac{d}{A} \quad \text{(Equation 2.2)}$$

where d is the pellet thickness, A is the pellet surface area, and R is the respective resistance deduced from the Nyquist and Bode plots. From the results obtained, it is certain that conductive additives such as CNF and CSP contribute to higher conductive values compared to the *40%PEGDME500* without additives. Among them, film sample *10%CSP* depicts the highest values of electrical conductivities. The small conductivity value gap observed between both *2%CSP* and *10%CSP* samples is justified by the aforementioned higher polymer amount contained in this latter.

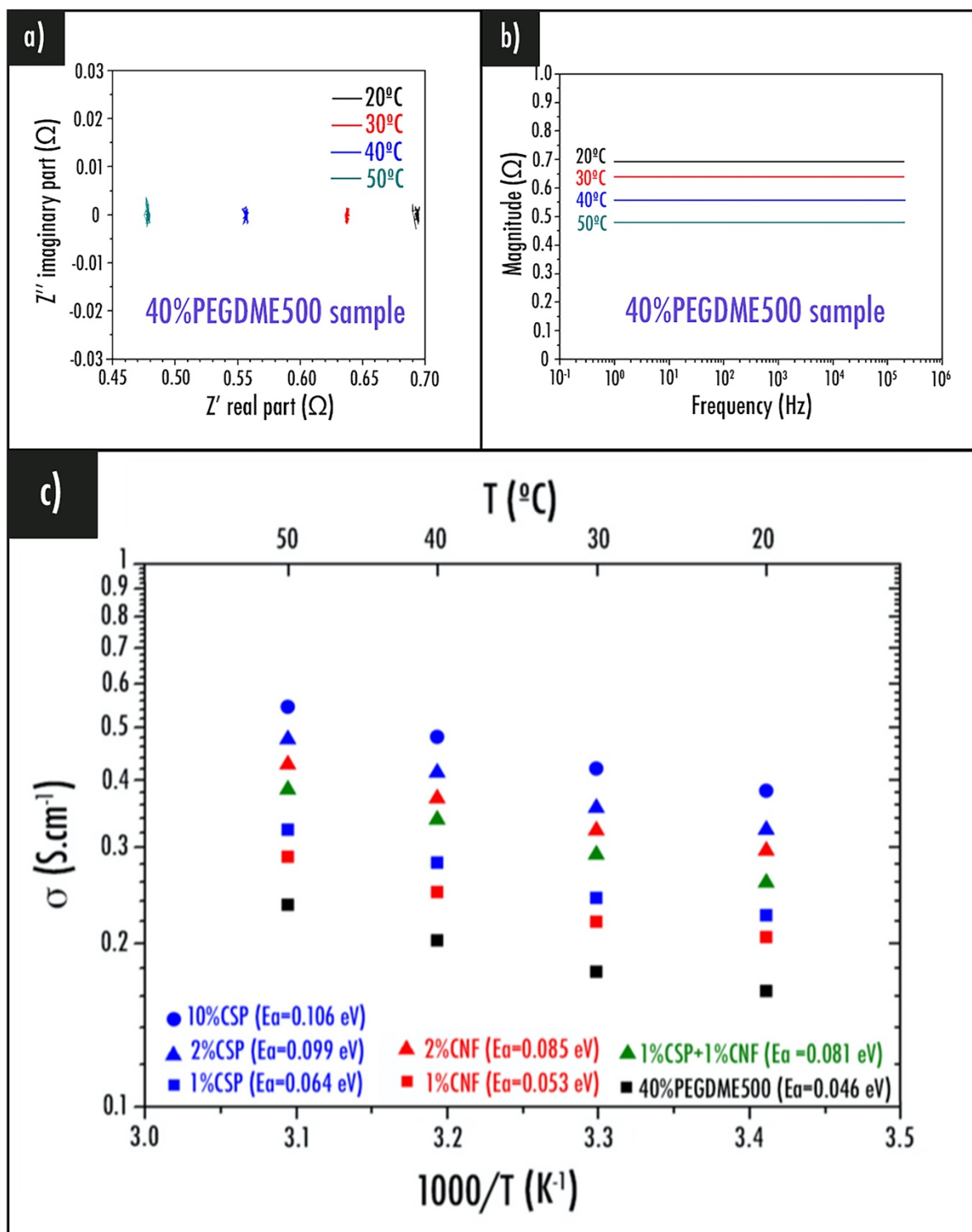


Figure 2.8. (a) Nyquist and (b) bode plot for the 40%PEGDME500 film sample; (c) Arrhenius plots of the electrical conductivity for samples containing CNF and/or CSP as conductive additives. Sample 10% CSP contains slightly higher amount of polymer to ensure the mechanical strength — cf. **Preface – I**.

2.2.1.4.2. Electrochemical characterization

For each film sample described in **Table 2.8** of the same dimension (60 μm -thick and 11 mm diameter, surface equal to 0.950 cm^2) obtained after slurry casting, Swagelok-type cells (**Figure 2.9**) were assembled in an argon filled glovebox ($\text{H}_2\text{O} < 0.1 \text{ ppm}$, $\text{O}_2 < 0.1 \text{ ppm}$). Samples were used as working electrode and metallic lithium as counter/reference electrode. Glass fiber separator was supplied by Whatman, GE Healthcare, United States. Used as liquid electrolyte (LP40, Merck KGaA, Germany), 150 μL of 1 M LiPF_6 in ethylene carbonate and diethyl carbonate (EC:DEC 1:1 weight ratio) was here introduced in excess. This particular electrolyte was chosen instead of the more conventional EC:DMC 1:1 weight ratio (LP30, Merck KGaA, Germany) as it was demonstrated experimentally that PLA tends to dissolve within DMC solvent. Nonetheless, an in-depth and extensive study must be accomplished in the future to identify the best liquid electrolyte mixture for PLA-based LIB components. In this regard, recently, Reyes et al.²⁰ precisely initiated such an optimization. According to the authors,²⁰ a 1:1 (volume ratio) solution of propylene carbonate (PC) and ethyl methyl carbonate (EMC) with 1 M LiClO_4 must be used in future research as PLA film infused within the mixture depicted an ionic conductivity of $8.5 \times 10^{-5} \text{ S cm}^{-1}$ (20 $^\circ\text{C}$) and retained its mechanical integrity.

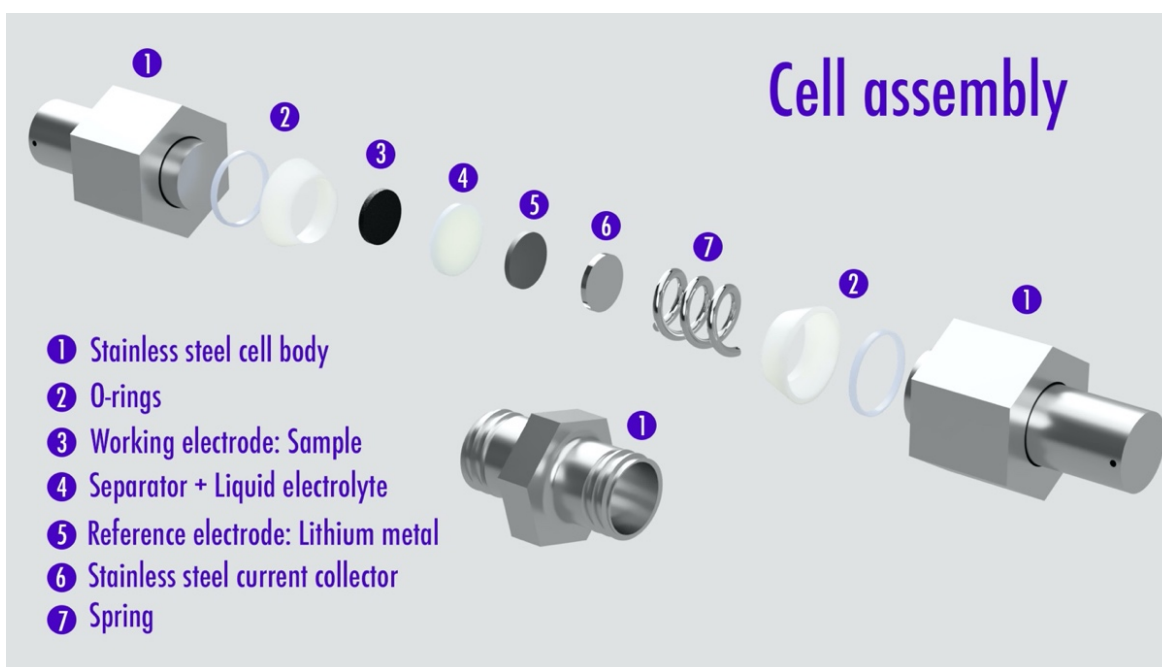


Figure 2.9. Swagelok-type cell assembly.

Cells were galvanostatically discharged (graphite lithiation) and charged (graphite delithiation) at different current densities calculated per gram of active material between 1.5 and 0.005 V (vs Li/Li⁺) using a BCS-805 (BioLogic, France). For each sample, the potential profiles versus specific capacity based on the active material, specific capacity versus cycle number, and differential capacity during the first lithiation were studied in detail at different current densities (18.6, 37.3, 74.5, and 186 mA g⁻¹ of active material corresponding to C/20, C/10, C/5, and C/2), as depicted in **Figure 2.10**.

Film samples *40%PEGDME500*, *2%CSP*, *2%CNF*, and *1%CNF+1%CSP* respectively display an irreversible capacity during the first cycle of 21, 23, 26, and 20 mAh g⁻¹ of active material, thus corresponding to quite similar percentage loss of 10, 11, 12, and 9% at a current density of 18.6 mA g⁻¹. While $\leq 2\%$ conductive additives incorporation improves the films' electronic conductivity, it does not seem to have a deleterious impact on the reversible capacity loss percentages despite the overall higher carbon surface area (+83% for the *2%CSP* sample and +32% for the *2%CNF*) theoretically available for the electrochemically induced passivation layer formation (also called solid electrolyte interphase, SEI).²¹ This phenomenon may be explained by the carbon additives partial isolation within the polymer matrix.

The differential capacity plots (**Figures 2.10.e,f**) feature a reduction peak around 0.8 V, assuming that the main component reduced to form the SEI during the first lithiation is the ethylene carbonate electrolyte solvent.²² Depending on the plasticizer nature, reduction may also occur. Indeed, according to the electrochemical stability sequence, carbonate, ester, and ether families are prone to reduce successively toward lower potential vs Li/Li⁺ and even co-intercalate into graphite as reported, especially for PC and ethers.²³ Concerning the PEGDME500, which is an ether used as plasticizer in this study, neither reduction nor co-intercalation are observed. It is also assumed that its low volume fraction (2% of the electrolyte) does not affect all electrolyte properties (solvation, conductivity).

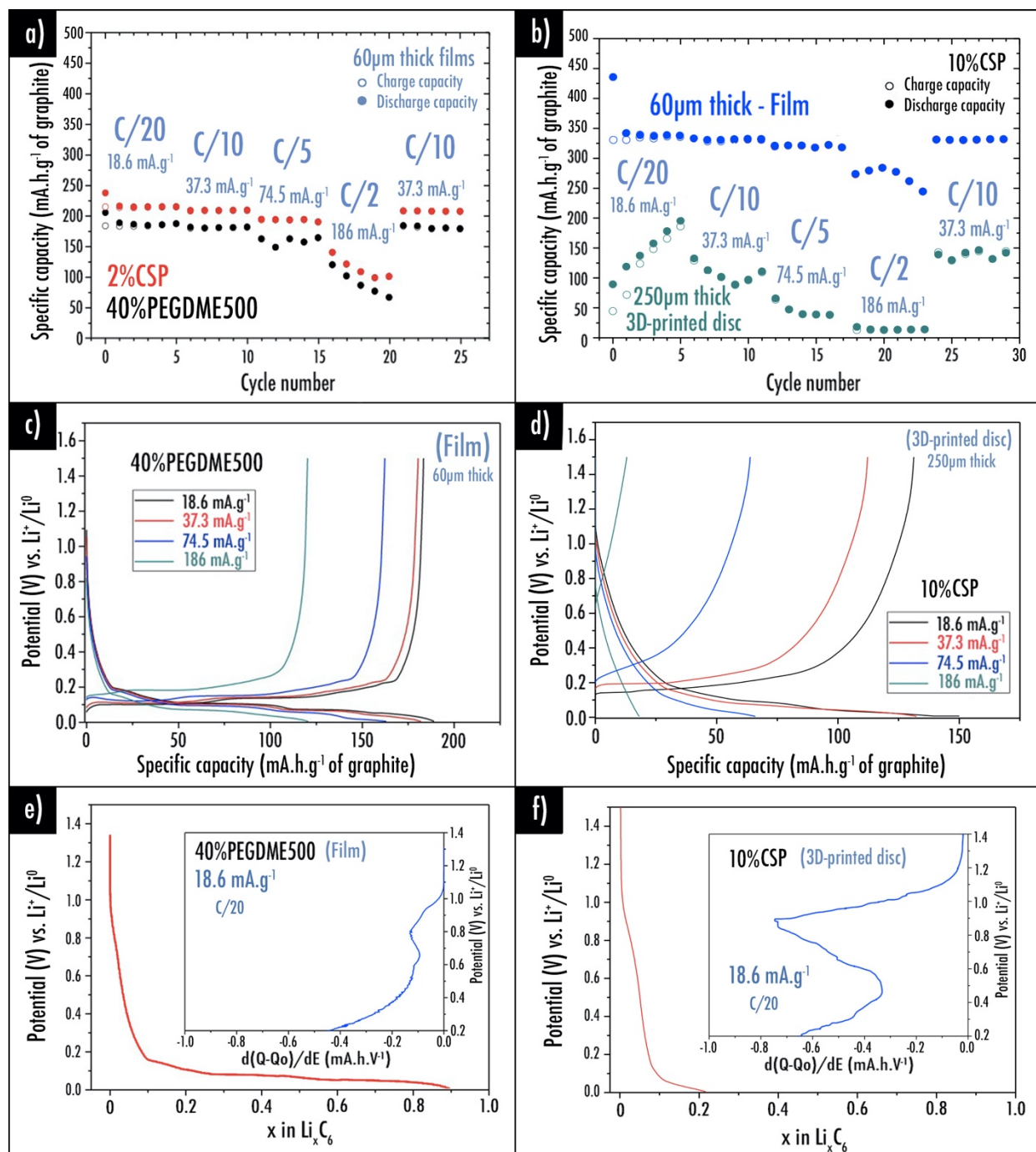


Figure 2.10. Capacity retention plots at different C-rate for (a) 40%PEGDME500 and 2%CSP films (60 μm thick) and (b) 10%CSP film (60 μm thick) and 10%CSP 3D printed disc (250 μm thick). Charge/discharge capacity profiles for (c) 40%PEGDME500 film and (d) 10%CSP 3D printed disc. First lithiation and differential capacity plots for (e) 40%PEGDME500 film and (f) 10%CSP 3D printed disc — cf. **Preface – I**.

It is worth mentioning that reversible capacity loss percentage values are slightly higher compared to those of commercial graphite electrodes (<10%) due to the absence of SEI reinforcing additives such as vinylene carbonate (VC) and binder (carboxymethyl cellulose, CMC) known to act as a relatively efficient passive layer in commercial cells.²⁴

Among the tested samples with $\leq 2\%$ conductive additive incorporated, 2%CSP depicted the highest value of specific capacity retention, while the film without any conductive additive displayed, as expected, the lowest (**Figure 2.10.a**). Intermediate values between those samples were observed for 2%CNF and 1%CNF+1%CSP. Indeed, at a current density of 18.6 mA g⁻¹, reversible capacity values of 184, 215, 214, and 209 mAh g⁻¹ were respectively obtained for 40%PEGDME500, 2%CSP, 2%CNF, and 1%CNF + 1%CSP samples during 5 cycles. The capacity values obtained at higher current densities of 37.3 and 74.5 mA g⁻¹ are slightly decreasing but are steadily maintained upon their respective 5 cycles. At the highest applied current density (186 mA g⁻¹), capacity retention is not well-preserved, suggesting the electrode has poor electronic and/or ionic conductivities. It is noteworthy that good capacity retention is still observed during 5 cycles while coming back at a lower current density of 37.3 mA g⁻¹. Therefore, by adding $\leq 2\%$ conductive additives, it was demonstrated that higher specific capacity is reached, indicating their incorporation enables some isolated active material particles to be electronically connected to the percolating network. However, those values are still far from the theoretical capacity (372 mAh g⁻¹) and, thus, can still be improved. An explanation could be that a small percentage of active material is still electronically and/or ionically inaccessible because of its complete confinement into the polymer matrix of PLA. The addition of a small amount of conductive additive (1 or 2 wt %) is still not enough to approach the theoretical value.

To address this issue, by adjusting the PLA/graphite ratio (wt.% 40/60), the film sample containing a higher amount of conductive additive, 10%CSP (weight ratio graphite:conductive additive 100:10), was investigated (**Figure 2.10.b**). It displays an irreversible capacity during the first cycle of 93 mAh g⁻¹ of active material, thus corresponding to a percentage loss of 27% at a current density of 18.6 mA g⁻¹ (C/ 20). The reversible capacity loss percentage is caused by the overall higher carbon surface area (+513% for the 10%CSP sample) theoretically available for the electrochemically induced passivation layer formation. At a current density of 18.6 mA g⁻¹ (C/20),

reversible capacity value of 342 mAh g⁻¹ of active material was obtained for 10%*CSP* during 5 cycles (**Figure 2.10.b**), thus almost reaching the theoretical capacity of the active material. The capacity values obtained at higher current densities of 37.3 and 74.5 mA g⁻¹ (C/10 and C/5) are slightly decreasing (respectively 333 and 322 mAh g⁻¹ of active material) but are steadily maintained upon their respective 5 cycles. Here again, at the highest applied current density 186 mA g⁻¹ (C/2), capacity retention is not well-preserved but still maintained to reversible capacity values up to 285 mAh g⁻¹ of active material. Good capacity retention is still observed during 5 cycles while coming back at a lower current density of 37.3 mA g⁻¹ (C/10). While there is only a small electrical conductivity gain observed between both 2%*CSP* and 10%*CSP* samples as mentioned previously, a significant specific capacity rise is observed. This behavior reflects a good electronic and ionic percolation within the matrix. An explanation could be that *CSP*, due to its high surface area, promotes the electrolyte impregnation, thus improving the ionic percolation, and allows the expanded percolating electronic network to reach the whole active material particles.

Finally, as theoretical capacity was approached with the 10%*CSP* (773 mg of active material per cm³ of composite) film sample (20% porosity), the corresponding optimized filament was prepared and a 250 μm-thick 3D printed negative electrode disc was obtained and subsequently characterized electrochemically (**Figure 2.10.b,d,f**).

The general homogeneity and the *CSP* dispersion within the PLA matrix of the produced 10%*CSP* filament was examined via transmission electron microscopy (TEM) by means of a FEI Tecnai F20 ST electron microscope operating at 200 kV. Beforehand, filament was cut and inserted in a capsule in which a LR white resin (Sigma-Aldrich) was added drop by drop. The resulting capsules were then placed in an oven at 70°C during 24h. A microtome (RMC Products, Boeckeler) was then used to cut the capsules in thin slices (sections) of material of 100 nm at a cutting speed of 21.5 mm sec⁻¹. Slices were finally deposited onto a holey carbon copper grid. As depicted in **Figure 2.11.a**, it appeared that the *CSP* particles were homogeneously distributed within the PLA matrix thus ensuring an efficient electronic percolation between the graphite particles that corroborates the EIS results. Finally, as depicted in **Figure 2.11.b and c**, classical graphene foils and their corresponding atomic arrangement were revealed at higher magnification on graphite particles.

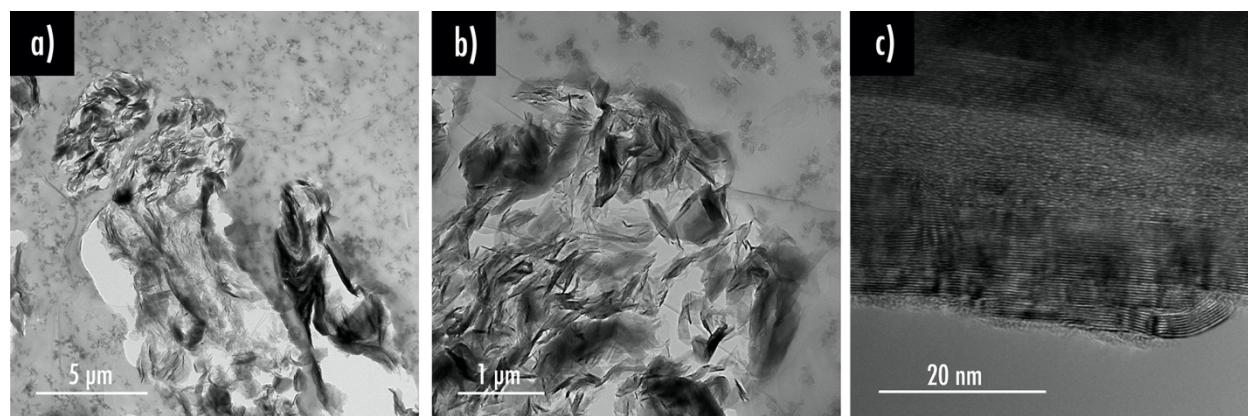


Figure 2.11. Cross-sectional TEM images of the 10%CSP negative electrode filament: (a) carbon black CSP spherical particles are well dispersed between the graphite particles; (b) At higher magnification, graphene foils are clearly visible (c) graphene foils atomic arrangement.

Finally, coming back to the electrochemical performances, the corresponding 3D-printed negative electrode disc depicted a reversible capacity of 200 mAh g^{-1} of active material ($154.6 \text{ mAh cm}^{-3}$) at current density of 18.6 mA g^{-1} ($C/20$) was achieved after 6 cycles. At higher current densities of 37.3 , 74.5 , and 186 mA g^{-1} ($C/10$, $C/5$, and $C/2$), capacity values reached respectively 140 , 49 , and 15 mAh g^{-1} of active material (108.2 , 37.9 , and 11.6 mAh cm^{-3}). Good capacity retention of about 140 mA g^{-1} ($108.2 \text{ mAh cm}^{-3}$) is still observed during 6 cycles while coming back at a lower current density of 37.3 mA g^{-1} ($C/10$). Due to the resolution of the nonmodified 3D printer, at this stage, it was not possible to obtain thinner 3D printed disc, thus explaining the gap between specific capacity values obtained for the film ($60 \text{ }\mu\text{m}$ - thick) and the 3D printed disc ($250 \text{ }\mu\text{m}$ thick), but also the increasing capacity at $C/20$ due to an impregnation issue.

To conclude, significant progress has been achieved regarding the capacity retention as compared to the pioneering study reported by Foster et al.⁹ in 2017 who used FDM technology to 3D print a 1 mm -thick negative electrode disc from a commercially available filament. They were aware that the low specific capacity values reported at that time (15.8 mAh g^{-1} of active material) at current density of 10 mA g^{-1} ($C/37$) were unfortunately caused by the use of a commercial filament containing only $8 \text{ wt } \%$ of graphene as active material and $92 \text{ wt } \%$ of PLA. In this work, the unprecedented obtained reversible capacity values (200 mAh g^{-1} after 6 cycles at current density of 18.6 mA g^{-1} , $C/20$; and 140 mAh g^{-1} of active material at current density of 37.3 mA

g^{-1} , C/10) for an FDM 3D printed disc (10% CSP) is logically due to the high graphite loading reaching 49.2 wt % and the high black carbon loading reaching 4.9 wt % of the total composite.

2.2.2. Positive electrode

2.2.2.1. Optimization of plasticizer content

Similar to what was achieved for the negative electrode (cf. **2.2.1. Negative electrode**), the elaboration of a highly loaded filament for the positive electrode was initiated to enhance the electrochemical performances while maintaining enough mechanical strength to allow printability. Nonetheless, for material saving purposes, it was here decided to start directly the elaboration from the optimized plasticizer composition wt.% PLA/PEGDME500 100:40, which was established beforehand as the most promising (cf. **2.2.1.3. Optimization of plasticizer content**). Lithium-iron phosphate (particle size: 1 μm), LiFePO_4 , (LFP) was here employed as active material for the positive electrode and introduced in large quantity within the composite sample (wt.% ratio PLA/LFP 40:60).

2.2.2.2. Optimization of conductive additives content

In order to enhance the positive electrode electrical conductivity and electrochemical performances, samples containing different amount of CSP (weight ratio LFP:CSP equals to 100: x with x from 5 to 20) were prepared from the optimized plasticizer composition. Slurry formulation for the positive electrode (**Table 2.9**) was achieved by following the experimental protocol described previously (cf. **2.1.1. Elaboration process**). Here again, carbon additives were premixed with LFP active material in a mortar prior to introduction into the slurry to guarantee meticulous mixing.

Table 2.9. Summary of the film compositions produced for the positive electrode at increasing conductive additives content (CSP). For weight-volume conversion, material densities were determined by helium pycnometer — cf. **Preface – II.**

Sample name	Weight ratio PLA:LFP	Weight ratio PLA:PEGDME500	Weight ratio LFP:Conductive additive	Wt.% total composite PLA/LFP/Plasticizer/Conductive additive	vol.% total composite PLA/LFP/Plasticizer/Conductive additive
Pure PLA	X	X	X	100/0/0/0	100/0/0/0
PLA/LFP	40:60	X	X	40/60/0/0	54/46/0/0
0% CSP	40:60	100:40	X	35/52/13/0	43/37/20/0
5% CSP	40:60	100:40	100:5	34/50/13/3	42/36/20/2
10% CSP	40:60	100:40	100:10	33/49/13/5	41/35/20/4
20% CSP	40:60	100:40	100:20	31/47/13/9	40/34/18/8

2.2.2.2.1. Electrical conductivity

The effect on electronic conductivity of carbon black, CSP, was studied. For samples obtained labeled in **Table 2.9**, specific impedance spectra were investigated at temperatures ranging between 20 °C to 50 °C. The exact same procedure than the one described in the previous section (cf. **2.2.1.4.1. Electrical conductivity**) was followed. Similarly, the achieved Nyquist and Bode curves are in accordance with an electronic conductor classical behavior as Nyquist plot portrays only Z' real part while $|Z|$ magnitude is remained steady for all frequencies. The electrical conductivity, for all samples of equal thickness and area, is rising with temperature as exhibited in **Figure 2.12** and activation energy values varying between 0.0001 eV and 0.052 eV were estimated. Conductive additive contributes to greater conductivity values compared to the *0% CSP* sample without additives, which is in good agreement with what was reported by Guy et al.²⁵ However, here, a higher loading of CSP is needed to reach similar values,²⁵ which is undoubtedly due to the high quantity (32.8 wt%) of the polymer matrix (PLA) having a detrimental effect on the

homogenization and CSP distribution which may be isolated. Amongst the various film samples tested, *20%CSP* exhibits the greatest values of electrical conductivities. Nevertheless, it is worth noticing that conductivity values are still relatively low due to the LFP insulator behavior (enhanced up to 0.16 S cm^{-1} for the *20%CSP* sample at $20 \text{ }^\circ\text{C}$) as compared to values obtained previously (cf. **2.2.1.4.1. Electrical conductivity**) for the graphite-based negative electrode (0.40 S cm^{-1} at $20 \text{ }^\circ\text{C}$). Carbon coating is therefore important when LFP is considered as active material.²⁶ Here, the incorporation of carbon additives such as CSP is essential when considering exotic composite compositions with such an important amount of PLA polymer matrix. While *20%CSP* sample appears as the most electronically conductive, printability tests (described in the next section — cf. **2.2.2.2.2. Printability and mechanical characterization**) were rather executed on the *10%CSP* as it will be demonstrated later that it is the most electrochemically-promising (cf. **2.2.2.2.4. Electrochemical characterization**).

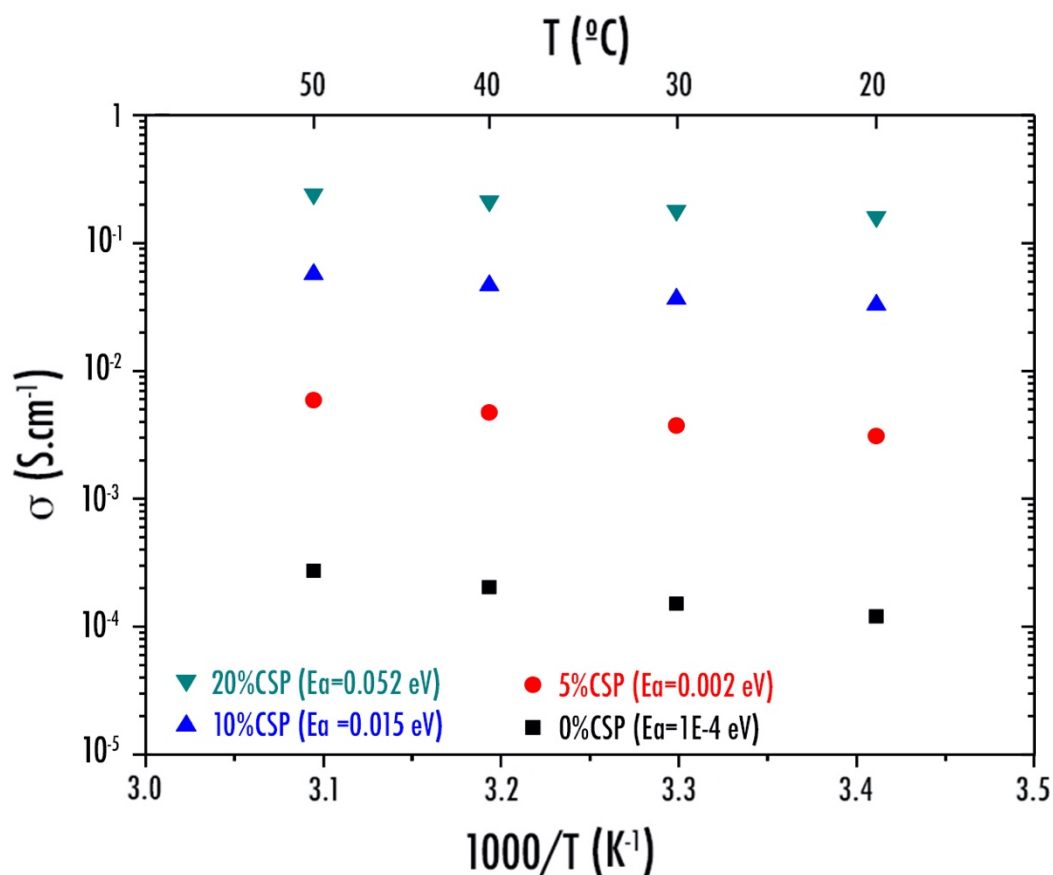


Figure 2.12. Arrhenius plots of the electrical conductivity for samples containing CSP as conductive additives — cf. Preface – II.

2.2.2.2.2. Printability and mechanical characterization

From our practical experiences, with a view to obtain enough mechanical performances to be printed, the total amount of charges (sum of active material and conductive additives) within the filament must not exceed a total of about 50 vol% when a plasticizer such as PEGDME500 is introduced. On the contrary, without the plasticizer introduction, the total amount of charges must not exceed about 30% otherwise the PLA-based filament will not be printable. As displayed in **Table 2.9**, in this study, the most electrochemically-promising *10%CSP* positive electrode filament contains 35 vol% of LFP and 4 vol% of CSP, which represents a total volume of charges equals to 39 vol% of the total composite. A compromise must nonetheless be found with a view to enhance the electrochemical performances (through a high amount of charges) while still maintaining suitable mechanical properties (thanks to polymer matrix and plasticizer). Following the same characterization procedure described previously (cf. **2.2.1.3.1. Mechanical characterization and printability**), mechanical performances for the *10%CSP* film sample such as the Young's modulus (223 ± 20 MPa), tensile strength (7.36 ± 0.45 MPa) and elongation at break ($14.04 \pm 1.35\%$), were determined from the stress-strain curves. As expected, those values are very low (except elongation at break) compared to pristine PLA (Young's modulus: 3500 MPa, tensile strength: 59 MPa, elongation at break: 7%)¹¹ due to the high loading of composite material here. Due to the lower LiFePO_4 particle size (~ 1 μm), the elongation at break for the positive electrode (*10%CSP* sample) was here multiplied by 5 in comparison with the optimized negative electrode composition containing graphite (~ 20 μm). Indeed, the LFP particles being more efficiently embedded, it results in a greater percolating polymer network than with graphite. In this case, the elongation at break is more dependent on the polymer properties than on the particles-polymer interface.

Similar to what was achieved previously for the negative electrode, the general homogeneity and the inner material (LFP and CSP) dispersion within the PLA matrix of the produced filament was examined by scanning electron microscope (5 kV) and transmission electron microscopy (200 kV). Prior TEM experiment, *10%CSP* filament sample was cut and inserted in a resin following the exact same protocol described previously (cf. **2.2.1.4.2. Electrochemical characterization**). SEM image (**Figure 2.13.a**) confirmed the homogeneous LFP particles distribution within the PLA polymer matrix. On the other hand, at higher

magnification, TEM images (**Figure 2.13.b**) revealed clearly the partially efficient percolation network generated by the CSP located in between the LFP particles.

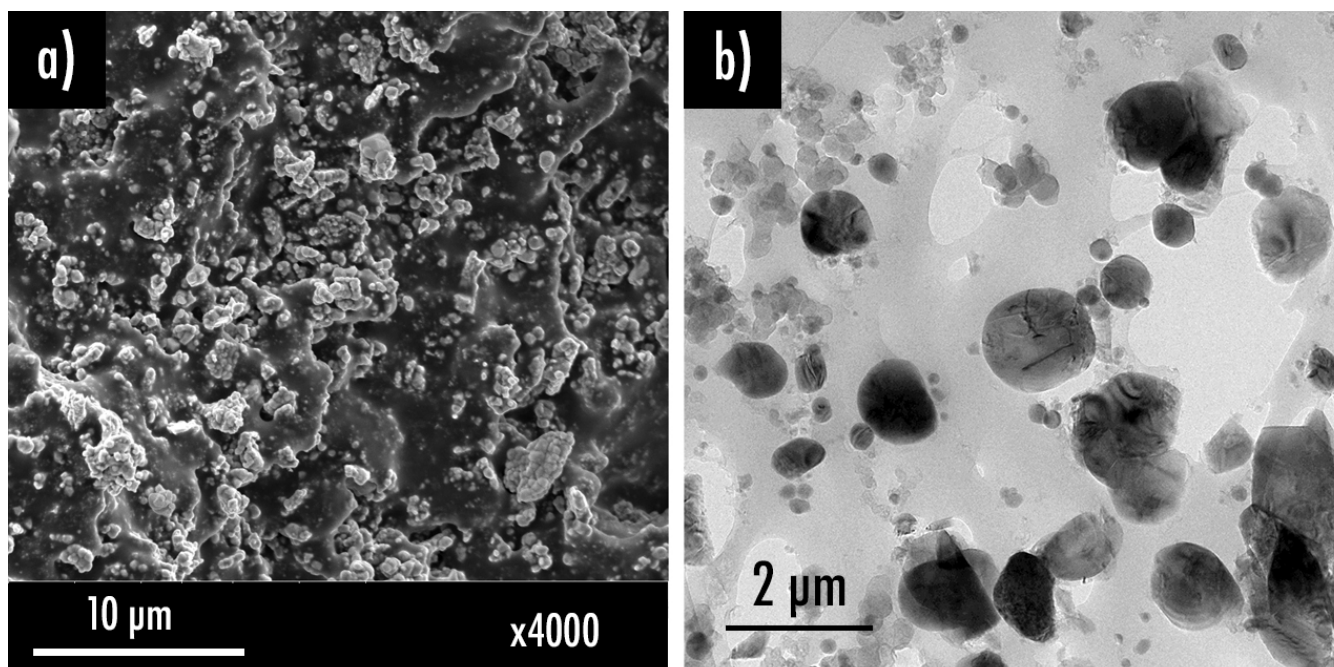


Figure 2.13. Cross-sectional (a) SEM and (b) TEM images of the 10%CSP positive electrode filament.

Finally, porosities for the *10%CSP* positive electrode after each step of the formulation (film, filament and 3D-printed disc) were calculated considering the complete plasticizer evaporation. While the film obtained after tape-casting originally depicts 17% porosity, it can be seen that after extrusion the filament displays only 14% of porosity. This may be easily explained by the extrusion process itself where charges are more efficiently embedded within the polymer matrix. Finally, the 3D-printed disc displays a porosity about 29% which is explicated by the successive pathways taken by the nozzle leading to a surface inhomogeneity creating high macro-porosity (**Figure 2.14**).

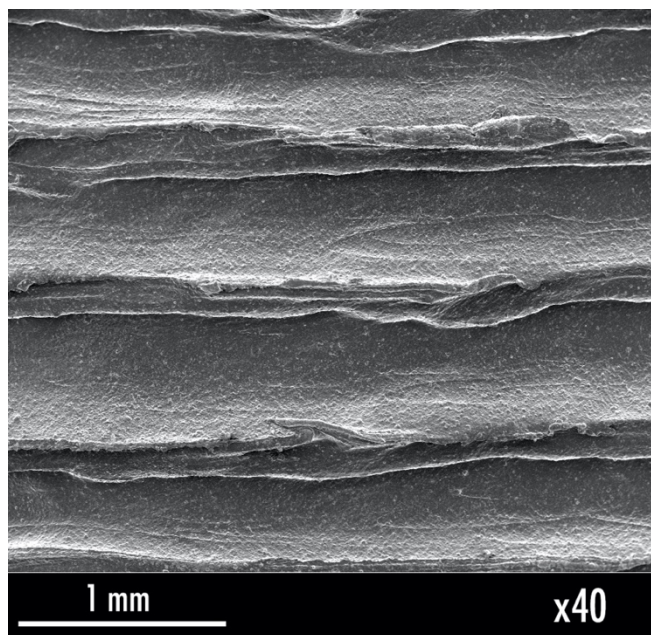


Figure 2.14. SEM image depicting the macro-porosity created by the nozzle during printing on top of the 10%CSP positive electrode 3D-printed disc.

2.2.2.2.3. Thermal characterization

DSC thermal characterization was here achieved by following the experimental protocol described previously (cf. **2.2.1.1. Preliminary tests**). **Figure 2.15.a** exhibits DSC plots of the composite films with various compositions of polymer, LFP, plasticizer and conductive additives (**Table 2.9**). Serving here as a reference, pure PLA displays an endothermic peak related to its melting (T_m) at 146 °C and a well-defined glass transition temperature (T_g) at 63 °C. By adding LFP as active material to the PLA matrix, the endothermic peak related to the melting temperature of the film called *PLA/LFP* (wt% 40:60) was a little altered to lower temperature emerging at 142 °C and the T_g is not perceptible anymore. Water desorption was detected around 100 °C by the presence of a minor endothermic peak. Compared to *PLA/LFP* sample which only shows a clear T_m peak, a little exothermic crystallization peak (T_c) around 80 °C is induced through the incorporation of a plasticizer, as observed for graphite-based matrix and in good agreement with literature.¹⁰ This is emblematic of plasticized thermoplastics, as plasticizers may facilitate

crystallization by enhancing chain mobility. As the temperatures difference T_c-T_g is reported to be constant (~ 80 °C) in the whole range of plasticizer concentration,¹⁰ the glass transition temperature (T_g) of the PLA polymer matrix should also appear in the range of the first endothermal peak at 4 °C imputed to the plasticizer PEGDME500 fusion. Plasticized PLA/LFP films display T_m inferior than without plasticizer, diminishing from 142 °C to about 132 °C. By increasing the CSP content, endothermal peaks at 4 °C and 132 °C, respectively corresponding to the PEGDME500 fusion and the composite film melting, remain unchanged. This behavior is however different for the exothermal crystallization peak (T_c) previously observed at 80 °C (0%*CSP* sample). Indeed, through the addition of CSP, crystallization peak is slightly altered to lower temperature, reaching 74 °C for the 20%*CSP* sample. This behavior may be explicated by the CSP presence within the PLA matrix impacting crystallinity behavior at the microscopic scale. In this context, the crystallinity percentage X_c (**Table 2.10**) for each film composition was calculated from the crystallization and melting enthalpies. From these results, it is clearly visible that the introduction of CSP particles impacts the crystallinity behavior. Indeed, while sample without CSP additives (0%*CSP*) depicts crystallinity percentage value of 32.5% (considering complete plasticizer evaporation), samples containing CSP within the polymer matrix, display higher X_c values of about 37.6 – 39.1%. These observations are in good agreement with what was observed by Nofar et al.¹⁸ who reported that nanosized carbon black introduction promoted PLA crystallization by inducing more crystal nucleation sites. According to literature,²⁷ crystallinity percentage X_c is expected to have an impact on the further mechanical properties. Indeed, Young's modulus tends to increase with higher X_c values. On the other hand, the crystallinity may impact the sample aging in presence of water, the liquid electrolyte impregnation as well as the viscosity behavior of the filament coming out from the nozzle during printing.

Plots achieved from DSC for the analogous 10%*CSP* film, filament and 3D-printed disc (**Figure 2.15.b**), display similar T_m value equals to 132 °C. Nevertheless, endothermal wide peak intensity related to the PEGMDE500 fusion at 4 °C tends to drop following extrusion and 3D-printing (performed respectively at 170 and 195 °C), indicating partial plasticizer evaporation occurs during both stages. Conveniently, the lower plasticizer content still confers sufficient filament flexibility in order to feed the 3D-printer as depicted hereabove (cf. **2.2.2.2.2. Printability and mechanical characterization**). Furthermore, after 3D-printing, the exothermal peak of

crystallization area emerging at 75 °C is more intense. This behavior may be explained by the fast cooling allowed by the fans, thus leading to a less crystallized state of the polymer chains. This behavior was confirmed by calculating the crystallinity percentages for the 10%CSP film, filament and 3D-printed disc (**Table 2.10**). Indeed, while extrusion was shown to slightly increase the crystallinity (39.1% for the film and 40.7% for the filament considering complete plasticizer evaporation), the 3D-printed disc depicts a much lower X_c value of about 25.8%. This last observation is similar to what was observed previously for the negative electrode (cf. **2.2.1.3.3. Thermal characterization**).

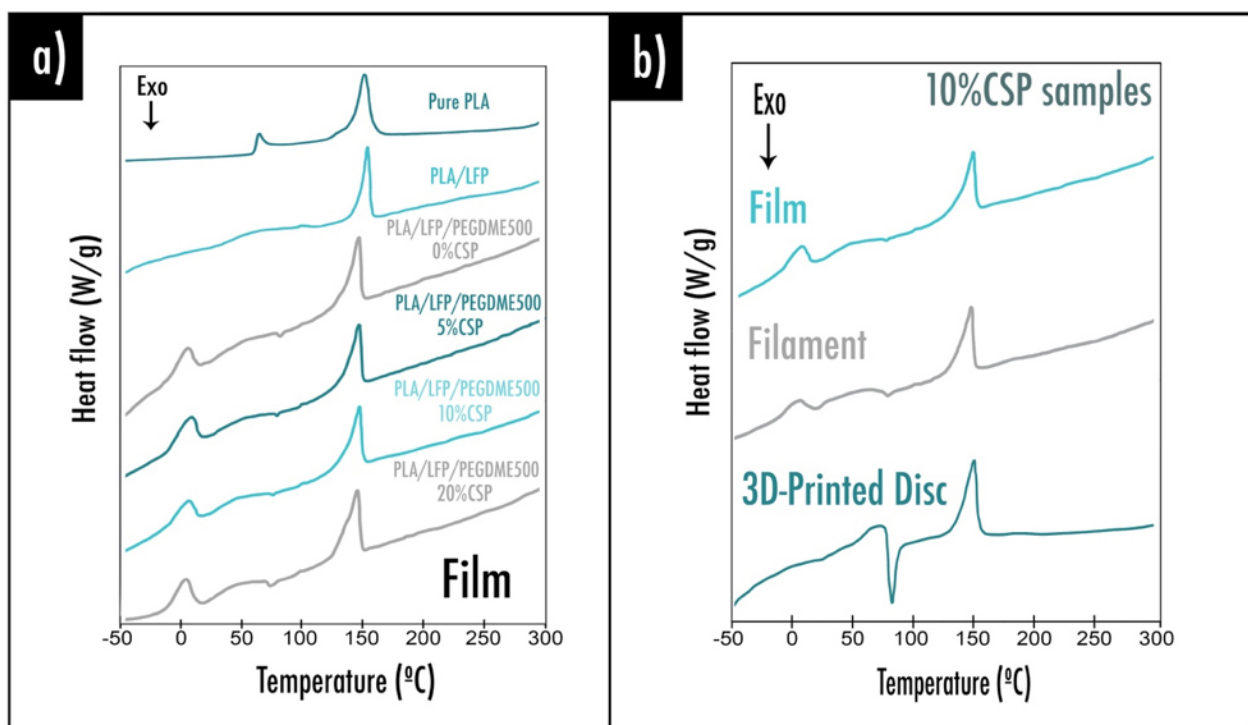


Figure 2.15. DSC curves: (a) pure PLA, PLA/LFP (wt% 40/60) and PLA/LFP/PEGDME500 films with different amount of conductive additive (CSP); (c) comparison between film, filament, and 3D-printed disc for the optimized 10%CSP sample — cf. **Preface – II**.

Table 2.10. Crystallinity percentage for the various film compositions, optimized 10%CSP filament and corresponding 10%CSP 3D-printed disc.

Sample	Xc (considering complete plasticizer evaporation)	Xc (considering null plasticizer evaporation)
Film 0%CSP	32.5%	37.4%
Film 5%CSP	37.6%	44.7%
Film 10%CSP	39.1%	44.9%
Filament 10%CSP	40.7%	46.8%
3D-printed disc 10%CSP	25.8%	29.7%
Film 20%CSP	38.0%	43.7%

2.2.2.2.4. Electrochemical characterization

A thorough characterization study was performed to establish the electrochemical behavior of the two most electrically conductive film samples *10%CSP* and *20%CSP* (**Figure 2.16**). For each sample of the same size (60 μm -thick and 11 mm diameter, surface equal to 0.950 cm^2) acquired after tape casting, Swagelok-type cells were assembled following the afore described exact same conditions (cf. **2.2.1.4.2. Electrochemical characterization**). Here also, 150 μL of 1 M LiPF_6 in ethylene carbonate and diethyl carbonate (EC:DEC 1:1 weight ratio) was used as liquid electrolyte (LP40) and purchased from Merck KGaA, Germany. Subsequently, cells were galvanostatically discharged (lithiation) and charged (delithiation) at different current densities calculated per gram of active material, between 3.8 and 2.6 V (vs Li/Li^+).

The potential profiles versus specific capacity based on the active material and specific capacity versus cycle number were examined at diverse current densities (8.5, 17, 34, and 85 mA g^{-1} of active material equivalent to $C/20$, $C/10$, $C/5$, and $C/2$). Among those samples, it was shown that *10%CSP* film displayed the best electrochemical performances reaching specific capacity value up to 165 and 162 mAh g^{-1} of active material at $C/20$ and $C/10$ respectively. It appears that

20%*CSP* film displays slightly inferior capacity values. Besides, this latter composition was discarded as *CSP* tends to agglomerate thus affecting the sample homogeneity.

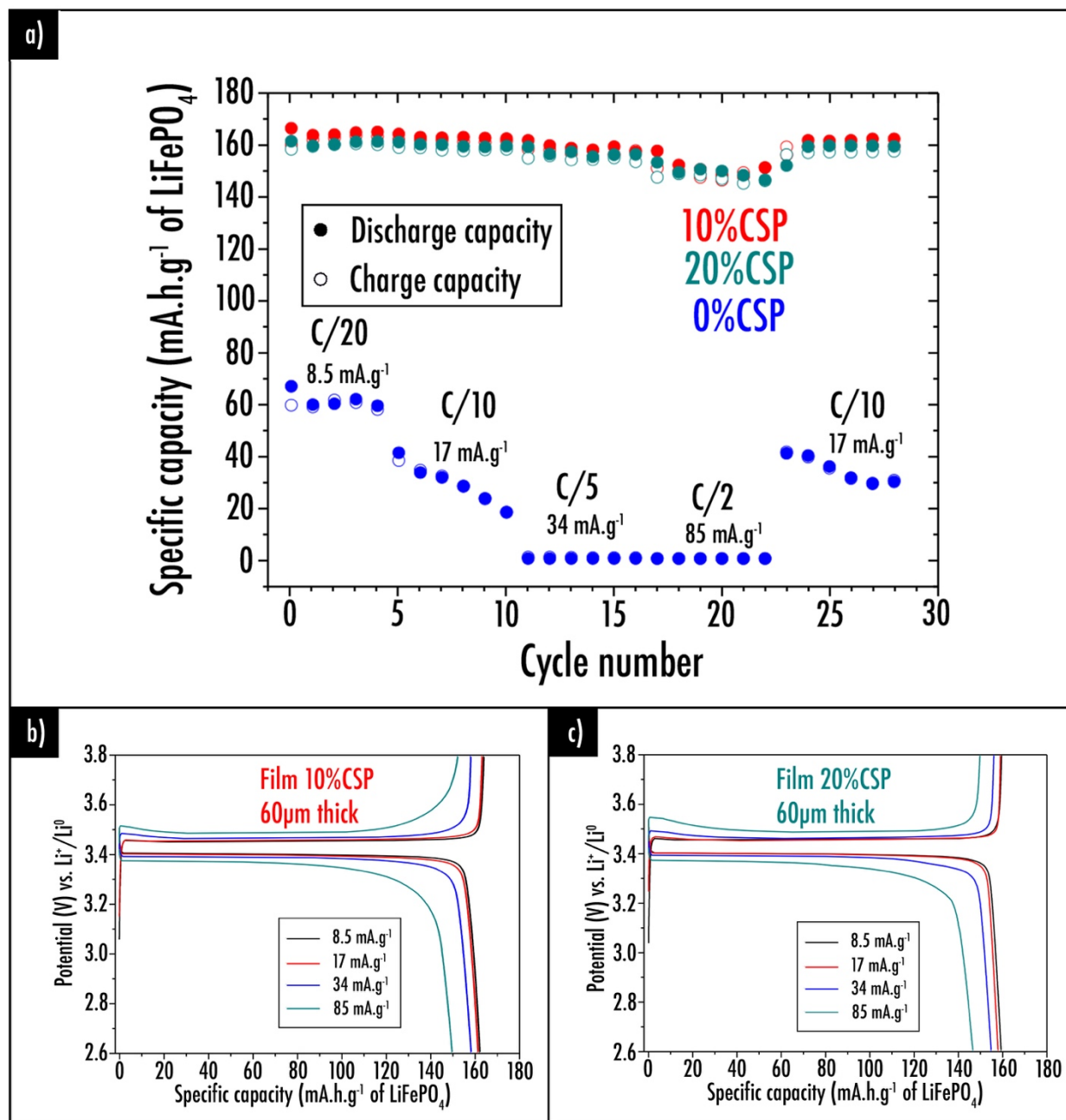


Figure 2.16. (a) Capacity retention plots at different C-rate for the 0%*CSP*, 10%*CSP* and 20%*CSP* positive electrode films; Potential profiles versus specific capacity based on the active material for (b) the 10%*CSP* and (c) the 20%*CSP* film samples — cf. Preface – II.

As theoretical capacity of LiFePO_4 (170 mAh g^{-1}) was almost reached with the *10%CSP* sample, it was consequently decided to focus our studies on this optimized sample for the positive electrode. Extrusion and 3D-printing were thus concentrated on the most electrochemically-encouraging *10%CSP* film sample as depicted hereabove (cf. **2.2.2.2.2. Printability and mechanical characterization**). Consequently, the corresponding homogeneous *10%CSP* filament (756 mg of active material per cm^3 of composite) was produced and $200\mu\text{m}$ -thick 3D-printed discs were characterized electrochemically (**Figure 2.17**).

Compared to specific capacity values obtained for the latter *10%CSP* $60\mu\text{m}$ -thick film, values displayed for the corresponding $200\mu\text{m}$ -thick 3D-printed disc were observed to be much lower: 87 mAh g^{-1} of active material at C/20 (equals to 43 mAh g^{-1} of the total composite or also 66 mAh cm^{-3} considering the total volume of the electrode) and 45 mAh g^{-1} of active material at C/10 (representing 22 mAh g^{-1} of the total composite or also 34 mAh cm^{-3}). This important gap is due to the difference of thickness between the film ($60 \mu\text{m}$) and the 3D-printed disc ($200 \mu\text{m}$) induced by the 3D-printer low thickness resolution on the first layer. 3D-printed disc shows an irreversible capacity during the first cycle of 38 mAh g^{-1} of active material, equivalent to a percentage loss of 42% at a current density of 8.5 mA g^{-1} (C/20). It is worth emphasizing that printing parameters such as the nozzle temperature may affect the percolation networks and thus final electrochemical performances. A too high nozzle temperature is expected to decrease the porosity as well as favoring particles sedimentation by gravity thus resulting in a non-homogeneous electrode sample.

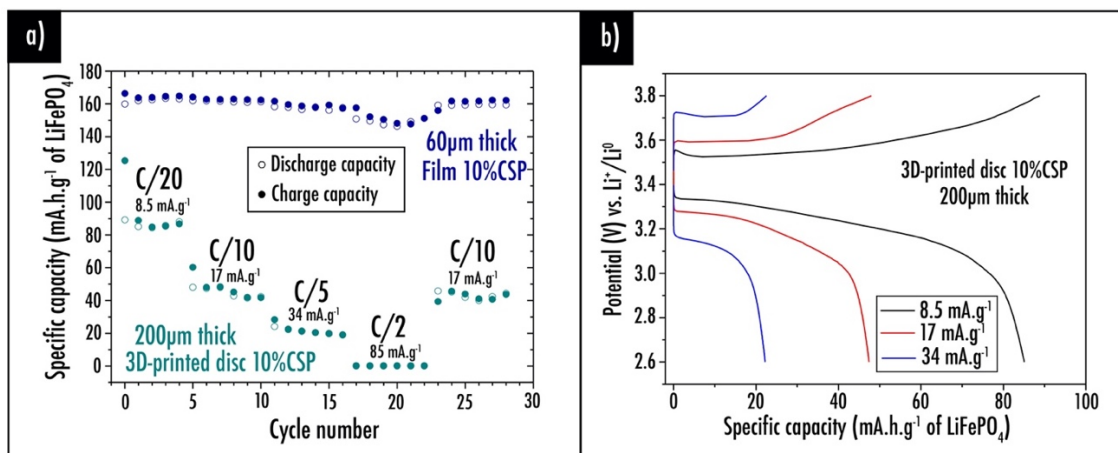


Figure 2.17. (a) Capacity retention plots at different C-rate for the film and 3D-printed disc 10%CSP sample; (b) Charge/ discharge capacity profiles for the 3D-printed disc 10%CSP sample. Note that for those experiments, a commercial fiber glass separator was used — cf. **Preface – II**.

2.2.3. Comparison with contemporary studies

In the meantime, while this PhD work was ongoing, other scientific groups also started concentrating their work on the FDM technique to print batteries. Similarly, studies were first mainly focused on the elaboration of homemade electrodes composite filaments comprising a higher amount of electrochemically active charges than what was previously reported by Foster et al.⁹ in 2017 (only 8 wt.% graphene compared to 92 wt.% PLA). **Table 2.11** depicts a chronological summary of the prepared filaments characteristics that were recently reported in literature. On the other hand, **Table 2.12** exhibits a summary of the reversible capacities reported for FDM 3D-printed disc in literature and their corresponding current densities. Regrettably, depending on the studies, it is important to note that units chosen by authors are not always analogous, making the comparison process particularly complicated. Hence, here, for both positive and negative electrode 3D-printed discs reported in this PhD thesis, gravimetric and areal current densities as well as gravimetric and volumetric reversible capacities are expressed.

Table 2.11. Summary of the filaments prepared for LIB and sodium-ion battery FDM 3D-printing that were reported in literature. For weight-volume conversion, material densities were determined by helium pycnometer — cf. **Preface – II and VI**. * Weight-volume conversion was deduced by considering the densities obtained for analogous materials via helium pycnometer.

Filaments	Total composite wt%	Total composite vol%	References
Graphene/PLA	8/92	5/95*	Foster et al. ⁹
LTO/Carbon additives/PLA LFP/Carbon additives/PLA	-	-	Ragones et al. ²⁸
LTO/Graphene/PLA	13/33/54*	6/24/70	Reyes et al. ²⁰
LMO/MWCNT/PLA	11/22/67*	4/16/80	
NaMnO ₂ /Carbon additives/PVA/ABS TiO ₂ /Carbon additives/PVA/ABS	-	-	Down et al. ²⁹
Graphene/PLA	20/80	12/88*	Foster et al. ³⁰
Nanographite/PLA	25/75	17/83*	Foster et al. ³¹
Graphite/CSP/PLA/PEGDME500	49/5/33/13	37/4/40/19	This PhD thesis (cf. Preface – I and II)
LFP/CSP/PLA/PEGDME500	49/5/33/13	35/4/41/20	

Chapter 2. Composite filaments elaboration for LIB 3D printing via fused deposition modeling

Table 2.12. Summary of the electrochemical performances (applied current density and corresponding reversible capacity) for FDM 3D-printed electrode discs. (blue: gravimetric; red: areal; green: volumic units) — cf. **Preface VI**

3D-printed disc	Applied current density	Reversible capacity	References
Graphene/PLA	10 mA g ⁻¹	15.8 mAh g ⁻¹ of graphene	Foster et al. ⁹
LFP/Carbon additives/PLA	9 μA cm ⁻²	60 mAh g ⁻¹ of LFP	Ragones et al. ²⁸
	44 μA cm ⁻²	50 mAh g ⁻¹ of LFP	
	88 μA cm ⁻²	20 mAh g ⁻¹ of LFP	
LTO/Graphene/PLA	10 mA g ⁻¹	0.34 mAh cm ⁻³ (total volume electrode)	Reyes et al. ²⁰
LMO/MWCNT/PLA	10 mA g ⁻¹	0.71 mAh cm ⁻³ (total volume electrode)	
Graphene/PLA	40 mA g ⁻¹	2.5 mAh g ⁻¹ of graphene	Foster et al. ³⁰
Graphite/CSP/PLA/PEGDME500	C/20 18.6 mA g ⁻¹ 322 μA cm ⁻²	200 mAh g ⁻¹ of graphite 155 mAh cm ⁻³ (total volume electrode)	This PhD thesis (cf. Preface – I and II)
	C/10 37.3 mA g ⁻¹ 646 μA cm ⁻²	140 mAh g ⁻¹ of graphite 108 mAh cm ⁻³ (total volume electrode)	
LFP/CSP/PLA/PEGDME500	C/20 8.5 mA g ⁻¹ 151 μA cm ⁻²	87 mAh g ⁻¹ of LFP 77 mAh cm ⁻³ (total volume electrode)	
	C/10 17 mA g ⁻¹ 303 μA cm ⁻²	45 mAh g ⁻¹ of LFP 40 mAh cm ⁻³ (total volume electrode)	
	C/5 34 mA g ⁻¹ 607 μA cm ⁻²	22 mAh g ⁻¹ of LFP 20 mAh cm ⁻³ (total volume electrode)	

In April 2018, Ragones et al.²⁸ reported the development of bespoke PLA/LTO negative electrode and PLA/LFP positive electrode composite filaments. While this study is very promising, the filament compositions are not precise enough. According to the authors, the filaments prepared by extrusion contain ~50-70% of active material, 10% carbon additives and ~20–40% PLA either in weight or volume percentages. Independent 3D-printed electrodes discs were subsequently tested in half-cells setup, soaked in 1 M LiPF₆ in 1 : 1 vol% EC: DEC + 2% vinylene carbonate (VC) electrolyte. The cycling of the cathode PLA/LFP finally resulted in 60, 50 and 20 mAh g⁻¹ of LFP capacities at current density of 9, 44 and 88 μA cm⁻², respectively. In comparison (**Table 2.12**), using similar units, the optimized 3D-printed positive electrode developed in this PhD thesis (cf. **2.2.2.2.4. Electrochemical characterization**) presents reversible capacity values of about 87, 45 and 22 mAh g⁻¹ of LFP at current density of 151, 303 and 607 μA cm⁻², respectively.

Few months later, in September 2018, Reyes et al.²⁰ reported the formulation of negative electrode PLA/LTO/graphene (vol.% 70/24/6) and positive electrode PLA/LMO/MWCNT (vol.% 80/4/16) filaments to feed a classical FDM 3D-printer. These filaments compositions were developed by first enhancing as high as possible the quantity of conductive additives to reach higher electronical conductivity without degrading printability. Then, active materials were respectively added in both filament and optimization of the electrochemical performances was accomplished. Finally, negative and positive half-cells displayed respectively 0.34 and 0.71 mAh cm⁻³ at a current density of 10 mA g⁻¹.

In February 2019, Down et al.²⁹ reported the preparation of composite electrodes filaments consisting of water soluble polymer polyvinyl alcohol (PVA) mixed with ABS, active materials for a sodium-ion battery (NaMnO₂ for the positive electrode and a TiO₂ for the negative electrode), along with the inclusion of conductive carbon. Interestingly, a porosity was created simply by soaking the filament in water. Regrettably, in this study again, the filaments compositions were not explicitly disclosed. Authors precise that electrodes filaments comprise about ~80% of polymer matrix. Unfortunately, no indications are unfortunately given to understand if these ratios are in weight or volume percentages. Focused on the LIB, the same group reported in April 2019 and February 2020, the elaboration of bespoke PLA/graphene (wt.% 80/20)³⁰ and PLA/nanographite (wt.% 75/25)³¹ filaments for their use as negative electrode.

To summarize, researchers working on this particular thematic were confronted to the same dilemma: establishing a compromise between electrochemical properties (through a high amount of active material) and mechanical properties/printability (through a significant amount of polymer). As depicted hereabove, so far, most of the reported studies described filaments containing a relatively low amount of active material thus having a detrimental effect on the final electrochemical performances of the battery. In comparison, as clearly demonstrated in this PhD thesis (**Table 2.12** — cf. **Preface – I and II**), this limitation can be overcome by introducing an appropriate plasticizer.

2.3. Separator filament formulation

2.3.1. Preparation

As depicted previously (cf. **1.1.2.2. Separator**), the separator acts as a physical barrier placed between both electrodes. While it must be electronically insulator, the ionic conductivity within the membrane must be enhanced as high as possible. In this context, similar to what was achieved for both electrodes (cf. **2.2. Highly-loaded electrodes filaments formulation**), the elaboration of a composite filament specially designed to be used as a separator within a LIB was initiated. For material saving purposes, it was here decided to start directly the elaboration from the optimized plasticizer composition wt.% PLA/PEGDME500 100:40, which was established beforehand as the most promising from the mechanical point of view (cf. **2.2.1.3. Optimization of plasticizer content**). Nonetheless, as depicted hereafter, the separator filament containing a lower amount of charges compared to the electrodes, an optimization must be performed in the future as the plasticizer ratio might be considerably reduced to improve printability.

Slurry formulation for the separator (**Table 2.13**) was achieved by following the experimental protocol described previously (cf. **2.1.1. Elaboration process**). After dissolution of the PLA, plasticizer was added (40 wt.% ratio PEGDME500/PLA). Then, amorphous SiO₂ nanoparticles (average size 7 nm), displayed in **Figure 2.18**, were added in the slurry and mixed until a homogeneous mixture was achieved. Subsequently, a free-standing separator film was obtained through tape-casting.

Table 2.13. Summary of the film compositions produced for the separator at increasing SiO₂ nanoparticles content — cf. Preface – II.

Sample name	Weight ratio PLA:SiO ₂	Weight ratio PLA:PEGDME500	Wt.% total composite PLA/SiO ₂ /Plasticizer
<i>0%SiO₂</i>	X	100:40	71/ 0 /29
<i>7%SiO₂</i>	100:10	100:40	66/ 7 /27
<i>13%SiO₂</i>	100:20	100:40	62/ 13 /25
<i>18%SiO₂</i>	100:30	100:40	59/ 18 /23
<i>22%SiO₂</i>	100:40	100:40	56/ 22 /22

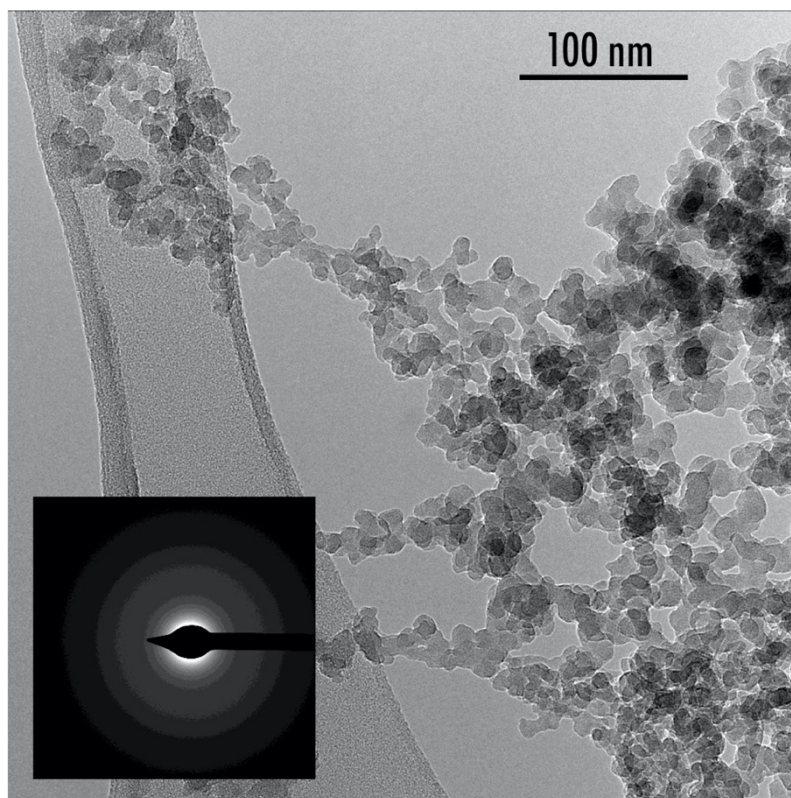


Figure 2.18. TEM image of the amorphous SiO₂ powder particles. Selected area electron diffraction (SAED) pattern is displayed in inset — cf. Preface – II.

2.3.2. Optimization of the ceramic content

Recently, Reyes et al.²⁰ reported the use of a pure PLA filament as separator soaked in a liquid electrolyte (1 M LiClO₄ EMC:PC vol% 1:1). After being immersed during 24h, the membrane subsequently exhibited an ionic conductivity of $7.5 \times 10^{-5} \text{ S cm}^{-1}$ (20°C) and an arguable significant volume change of 29%. In this PhD thesis, it was decided to go further through the introduction of ceramic fillers within the polymer matrix. Indeed, it has lately attracted substantial attention in literature,³² due to the ability of these particles to improve thermal stability, mechanical strength as well as ionic conductivity of the separators. In order to enhance those last parameters, the nanosilica content was optimized from 0 to 22 wt.%. For each separator sample described in **Table 2.13**, specific impedance spectra were investigated at 25 °C under argon after immersion within the electrolyte (1 M LiPF₆ in ethylene carbonate and diethyl carbonate EC:DEC 1:1 weight ratio) during 1 h and 10 h (**Figure 2.19**).

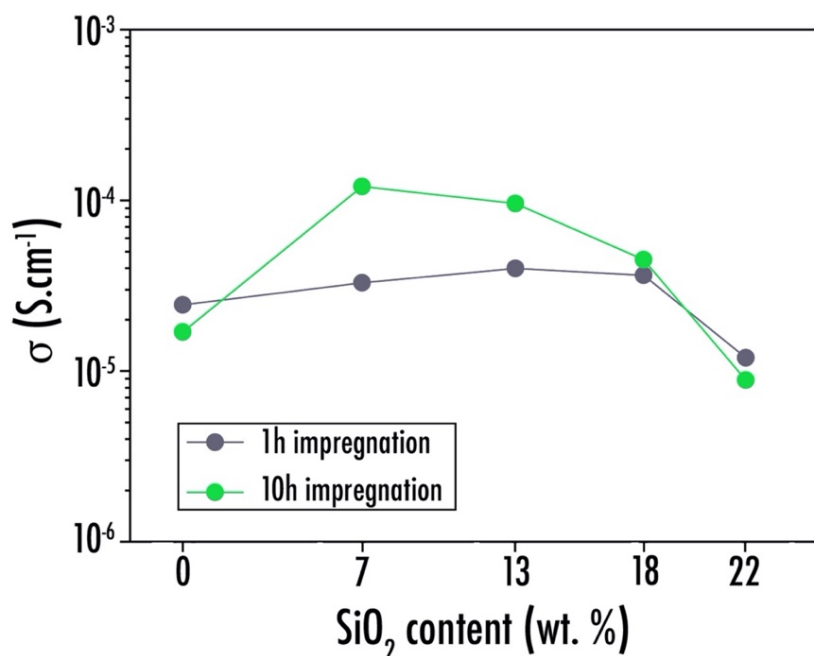


Figure 2.19. Ionic conductivity after 1 h and 10 h within the electrolyte 1 M LiPF₆ in EC:DEC 1:1 vol% for samples containing different SiO₂ content — cf. **Preface – II**.

First of all, by introducing SiO₂ nanoparticles within the PLA polymer matrix, it was shown that swelling percentage tends to decrease. Indeed, after being immersed 10 h within the electrolyte, 22%SiO₂, 18%SiO₂, 13%SiO₂, 7%SiO₂ and 0%SiO₂ samples depicted a swelling percentage equals to +2%, +4%, +5%, +8% and +14% respectively, in good agreement with what was observed by Reyes et al.²⁰ with a similar electrolyte. Moreover, after 1 h immersed within the electrolyte, conductivity was improved up to $3.96 \times 10^{-5} \text{ S cm}^{-1}$ for the 13%SiO₂ sample compared to value reaching only $2.41 \times 10^{-5} \text{ S.cm}^{-1}$ for sample 0%SiO₂. After 10 h immersion, the most conductive sample was 7%SiO₂ displaying $1.20 \times 10^{-4} \text{ S cm}^{-1}$, thus corresponding to seven times the conductivity value obtained for the reference 0%SiO₂ (only $1.67 \times 10^{-5} \text{ S cm}^{-1}$) and approaching the conductivity reference value of $1.30 \times 10^{-3} \text{ S cm}^{-1}$ (25°C) corresponding to porous polyolefin-based commercial (Celgard 2500) separator soaked with similar electrolyte during 4 days. An explanation of this behavior is that composite separators have higher electrolyte uptake due to the SiO₂ particles introduction improving wettability compared to the pristine separator.³³ Considering the complete plasticizer evaporation, the optimized sample 7%SiO₂ presents 11.3 mol% of SiO₂ (9.6 wt%), close to the optimized silica amount of 15.7 mol% (4 wt%) reported by Caillon-Caravanier et al.³⁴ Through the SiO₂ addition, a more porous structure is formed, thus contributing to faster electrolyte uptake. As also described by Caillon-Caravanier et al.³⁴, it is worth mentioning that a too high content of SiO₂ can have a detrimental effect on ionic conductivity as it is clearly visible for the 22%SiO₂ sample ($8.71 \times 10^{-6} \text{ S cm}^{-1}$ after 10 h). When maximum porosity is reached, further addition reduces absorption ability and conductivity by limiting the porous volume and by interaction of some fraction of the lithium cation with silica.³⁵ Thus, the optimized 7%SiO₂ composition was chosen and the resulting separator filament was prepared.

In parallel, a thermal study on the separator samples was completed through differential scanning calorimetry (**Figure 2.20**). DSC thermal characterization was achieved following the experimental protocol described previously (cf. **2.2.1.1. Preliminary tests**). Serving here as a reference, sample 0%SiO₂, composed of only PLA and PEGDME500, displays an endothermal peak related to its melting (T_m) at 139 °C and a well-defined crystallization peak (T_c) at 83 °C. By introducing SiO₂ nanoparticles within the PLA polymer matrix, the T_m of the film called 7%SiO₂ was slightly altered to lower temperature emerging at 134 °C while the T_c was unchanged. This behavior was also confirmed when a greater quantity of ceramic nanoparticles was added. Indeed,

22%SiO₂ film sample exhibits a T_m of 122°C (onset value) and an unchanged T_c. Nonetheless, through the addition of nano-silica, crystallinity percentage (X_c) of PLA within the composite films was shown to decrease slightly as depicted in **Table 2.14**. Indeed, X_c decreased from 71.3% for the 0%SiO₂ sample down to 60.2% for 22%SiO₂ (when plasticizer evaporation is not considered). Clearly, it appears that the SiO₂ presence within the PLA matrix impacts the crystallinity at the microscopic scale. However, this tendency is dissimilar with what was observed previously for the positive electrode at increasing carbon black concentration (cf. **2.2.2.2.3. Thermal characterization**). While previously the introduction of carbon black was shown to increase the crystallinity, here, the addition of SiO₂ seems to diminish it. An explanation to these contradictory results might be related to the high charges loading within the positive electrode impacting the crystallinity. Indeed, here for the separator, no active material (such as LiFePO₄ for the positive electrode) was introduced. On the other hand, plots achieved from DSC for the analogous 7%SiO₂ film, filament and 3D-printed disc (**Figure 2.20**), display similar values of T_m (equals to 134 °C) and T_c (between 83 and 79°C). By calculating the crystallinity percentages for these samples (**Table 2.14**), it appears that while extrusion was shown to slightly increase the crystallinity (51.4% for the film and 55.7% for the filament considering complete plasticizer evaporation), the 3D-printed disc depicted a lower X_c value of 50.0%. This last observation corroborates what was observed previously for both the negative and positive electrode (cf. **2.2.1.3.3. Thermal characterization** and **2.2.2.2.3. Thermal characterization**).

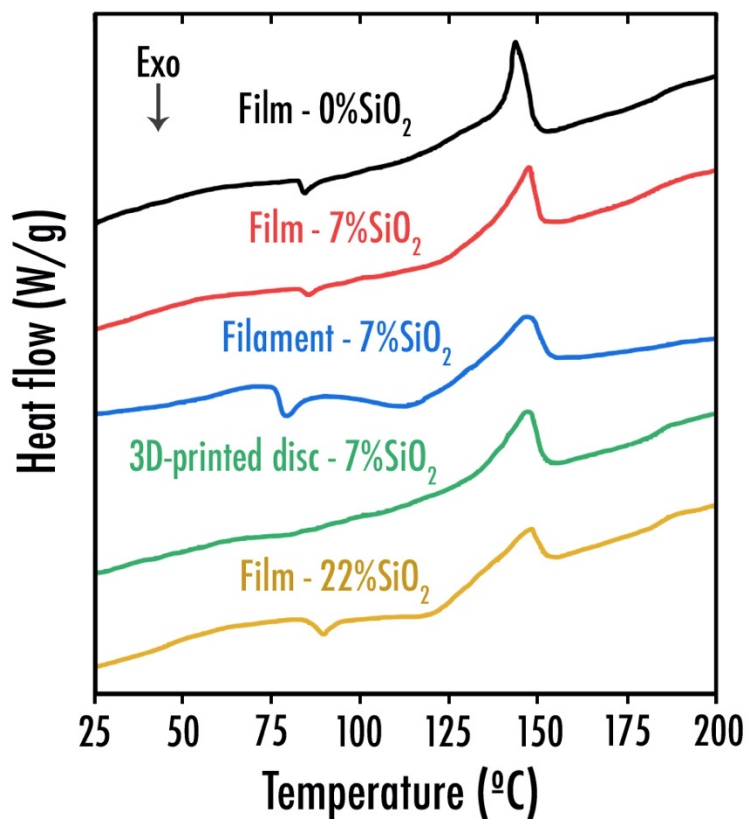


Figure 2.20. DSC curves for tested film, filament and 3D-printed disc separator samples.

Table 2.14. Crystallinity percentage for the various film compositions, optimized 7%SiO₂ filament and corresponding 7%SiO₂ 3D-printed disc.

Sample	Xc (considering complete plasticizer evaporation)	Xc (considering null plasticizer evaporation)
Film 0%SiO ₂	50.6%	71.3%
Film 7%SiO ₂	51.4%	70.4%
Filament 7%SiO ₂	55.7%	76.4%
3D-printed disc 7%SiO ₂	50.0%	68.5%
Film 22%SiO ₂	47.0%	60.2%

Finally, similar to what was achieved previously for both electrode filaments, the general homogeneity and the inner material (SiO_2) dispersion within the PLA matrix of the produced filament was examined by transmission electron microscopy (200 kV). Prior TEM experiment, 7% SiO_2 filament sample was cut and inserted in a resin following the exact same protocol described previously (cf. **2.2.1.4.2. Electrochemical characterization**). TEM image (**Figure 2.21**) confirmed the homogeneous SiO_2 particles distribution within the PLA polymer matrix. On the other hand, almost no porosity was found. This latter, directly linked to the liquid electrolyte impregnation, must be enhanced in the future by fine-tuning the extrusion and printing parameters. Indeed, so far, for these experiments focused on the separator, both extrusion and printing temperatures were set at the relatively high temperature of 195°C (about 60°C above the deduced temperature from DSC).

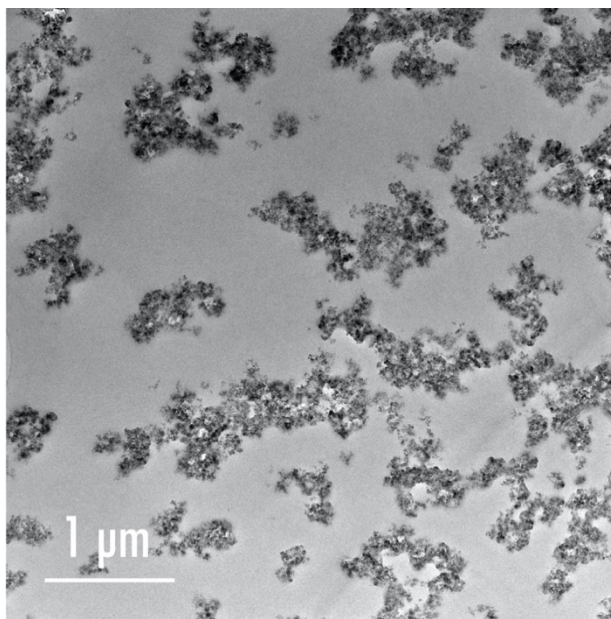


Figure 2.21. Cross-sectional TEM image of the 7% SiO_2 separator filament.

2.4. Current collector filament formulation

The elaboration of a PLA-based filament for its use as a current collector in a LIB after printing was initiated. This work being ongoing at the moment this PhD is written, only preliminary results (cf. **Preface — V**) will be presented in the following sections.

As depicted previously (cf. **1.1.2.4. Current collectors**), current collectors, being the direct contact between the electrode and the external circuit, must exhibit electrical conductivity as high as possible. In this context, metals, such as copper or aluminum (presenting adequate electrochemical stability window at the negative and positive electrode respectively), are materials of choice that are nowadays commonly employed in commercial LIB. In the sections hereafter, the formulation of a bespoke PLA/copper composite filament for its use as a current collector at the negative electrode side is described.

2.4.1. Silver coated copper powder

Neat copper powder ($d_{50}=20\mu\text{m}$) was first characterized by SEM and EDS. Noticeably, as depicted in **Figure 2.22**, it appeared that an insulative oxide CuO layer was present at the surface of the Cu particles thus representing a significant issue for its use as current collector. Additional TEM experiment must be performed in the future to precisely determine the thickness of this latter.

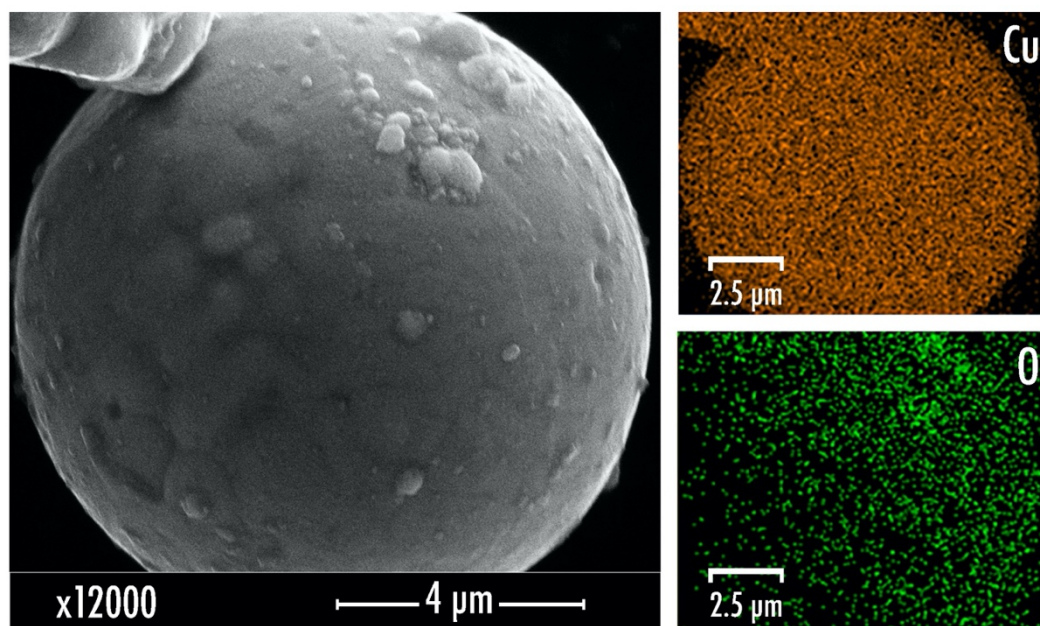
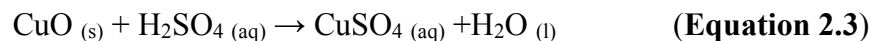


Figure 2.22. Neat Cu SEM image and element distribution map (Cu and O) obtained by Energy Dispersive X-ray Spectroscopy (EDS).

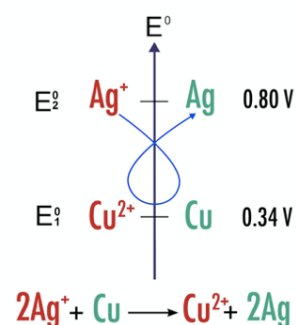
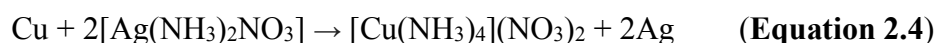
Since such CuO layer is known to be highly insulator, a protocol was established to dissolve it and subsequently deposit a homogeneous Ag layer on top of the Cu particles. This was done with a view to prevent surface copper from oxidation and enhance the electronic conductivity. First of all, 50g copper powder was introduced in a diluted sulfuric acid (97%, Sigma Aldrich) solution (volume ratio H₂SO₄ : DI water of 1:20) for 2 minutes in order to remove the oxide layer, following the chemical reaction (**Equation 2.3**) below:



According to Lee et al.³⁶, for such a H₂SO₄ concentration and reaction time, 2.7nm of oxide layer are estimated to be etched. This must be corroborated in the future by performing TEM experiment. Subsequently, the resulting clean copper powder was filtered using a Büchner funnel and washed with DI water until the pH of the filtrate solution matched the one of DI water. The washed copper powder was finally kept in 100ml DI water. On the other hand, 7.85g of silver nitrate (99.9%, Sigma Aldrich), 100g of ammonium carbonate (99%, Sigma Aldrich), and 114mL of ammonia water (28%, Sigma Aldrich) were mixed together with 100ml of DI water. According

to Koto et al.,³⁷ there is no particular restriction with respect to the ratio of copper to silver nitrate. Nonetheless, a compromise must be reached as the final product becomes expensive as the amount of the silver coating increases while a minimum weight of silver nitrate must be provided in order to cover the entire surface of copper powder. The silver complex solution was then added dropwise into the afore-mentioned copper mixture over a period of 5 minutes at room temperature. The resulting solution was stirred for an additional hour to allow the silver deposition on the copper powder. Finally, the resulting Ag-Cu powder was filtered using a Büchner funnel and washed several times using DI water to remove the residual chemicals and impurities, until the pH of the filtrate solution matched the one of DI water. Lastly, the powder was dried at 50 °C under vacuum during 5 days prior performing characterization experiments.

As reported in literature,³⁸ when the silver complex solution is poured into copper suspension, the redox reaction between the activated surfaces of copper particles and silver complex ions occurs as depicted in the **Equation 2.4** below. Silver is thus deposited on the activated surface of copper particles.



The pH reported to significantly impact the deposition rate, surface morphology and further impedance behavior,³⁹ a mixture of ammonia water and ammonium carbonate solution was here employed as buffer (pKa = 9.25). According to literature,³⁷ the ideal molar ratio of the ammonium carbonate compound to ammonia water is from 0.1 to 3. Hence, in this experiment, a molar ratio of 1.08 was employed.

Last but not least, the resulting Ag-Cu powder was characterized via SEM/EDS. Noticeably, as depicted in **Figure 2.23**, it appears that the aforementioned protocol worked properly as Ag was clearly identified on top of the Cu particles. Nonetheless, it is worth mentioning that further thorough TEM experiments must be performed in the future to precisely determine the thickness of the deposited Ag layer.

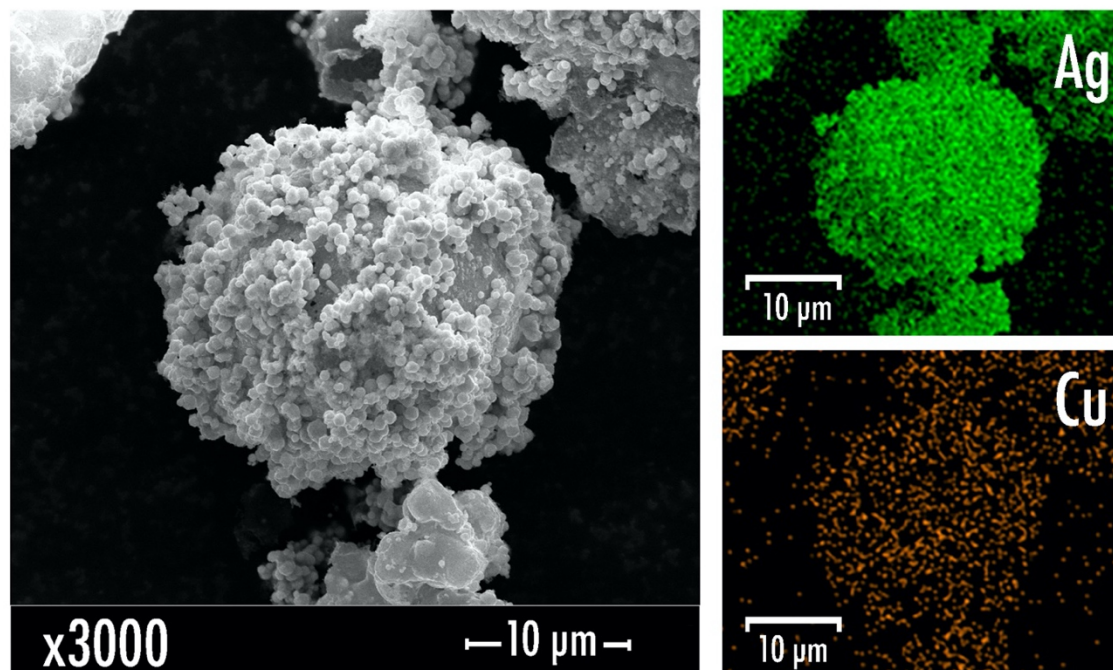


Figure 2.23. Ag-Cu powder SEM image and element distribution map (Ag and Cu) obtained by Energy Dispersive X-ray Spectroscopy (EDS).

2.4.2. Composite film and filament

Similar to what was achieved for both electrodes and separator previously, the elaboration of a composite filament specially designed to be used as a current collector within a LIB was initiated. For material saving purposes, it was here again decided to start directly the elaboration from the optimized plasticizer composition wt.% PLA/PEGDME500 100:40, which was established beforehand as the most promising from the mechanical point of view (cf. **2.2.1.3. Optimization of plasticizer content**).

Slurry formulation for the current collector (**Table 2.15**) was achieved by following the experimental protocol described previously (cf. **2.1.1. Elaboration process**). After dissolution of the PLA, plasticizer was added (40 wt.% ratio PEGDME500/PLA). Then, the Cu or Ag-Cu powder was introduced within the slurry (weight ratio PLA : Cu-based powder equals to 10:90) and mixed until a homogeneous mixture was achieved. Subsequently, after tape-casting, two free-standing current collector films were obtained.

Table 2.15. Summary of the film compositions produced for the current collector.

Sample name	Weight ratio PLA : PEGDME500	Weight ratio PLA : Cu-based powder	Wt.% total composite PLA/ Cu-based powder /PEGDME500
Neat Cu	100 : 40	10 : 90	9.7 / 86.5 / 3.8
Ag-Cu (cf. 2.4.1. Silver coated copper powder)	100 : 40	10 : 90	9.7 / 86.5 / 3.8

The electronic conductivity of both films was studied via specific impedance spectroscopy at temperatures ranging between 20 °C to 60 °C. The exact same procedure than the one described in the previous section (cf. **2.2.1.4.1. Electrical conductivity**) was followed. Similarly, the achieved Nyquist and Bode curves are in accordance with an electronic conductor classical behavior as Nyquist plot portrays only Z' real part while $|Z|$ magnitude is remained steady for all frequencies. Here, due to their composite nature, the electrical conductivity for both samples of equal thickness and area, exhibits a semiconductor-type behavior as it is rising with temperature as exhibited in **Figure 2.24** and activation energy values of 0.678 meV for sample with neat Cu and 0.071 meV for sample containing Ag-Cu powder were estimated. The opposite behavior (increase of temperature causing conductivity values to decrease) is usually exhibited by pure metals. Interestingly, it appears that composite film containing neat Cu is very poorly conductive ($4.2 \times 10^{-10} \text{ S cm}^{-1}$ at 20°C). Hence, its use as current collector in a LIB is highly compromised. This trend clearly corroborates the aforementioned SEM/EDS observations that highlighted the CuO insulative layer presence. On the other hand, sample containing the afore-prepared Ag-Cu powder exhibits a drastically higher conductivity reaching 11.3 S cm^{-1} at 20°C and pave the way towards the preparation of a highly conductive current collector filament.

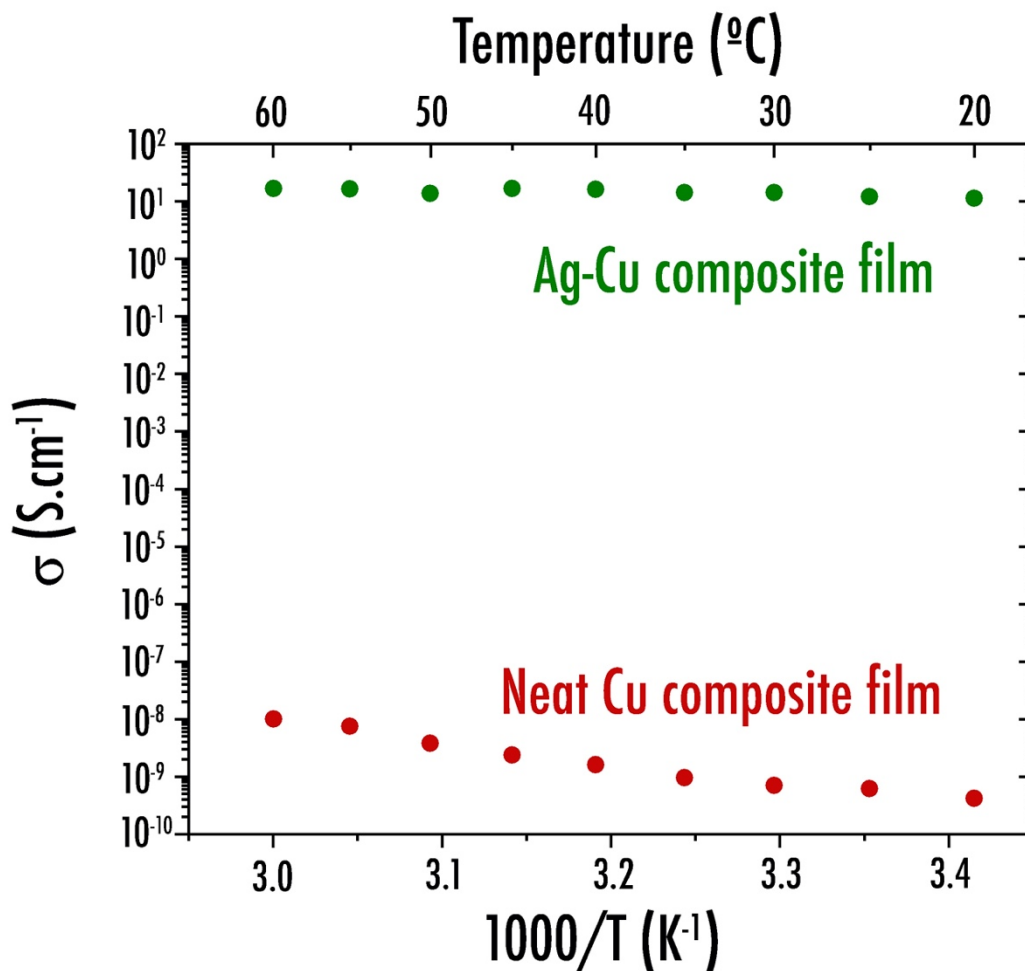


Figure 2.24. Arrhenius plots of the electrical conductivity for both composite film samples of the same composition ratio containing neat Cu or Ag-Cu.

Finally, from the DSC experiment, the PEGDME500 melting temperature appeared at about $5^{\circ}C$, the crystallization temperature at $75^{\circ}C$ and the T_m of the Ag-Cu composite film emerged at $142^{\circ}C$ (**Figure 2.25**). A crystallinity of about 47% (not considering the plasticizer evaporation) was calculated. From these values, it was decided to produce the corresponding filament by fixing the extruder temperature at a slightly higher temperature of $160^{\circ}C$.

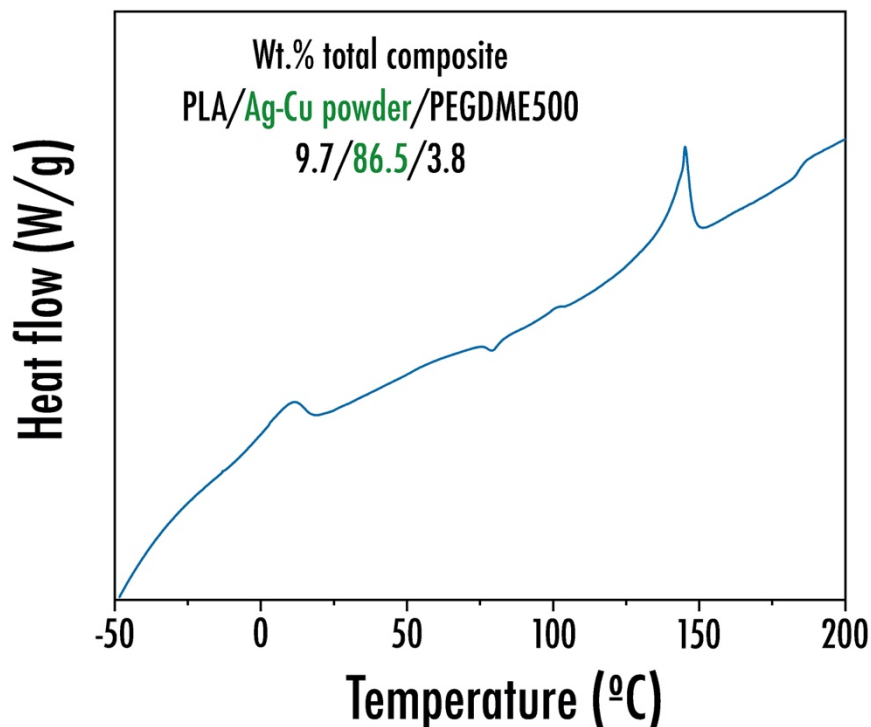


Figure 2.25. DSC curve for the prepared PLA/Ag-Cu powder/PEGDME500 film sample.

Last part of this study was concentrated on the comparison with commercially available conductive filaments. Hence, a filament length of 10 cm was cut and resistance was measured with a multimeter from both ends. Following the protocol established by the company Multi3D LLC in their website (<https://www.multi3dllc.com>), silver paste was applied to the ends of the filament before performing the measurement in order to reduce contact resistance between the probes and the filament. Subsequently, the resistivity values were calculated according to the following **Equation 2.5**:

$$\rho = \frac{R \times \pi r^2}{L} \quad \text{(Equation 2.5)}$$

where ρ is the resistivity of the filament in Ω cm, R is the resistance in Ω , L corresponds to the filament length in cm and r is the radius of the filament in cm.

After calculations, it appears that the Ag-Cu filament produced in this PhD thesis depicts a resistivity of $0.112 \Omega \text{ cm}$. This latter is thus much more conductive than commercial filaments produced from Proto-Pasta ($4.340 \Omega \text{ cm}$ — PLA/graphite) and Black Magic 3D ($\sim 0.6 \Omega \text{ cm}$ — PLA/graphene) but less conductive than the commercial Electrifi filament (Multi3D LLC) (resistivity value of about $0.006 \Omega \text{ cm}$). Hence, the electrical performances could still be optimized through the addition of conductive additives (CSP, CNF or CNT) prior to further printing. Future study on the current collector must also be concentrated on the use of another polymer matrix (such as PP), as PLA swells when soaked in the liquid electrolyte thus suspected to have a detrimental effect on the electronic conductivity.

Conclusions

To conclude, the first stage of this PhD thesis was focused on the development and optimization of PLA-based composite filaments, corresponding to each part of a LIB based on a liquid electrolyte configuration, to feed a FDM 3D-printer. Electrochemical performances were here maximized while still maintaining just enough mechanical strength for handling and printing.

In order to mix all the components (polymer, additives and charges), the solvent method was here employed as it is really adapted to obtain homogeneous composite at the laboratory scale. However, because of the toxicity of dichloromethane, alternatives to this method must be envisaged in the future. Double screw extruder must be a good substitute to obtain homogeneous mixture in a mechanical way. After solvent evaporation, composite films were cut into small pieces and extruded to produce a filament. Printability behavior of the composite filaments was tested. Through mechanical characterization and printability tests, it was demonstrated that plasticizer was needed to be incorporated during the formulation step to provide a certain flexibility to the filament and avoid brittleness. Finally, PEGDME500 was chosen as plasticizer and a weight ratio PLA:PEGDME500 equals to 100:40 was defined as the most printable filament. Indeed, it was deduced by performing DSC experiments that samples containing PC as plasticizer had tendency to become brittle due to the plasticizer evaporation while filament samples containing ATBC or PEGDME2000 have tendency to weep and become brittle too after few days, reflecting a certain incompatibility with PLA.

Considering the optimized plasticizer composition, an exhaustive study was carried out to identify and optimize the electrical and/or electrochemical impact of conductive additives such as CSP and/or CNF within the electrodes, ceramic nanoparticles of SiO₂ within the separator, and Ag-Cu powder in the current collector. Active material loading was increased as high as possible within the electrodes to enhance the electrochemical performances. Optimized 3D-printed electrode discs still showed high irreversible capacity loss (first cycle) in comparison with commercial electrodes. Moreover, so far, reversible capacity values of the 3D printed electrode discs are limited because of the FDM 3D printer resolution limitation (about 200 μm thick for the first layer). Incorporation of SEI reinforcing additives should be studied in more details in the future to further improve the electrochemical performances. Post-mortem studies should be performed to evaluate the printed components stability and degradation (PLA in particular) during long cycling as function of the liquid electrolyte composition, and accordingly, polymers should be adapted to ensure long-term cyclability. On the other hand, SiO₂ ceramic particles content was optimized to enhance the ionic conductivity of the separators when soaked within a liquid electrolyte. Regarding the current collector, optimization still needs to be carried out (addition of conductive additives) with a view to maximize the electronic conductivity.

Finally, the good homogeneity of the composite filaments was confirmed through textural analysis (SEM, TEM, Raman, optical microscopy). Unfortunately, during the extrusion process, it was shown that samples may unfortunately be combined with neat PLA used to purge the machine. To overcome this particular issue, at least 100 g of material corresponding to the same sample composition must be introduced within the extruder hopper.

As the optimized composite filaments compositions are now established for each part of the LIB, next chapter appears as a logical follow-up devoted to the complete LIB assembly through FDM, both separately but also in one-single step.

References

1. Robertson, G. L., *Food Packaging: Principles and Practice, Third Edition*. CRC Press: 2012.
2. Conn, R. E.; Kolstad, J. J.; Borzelleca, J. F.; Dixler, D. S.; Filer, L. J.; Ladu, B. N.; Pariza, M. W., Safety assessment of polylactide (PLA) for use as a food-contact polymer. *Food and Chemical Toxicology* **1995**, 33, (4), 273-283.
3. Fazita, M. R. N.; Jayaraman, K.; Bhattacharyya, D.; Hossain, M. S.; Haafiz, M. K. M.; Khalil, H., Disposal Options of Bamboo Fabric-Reinforced Poly(Lactic) Acid Composites for Sustainable Packaging: Biodegradability and Recyclability. *Polymers* **2015**, 7, (8), 1476-1496.
4. Jamshidian, M.; Tehrany, E. A.; Imran, M.; Jacquot, M.; Desobry, S., Poly-Lactic Acid: Production, Applications, Nanocomposites, and Release Studies. *Comprehensive Reviews in Food Science and Food Safety* **2010**, 9, (5), 552-571.
5. Sato, S.; Gondo, D.; Wada, T.; Kanehashi, S.; Nagai, K., Effects of various liquid organic solvents on solvent-induced crystallization of amorphous poly(lactic acid) film. *Journal of Applied Polymer Science* **2013**, 129, (3), 1607-1617.
6. Leigh, S. J.; Bradley, R. J.; Pursell, C. P.; Billson, D. R.; Hutchins, D. A., A Simple, Low-Cost Conductive Composite Material for 3D Printing of Electronic Sensors. *Plos One* **2012**, 7, (11).
7. Dul, S.; Fambri, L.; Pegoretti, A., Fused deposition modelling with ABS-graphene nanocomposites. *Composites Part a-Applied Science and Manufacturing* **2016**, 85, 181-191.
8. Wei, X. J.; Li, D.; Jiang, W.; Gu, Z. M.; Wang, X. J.; Zhang, Z. X.; Sun, Z. Z., 3D Printable Graphene Composite. *Scientific Reports* **2015**, 5.
9. Foster, C. W.; Down, M. P.; Zhang, Y.; Ji, X. B.; Rowley-Neale, S. J.; Smith, G. C.; Kelly, P. J.; Banks, C. E., 3D Printed Graphene Based Energy Storage Devices. *Scientific Reports* **2017**, 7, 11.
10. Wypych, G., Effect of plasticizers on properties of plasticized materials. In *Handbook of Plasticizers: Third Edition*, 2017; pp 209-219.
11. Farah, S.; Anderson, D. G.; Langer, R., Physical and mechanical properties of PLA, and their functions in widespread applications - A comprehensive review. *Advanced Drug Delivery Reviews* **2016**, 107, 367-392.

12. Ferrari, A. C., Raman spectroscopy of graphene and graphite: Disorder, electron-phonon coupling, doping and nonadiabatic effects. *Solid State Communications* **2007**, 143, (1-2), 47-57.
13. Pimenta, M. A.; Dresselhaus, G.; Dresselhaus, M. S.; Cancado, L. G.; Jorio, A.; Saito, R., Studying disorder in graphite-based systems by Raman spectroscopy. *Physical Chemistry Chemical Physics* **2007**, 9, (11), 1276-1291.
14. Kister, G.; Cassanas, G.; Vert, M., Effects of morphology, conformation and configuration on the IR and Raman spectra of various poly(lactic acid)s. *Polymer* **1998**, 39, (2), 267-273.
15. Kang, S. H.; Hsu, S. L.; Stidham, H. D.; Smith, P. B.; Leugers, M. A.; Yang, X. Z., A spectroscopic analysis of poly(lactic acid) structure. *Macromolecules* **2001**, 34, (13), 4542-4548.
16. Ragonés, H.; Vinegrad, A.; Ardel, G.; Goor, M.; Kamir, Y.; Dorfman, M. M.; Gladkikh, A.; Golodnitsky, D., On the Road to a Multi-Coaxial-Cable Battery: Development of a Novel 3D-Printed Composite Solid Electrolyte. *Journal of the Electrochemical Society* **2019**, 167, (1).
17. Li, F. J.; Zhang, S. D.; Liang, J. Z.; Wang, J. Z., Effect of polyethylene glycol on the crystallization and impact properties of polylactide-based blends. *Polymers for Advanced Technologies* **2015**, 26, (5), 465-475.
18. Nofar, M.; B., P. C., *Polylactide Foams: Fundamentals, Manufacturing, and Applications*. In 2017.
19. Panabiere, E.; Badot, J. C.; Dubrunfaut, O.; Etiemble, A.; Lestriez, B., Electronic and Ionic Dynamics Coupled at Solid-Liquid Electrolyte Interfaces in Porous Nanocomposites of Carbon Black, Poly(vinylidene fluoride), and gamma-Alumina. *Journal of Physical Chemistry C* **2017**, 121, (15), 8364-8377.
20. Reyes, C.; Somogyi, R.; Niu, S.; Cruz, M. A.; Yang, F.; Catenacci, M. J.; Rhodes, C. P.; Wiley, B. J., Three-Dimensional Printing of a Complete Lithium Ion Battery with Fused Filament Fabrication. *ACS Applied Energy Materials* **2018**, 1, (10), 5268-5279.
21. Peled, E., The electrochemical-behavior of alkali and alkaline-earth metals in non-aqueous battery systems - the solid electrolyte interphase model. *Journal of the Electrochemical Society* **1979**, 126, (12), 2047-2051.
22. Kim, H.; Grugeon, S.; Gachot, G.; Armand, M.; Sannier, L.; Laruelle, S., Ethylene bis-carbonates as telltales of SEI and electrolyte health, role of carbonate type and new additives. *Electrochimica Acta* **2014**, 136, 157-165.

23. Xiang, H. F.; Chen, C. H.; Zhang, J.; Amine, K., Temperature effect on the graphite exfoliation in propylene carbonate based electrolytes. *Journal of Power Sources* **2010**, 195, (2), 604-609.
24. Peled, E.; Menkin, S., Review-SEI: Past, Present and Future. *Journal of the Electrochemical Society* **2017**, 164, (7), A1703-A1719.
25. Guy, D.; Lestriez, B.; Bouchet, R.; Guyomard, D., Critical role of polymeric binders on the electronic transport properties of composites electrode. *Journal of the Electrochemical Society* **2006**, 153, (4), A679-A688.
26. Busson, C.; Blin, M. A.; Guichard, P.; Soudan, P.; Crosnier, O.; Guyomard, D.; Lestriez, B., A primed current collector for high performance carbon-coated LiFePO₄ electrodes with no carbon additive. *Journal of Power Sources* **2018**, 406, 7-17.
27. Dowling, N. E., *Mechanical behavior of materials, 4th edition*, Pearson. 2013.
28. Ragonés, H.; Menkin, S.; Kamir, Y.; Gladkikh, A.; Mukra, T.; Kosa, G.; Golodnitsky, D., Towards smart free form-factor 3D printable batteries. *Sustainable Energy & Fuels* **2018**, 2, (7), 1542-1549.
29. Down, M. P.; Martinez-Perinan, E.; Foster, C. W.; Lorenzo, E.; Smith, G. C.; Banks, C. E., Next-Generation Additive Manufacturing of Complete Standalone Sodium-Ion Energy Storage Architectures. *Advanced Energy Materials* **2019**, 9, (11), 7.
30. Foster, C. W.; Zou, G. Q.; Jiang, Y. L.; Down, M. P.; Liauw, C. M.; Ferrari, A. G. M.; Ji, X. B.; Smith, G. C.; Kelly, P. J.; Banks, C. E., Next-Generation Additive Manufacturing: Tailorable Graphene/Polylactic(acid) Filaments Allow the Fabrication of 3D Printable Porous Anodes for Utilisation within Lithium-Ion Batteries. *Batteries & Supercaps* **2019**, 2, (5), 448-453.
31. Foster, C. W.; Elbardisy, H. M.; Down, M. P.; Keefe, E. M.; Smith, G. C.; Banks, C. E., Additively manufactured graphitic electrochemical sensing platforms. *Chemical Engineering Journal* **2020**, 381.
32. Shin, W. K.; Kim, D. W., High performance ceramic-coated separators prepared with lithium ion-containing SiO₂ particles for lithium-ion batteries. *Journal of Power Sources* **2013**, 226, 54-60.
33. Liu, H. Y.; Xu, J.; Guo, B. H.; He, X. M., Effect of SiO₂ Content on Performance of Polypropylene Separator for Lithium-Ion Batteries. *Journal of Applied Polymer Science* **2014**, 131, (23).

34. Caillon-Caravanier, M.; Claude-Montigny, B.; Lemordant, D.; Bossier, G., Absorption ability and kinetics of a liquid electrolyte in PVDF-HFP copolymer containing or not SiO₂. *Journal of Power Sources* **2002**, 107, (1), 125-132.
35. Lee, K. H.; Lee, Y. G.; Park, J. K.; Seung, D. Y., Effect of silica on the electrochemical characteristics of the plasticized polymer electrolytes based on the P(AN-co-MMA) copolymer. *Solid State Ionics* **2000**, 133, (3-4), 257-263.
36. Lee, Y.-S.; Yoon, J.-S.; Jo, Y.-R.; Lee, H.; Rha, S.-K., Dilute H₂SO₄ solution for copper seed cleaning in electroplating. *Transactions of Nonferrous Metals Society of China* **2013**, 23, (2), 562-566.
37. Koto, N.; Yukawa, J.; Mori, T. Process for the production of a silver coated copper powder and conductive coating composition. 1987.
38. Hai, H. T.; Ahn, J. G.; Kim, D. J.; Lee, J. R.; Chung, H. S.; Kim, C. O., Developing process for coating copper particles with silver by electroless plating method. *Surface & Coatings Technology* **2006**, 201, (6), 3788-3792.
39. Anik, T.; Touhami, M. E.; Himm, K.; Schireen, S.; Belkhmima, R. A.; Abouchane, M.; Cisse, M., Influence of pH Solution on Electroless Copper Plating Using Sodium Hypophosphite as Reducing Agent. *International Journal of Electrochemical Science* **2012**, 7, (3), 2009-2018.

Chapter 3.

3D-Printing of a complete LIB cell via fused deposition modeling

Chapter 3. 3D-Printing of a complete LIB cell via fused deposition modeling

3.1. Introduction.....	118
3.2. Overview of the faced printability issues.....	119
3.2.1. Composite filament-related issues.....	119
3.2.2. Classical FDM issues.....	121
3.2.2.1. Temperature issues.....	121
3.2.2.2. Build platform level calibration related issues.....	124
3.2.3. 3D-printers related issues and optimization.....	125
3.3. Complete LiFePO ₄ /graphite LIB 3D-printing.....	127
3.3.1. Cell assembly from independent 3D-printed components.....	127
3.3.1.1. Preliminary tests.....	127
3.3.1.2. Separator infill pattern.....	128
3.3.2. Cell 3D-printing in one-shot.....	132
3.3.2.1. Experimental procedure.....	132
3.3.2.2. Preliminary tests.....	133
3.3.2.3. Separator infill pattern.....	134
3.4. Towards the printability of complex 3D LIB architectures.....	140
3.4.1. 3D architectures impact on electrochemical performances.....	140
3.4.1.1. Introduction to the tested 3D architectures.....	140
3.4.1.2. Theoretical models and assumptions.....	144
3.4.1.3. Finite element model.....	146
3.4.1.4. Results and discussion.....	148
3.4.2. Multi-materials FDM printing.....	152
3.4.2.1. Commercially available options comparison.....	152
3.4.2.2. First tests.....	154
Conclusions.....	157
References	159

3.1. Introduction

Starting from the afore-optimized filaments compositions (cf. **Chapter 2**) recalled in **Table 3.1**, this chapter is now dedicated to the 3D-printing of a complete lithium-ion battery cell based on a liquid electrolyte technology. First, an overview of the printability issues faced during this PhD thesis is portrayed. On the other hand, LIB assembly (stacking) from 3D-printed independent components (electrodes and separator) as well as the complete LIB printability in one single step (one-shot) is described. Taking advantage of the new design capabilities conferred by Fused Deposition Modeling, separator infill patterns and density are examined to improve the liquid electrolyte impregnation and avoid short-circuits. Electrochemical performances of the complete cells are evaluated by performing galvanostatic tests.

Table 3.1. Summary of the optimized filaments compositions. For weight-volume conversion, material densities were determined by helium pycnometer.

Optimized sample	Wt.% total composite	Vol.% total composite
Negative electrode	PLA/graphite/CSP/PEGDME500 33/49/5/13	PLA/graphite/CSP/PEGDME500 40/37/4/19
Positive electrode	PLA/LiFePO ₄ / CSP/PEGDME500 33/49/5/13	PLA/LiFePO ₄ / CSP/PEGDME500 41/35/4/20
Separator	PLA/SiO ₂ /PEGDME500 56/22/22	PLA/SiO ₂ /PEGDME500 59/13/28

Finally, the electrochemical aptitude of various LIB complex 3D architectures, in comparison with classical 2D planar design, is thoroughly studied by means of a modeling study. The direct printing capability in one-shot, by means of multi-materials printing options, of such complex 3D designs is then considered. Note that results presented in the sections hereafter are already part of *published* or *in preparation* articles (cf. **Preface — II and IV**).

3.2. Overview of the faced printability issues

As reported in the previous **Chapter 2**, a thorough study on the formulation of composite filaments corresponding to each component of the battery (**Table 3.1**) was conducted with the difficult objective of achieving maximum electrochemical performances while still maintaining just enough mechanical strength to allow proper handling and printing. Although the printability of each filament was demonstrated, it is important to emphasize that it remains a complicated task because of their exotic nature, particularly when high loading of charges is introduced. In the subsections below, an extensive list of the most common FDM 3D-printing issues faced along this project is depicted.

3.2.1. Composite filament-related issues

Due to the atypical composition of the produced composite filaments, most common issue faced along this project was related to the filament extrusion. While the composite filament was introduced thoroughly within the extruder part of the FDM 3D-printer, material was sometimes not coming out of the heated nozzle properly. This phenomenon was perceived randomly, at start (**Figure 3.1.a**) or in middle of a print (**Figure 3.1.b**). Consequently, print was stopped and machine maintenance was needed in order to fix the issue.

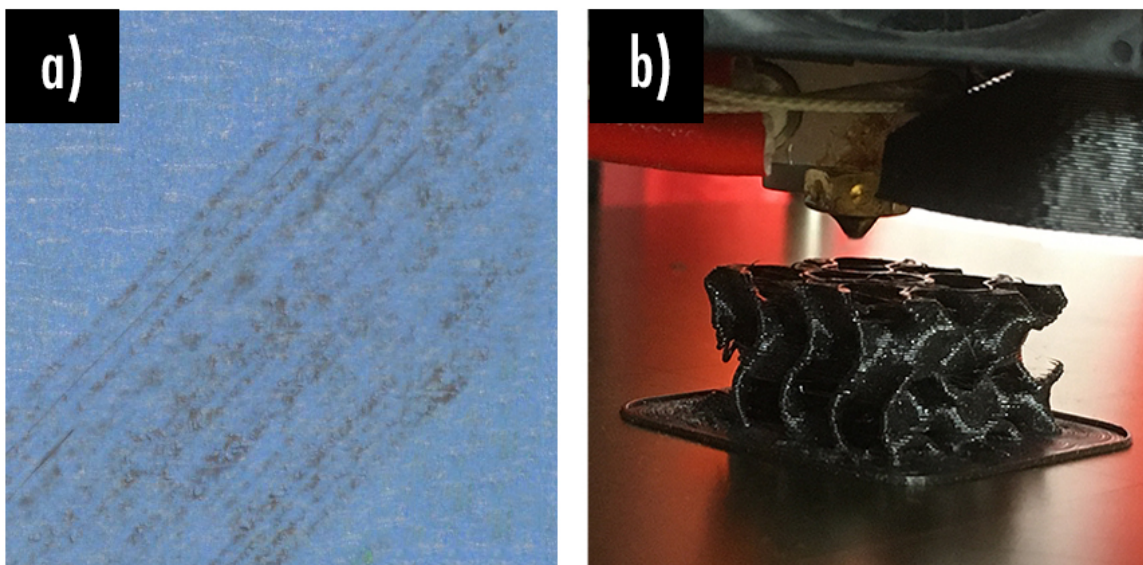


Figure 3.1. Extrusion issues: (a) at start; (b) in a middle of a print.

This major problem was caused by different identified phenomena (**Figure 3.2**). First of all, due to their brittle mechanical behavior, optimized highly loaded electrodes and current collector filament had tendency to break within the extruder gears (**Figure 3.2.b**), when the idler tensioner was too tight. Besides, due to its more flexible behavior, a buckling phenomenon¹ was occasionally witnessed while printing the optimized separator filament (**Figure 3.2.c**). This phenomenon is particularly amplified when the distance between the extruder and the nozzle is important. Hence, this gap must be reduced as small as possible or a guide system must be introduced. To prevent this issue, PEGDME500 ratio within the separator filament must be optimized in the future. In both cases (filament break or buckling), the nozzle was not fed correctly, thus leading to extrusion problems.

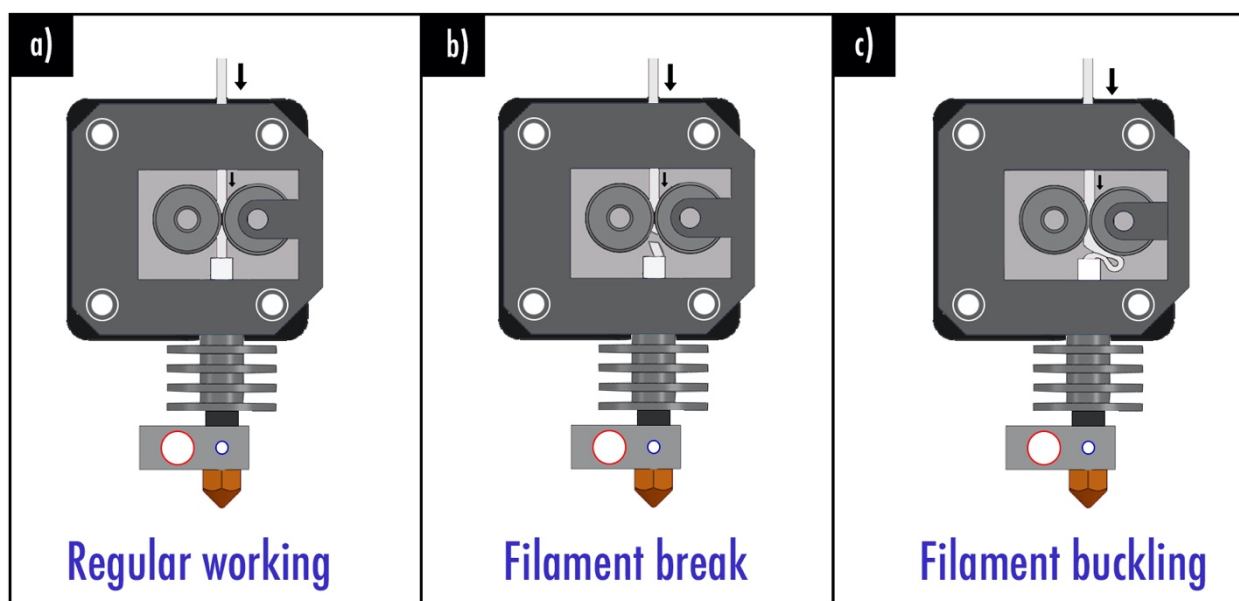


Figure 3.2. (a) Regular working process; Extrusion issues due to (b) filament break within the gears; (b) filament buckling phenomenon.

On the other hand, such concern may also be caused by the laboratory-made filaments usually depicting irregular diameter. If this latter is superior to 1.75 mm, the filament is not able to enter properly the nozzle inlet. The irregularity of the filament due to the notches on the surface can lead to a premature collapse (failure or buckling) of the filament. To resolve that particular issue in the future, a semi-industrial scale extrusion line including a diameter control sensor must be used.

Last but not least, this concern could also be related to a clogged nozzle.^{2, 3} Through printing, an accumulation of charges particles occasionally occurs within the nozzle head, thus blocking the 0.4 mm nozzle outlet. To avoid this annoying issue, charges particle size must definitely be considered when designing each composite filament. In order to fix this problem, the easiest method consisted in introducing an acupuncture needle while the nozzle temperature was fixed at high temperature of 260°C. Subsequently, a classical commercial filament was pushed manually through the extruder gears. In many cases, this trouble was resolved after both steps, without the necessity of replacing the nozzle.

3.2.2. Classical FDM issues

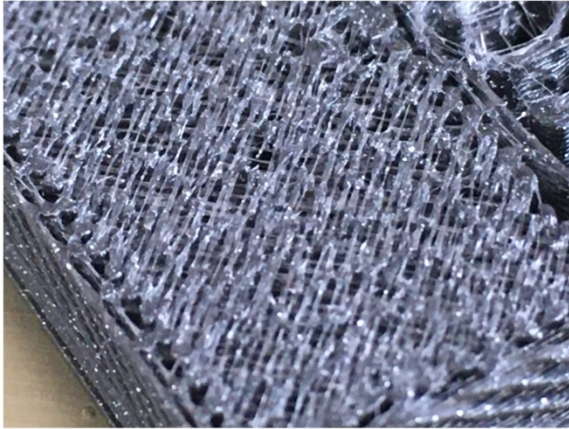
This section is now dedicated on the description of more classical FDM-related printing issues, that were also faced during this PhD thesis project.

3.2.2.1. Temperature issues

Printing temperature is a key-parameter to consider as it can lead to many undesired phenomena. Under-extrusion (**Figure 3.3**) was sometimes observed, due to a too low nozzle temperature, resulting in thin layers with unwanted gaps or in missing layers.⁴ It is however important to note that this phenomenon was sometimes caused by the too thin filament diameter which does not match the diameter set in the slicing software. As a consequence, the extruded amount of material is too low because of faulty slicer software settings. The opposite phenomenon called over-extrusion⁵ (**Figure 3.3**) was witnessed when a too high temperature was set in combination with an improperly set extrusion multiplier parameter.

On the other hand, overheating phenomenon was observed when cooling of the printed object was not done fast enough. By decreasing slightly the nozzle temperature and immediately cooling efficiently the deposited layers (fans power: 100%), overheating as well as other issues such as undesired stringing and poor bridging (**Figure 3.4**) can be avoided.

Under-extrusion



Over-extrusion

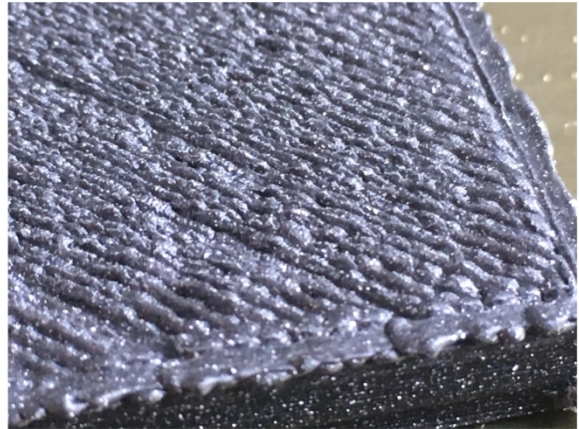


Figure 3.3. Temperature related issues: (left) under-extrusion; (right) over-extrusion.

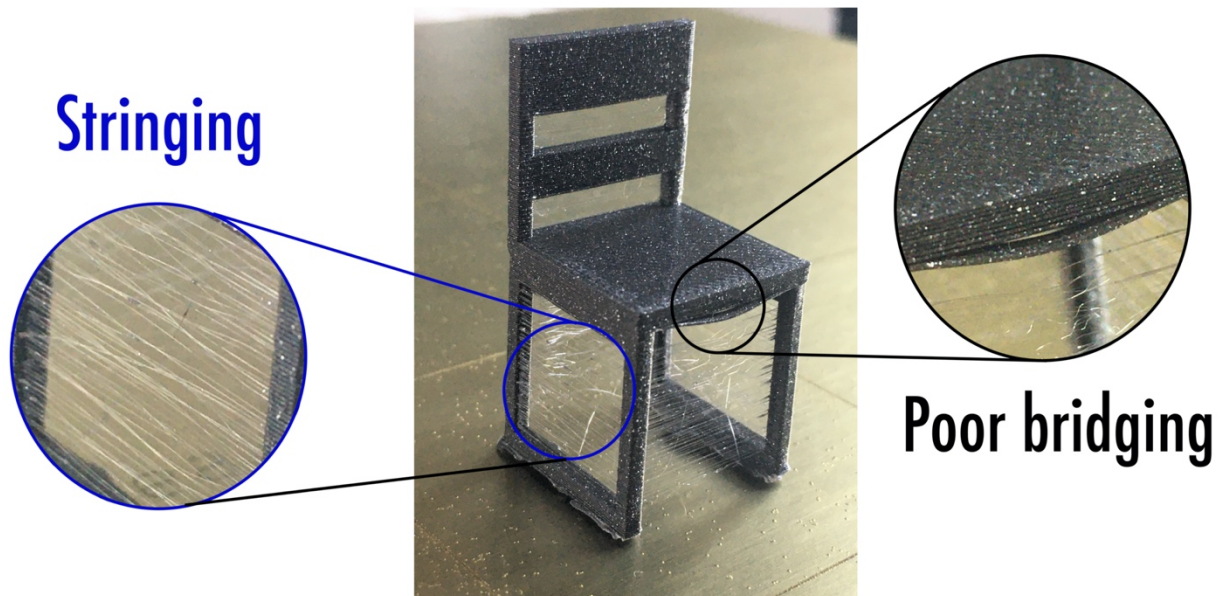


Figure 3.4. Temperature related issues: stringing and poor bridging phenomena.

Finally, it is worth mentioning that warping^{6, 7} (**Figure 3.5**) was witnessed during this project. It consists usually in a corner of a print that slightly lifts during printing due to material shrinkage upon cooling. While this phenomenon is usually common for amorphous polymer-based filament such as ABS, it was nonetheless occurring occasionally while printing semi-crystalline PLA-based filaments. It is worth-noting that this phenomenon tends to disappear by adjusting the build platform temperature to 60 °C for PLA-based filaments. Moreover, it was deduced that this phenomenon was less prone to occur with a higher loading of charges (active material, conductive additives, ceramic additives) exhibiting a relatively low expansion coefficient. An explanation is that they may counteract the shrinkage effect as these latter do not expand or contract with temperature changes.



Figure 3.5. Warping phenomenon.

3.2.2.2. Build platform level calibration related issues

To ensure a good adhesion to the build plate, the released material must be slightly squished against the build plate. Depending on the employed printer, this Z-axis first layer calibration (**Figure 3.6**) must be achieved manually or by adjusting hardware settings. A too high Z-axis first layer parameter will result in the first layer which does not stick to the bed resulting immediately in print failure. On the other hand, a too low Z-axis first layer parameter could either damage the extruder or the bed and here also lead in print failure.

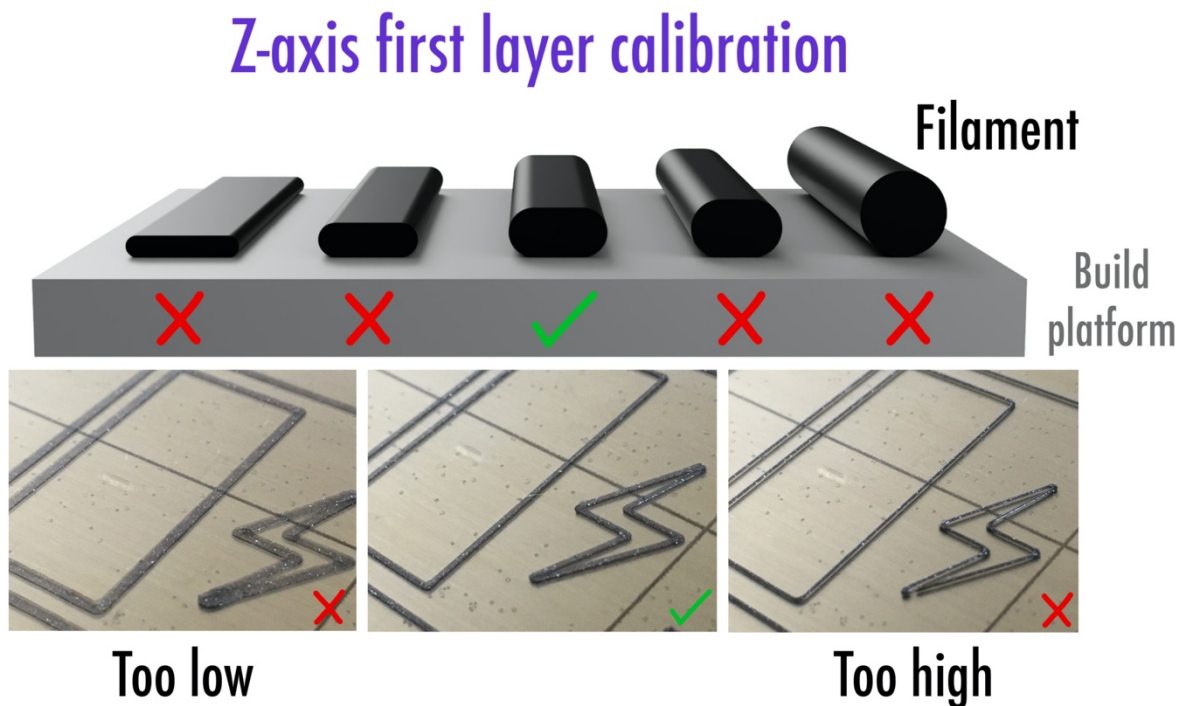


Figure 3.6. Z-axis first layer calibration.

3.2.3. 3D-printers related issues and optimization

Along this PhD thesis project, many different 3D printers were used (**Figure 3.7**). Unfortunately, some observed printing issues were directly linked to the type of printer that was employed.

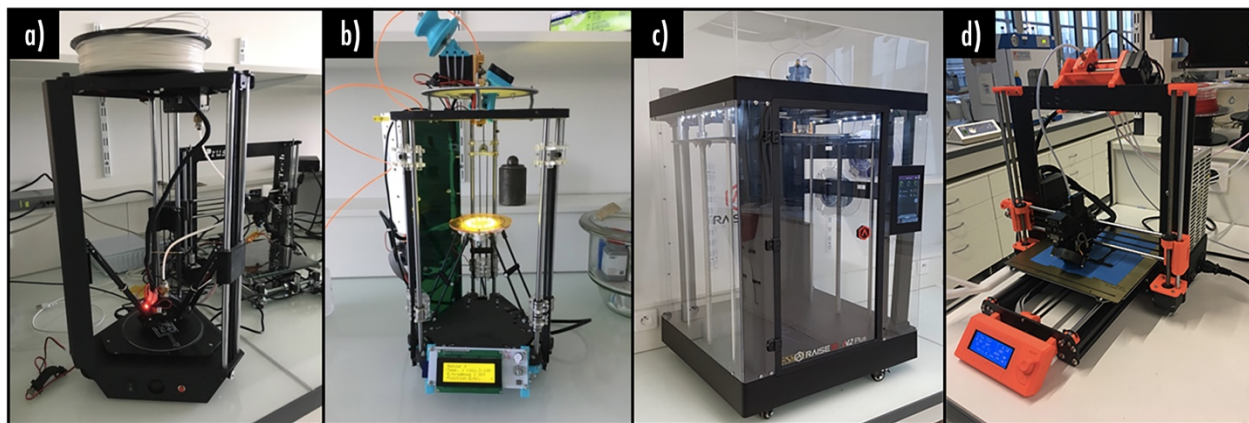


Figure 3.7. FDM 3D-printers employed during this project: (a) MicroDelta Rework; (b) Homemade Delta Printer; (c) Raise 3D Pro2 Plus; (d) Prusa MK3S.

At the very beginning of this project, a self-assembled Micro Delta Rework 3D printer (Emotion-tech, Toulouse, France) was employed (**Figure 3.7.a**). Unfortunately, due to its extruder motor which is not directly connected to the nozzle, filament must pass through a polytetrafluoroethylene pipe. Commercial pure polymer filaments can be printed easily but composite filament produced had tendency to broke inside the pipe due to the forces and vibrations applied while printing. This phenomenon being totally undesired, a second printer (homemade) specially conceived to print fragile composite filaments and based on the MicroDelta Rework architecture with some modifications, was used (**Figure 3.7.b**). In this configuration, nozzle position was kept fixed in a way that only bed is moving during printing. The extrusion motor was directly connected to the head of the nozzle, thus facilitating the insertion of the composite filament and its printing. Main drawback of this printer is its mechanical skeleton which was not perfectly symmetric leading to a non-horizontal bed during the printing. Calibration step which had to be done manually resulted, as a consequence, in a not perfectly precise machine. A third test was performed with an already built and commercially available Raise 3D Pro2 Plus (**Figure 3.7.c**).

Unfortunately, it immediately appeared that this machine was not adapted to print the highly loaded composite filaments. Indeed, dismantling the various parts of the printer to fix the several extrusion issues (cf. **3.2.1. Composite filament-related issues**) was a time-consuming and tedious process. Moreover, mechanical modifications of this printer were strictly limited.

Finally, it was decided to look for the cheapest (<\$1000) commercially available FDM 3D-printer presenting the advantages of being suitable for highly loaded composite filaments, presenting an automatic Z-axis first layer calibration, and easily dismantlable and modifiable. Produced by Prusa Research (Czech Republic), the Prusa MK3S (**Figure 3.7.d**) was thus definitively chosen for this project and self-assembled. Moreover, it is worth mentioning that this machine presents the advantage of using Bondtech Extruder Drive thus meaning that filament is driven from both sides. This feature is particularly imperative when printing of composite filaments is requested. This printer also comprises an aluminum magnetic and flexible bed as well as sensors to detect and recover the print in case of shifted layers or power loss. Last but not least, a multi-material option (cf. **3.4.2. Multi-materials FDM printing**), allowing the printability up to 5 filaments at the same time, is offered in option (\$360), thus making this printer very appealing while considering the further LIB FDM printing in one single step.

3.3. Complete LiFePO₄/graphite LIB 3D-printing

3.3.1. Cell assembly from independent 3D-printed components

3.3.1.1. Preliminary tests

Considering the electrodes and separator optimized filament compositions (**Table 3.1**), independent 200 μm -thick discs (11mm diameter) were 3D-printed independently. In order to investigate the resulting electrochemical performances of the assembled complete system, the different components were then gathered and stacked within a Swagelok-type cell. The latter was assembled in an argon filled glovebox ($\text{H}_2\text{O} < 0.1 \text{ ppm}$, $\text{O}_2 < 0.1 \text{ ppm}$). 150 μL of 1 M LiPF₆ in ethylene carbonate and diethyl carbonate (EC:DEC 1:1 weight ratio), purchased from Merck KGaA, Germany, was added in excess as liquid electrolyte (LP40). Subsequently, cells were galvanostatically discharged (lithiation) and charged (delithiation) at current density of 4.24 mA g⁻¹ (C/40) calculated per gram of active material, between 3.8 and 2.6 V (vs Li/Li⁺).

Capacity retention for the system is displayed in **Figure 3.8**. A very low reversible capacity value of about 12 mAh g⁻¹ of active material was obtained after 10 cycles at 4.25 mA g⁻¹ (C/40). Those poor performances are induced by the 3D-printer first layer thickness limitation as it is not possible to obtain <200 μm electrodes and separator. Thus, balancing of the cell was not possible. Last but not least, after being impregnated within the electrolyte during 1h, the system still displays an increasing capacity during the first cycles. This behavior is typical of non-sufficient electrolyte uptake and should be addressed.

LIB assembly from independent 3D-printed discs (optimized compositions)

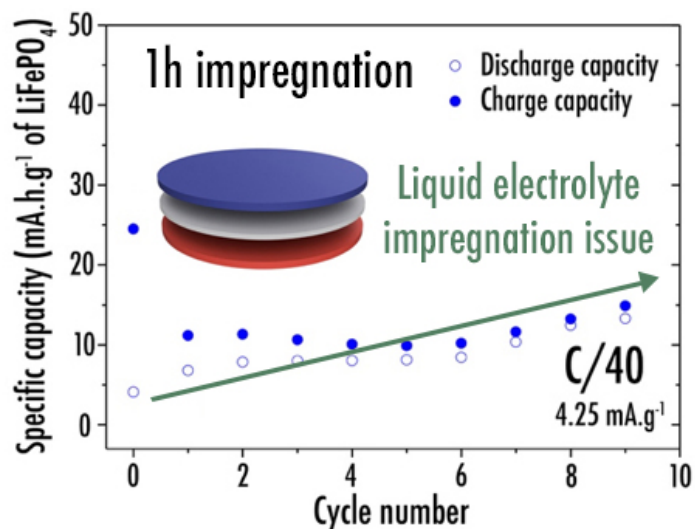
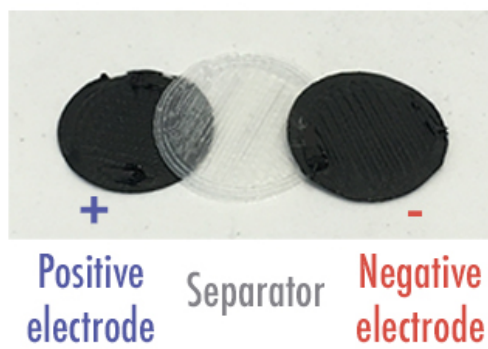


Figure 3.8. Capacity retention plot at 4.25 mA g⁻¹ (C/40) for the complete assembled battery after 1h impregnation within the liquid electrolyte. Independent discs (200µm thick) were 3D-printed from their respective optimized filaments compositions — cf. **Preface – II**.

3.3.1.2. Separator infill pattern

With a view to favor the liquid electrolyte uptake within the system, it was decided to take advantage of the new design capabilities conferred by 3D-printing. Indeed, various infill patterns^{8,9} (**Figure 3.9**) can be easily obtained (automatically generated) by using classic 3D-printing slicer software. One can easily understand that by 3D-printing the separator with an open-design pattern such as the Hilbert curves, Archimedean chords or Octogram spiral, the spread of liquid electrolyte compared to closed-designs (rectilinear, grid, triangle, stars, cubic, line, concentric, honeycomb and gyroid) will be favored. Here, in order to be able to further assemble the complete LIB (independent 3D-printed components), Archimedean chords pattern was chosen among the open-designs to print the separator as it is the only pattern that can be printed in one fragment and thus be manipulated.

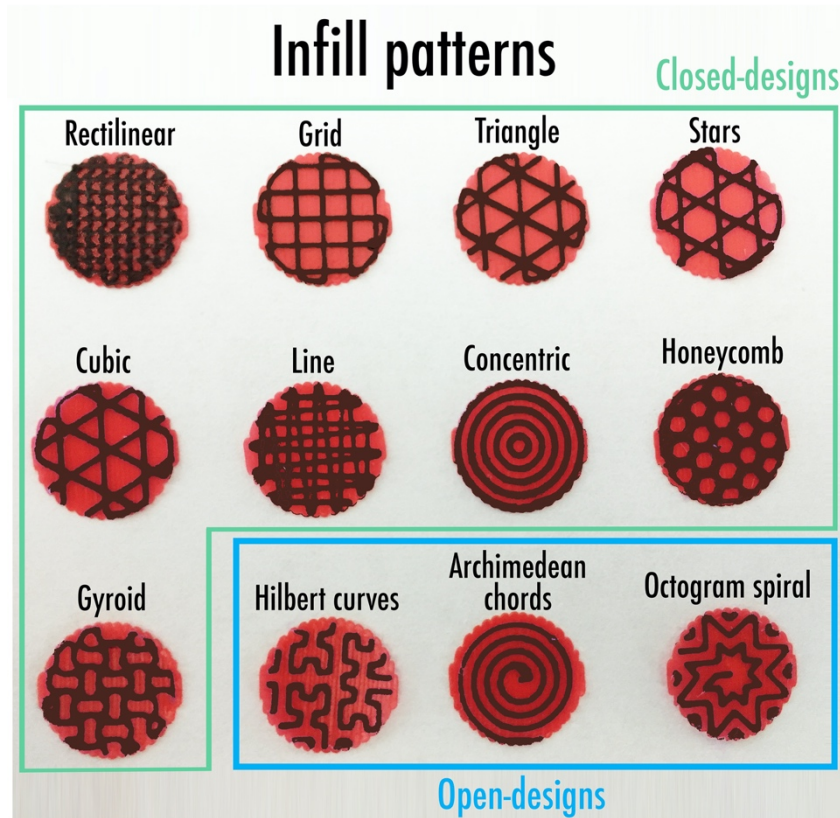


Figure 3.9. Various infill patterns (brown color) that can be obtained with classical 3D-printing slicer software. Here, a perimeter value of 0 and an arbitrary infill density value of 40% were set — cf. **Preface – II**.

On the other hand, the infill density must be set properly (measured in percent). Printing a separator with low infill density (**Figure 3.10**) will favor the electrolyte uptake while it will also favor short-circuits. Thus, a compromise must be reached.

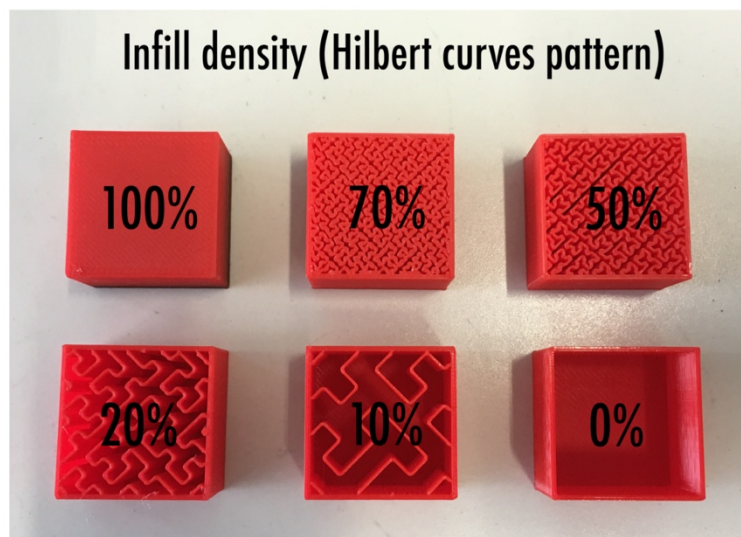


Figure 3.10. Various infill densities of the same infill pattern (Hilbert curves). Here, a perimeter value of 3 was arbitrary set — cf. **Preface – II**.

For the following experiments, infill density was set to 70% as it seemed enough, at first glance, to avoid short-circuits. An in-depth optimization of this parameter must nonetheless be investigated in the future. The perimeter setting, corresponding to the contour profile of the print, was fixed to 0 to enhance the electrolyte impregnation. Distinct from what was observed previously (cf. **3.3.1.1. Preliminary tests**) for the system using a full (100% infill density) separator disc, here, at the same current density of 4.25 mA g^{-1} ($C/40$), good capacity retention of 15 mAh g^{-1} was observed after 1h impregnation with the 70% Archimedean chords pattern for the separator as it enables faster liquid electrolyte uptake (**Figure 3.11**). Indeed, reversible capacity values are not increasing anymore during the first cycles. Electrochemical performances depicted for the assembled LIB are nonetheless still very low and could be enhanced in the future by overcoming the 3D-printer first layer thickness limitation.

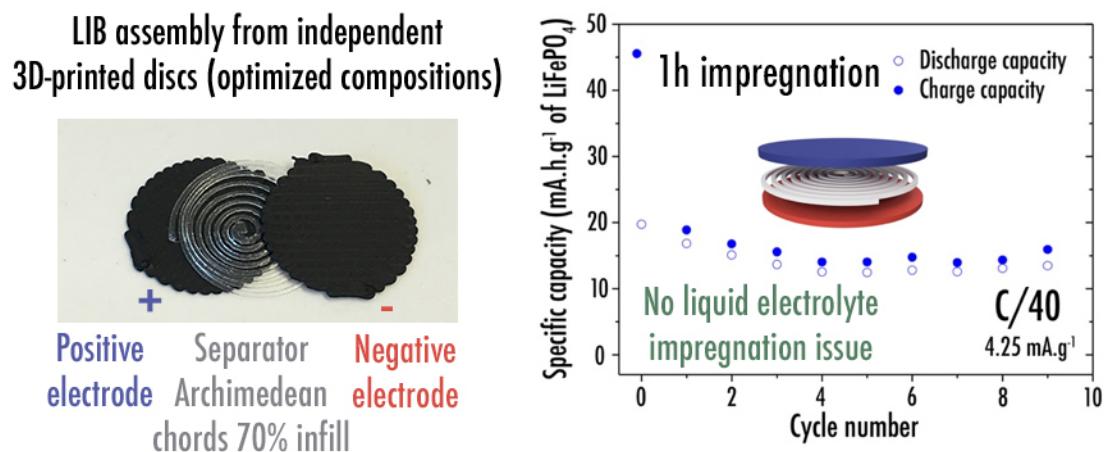


Figure 3.11. Capacity retention plot at 4.25 mA g⁻¹ (C/40) for the complete assembled battery after 1h impregnation within the liquid electrolyte. Independent components (200μm thick) were 3D-printed from their respective optimized filaments compositions — cf. **Preface – II**.

3.3.2. Cell 3D-printing in one-shot

3.3.2.1. Experimental procedure

The printability of a complete LFP/graphite LIB in a single print, referred to as “one-shot”, was successfully completed after a succession of numerous crucial technical steps. One after another, filaments (**Table 3.1**) were loaded, 3D-printed on top of the precedent layer, and unloaded by pausing the printer manually. Cleaning steps of the nozzle were unavoidable to ensure good homogeneity. These tedious steps might be simplified and automated in the future by using an adapted FDM 3D-printer equipped with a multi-materials option (cf. **3.4.2. Multi-materials FDM printing**). Complete lithium-ion batteries of any shape were thus easily printed as depicted in **Figure 3.12**. Each layer was printed and fused on top of the precedent to favor adhesion (**Figure 3.12.c**). Similarly, this particular methodology was also related by Reyes et al.¹⁰ who reported the printability of a complete LMO/LTO LIB in a single print, in September 2018.

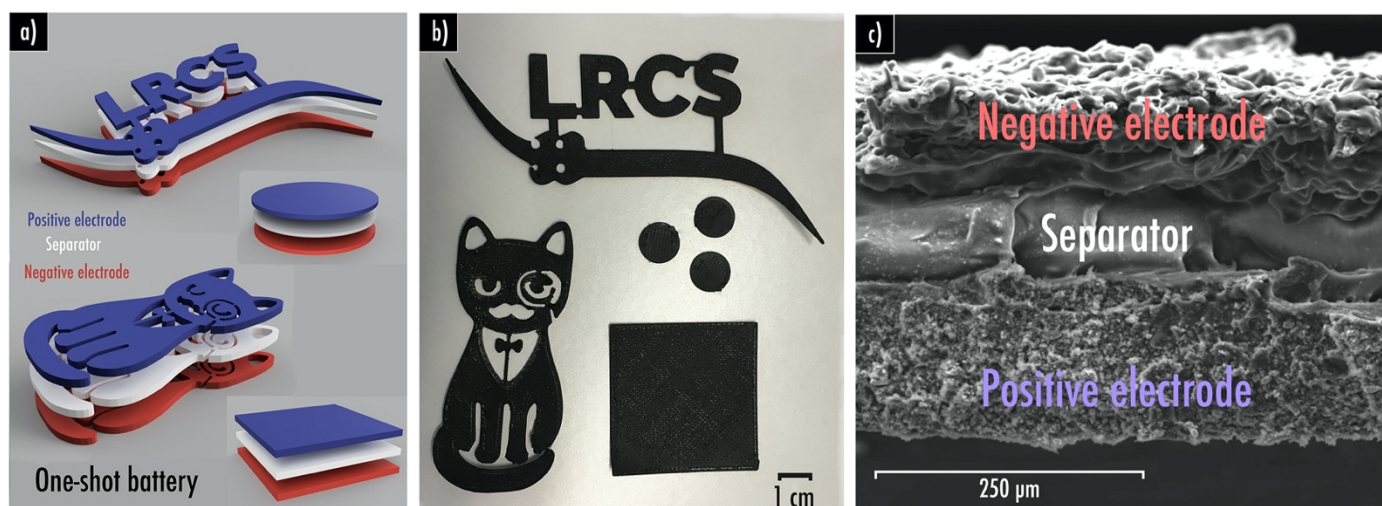


Figure 3.12. Complete LIB (a) Design; (b) 3D-printed in one-shot; and (c) cross-sectional SEM image. Note that sample was beforehand soaked and cut into liquid nitrogen — cf. **Preface – II**.

3.3.2.2. Preliminary cycling tests

Preliminary electrochemical tests were performed on the 3D-printed LIB disc (11mm diameter). The latter was inserted within a Swagelok-type cell assembled in an argon filled glovebox ($\text{H}_2\text{O} < 0.1$ ppm, $\text{O}_2 < 0.1$ ppm). 150 μL of 1 M LiPF_6 in ethylene carbonate and diethyl carbonate (EC:DEC 1:1 weight ratio) was her also used as liquid electrolyte (LP40). Subsequently, cells were galvanostatically discharged (lithiation) and charged (delithiation) at the same current density of 4.24 mA g^{-1} ($C/40$) calculated per gram of active material, between 3.8 and 2.6 V (vs Li/Li^+). Capacity retention for the system is displayed in **Figure 3.13**. A very low reversible capacity value of about 15 mAh g^{-1} of active material is displayed at 4.25 mA g^{-1} ($C/40$). At higher current densities of 8.5 ($C/20$) and 17 mAh g^{-1} ($C/10$), reversible capacities of 8 and 2 mAh g^{-1} are obtained. As it was previously observed for the assembled configuration (cf. **3.3.1. Cell assembly from independent 3D-printed components**), after being impregnated within the electrolyte during 1h, the one-shot system here investigated still displays an increasing capacity during the first cycles. Once again, this behavior is typical of non-sufficient electrolyte uptake and could be addressed by introducing a separator infill pattern.

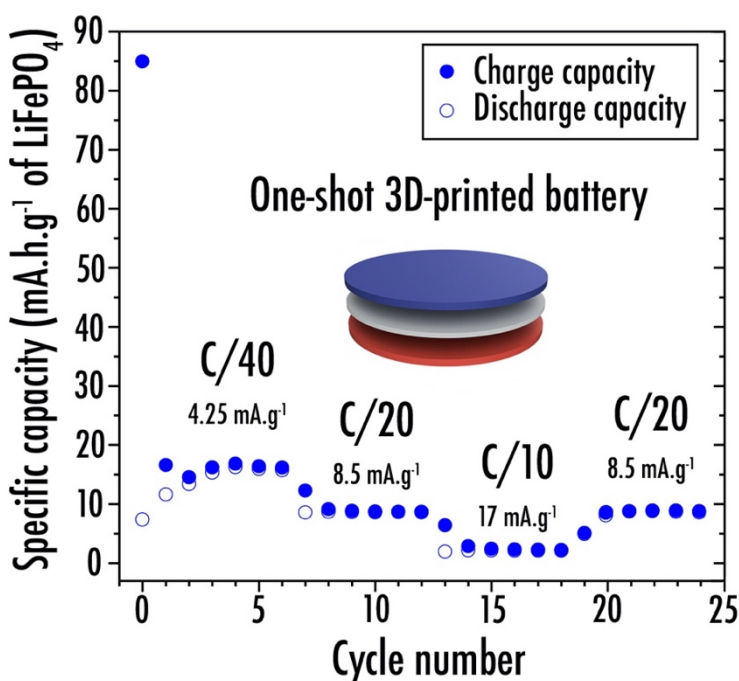


Figure 3.13. Capacity retention plot at various current density for the 3D-printed one-shot lithium-ion battery after 1h impregnation within the liquid electrolyte. Independent components (200 μm thick) were 3D-printed on top of each other from their respective optimized filaments compositions.

3.3.2.3. Separator infill pattern

Here again, in order to favor the liquid electrolyte uptake within the “printed in one-shot” system, we also decided to set an infill pattern for the separator. Among the open-designs (**Figure 3.9**), Hilbert curves seems to be the most promising as this is the only pattern enabling liquid electrolyte to enter using different paths. Indeed, Archimedean chords and Octogram spiral display only one entry for the electrolyte (considering a perimeter factor set to 0). Short-circuits are more complicated to avoid in the “one-shot” configuration as printing is performed at relatively high temperature of 195°C with this specific 3D-printer to prevent under-extrusion resulting in gaps or missing layers strongly prejudicing the print quality. Indeed, even with a 70% infill density separator (150 μm thick), the above layer corresponding to the positive electrode has tendency to collapse naturally by gravity to fill the gaps created by the separator pattern, thus leading to short-circuits. This phenomenon is easily observable by scanning electron microscopy (**Figure 3.14**).

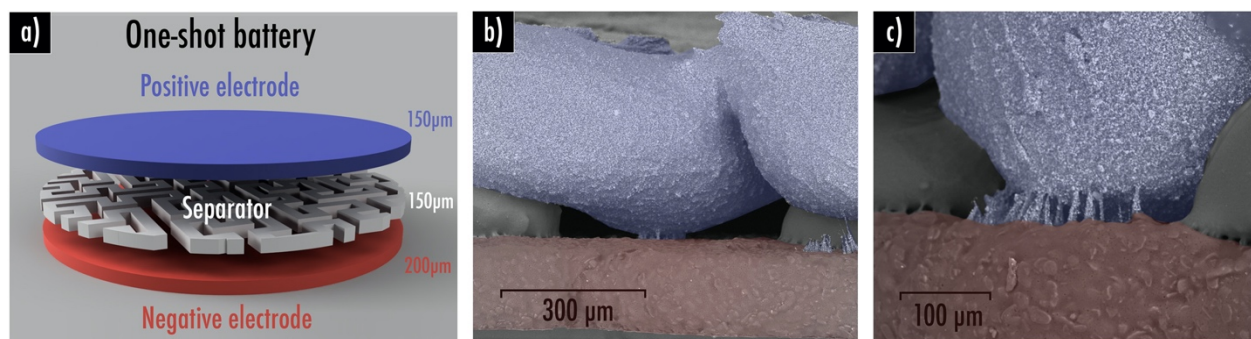


Figure 3.14. (a) Scheme of the 3D-printed in “one-shot” lithium-ion battery using Hilbert curves pattern 70% infill density as separator layer (150 μm thick). (b and c) Colored backscattered electron SEM images of the short-circuits observed within this system (positive electrode in blue, separator in grey, and negative electrode in red) — cf. **Preface – II**.

To prevent this behavior, it was decided to add a 100% infill density separator layer (100 μm) above the 70% infill density Hilbert curves pattern (50 μm) as displayed in **Figure 3.15**.

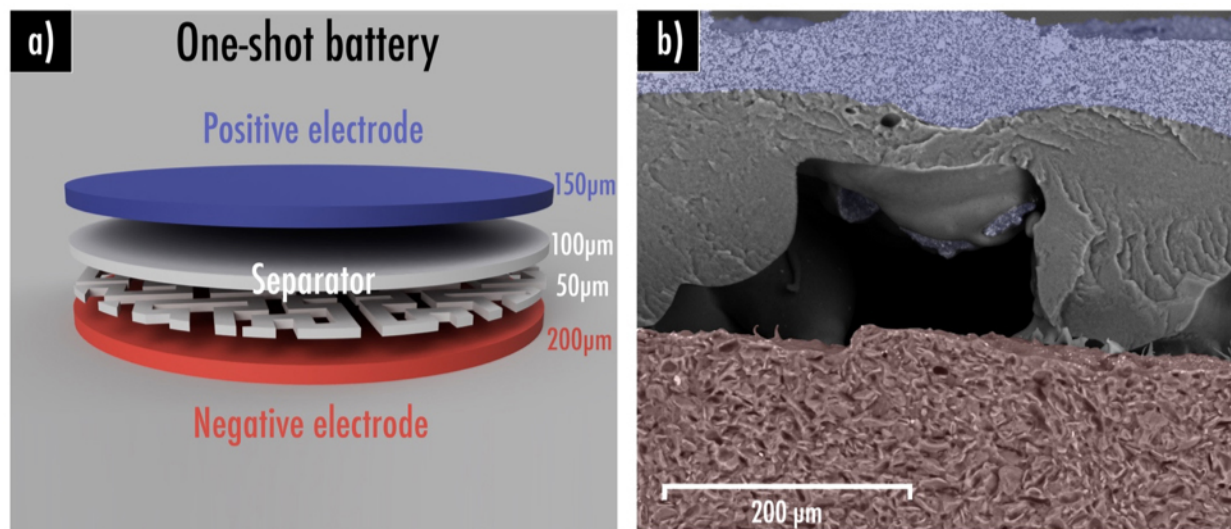


Figure 3.15. (a) Scheme of the 3D-printed in “one-shot” lithium-ion battery using Hilbert curves pattern 70% infill density as first separator layer (50 μm thick) and 100% infill density (100 μm thick) as second separator layer; (b) Backscattered electron SEM colored-image of the system (blue: positive electrode; red: negative electrode). Note that sample was beforehand soaked and cut into liquid nitrogen — cf. **Preface – II**.

Narrow caves created by the separator pattern can be observed by SEM/EDS (**Figures 3.15 and 3.16**). Ceiling of those cavities is homogeneously covered by a separator PLA-SiO₂ thin layer thus preventing any contact between both electrodes. Noteworthy that this uppermost separator layer might also prevent lithium dendrite propagation while subjected to improper cycling conditions as low temperature and high rate.

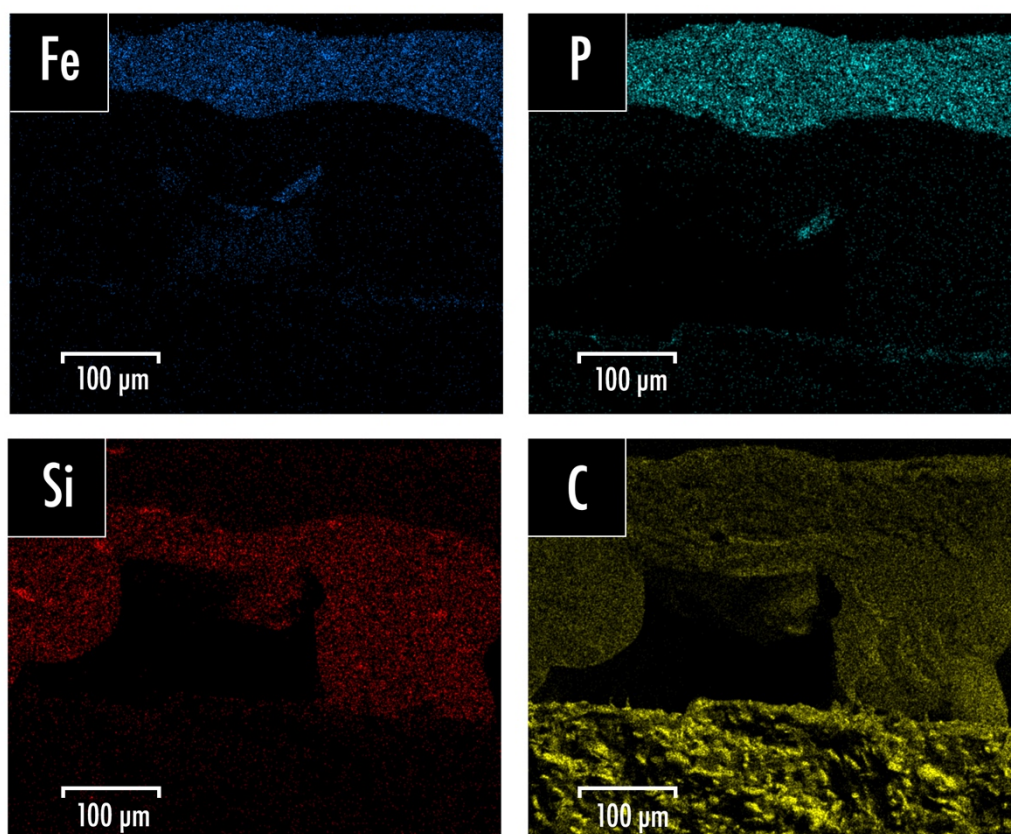


Figure 3.16. Element distribution map (Fe, P, Si, C) was obtained by Energy Dispersive X-ray Spectroscopy (EDS) — cf. Preface – II.

Figure 3.17 depicts the capacity retention plots at different C-rates for the one-shot fully 3D-printed disc system. In this configuration, as separator thickness diminution as well as balancing of the cell are now possible, slightly higher reversible capacity values were reached (30 mAh g⁻¹ of active material at C/40, corresponding to 15 mAh g⁻¹ of the total composite or also 6.5 mAh cm⁻³ considering both electrodes and separator total volume) compared to the assembled cell (15 mAh g⁻¹ of active material at C/40). Nonetheless, these values still remain very low because of the 200 μm first layer (here corresponding to the negative electrode) resolution limitation which was discussed previously (cf. **3.3.1.1. Preliminary tests**).

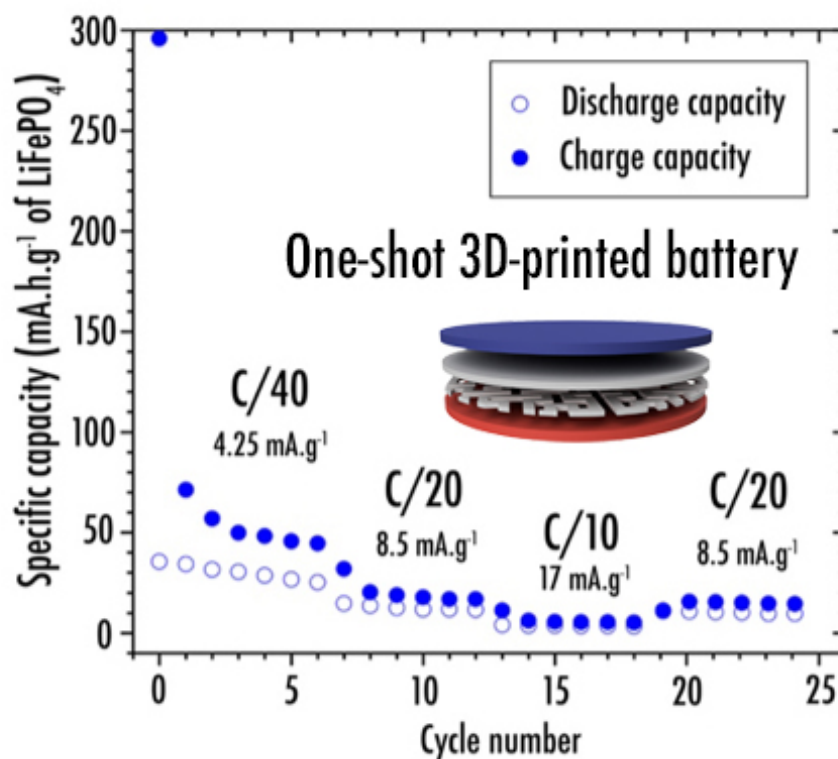


Figure 3.17. Capacity retention plot at various current density for the 3D-printed one-shot lithium-ion battery using Hilbert curves pattern 70% infill density as first separator layer (50 μm thick) and 100% infill density (100 μm thick) as second separator layer. Experiment was performed after 1h impregnation within the liquid electrolyte. Independent components (150μm thick positive electrode, 200μm thick negative electrode, and separator) were 3D-printed from their respective optimized filaments compositions — cf. **Preface – II**.

After cycling, it is worth mentioning that cracks were observed within the negative electrode layer (**Figure 3.18**). It is well known that the volume expansion $\Delta V/V$ is equal to the trace of the strain tensor $\Delta V/V = \text{Trace}(\epsilon) = 3 \cdot \epsilon_{xx}$ with ϵ_{xx} the extensional strain along the coordinate axis x equal to the two others under the assumption of isotropic swelling.¹¹ Knowing that graphite exhibits a volume expansion up to 10% when lithiated leading to a strain $\epsilon_{xx} \cong 3.3\%$, higher than the elongation at break closed to 3% obtained from the stress-strain curve of the negative electrode (cf. **2.2.1.3.1. Mechanical characterization and printability**). On the contrary, as expected, this phenomenon is not observed for the positive electrode as it starts to shrink because of the lithium departure upon first charge. Moreover, owing to the lower LFP particle size ($\sim 2 \mu\text{m}$), the elongation at break for the positive electrode (about 14%) was almost multiplied by 5 in comparison with the negative electrode containing graphite ($\sim 20 \mu\text{m}$). Hence, graphite granulometry could eventually be decreased to favor the particles dispersion within the polymer matrix, better accommodate the volume constraints and thus prevent cracks upon cycling.

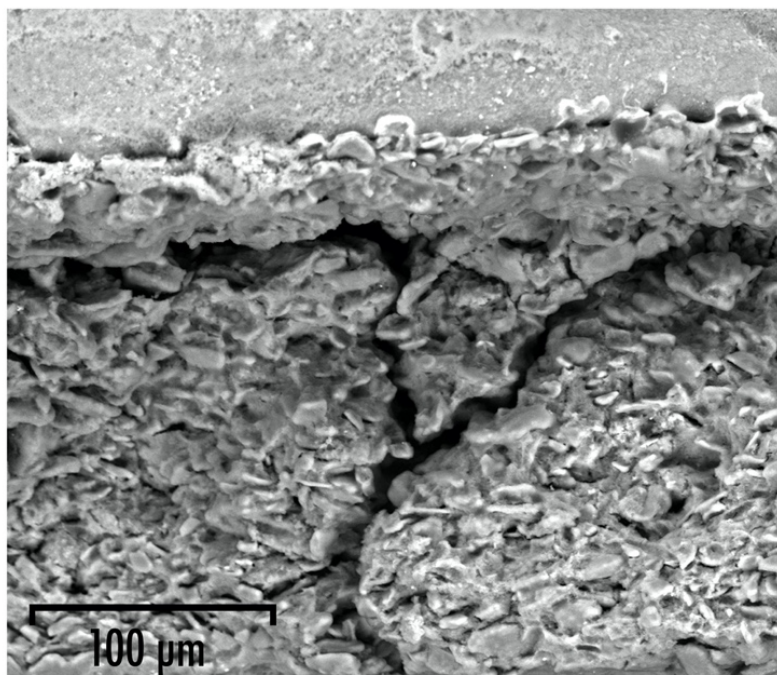


Figure 3.18. Backscattered electron SEM image of the cracks observed within the negative electrode after cycling — cf. Preface – II.

With the objective of improving the overall system, next step would be to use the future optimized current collector filament in order to print the first layer subjected to the 200 μm thickness limitation (**Figure 3.19**). Hence, it would be possible to print thinner (down to 50 μm) and balanced electrodes on top of it and thus further improve the electrochemical performances.

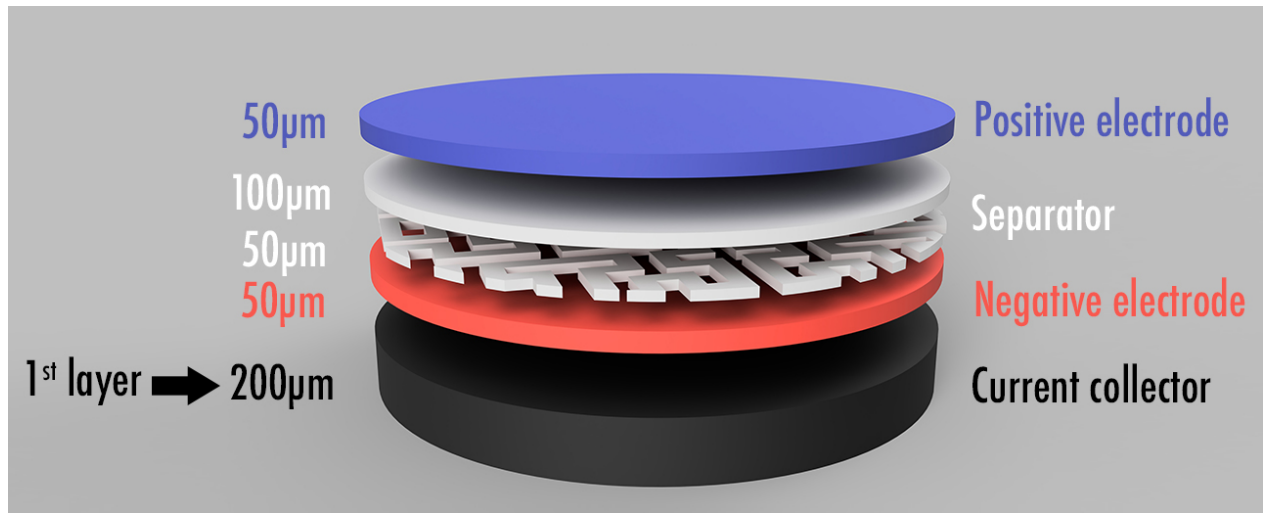


Figure 3.19. LIB system to consider in the future in order to overcome the first layer resolution limitation from the FDM 3D-printer.

3.4. Towards the printability of complex 3D LIB architectures

3.4.1. 3D architectures impact on electrochemical performances

The aim of this section is to evaluate the gain of performance of a LIB battery based on a 3D architecture. Hereafter, the influence of the various designs is evaluated by modeling the electrochemical behavior of a representative cell with the finite element method.

3.4.1.1. Introduction to the tested 3D architectures

Battery performances are usually defined by different characteristics such as the capacity Q (Ah), the energy W (Wh) and the power P (W). These values can be scaled as volumetric, areal, or gravimetric densities. To improve the performances of a battery for a given composition of the electrodes (amount of the active particles, porosity) and to find a tradeoff between power and energy, it is necessary to propose new designs by varying the shapes and the sizes of the electrodes and the volume fraction between the electrodes and electrolyte. It is well known that the key advantage associated with the 3D battery structures is the ability to achieve large areal energy capacities without making sacrifices in power density. This can be achieved with a high electrode area-to-volume ratio and short transport distances. It is worth noting that the improvement of the performances depends not only on these geometrical parameters but also on electronic conductivity of the electrode materials and the ionic conductivity of the electrodes and electrolyte. Long et al.¹² have given a classification of the different potential designs based on the diffusion path (1D, 2D and 3D). From a mathematical point of view, the diffusion path is generally 1D (normal to the surface) depending on the conductivity properties of the materials^{12, 13} (**Figure 3.20**).

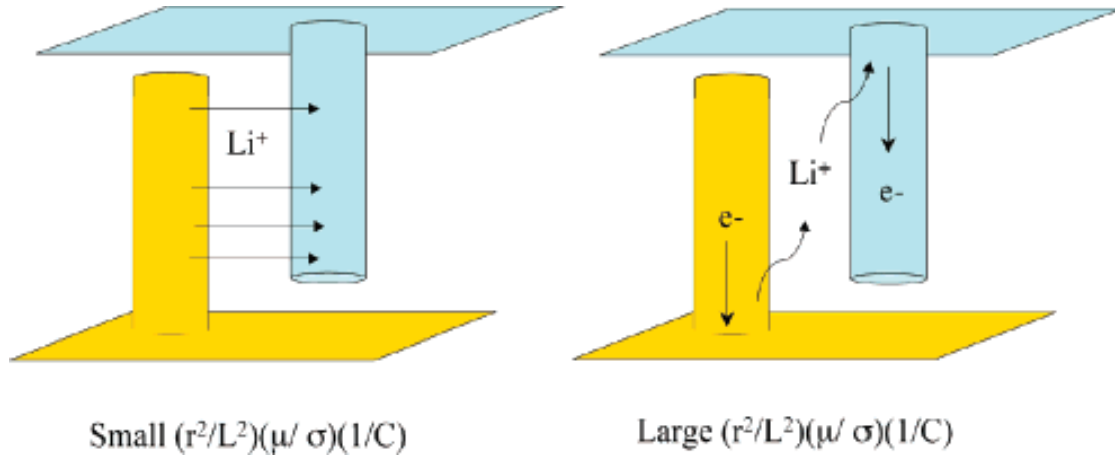


Figure 3.20. Diffusion path depending on the electrode geometry and conductivity properties of the active materials. Reproduced with permission from ¹². σ is the electronic conductivity of the electrode materials, μ is the ionic mobility of cations (Li^+), and C is the volumetric energy capacity (C/cm^3) and L and r are the length and radius of the electrodes, respectively. Copyright 2004 ACS.

In order to demonstrate the advantages of LIB 3D architectures, four types (**Figure 3.21**) of cubic periodic unit cells (PUC) were considered:

- Planar:** Interdigitated plate array of cathode and anode. Although this architecture is a 3D one, it will be classified as 1D because Li^+ ion diffusion occurs only in one direction perpendicular to the surfaces of the electrodes.
- Interdigitated:** Array of alternating cylindrical cathodes and anodes which is classified as 2D diffusion.
- Cube:** Two interlaced arrays of electrodes.¹⁴ In this case, ion diffusion is homogeneous and occurs in the 3 directions.
- Gyroid:** A double-gyroid cubic unit cell which is triply periodic.¹⁵ The interfaces are defined by the following double surface (**Equation 3.1**):

$$\sin\left(\frac{2\pi}{L_C}x\right)\cos\left(\frac{2\pi}{L_C}y\right) + \sin\left(\frac{2\pi}{L_C}y\right)\cos\left(\frac{2\pi}{L_C}z\right) + \sin\left(\frac{2\pi}{L_C}z\right)\cos\left(\frac{2\pi}{L_C}x\right) = \pm t \quad (\text{Equation 3.1})$$

With L_C , the cubic unit cell length and $0 < t \leq 1.413$.

The double-gyroid unit cells were generated with the help of Matlab software and specific available tools (isosurface, isocaps and stlwrite). For a given parameter t , the program provides the geometry (stl file), the volume and the surface of the electrodes and the electrolyte.

For each considered PUC, the type of diffusion path, the surface area (S_a), the volume (V_a) and the volume fraction (V_f) of the electrode but also the area-to-volume ratio S_a/V_a are given (Table 3.2).

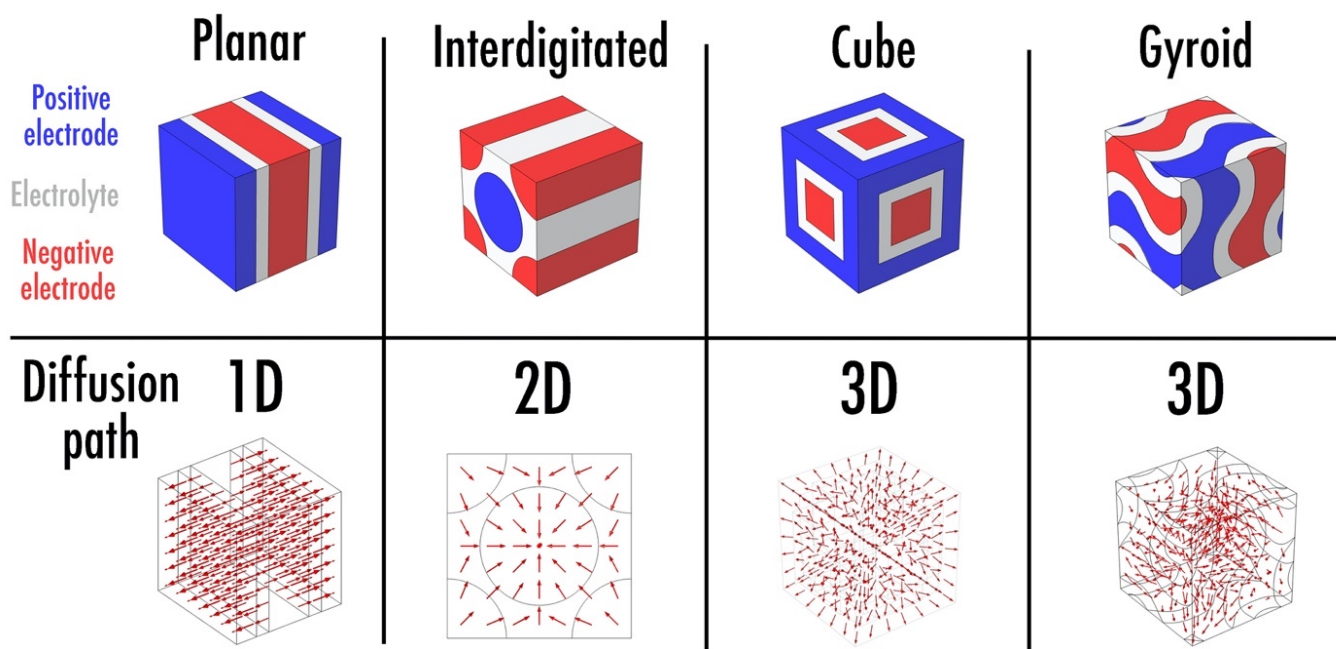


Figure 3.21. Summary of the investigated periodic unit cells and their respective Li^+ diffusion path. While commercial LIB consists in parallel plates (planar design), complex LIB architectures (interdigitated, cube, gyroid) could be obtained through additive manufacturing processes — cf. **Preface – IV**.

Table 3.2. Characteristics of the unit cells — cf. **Preface – IV**.

Type	Planar	Interdigitated	Cube	Gyroid
Surface Area S_a	$S_a = 2L_C^2$	$S_a = 2\pi aL_C$	$S_a = 12a(L_C - a)$	Depends on t
Electrode Volume V_a	$V_a = aL_C^2$	$V_a = \pi a^2L_C$	$V_a = 3a^2L_C - 2a^3$	Depends on t
S_a/V_a ratio	$S_a/V_a = \frac{2}{a}$	$S_a/V_a = \frac{2}{a}$	$S_a/V_a = \frac{12(L_C - a)}{3aL_C - 2a^2}$	Depends on t
Electrode Volume fraction V_f	$V_f = a/L_C$	$V_f = \pi a^2/L_C^2$	$V_f = \frac{3a^2L_C - 2a^3}{L_C^3}$	Depends on t (t=0.64 for $V_f=0.325$)

To respect balancing between anode and cathode, the volume of the electrodes is assumed to be equal (it is not a sine qua none condition), leading to the following cubic unit cell length (L_C) defined as $L_C = 2a + 2e$ where a and e are, respectively, the thickness of an electrode and the electrolyte (in the case of interdigitated cylindrical electrodes a is the radius of the electrode and $2e$ the smallest distance between two adjacent anodes or cathodes). As the performance of a battery depends on different parameters, several of them can be fixed by considering the same materials volume fractions across the unit cell (cathode/anode/electrolyte volume fractions equal to 0.325/0.325/0.35) and the same size of the unit cell ($L_C=300 \mu\text{m}$). With these parameters, the following area-to-volume ratios are obtained: $0.02 \mu\text{m}^{-1}$ for planar and interdigitated geometries and $0.029 \mu\text{m}^{-1}$ for cube and gyroid ones. For the two last geometries, the area-to-volume ratio is increased of 50%. The obtained gains on the area-to-volume ratio are different from the previous studies.^{12, 16} However, it is important to emphasize that, in comparison with literature where the considered unit cells are rectangular with different heights¹², rectangular for interdigitated geometry and cubic for the others¹⁶, here, only cubic ones were considered in this PhD thesis.

3.4.1.2. Theoretical models and assumptions

To evaluate the electrochemical performances (capacity, energy and power) of the different configurations, calculations are required. Due to the complexity of the geometry and the non-linear phenomena, these latter are usually achieved by means of numerical methods. The development of efficient model of simulating battery models is an active area of research and many researchers have published various mathematical techniques and methods physics-based to simulate the behavior of batteries.¹⁷ Mathematical models for lithium-ion batteries vary widely in terms of complexity, computational requirements, and reliability of their predictions (**Figure 3.22**). Including more detailed physicochemical phenomena in a battery model would improve its predictions while increasing considerably the computational requirements. Models for the prediction of battery performance can be roughly grouped into four categories: empirical models, electrochemical engineering models, multiphysics models, and molecular/atomistic models.¹⁷

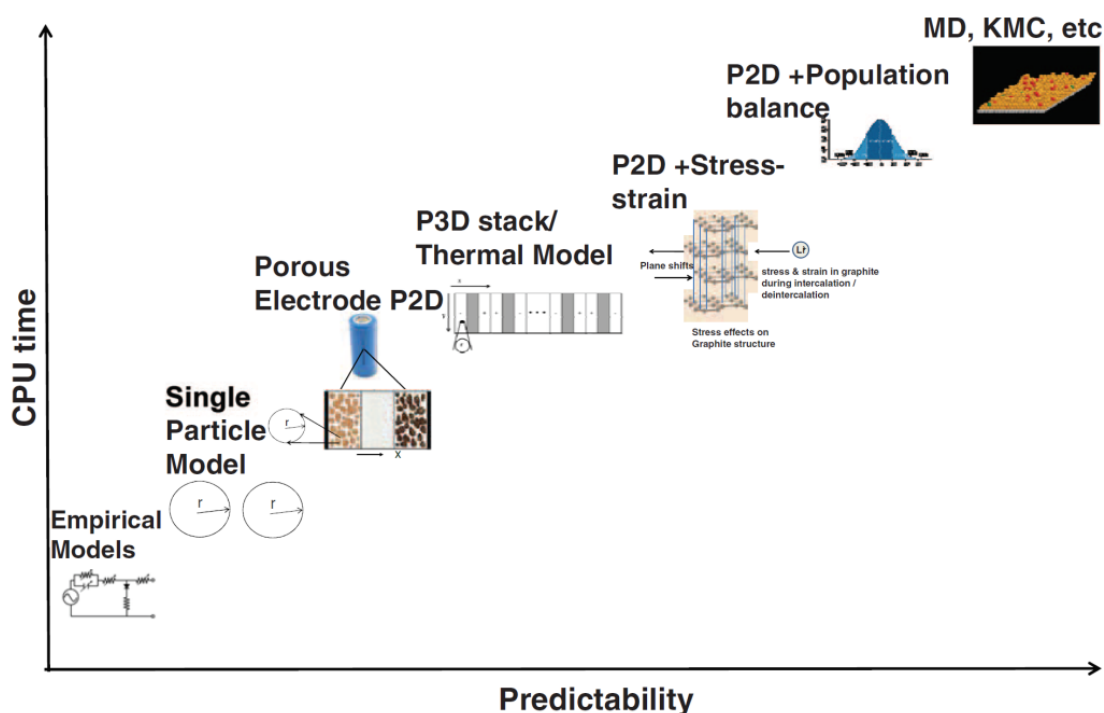


Figure 3.22. CPU time versus accuracy of the models. Reproduced with permission from ¹⁷. P2D = pseudo 2D model; P3D = pseudo 3D model ; MD = Molecular dynamics; KMC = Kinetic Monte Carlo. Copyright 2012 JES.

As the aim of this section was only focused on assessing the performance gain obtained with 3D architectures, an electrochemical engineering model, efficient enough but without leading to excessive CPU time, was thus selected. The retained model is based on a homogenized approach for describing porous electrodes,¹⁸ which solves simultaneously for the electrode phase and electrolyte phase potentials (**Equations 3.3 and 3.4**) in the same domain, and for defining the electrode reactions by the use of source terms (**Equation 3.6**). The macroscopic conductivity properties of the electrodes, called effective conductivities, are defined from the porosity and the conductivity properties of the active materials with the help of Bruggeman relation for spherical particles which is efficient enough for our study.¹⁹ The diffusivity is treated similarly. The lithium diffusion into the solid electrode particles is modeled with the Fick's law and by the use of an extra dimension, representing an average particle for a certain position in the electrode (**Equation 3.4**).²⁰ Other models consider electrodes as non-porous and Li^+ insertion is described by the boundary conditions, not as source term, resulting in a slightly modified mathematical description.^{13, 16} The equations governing the physical phenomena and the assumptions are summarized in **Table 3.3**.

To solve these equations, Comsol Multiphysics 5.5 finite element software was used. To study the unit cell discharge behavior, a generalized α -integrator in conjunction with PARDISO solver was employed to solve time-dependent matrix equation. The relative and absolute tolerances were equal to 0.001. Following the applied C-rate, a different maximum time step was applied (automatic one for C-rates less than 1 and 1s for C-rates higher than 1). The geometries were discretized automatically using a physics-controlled mesh with normal size leading to approximately 80,000 quadratic second order tetrahedral elements and 10,500 triangular elements for the interfaces. Calculations were performed on a Dell Workstation equipped with 32 cores on Intel Xeon 5680 processors and a memory of 64 Gb.

Table 3.3. Electrochemical model equations — cf. **Preface – IV.**

Governing Equations	Hypotheses
<p>Conservation of Li⁺ species for a binary salt concentrated electrolyte</p> $\varepsilon_m \frac{\partial c_l}{\partial t} = D_{eff,m} \nabla^2 c_l + (1 - t_+) j_m \quad (\text{Equation 3.2})$ <p>$m = p \text{ or } n \text{ or } s$ (p=positive, n=negative, s=separator)</p>	<ul style="list-style-type: none"> • Solvent velocity equals to zero • Constant transport properties • Constant porosity • Structural properties-porosity and tortuosity integrated in $D_{eff,m} = D_e \varepsilon_m^{1.5}$ (Bruggeman relation)
<p>Charge conservation in solution (electrolyte phase)</p> $\nabla \cdot (-\kappa_{eff,m} \nabla \Phi_l + \kappa_{D,m} \nabla \ln c_l) = F j_m \quad (\text{Equation 3.3})$ <p>With $\kappa_{D,m}$ diffusional conductivity $\kappa_{D,m} = \frac{2\kappa_{eff} RT}{F} (1 - t_+)$</p>	<ul style="list-style-type: none"> • Structural properties-porosity and tortuosity integrated in $\kappa_{eff,m} = \kappa \varepsilon_m^{1.5}$ (Bruggeman relation) • No reaction in the separator
<p>Potential distribution in solid phase</p> $\sigma_{eff,m} \nabla^2 \Phi_s = F j_m \quad (\text{Equation 3.4})$	<ul style="list-style-type: none"> • Structural properties-porosity integrated in $\sigma_{eff,m} = \sigma_s \varepsilon_m$
<p>Conservation of Li⁺ species in solid phase</p> $\frac{\partial c_s}{\partial t} = \frac{1}{r} \frac{\partial}{\partial r} \left(D_m r \frac{\partial c_s}{\partial r} \right) \quad (\text{Equation 3.5})$	<ul style="list-style-type: none"> • Spherical particles with a radius of 1 μm • Uniform size and distribution of particles
<p>Reaction rate at the surface of particles (Butler-Volmer equation)</p> $j_m = j_{0m} \left(\exp\left(\frac{\alpha_n F}{RT} (\Phi_s - \Phi_l - U)\right) - \exp\left(\frac{\alpha_p F}{RT} (\Phi_s - \Phi_l - U)\right) \right) \quad (\text{Equation 3.6})$	

3.4.1.3. Finite element model

The LiFePO₄-graphite system studied in this PhD thesis was here considered. The materials properties and geometrical parameters required for the modeling are reported in **Table 3.4**. Some data are extracted from the literature^{21, 22} and others are adjusted. The porosities and the active material volume fractions were here collected from the aforementioned parts focused on the FDM 3D-printing of electrodes (**Table 3.1**). The initial state of charges (SOCs) were defined considering a charge balance between the cathode and the anode thanks to the following **Equation 3.7**:

$$Q_m = \varepsilon_{am} F V_m c_{s,m,max} |y_{100\%} - y_{0\%}| \quad (\text{Equation 3.7})$$

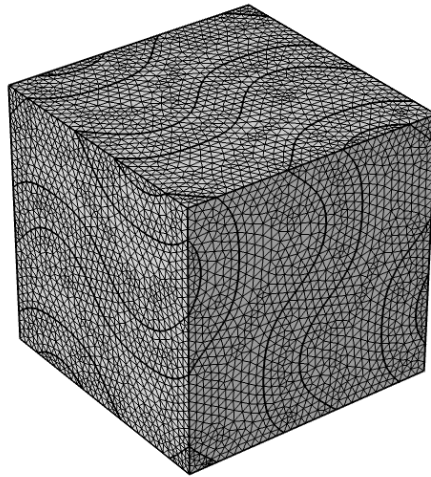
Where m is p or n for, respectively, the *positive* and *negative* electrode. Q_m is the capacity, V_m the electrode volume, $c_{s,m,max}$ the maximum concentration of lithium in the solid phase and $y_{100\%}$ the stoichiometry at 100% SOC. This leads to a nominal capacity Q of 1.9 μAh .

Table 3.4. Design parameters (for $V_f=0.325$) and materials properties — cf. **Preface – IV**.

	Parameter	Symbol	Unit	Positive electrode	Separator	Negative electrode
Design specifications	Electrode feature	a	μm	97.5/96/114*		97.5/96/114*
	Electrolyte feature	e	μm		52.5/54/36*	
	Porosity	ε_m		0.2	0.3	0.2
	Active material volume fraction	ε_{am}		0.4		0.4
Solid and electrolyte phase Li^+ concentration	Maximum solid phase concentration	$c_{s,max}$	mol/m^3	22806		31450
	Initial SOC	SOC _m		0.012		0.477
	Average electrolyte concentration	c_l	mol/m^3		1000	
Kinetic and transport properties	Exchange current density	j_{om}	A/m^2	$5e^{-2}$		0.5
	Charge transfer coefficient	α_m		0.5		0.5
	Li transport number	t_+			0.363	
	Solid phase Li diffusion	D_s	m^2/s	$3.2e^{-13}$		$1.6e^{-14}$
	Electrolyte phase Li^+ diffusion	D_e	m^2/s		$5e^{-10}$	
	Ionic conductivity of electrolyte	κ	S/m		1.3	

* corresponds to the values for planar/interdigitated/cube geometries. The dimensions are not uniform for gyroid geometry.

To investigate the rate capability, the cell was discharged from its fully charged state. This was done for different current loads, defined in terms of C-rate with 1C being the current load to discharge a fully charged battery completely in 1 hour. For a $1.9 \mu\text{Ah}$ cell, 1C is thus equal to $1.9 \mu\text{A}$. The current is applied on a surface of the positive electrode current collector and mass on the negative electrode current collector while periodic boundary conditions are applied on the other surfaces. To impose these boundary conditions, it requires a periodic mesh, where the opposite faces are meshed identically (**Figure 3.23**).


Figure 3.23. Triply periodic mesh of the gyroid geometry with 104,600 tetrahedral elements.

3.4.1.4. Results and discussion

The solving of equations described in **Table 3.3** gives access to the potentials ϕ_s and ϕ_l respectively in the electrodes and the electrolyte and also the respective concentrations in lithium cations c_s and c_l . **Figure 3.24** displays the evolution of Li^+ in the solid phases (electrodes) for the gyroid geometry. A high gradient of lithium ions concentration occurs in the negative electrode during the discharge process. Knowing these quantities, other data can be evaluated such as the density and the power of the cell by post-treatment. The energy is calculated according to the following **Equation 3.8**:

$$W = \int_0^t (I \cdot E_{\text{cell}}) dt \quad (\text{Equation 3.8})$$

where I is the applied current and E_{cell} the cell voltage. The power is computed by dividing the energy with the discharge time which is here the time to reach a cut-off voltage of 2.6V.

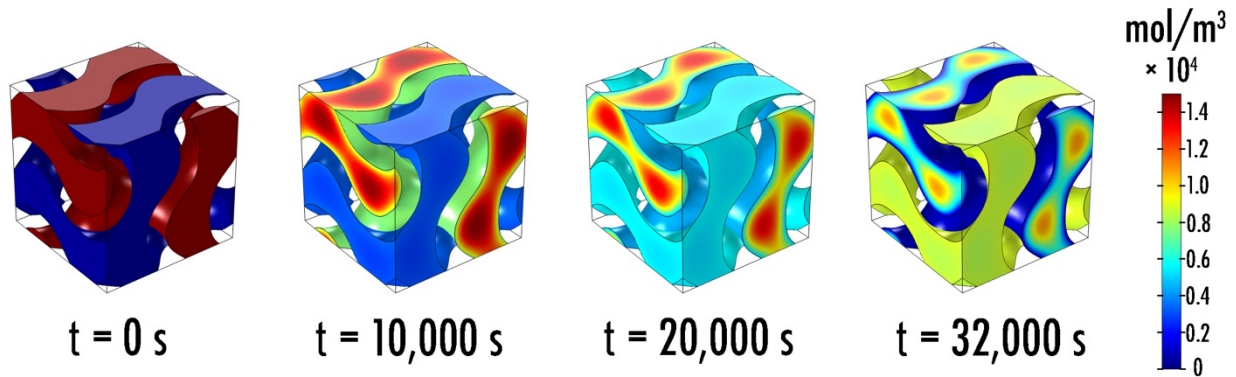


Figure 3.24. Negative and positive electrodes lithium concentration (mol/m^3) during discharge with a C-rate of $C/20$.

To compare the performances of the different architectures, 13 calculations at different applied discharge current loads corresponding to C-rates from 0.05C to 20C were performed, leading to a total of 52 simulations. Subsequently, a Ragone plot, exhibiting the energy versus the power, was generated (**Figure 3.25**).

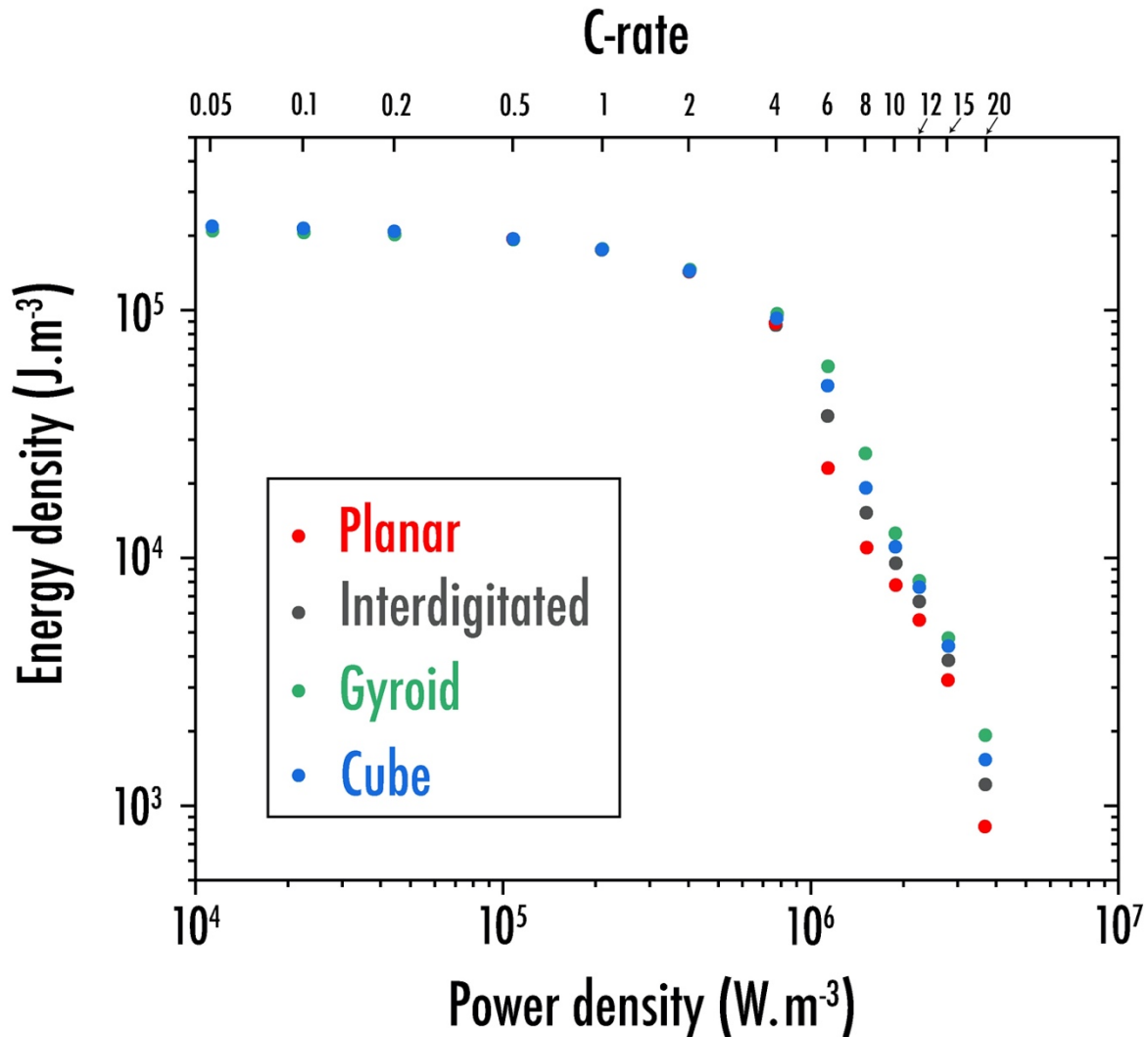


Figure 3.25. Ragone plot for all the geometries at different C-rate — cf. Preface – IV.

With increased energy output, less power is obtained and vice versa. Clearly, it appears that the shape of the Ragone plot is altered by the battery design. For low C-rate current loads ($< 4C$), all the geometries display very closed behavior. At higher C-rates, best performances are achieved with the 3D gyroid architecture while the 1D planar depicts the worst. The effect on a multiaxial diffusion path can be underlined by comparing energy density for planar and interdigitated geometries for which the S_a/V_a ratio is equal (Table 3.2) The same remark can be done by comparing the results for interlaced cube and gyroid for which we have the same area-to-volume ratio. It can be observed that the performances between the geometries are not proportional to the

applied C-rates. Compared to planar geometry, gyroid and cube respectively exhibit significantly improved energies of +158% and +115% at a current density of 6C, and +134% and +86% at 20C (Table 3.5).

Table 3.5. Energy density improvement (%) for the different geometries compared to planar one — cf. Preface – IV.

C-rate	Interdigitated	Cube	Gyroid
C/20	0.0%	0.0%	-4.2%
C/10	0.0%	0.0%	-3.8%
C/5	0.0%	0.1%	-3.0%
C/2	-0.1%	0.1%	-0.7%
C	-0.3%	0.2%	0.5%
2C	-0.5%	0.3%	1.4%
4C	-1.9%	4.4%	9.0%
6C	62.4%	115.1%	158.2%
8C	38.0%	73.8%	139.7%
10C	22.6%	42.7%	61.4%
12C	18.6%	35.4%	43.8%
15C	19.7%	37.3%	47.4%
20C	48.1%	86.5%	134.2%

The drop of the energy for a C-rate of 6C can be explained by the shape of the discharge profiles (Figure 3.26). At this particular current density, the shapes of the curves for the considered geometries are different (this is due to a higher gradient of concentration for planar geometry than for the other ones) although at 10C, the shapes of the curves are identical. Despite its better performance, gyroid geometry is more complex to print for small unit cell size. Interlaced cube geometry seems to be a good compromise between both electrochemical performances and printability parameters.

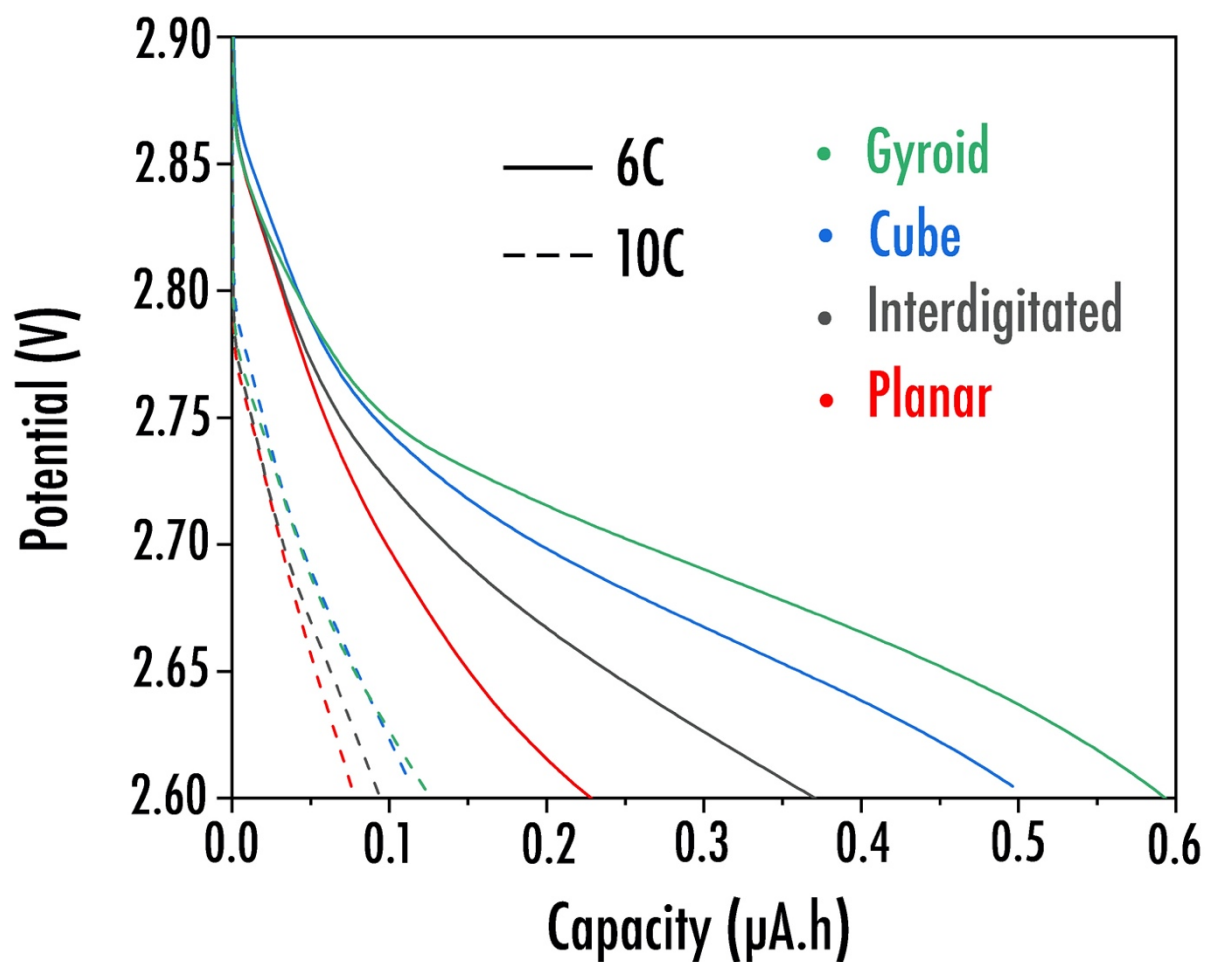


Figure 3.26. Discharge profiles for all the LIB geometries, at 6C and 10C current densities — cf. Preface – IV.

The ultimate goal of this project being the printability of the complete lithium-ion battery in one single step, the multi-material printing abilities for the FDM process must be examined.

3.4.2. Multi-materials FDM printing

3.4.2.1. Commercially available options comparison

FDM printing already offers many different multi-material commercial options with a view to print these complete LIB complex architectures in one single step (**Figure 3.27** and **Table 3.6**).

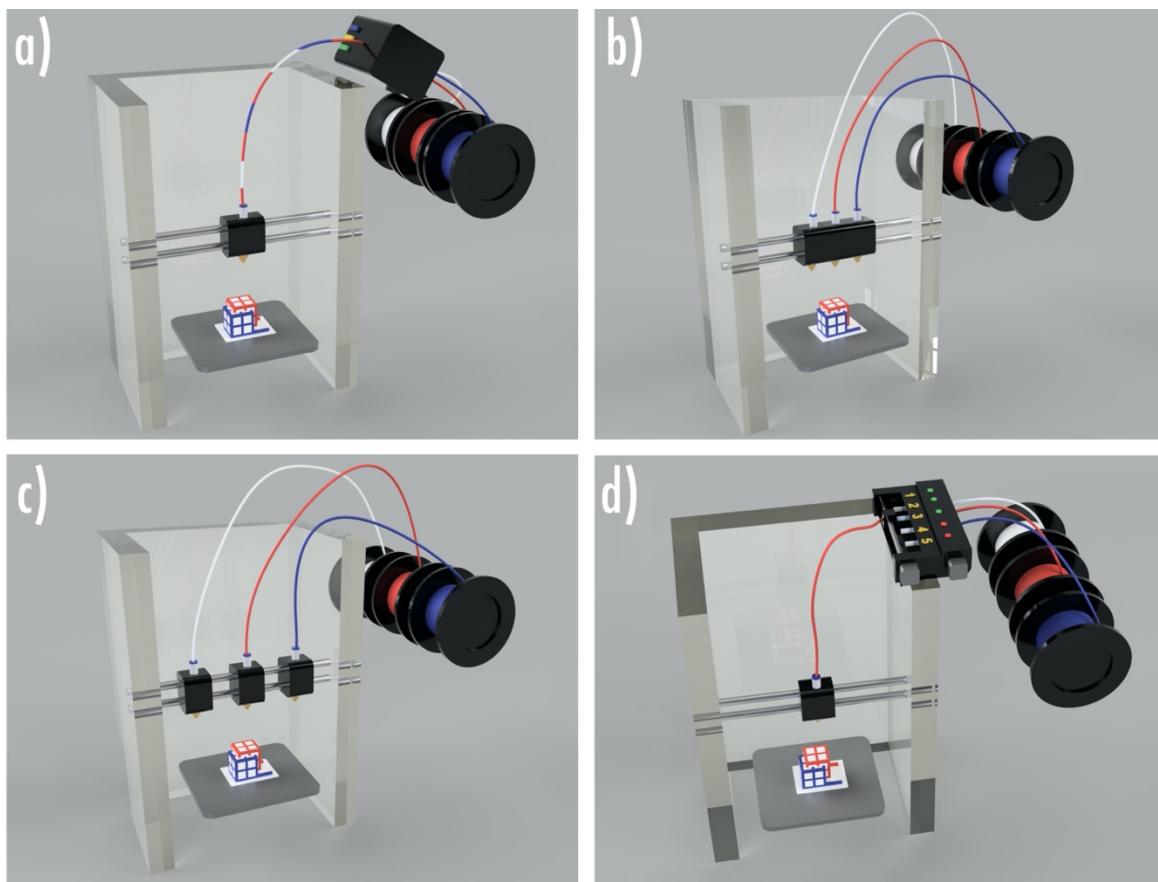


Figure 3.27. Scheme depicting the commercially available FDM multi-materials options: (a) Monofilament multi-materials; (b) Multi dependent extruder-heads; (c) Multi independent extruder-heads; (d) Mono extruder multifilament. — cf. **Preface – IV**.

The Canadian company Mosaic Manufacturing, founded in 2014, created Palette2S, additional box, in which up to four filaments can be combined together in order to create a single monofilament that will be used to feed the printer (**Figure 3.27.a**). While this process works well to even combine different types of materials together, such as PLA or PETG, the ability to combine

very brittle composite filaments such as the one developed to print the Li-ion battery electrodes makes it very challenging to overcome.

Another offered option (**Figure 3.27.b**) includes many extruder-heads placed on the same X-axis carriage. Nozzles are thus not free to move independently. First issue regarding this option is based on the nozzles temperature control. Indeed, when considering the LIB complete printing, it is important to emphasize that printing temperature for each filament will be different and thus nozzles temperature needs to be thoroughly controlled independently. Imagining that this problem could be easily resolved by tuning the printer firmware, another concern pops up: the retraction parameter. Indeed, filament leftovers generally come out from the nozzle when the latter is not printing. This is really problematic when the LIB printing is considered as it may result immediately in short-circuits if leftovers from the negative electrode filament are in contact with the positive one.

Third option involves the use of independent nozzles (**Figure 3.27.c**). While dual independent extruders already exist and can be found widely in the market, the ability to have more than 2 nozzles is not widely established for now due to the complexity to control their movement and temperature independently. Moreover, very often, this option involves independent extruders that are placed on the same X-axis thus reducing considerably the printing area. A solution would be to have all-axis-independent extruders that could be placed in mechanically controlled arms; Unfortunately, this option still remains too expensive.

Finally, last option to print the complete LIB via FDM was developed by the Czech company Prusa Research. Their option called MMU2S is based on an additional device (**Figure 3.27.d**), placed on the top of the printer, that will act as filament selector. A motor operates an idler and selects the bearing that will engage the drive gear to push the filament. A second motor rotates all of the drive gears. At any given time, only one of them pushes the filament further, depending on the idler rotation. The third motor moves the filament selector so only one of the five filaments is sent to the extruder. A mechanical P.I.N.D.A probe used as filament sensor is used during each filament change to detect proper filament load and unload. The filament gets pushed by the Bondtech gears and reaches the nozzle. This option seems to be the most promising to entirely print the future all solid-state lithium-ion battery in one single step as its main advantage is that only one nozzle is used. Moreover, unlike the others options involving many nozzles, the calibration on the

Z axis is here relatively easy to perform. To deal with the material transition after filament change, an almost hollow purge tower is built in a corner of the bed. This unfortunately still creates material waste that developers are trying to reduce. Last but not least, this option remains relatively cheap as the printer equipped with the MMU2S option costs about 1,000\$.

Table 3.6. Summary of the commercially available FDM multi-materials options.

Technology	Product designation	Company	Price (€)
Monofilament multi-materials	Palette 2s	Mosaic Manufacturing	<1000
Multi dependent extruder-heads (at least 3 heads)	Hydra 16 A	Hyrel 3D	27 000
Multi independent extruder-heads	S 600D	Lynxter	36 000
	Multirap M500	Multec	46 000
	3Dn-Quad-Head	Nscrypt	280 000
Mono extruder multifilament	MMU2S	Prusa	<1000

3.4.2.2. First tests

After installing the multi-material option (MMU2S, Prusa Research) on top of the 3D-printer and performing the challenging but required calibration, printability of the electrochemically promising complex LIB 3D-structures such as the interpenetrated cube lattices (cf. **3.4.1. 3D architectures impact on electrochemical performances**) was explored (**Figure 3.28**). So far, first tests were only performed using commercially available pure PLA filaments. In the future, blue, red and white PLA filaments (**Figure 3.28**) are envisioned to be replaced by the optimized filaments for the positive, negative electrode and separator respectively. Moreover, parts corresponding to the current collector must be integrated to the system design. It is important to note that each component must be added separately as a .stl file within the slicer software. Hence, the final structure presenting 3 different filaments in its core, was beforehand composed of 3 independent .stl files. As mentioned earlier (cf. **3.4.2.1. Commercially available options comparison**), a purge tower is built in a corner of the bed to allow the material transition after filament change. This procedure should considerably limit the short-circuits when considering the LIB printing.

Multi-materials FDM printing of 3D-complex structure Preliminary tests were performed using commercial pure PLA filaments

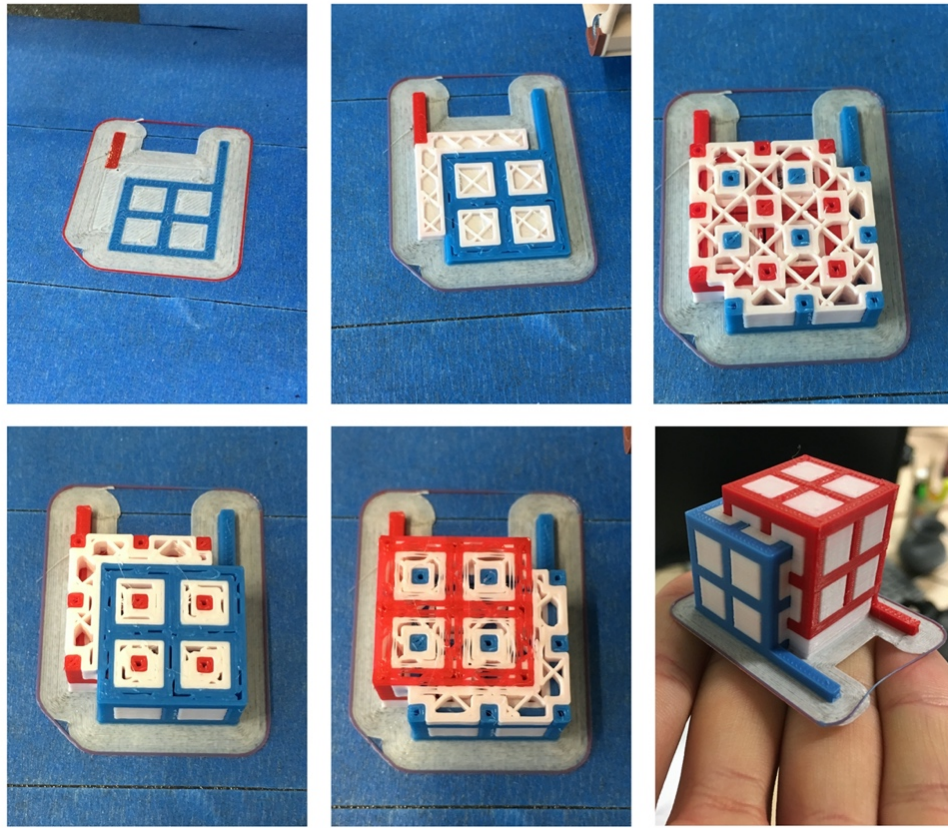


Figure 3.28. Multi-materials FDM 3D-printing of an interpenetrated cube lattices structure that it is envisaged for further LIB printing. Note that here, the infill density was set to only 10% in order to allow a better visibility.

While this option seems very promising to envision the future printability of a complete LIB complex design in one-shot, some technical concerns still need to be addressed. So far, even printability of commercial pure polymer filaments still remains highly demanding as portrayed by various experimented users in various 3D-printing forum on the internet. This system (**Figure 3.29**) being very recent (first MMU version launched in 2017), it obviously still requires some adjustments from the manufacturer. Hence, when considering the multi-material printability of highly loaded composite filaments for LIB (cf. **Chapter 2**), one can easily understand that in-depth machine and firmware modifications are first required with a view to facilitate their printability. As an example, the presence of polytetrafluoroethylene tubes, used to guide the filaments to the nozzle, must be avoided. These latter are inducing vibrations and composite filaments have

tendency to break during printing as depicted beforehand (cf. **3.2.3. 3D-printers related issues and optimization**). On the other hand, the rotation speed of the gears, both within the multi-material system and within the nozzle, must be decreased considerably and perfectly synchronized to reduce forces induced onto the filament resulting in cracks and breaks.

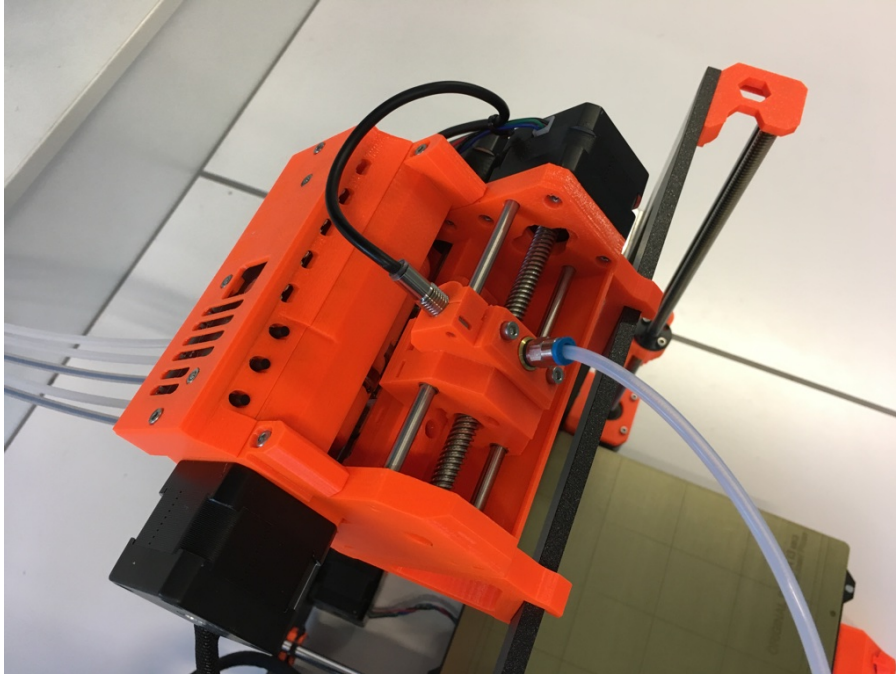


Figure 3.29. Multi-materials FDM 3D-printing option used during this project. Up to 5 different filaments can be printed inserted in the device.

Conclusions

This chapter was dedicated to the 3D-printing of a complete lithium-ion battery cell based on a liquid electrolyte technology, starting from the afore-optimized filaments compositions (cf. **Chapter 2**).

First of all, printability issues were identified and fixed mostly through the use of an adapted 3D-printer being suitable for highly loaded composite filaments, presenting an automatic Z-axis first layer calibration, and easily dismantlable and modifiable. By means of this later, LIB assembly (stacking) from independent 3D-printed components (electrodes and separator) as well as the direct printing of the complete LIB in a single step (one-shot) was performed. Separator infill patterns and density were tuned to improve the liquid electrolyte impregnation and avoid short-circuits. While electrochemical performances of the complete cells are still relatively limited, the complete LIB FDM 3D-printing proof of concept was demonstrated.

To go further, future research may be devoted on decreasing the graphite granulometry to favor the particles dispersion within the polymer matrix, better accommodate the volume constraints through an improved elongation at break and thus prevent cracks upon cycling within the negative electrode. The impact of the particle size on electrochemical and mechanical performances must be investigated thoroughly. Nozzle clogging concern must be overcome thanks to this adjustment. On the other hand, with the aim of improving the overall LIB electrochemical performances, next step would be to use the optimized current collector filament to print the first layer subjected to the 200 μm thickness limitation. Hence, this will allow printability of thinner (down to 50 μm) and balanced electrodes on top of it. Finally, an optimization of the liquid electrolyte (solvents) must be performed in order to favor its impregnation within the separator.

Last but not least, by performing an in-depth modeling study, the electrochemical ability of various complex 3D LIB architectures, in comparison with classical 2D planar design, was investigated. Clearly, it appears that the electrochemical performances of the complete battery in terms of power can be improved with 3D architectures. Here, it is important to emphasize that the simulations were restricted to cubic unit cell with theoretical geometric parameters. Further investigations are now required to compare and validate the model with experimental results

obtained from these 3D designs. Subsequently, their optimization from the geometrical and material point of view must be considered. The printing capability in one-shot of such complex 3D architectures was then considered by means of multi-materials printing options. Preliminary printing tests were thus performed using commercial filaments. Important machine and firmware modifications are now required to allow multi-material printing of highly loaded composite filaments.

References

1. Kumar, N.; Jain, P. K.; Tandon, P.; Pandey, P. M., Extrusion-based additive manufacturing process for producing flexible parts. *Journal of the Brazilian Society of Mechanical Sciences and Engineering* **2018**, 40, (3), 12.
2. Tekinalp, H. L.; Kunc, V.; Velez-Garcia, G. M.; Duty, C. E.; Love, L. J.; Naskar, A. K.; Blue, C. A.; Ozcan, S., Highly oriented carbon fiber-polymer composites via additive manufacturing. *Composites Science and Technology* **2014**, 105, 144-150.
3. Patanwala, H. S.; Hong, D. T.; Vora, S. R.; Bognet, B.; Ma, A. W. K., The microstructure and mechanical properties of 3D printed carbon nanotube-poly(lactic acid) composites. *Polymer Composites* **2018**, 39, E1060-E1071.
4. Tanikella, N. G.; Wittbrodt, B.; Pearce, J. M., Tensile strength of commercial polymer materials for fused filament fabrication 3D printing. *Additive Manufacturing* **2017**, 15, 40-47.
5. Comminal, R.; Serdeczny, M. P.; Pedersen, D. B.; Spangenberg, J., Motion planning and numerical simulation of material deposition at corners in extrusion additive manufacturing. *Additive Manufacturing* **2019**, 29, 17.
6. Wu, W. Z.; Geng, P.; Zhao, J.; Zhang, Y.; Rosen, D. W.; Zhang, H. B., Manufacture and thermal deformation analysis of semicrystalline polymer polyether ether ketone by 3D printing. *Materials Research Innovations* **2014**, 18, 12-16.
7. Ligon, S. C.; Liska, R.; Stampfl, J.; Gurr, M.; Mulhaupt, R., Polymers for 3D Printing and Customized Additive Manufacturing. *Chemical Reviews* **2017**, 117, (15), 10212-10290.
8. Fernandez-Vicente, M.; Calle, W.; Ferrandiz, S.; Conejero, A., Effect of Infill Parameters on Tensile Mechanical Behavior in Desktop 3D Printing. *3d Printing and Additive Manufacturing* **2016**, 3, (3), 183-192.
9. Mantihal, S.; Prakash, S.; Bhandari, B., Textural modification of 3D printed dark chocolate by varying internal infill structure. *Food Research International* **2019**, 121, 648-657.
10. Reyes, C.; Somogyi, R.; Niu, S.; Cruz, M. A.; Yang, F.; Catenacci, M. J.; Rhodes, C. P.; Wiley, B. J., Three-Dimensional Printing of a Complete Lithium Ion Battery with Fused Filament Fabrication. *ACS Applied Energy Materials* **2018**, 1, (10), 5268-5279.
11. Gould, P. L., *Introduction to linear elasticity*. 2013; p 1-346.
12. Long, J. W.; Dunn, B.; Rolison, D. R.; White, H. S., Three-dimensional battery architectures. *Chemical Reviews* **2004**, 104, (10), 4463-4492.

13. Zadin, V.; Kasemagi, H.; Aabloo, A.; Brandell, D., Modelling electrode material utilization in the trench model 3D-microbattery by finite element analysis. *Journal of Power Sources* **2010**, 195, (18), 6218-6224.
14. Ragonés, H.; Menkin, S.; Kamir, Y.; Gladkikh, A.; Mukra, T.; Kosa, G.; Golodnitsky, D., Towards smart free form-factor 3D printable batteries. *Sustainable Energy & Fuels* **2018**, 2, (7), 1542-1549.
15. Scherer, M. R. J., Double-Gyroid-Structured functional materials: synthesis and applications. In Springer Science & Business Media: 2013.
16. Trembacki, B.; Duoss, E.; Oxberry, G.; Stadermann, M.; Murthy, J., Mesoscale Electrochemical Performance Simulation of 3D Interpenetrating Lithium-Ion Battery Electrodes. *Journal of the Electrochemical Society* **2019**, 166, (6), A923-A934.
17. Ramadesigan, V.; Northrop, P. W. C.; De, S.; Santhanagopalan, S.; Braatz, R. D.; Subramanian, V. R., Modeling and Simulation of Lithium-Ion Batteries from a Systems Engineering Perspective. *Journal of the Electrochemical Society* **2012**, 159, (3), R31-R45.
18. Newman, J.; Tiedemann, W., Porous-electrode theory with battery applications. *AIChE Journal* **1975**, 21, (1), 25-41.
19. Chung, D. W.; Ebner, M.; Ely, D. R.; Wood, V.; Garcia, R. E., Validity of the Bruggeman relation for porous electrodes. *Modelling and Simulation in Materials Science and Engineering* **2013**, 21, (7).
20. Doyle, M.; Fuller, T. F.; Newman, J., Modeling of galvanostatic charge and discharge of the lithium polymer insertion cell. *Journal of the Electrochemical Society* **1993**, 140, (6), 1526-1533.
21. Prada, E.; Di Domenico, D.; Creff, Y.; Bernard, J.; Sauvant-Moynot, V.; Huet, F., Simplified Electrochemical and Thermal Model of LiFePO₄-Graphite Li-Ion Batteries for Fast Charge Applications. *Journal of the Electrochemical Society* **2012**, 159, (9), A1508-A1519.
22. Taleghani, S. T. Modélisation et simulation des piles aux lithium ions. University of Sherbrooke, Canada, 2019.

Chapter 4.

**Solid polymer electrolyte filament
elaboration for LIB 3D-printing via
fused deposition modeling**

Chapter 4. Solid polymer electrolyte filament elaboration for LIB 3D-printing via fused deposition modeling

4.1. Introduction.....	163
4.1.1. Materials choice.....	163
4.1.2. Elaboration process.....	164
4.2. Determination of the optimized composition.....	164
4.2.1. Infrared analysis.....	165
4.2.2. Correlation between electrical and thermal characterization.....	166
4.3. Influence of the sample holder on conductivity values	173
4.3.1. Introduction to the various sample holders.....	173
4.3.1.1. Lateral sample holder.....	174
4.3.1.2. Sandwich sample holder.....	174
4.3.1.3. Interdigitated-comb sample holder.....	174
4.3.2. Distinct ionic conductivity values for a same sample.....	175
4.4. PEO/LiTFSI solid polymer electrolyte extrusion and 3D-printing.....	177
4.4.1. Filament extrusion.....	177
4.4.2. Mechanical properties deduced via nano-indentation.....	181
4.4.3. FDM 3D-printing.....	185
4.4.3.1. Classical 3D-printer.....	185
4.4.3.2. Modified 3D-printer.....	187
4.4.4. Comparison with contemporary studies.....	189
Conclusions.....	192
References	193

4.1. Introduction

Previous chapters (cf. **Chapters 2 and 3**) were dedicated to the liquid electrolyte LIB technology. Nonetheless, the long-term objective of such scientific project would be to demonstrate the FDM printability of a complete all-solid-state LIB as solid electrolyte represents a safer alternative to the classical volatile and flammable organic solvent-based liquid electrolyte. Hence, many studies were recently focused on the development of high-performance solid electrolytes (ceramic or polymer).¹

Fused Deposition Modeling (FDM) involving the use of a thermoplastic filament as material source for the 3D-printer, it was decided to fully dedicate this chapter on the elaboration of a solid polymer electrolyte filament. This latter will pave the way toward the future direct printability of a fully 3D-printed functional object containing the electronics and LIB in its core, without the necessity to introduce any liquid electrolyte after printing. Note that the results presented in the following sections are already part of published articles (cf. **Preface — III**).

4.1.1. Materials choice

Last decades have witnessed the introduction of solid polymer electrolytes (SPE) representing an exciting alternative thanks to their good flexibility and safety behavior with lithium metal.¹⁻⁸ In particular, thanks to its faculty to solvate lithium cations through interaction of its ether oxygens, leading to relatively high ionic conductivity values, PEO has been investigated extensively (cf. **1.1.2.3.2. Solid electrolyte and gel electrolyte**). Therefore, the development of a PEO-based SPE filament appeared here as a clear evidence. On the other hand, the lithium salt choice is decisive as it highly contributes to the ionic conductivity, electrochemical stability and transference number. In this work, LiTFSI was chosen due to its good thermal stability, enabling extrusion at high temperature, and efficient ion pair dissociation known to have an encouraging impact on the final membrane conductivity.⁹ Nonetheless, it is worth mentioning that this latter is still relatively expensive (100 US\$ kg⁻¹ in 2018) in comparison with LiPF₆ (25 US\$ kg⁻¹ in 2018).⁹ Its price is fortunately expected to decrease in the next few years, to reach 45US\$ kg⁻¹ in 2023.⁹ Lastly, looking at the environmental aspects, PEO is biodegradable and non-toxic while TFSI,

although moderately irritant, is permanent in the environment. This latter is however reported to be easily recyclable.⁹

4.1.2. Elaboration process

Similar to what was achieved for both electrodes, separator and current collector (cf. **Chapter 2**), the elaboration of a composite filament specially designed to be used as a solid polymer electrolyte (SPE) within a LIB was initiated. Slurry formulation was achieved by following the experimental protocol described previously (cf. **2.1.1. Elaboration process**). LiTFSI salt being hygroscopic, it is important to note that all experiments described hereafter were performed in a dry room (dew point ≤ -50 °C). DCM was used as solvent to ensure proper dissolution of PEO and homogeneous dispersion with the desired amount of LiTFSI, at room temperature, under magnetic stirring for 3 h in a closed flask. Slurries were subsequently tape-casted onto an EIS sample holder to endure electrical characterization, or onto a PTFE foil to obtain freestanding films. In both cases, after complete evaporation of the solvent at room temperature in a dry room, further drying was achieved under vacuum during 24 h to remove any trace of solvent. The most promising SPE composition, corresponding to the best compromise between ionic conductivity and mechanical properties, was finally chosen to undergo extrusion and 3D-printing.

4.2. Determination of the optimized composition

In order to better identify the impact of the salt LiTFSI, the PEO composition was kept unchanged for all experiments. It consisted of a ratio 90 wt% PEO Mn~100,000 and 10 wt% PEO Mn~5,000,000. Samples with various O/Li⁺ molar ratio equals to 30, 25, 20, 15 and 10 were prepared. Structural (IR), electrical (EIS) and thermal (DSC) characterization of the SPE was implemented on the tape casted films. Among these tested compositions, the optimum content of lithium salt was thus determined to further prepare a 3D-printable filament with high ionic conductivity and maintaining enough mechanical properties.

4.2.1. Infrared

For each sample, the Fourier transform IR spectra were recorded to make sure that these latter were free of water and solvent. Experiments were completed at room temperature with a Nicolet iS20 apparatus placed in a dry room, between 4000 and 400 cm^{-1} in attenuated total reflectance mode (diamond crystal). Spectra were averaged from 32 scans with a resolution of 4 cm^{-1} . As depicted in **Figure 4.1**, IR spectra exhibit the characteristic bands assigned to the PEO-LiTFSI complexes in good agreement with literature.¹⁰ No extra peak corresponding to water in the 3500 cm^{-1} region (**Figure 4.2**) neither DCM solvent distinguishable band at 706 cm^{-1} was detected. Finally, it is worth-mentioning that every sample (except PEO/LiTFSI 10:1) was self-standing.

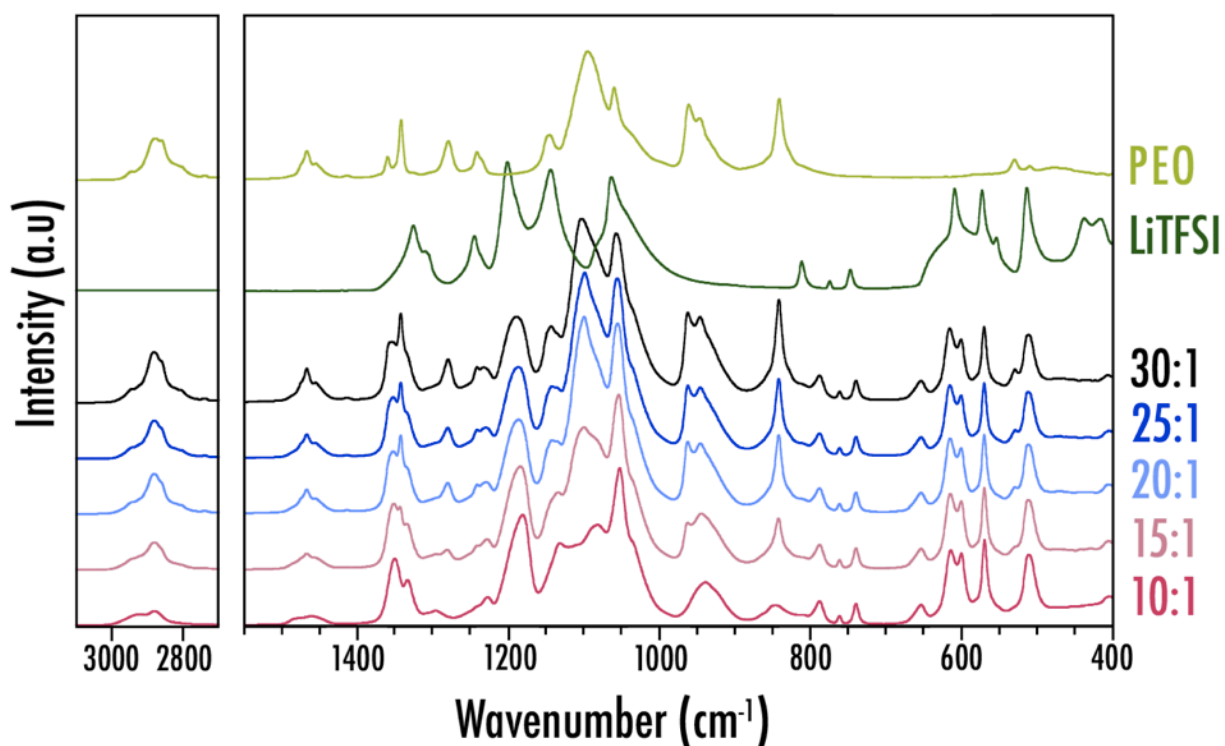


Figure 4.1. Infrared spectra of PEO/LiTFSI complexes in the 3100–2700 cm^{-1} and 1550–400 cm^{-1} regions (cf. **Preface – III**).

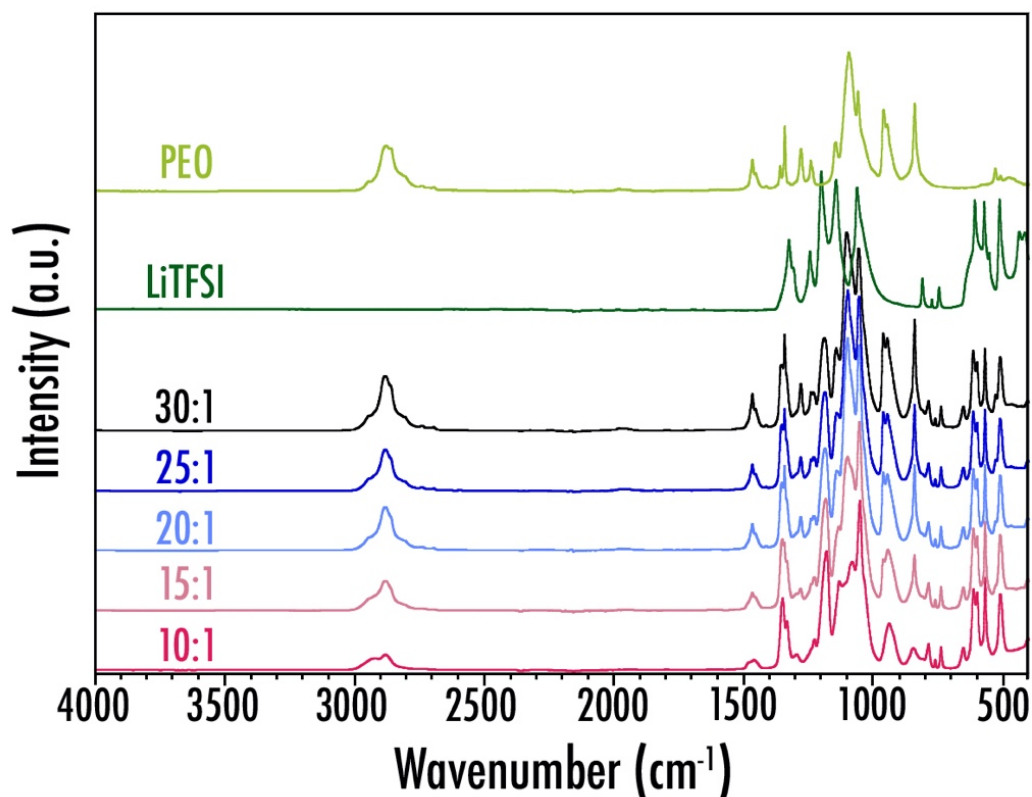


Figure 4.2. Infrared spectra of PEO/LiTFSI complexes in the 4000–400 cm^{-1} regions (cf. **Preface – III**).

4.2.2. Correlation between electrical and thermal characterization

A MTZ-35 frequency response analyzer and an intermediate temperature system (ITS) developed by BioLogic, France, were used to perform the electrochemical impedance spectroscopy (EIS) analysis. For each sample, the respective interdigitated-comb sample holder on which the SPE slurry was deposited beforehand (cf. **4.1.2. Elaboration process**) was then introduced into a controlled environment sample holder (CESH). This procedure was achieved in an argon filled glovebox ($\text{O}_2 < 0.1 \text{ ppm}$, $\text{H}_2\text{O} < 0.1 \text{ ppm}$). Subsequently, the system was kept at 100 °C during 2 h before performing AC impedance measurements under argon at various stabilized temperatures ranging from 20 °C to 90 °C (upon heating and cooling in steps of 10 °C, ramp rate of 1.0 °C min^{-1} , soak time before measure of 15 min). A frequency range of 30 MHz to 0.1 Hz (20 points per decade

and 10 measures per points) and an excitation voltage of 0.05 V were used for the measurements. From the Nyquist and Phase-Bode plots of the complex impedance, the ionic conductivities were obtained.

In parallel, in order to have a better understanding of the correlation between thermal behavior and conductivity, the exact same procedure was reiterated with measurements performed every 2 °C between 20 and 60 °C (interdigitated-comb EIS holder). Thermal analysis of the PEO/LiTFSI films was performed on a DSC204F1 (NETZSCHGerätebau GmbH, Germany) machine from -60 to 100 °C in argon atmosphere (upon heating and cooling), using approximately 6 mg of sample and a heating rate of 10 °C min⁻¹.

At 20 °C, SPE film with the highest amount of LiTFSI salt (PEO/LiTFSI 10:1) is the most conductive (3.79×10^{-6} S cm⁻¹) as displayed in **Figure 4.3**. The Nyquist plot corresponding to this particular measurement is depicted in **Figure 4.4**. By decreasing the amount of lithium salt within the membrane, the conductivity values at 20 °C tend to decrease: 1.07×10^{-6} S cm⁻¹, 7.83×10^{-7} S cm⁻¹, 5.15×10^{-7} S cm⁻¹, 2.31×10^{-7} S cm⁻¹, respectively for samples with O/Li⁺ molar ratio equals to 15, 20, 25 and 30.

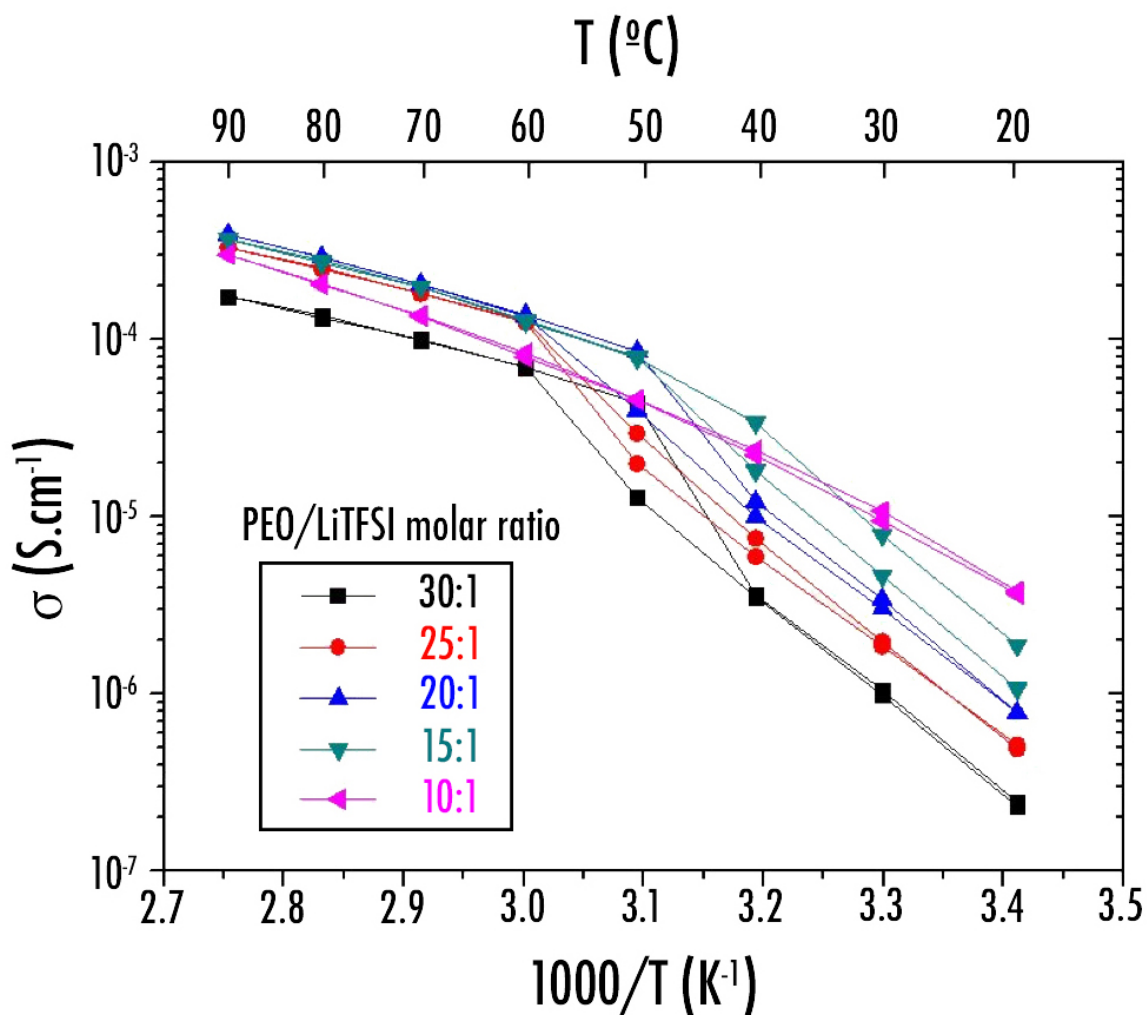


Figure 4.3. Arrhenius plots of the ionic conductivity for PEO/LiTFSI polymer electrolyte complexes (cf. Preface – III).

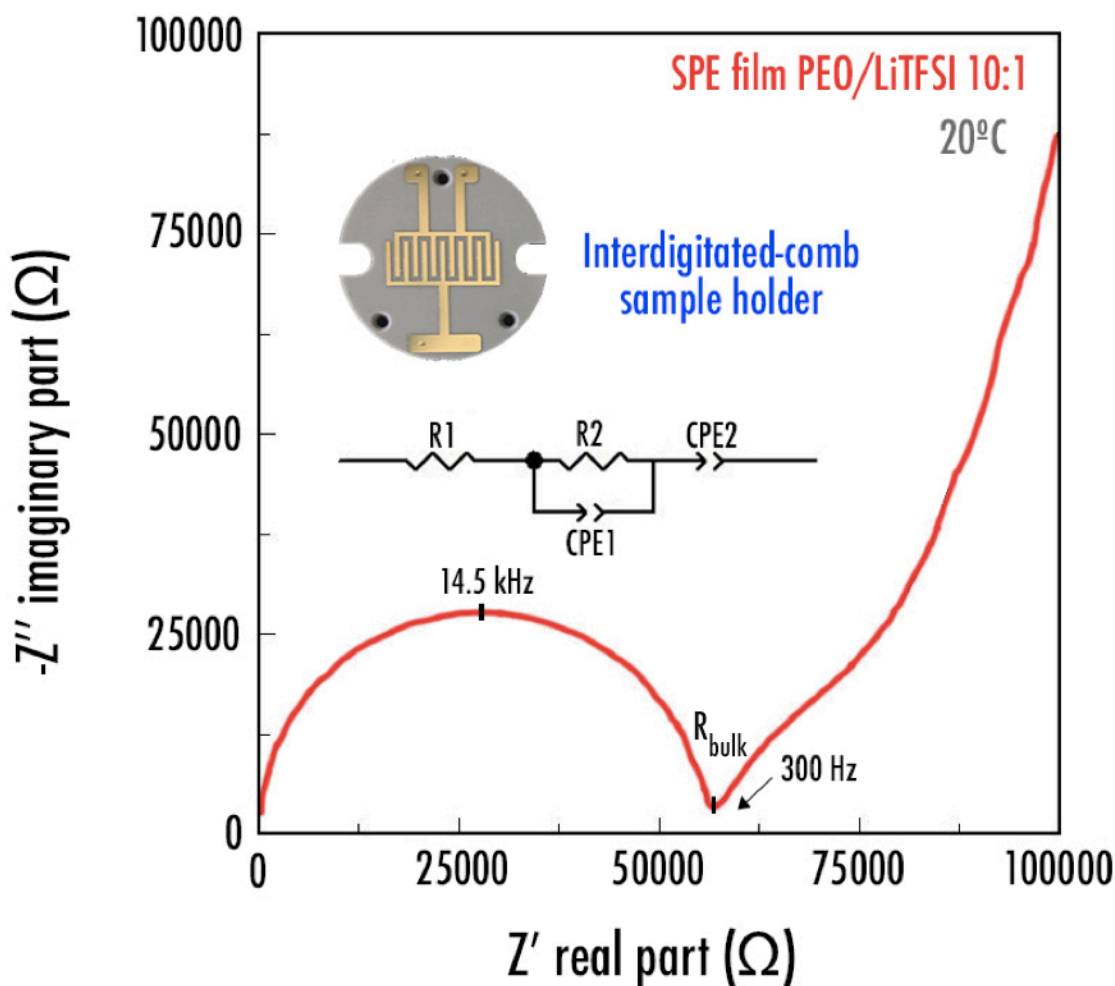


Figure 4.4. Nyquist plot for the SPE film sample PEO/LiTFSI 10:1 using the interdigitated-comb EIS holder (cf. Preface – III).

Among all the samples tested, PEO/LiTFSI 10:1 is the only one exhibiting a VTF behavior along the whole range of tested temperatures (between 20 °C and 90 °C) in good agreement with literature.^{11, 12} Induced by the LiTFSI incorporation, this behavior is typical of a completely amorphous high-molecular weight SPE as reported by Mindemark et al.⁵. On the other hand, for other samples with O/Li⁺ molar ratio equals to 30, 25, 20 and 15, the Arrhenius law is first respected between 20 °C and the melting temperature around 50 °C, while then the VTF law is applied up to 90 °C. The latter behavior is exhibited in **Figure 4.5** showing the differential scanning calorimetry and ionic conductivity behavior respectively upon heating and cooling, for the sample PEO/LiTFSI 20:1.

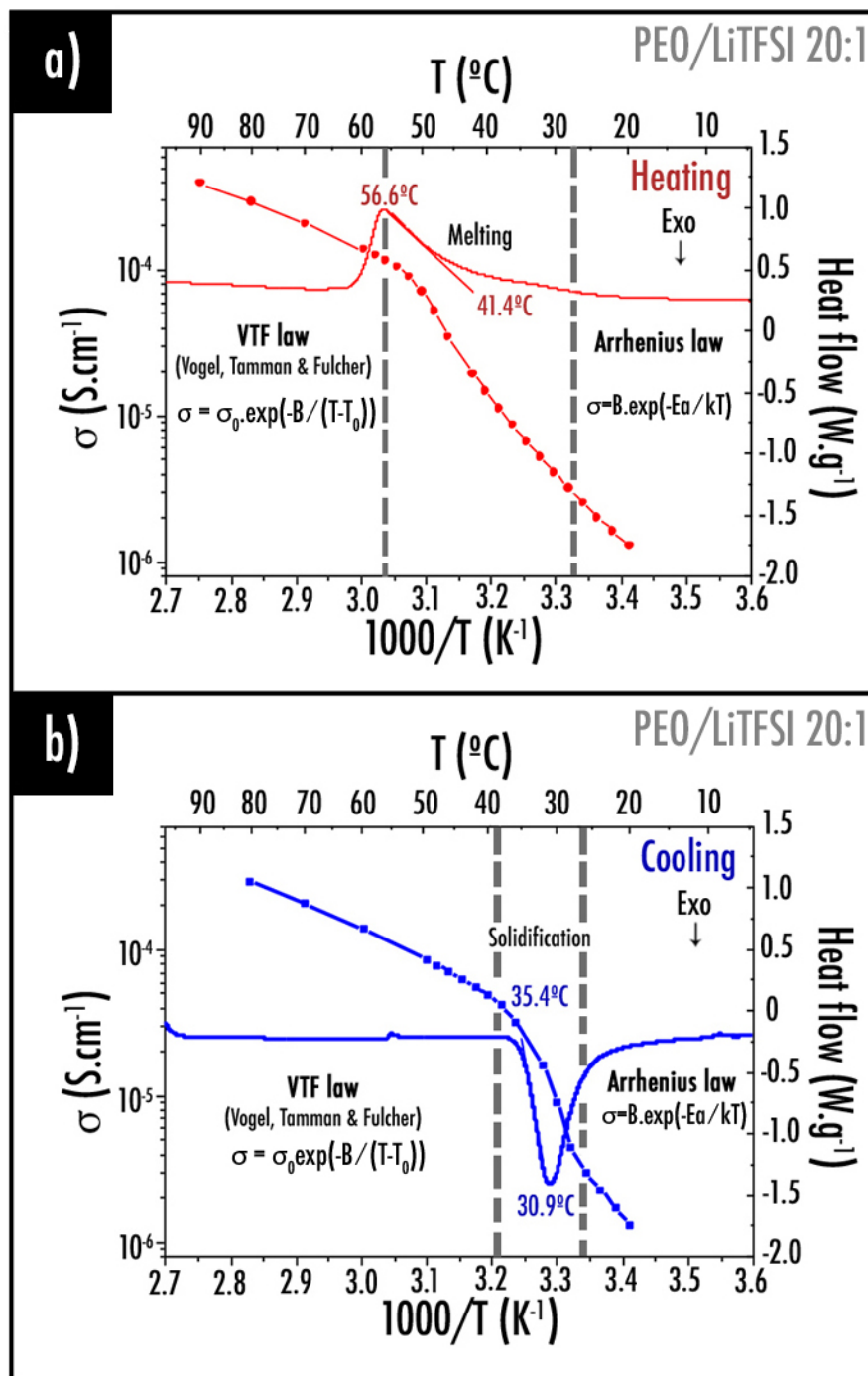


Figure 4.5. Correlation between DSC and EIS measurements for SPE film sample PEO/LiTFSI 20:1 upon (a) heating and (b) cooling (cf. Preface – III).

Upon heating, melting temperature onset appears at 41.4 °C and clearly corresponds to the ionic conductivity slope knee moving from an Arrhenius behavior to a Vogel-Tamman-Fulcher (VTF) behavior. Upon cooling, solidification temperature onset emerges at 35.4 °C and perfectly matches here again with the slope knee changing here from a VTF behavior to an Arrhenius behavior. As reported in literature,⁵ this conduct is typical of semi-crystalline polymers such as PEO-based systems.

Ionic conductivity values being relatively low at ambient temperature for its commercial use, SPE are usually considered for applications at higher temperature up to 90 °C.¹³ In this temperature range, the solid-polymer electrolyte is in a viscous state, facilitating the lithium-ion displacement. Thus, it is interesting to compare conductivity values for each sample at this particular temperature. As depicted in **Figure 4.6**, at 90 °C, the highest conductivity value ($3.92 \times 10^{-4} \text{ S cm}^{-1}$) was exhibited by the PEO/LiTFSI sample with a molar ratio 20:1. It is worth-mentioning that the reported classical parabola shape⁵ for the salt-in-polymer domain was here obtained. For higher salt concentration, the conductivity is decreasing due to the ionic mobility drop resulting from the Tg rise with salt concentration increasing the viscosity but also because of the rising ion-ion pairing forming doublets or triplets.¹⁴⁻¹⁷ As a consequence, it was decided to focus further experiments such as extrusion and 3D-printing on the most promising film sample PEO/LiTFSI 20:1 only.

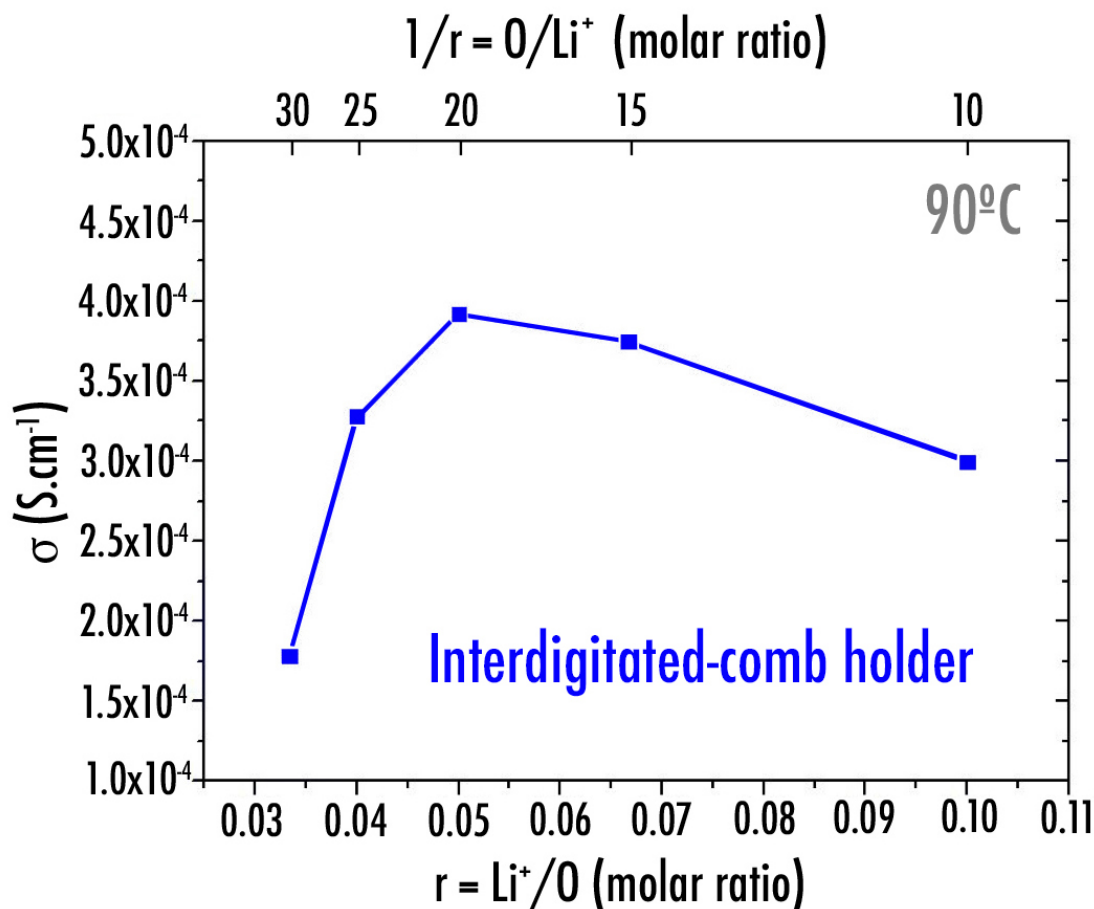


Figure 4.6. Variation of the ionic conductivity at 90 °C in function of the salt concentration (cf. Preface – III).

Finally, it must be emphasized that conductivity values reported here are relatively low compared to other studies in literature for similar samples.^{5, 18} This tendency can be explained by the sample holder itself. Indeed, values were here obtained using an interdigitated-comb holder while sandwich holder (cf. 4.3.1.2. **Sandwich sample holder**) are usually employed in literature. Advantage of interdigitated-comb sample holder is that sample dimensions (thickness) are not required to calculate the conductivity value, thus preventing from any eventual measurement errors. Besides, slurries corresponding to a non-self-standing sample can directly be cast on the holder. In the next section, the impact of the sample holder design on ionic conductivity is addressed.

4.3. Influence of the sample holder on conductivity values

4.3.1. Introduction to the various sample holders

For each SPE composition, Electrochemical Impedance Spectroscopy (EIS) analyses were completed, using the three different electrochemical impedance spectroscopy sample holders depicted in **Figure 4.7** (lateral, sandwich and interdigitated-comb). The exact same protocol established previously (cf. **4.2.2. Correlation between electrical and thermal characterization**) was followed.

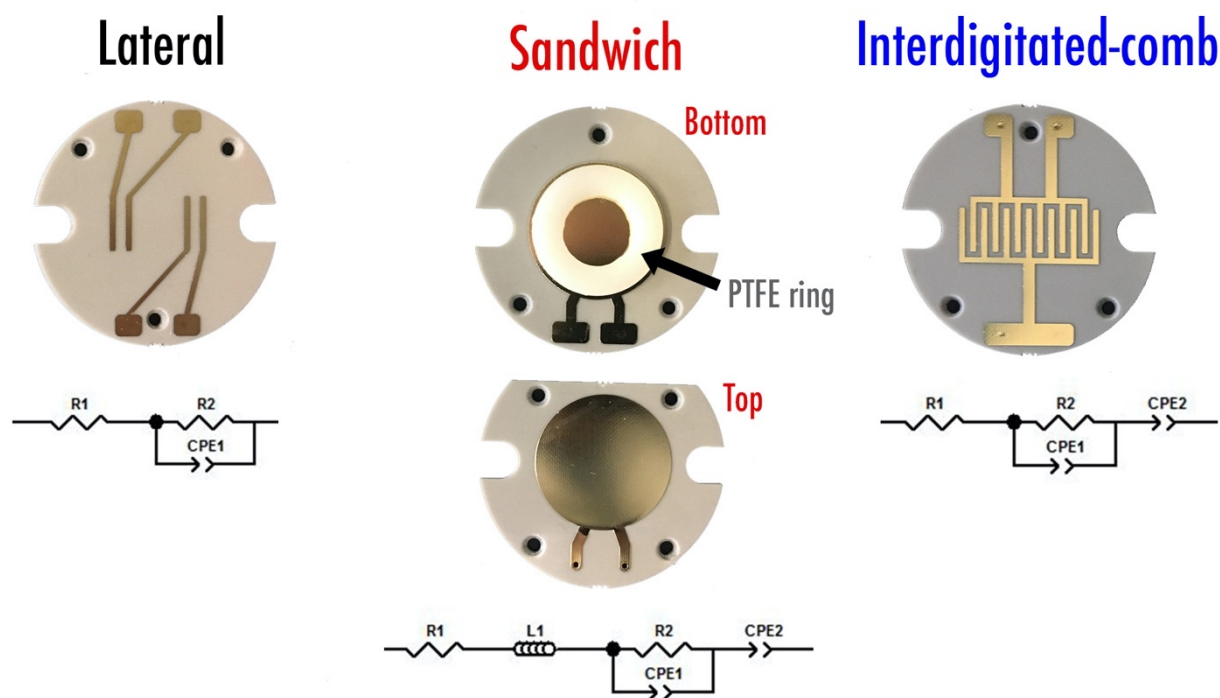


Figure 4.7. Three types of sample holder used in this study and their respective equivalent circuits (cf. **Preface – III**).

4.3.1.1. Lateral sample holder

Conductivities with the lateral-type holder were calculated from the **Equation 4.1**:

$$\sigma = \frac{1}{R} \times \frac{l}{e \times l'} \quad (\text{Equation 4.1})$$

where e is the sample thickness, l is the spacing between fingers, l' is the finger length and R is the respective resistance deduced from the Nyquist and Bode plots.

4.3.1.2. Sandwich sample holder

Conductivities with the sandwich-type holder were calculated from the **Equation 4.2**:

$$\sigma = \frac{1}{R} \times \frac{d}{A} \quad (\text{Equation 4.2})$$

where d is the sample thickness, A is the sample surface area, and R is the respective resistances deduced from the Nyquist and Bode plots. As depicted in **Figure 4.7**, a PTFE ring was inserted between both parts of the sandwich holder-type so the sample diameter and thickness were kept unchanged during the whole experiment.

4.3.1.3. Interdigitated-comb sample holder

Conductivities with the interdigitated-type holder were calculated from the **Equation 4.3**:

$$\sigma = \frac{K_{cell}}{R} \quad (\text{Equation 4.3})$$

where R is the resistance deduced from the Nyquist and Bode plots and K_{cell} the constant cell parameter obtained from the **Equation 4.4** deduced from literature.^{19, 20}

$$K_{cell} = \frac{2 \times \left(\frac{S}{W}\right)^{1/3}}{L \times (N-1)} \quad (\text{Equation 4.4})$$

where N is the number of fingers, S the finger spacing, W the finger width and L the finger length.

4.3.2. Distinct ionic conductivity values for a same sample

Figure 4.8 depicts the conductivity measurements for the sample PEO/LiTFSI 20:1 performed using the three different sample holders (lateral, sandwich and interdigitated-comb). Interestingly, it appears that for the exactly same sample, values obtained are quite different from one holder to another. Lateral holder attains the highest values while the interdigitated-comb holder corresponds to the lowest conductivity. Finally, the values depicted by the sandwich holder match perfectly the ones obtained using the lateral at high temperature (90 °C) and the interdigitated-comb at low temperature (20 °C). It is worth noting that this behavior was observed for each composition and measurements were repeatable.

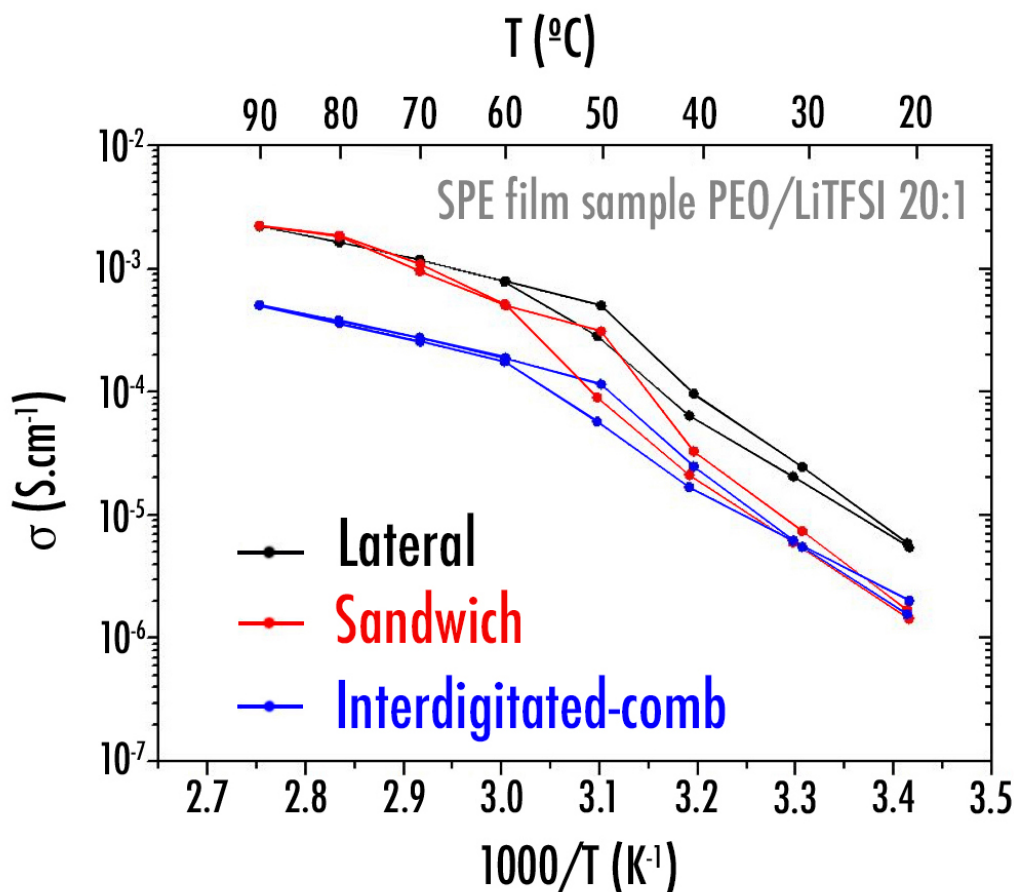


Figure 4.8. Arrhenius plots of the ionic conductivity for PEO/LiTFSI 20:1 sample using various EIS sample holders (cf. Preface – III).

Through IR analysis, several prospective explanations were discarded: No interactions were observed at the interface between the polystyrene holder (appearing at 702 cm^{-1} — **Figure 4.9**) and electrolyte. No significant concentration gradients were identified through the very weak different intensity values between sample top and bottom analysis.

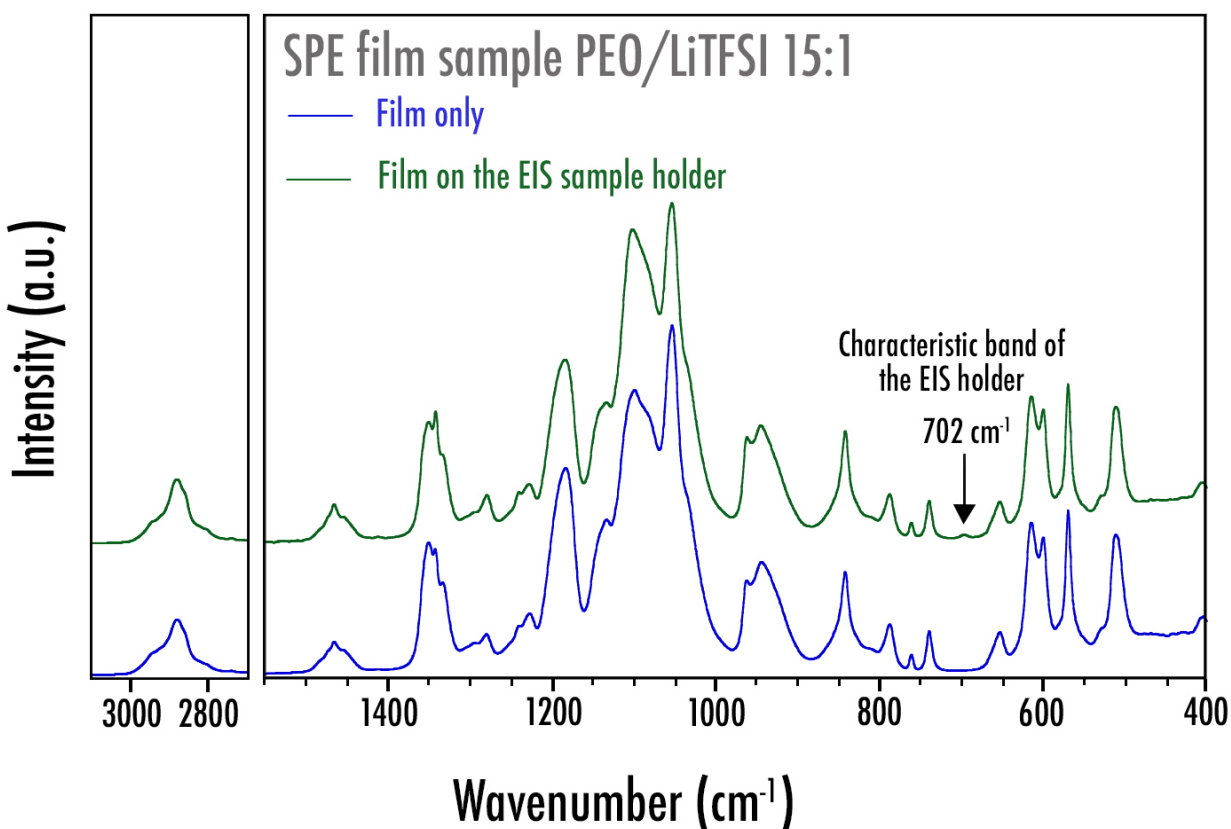


Figure 4.9. Infrared spectra of SPE film sample PEO/LiTFSI 15:1 in the $3100\text{--}2700\text{ cm}^{-1}$ and $1550\text{--}400\text{ cm}^{-1}$ regions with a view to identify any interaction between the membrane and the EIS sample holder (cf. **Preface – III**).

The conductivity difference (at temperatures $< 90\text{ }^{\circ}\text{C}$) between the lateral and sandwich configurations could be explained by the polymer chains orientation along the substrate (XY plane) as assertively claimed by Golodnitsky et al.²¹ with other salts (LiI and LiCF_3SO_3). According to the accepted model for Li^+ motion within the polymer matrix, it is conceivable that such chain orientation leads to higher conductivity along the substrate. Indeed, it is well known that pristine PEO has a helical structure consisting of seven $\text{--CH}_2\text{--CH}_2\text{--O--}$ groups in two turns of the helix²¹

which adjust to wrap Li cations coordinated with three ether oxygens. Armand²² suggested that the intra-helix location of Li^+ and its possible motion by hopping from one coordination site to another along the helix, may explain that the alignment of the PEO chains should result in an enhancement of the ionic conductivity. In this case, this orientation could not be much pronounced due to chains entangling as being part of the “De Gennes zone”^{16,23} and the large TFSI⁻ anion size. At 90 °C, the orientation effects vanish due to the polymer melting and des-entangling, thus resulting in the exact same conductivity values. It is worth noting that the shape of conductivity behavior of the interdigitated-comb and lateral configurations is similar, though values differ by a factor 4. The presence of an exclusion zone between the gold electrode pattern and the polymer may be an explanation, as the chains kept in-between might not be considered in the conductivity calculation. To confirm this assumption, future research involving the variation of the number of teeth in the combs must be accomplished. Besides, it may also be extended to other polymers and salts.

These original results raise a number of questions regarding all of the ionic conductivity values reported in literature up to now. In future studies, authors may preferably report a thorough delimited zone to a very precise value of conductivity.

4.4. PEO/LiTFSI solid polymer electrolyte extrusion and 3D-printing

As mentioned hereabove (cf. **4.2.2. Correlation between electrical and thermal characterization**), it was decided to focus further experiments such as extrusion and 3D-printing on the most promising film sample PEO/LiTFSI 20:1 only as at 90 °C, the highest conductivity value was obtained for this latter. Considering the hydrophilic nature of LiTFSI, it is important to note that the extruder and 3D-printer were both located in a dry room. Printability, mechanical (nano-indentation) as well as morphological characterization (SEM) was performed.

4.4.1. Filament extrusion

In a mortar, PEO and LiTFSI powders, corresponding to the most promising composition (molar ratio O/Li = 20) deduced from the film samples characterization, were pre-mixed. The resulting powder blend was used to feed homogeneously the extruder (Filabot Original, Filabot

Triex LLC, USA) as depicted in **Figure 4.10.a**. Subsequently, a regular ~ 1.75 mm diameter 3D-printing SPE filament was obtained. Temperature of the extruder was fixed at 85 °C. The filament coming out from the extruder nozzle was rolled manually around a beaker and then rolled around a spool by using a Filabot spooler (Filabot Triex LLC, USA). Prior extrusion of each sample, the extruder was cleaned thoroughly with neat PEO Mn $\sim 100,000$. To make sure that the extruded SPE filament composition corresponded to the desired sample, at least 75 grams of powder were required to eliminate residual traces of previous blend. Finally, a free-standing PEO/LiTFSI 20:1 SPE filament specially designed to feed a FDM 3D-printer was obtained as depicted in **Figure 4.10.b**.

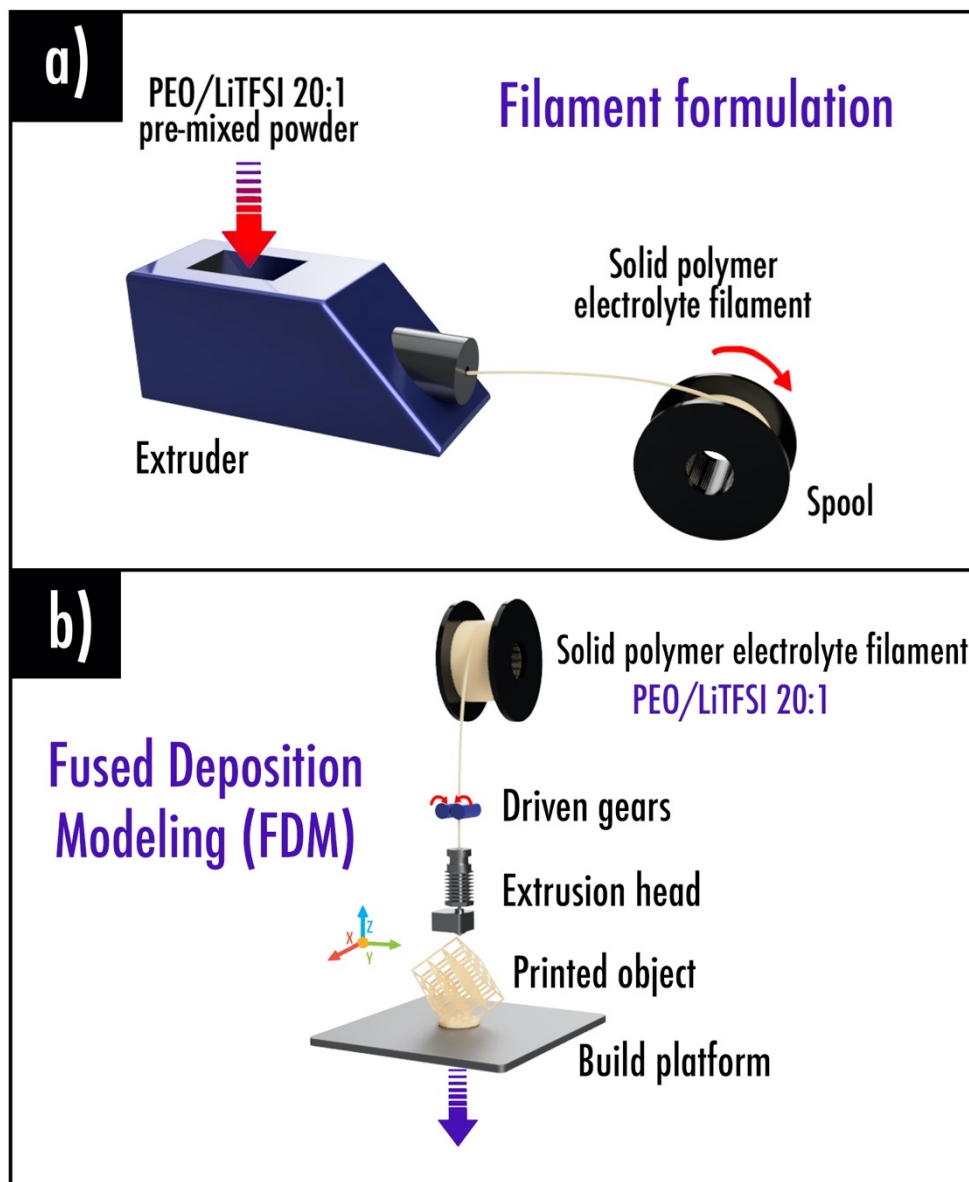


Figure 4.10. (a) SPE filament formulation through extrusion; (b) SPE 3D-printing via fused deposition modeling (cf. Preface – III).

The good homogeneity of the SPE filament was thenceforward confirmed through IR and SEM analysis of the cross section. As it can be seen in **Figure 4.11**, no major difference was observed between film and filament via IR, thus confirming the purity of the filament obtained.

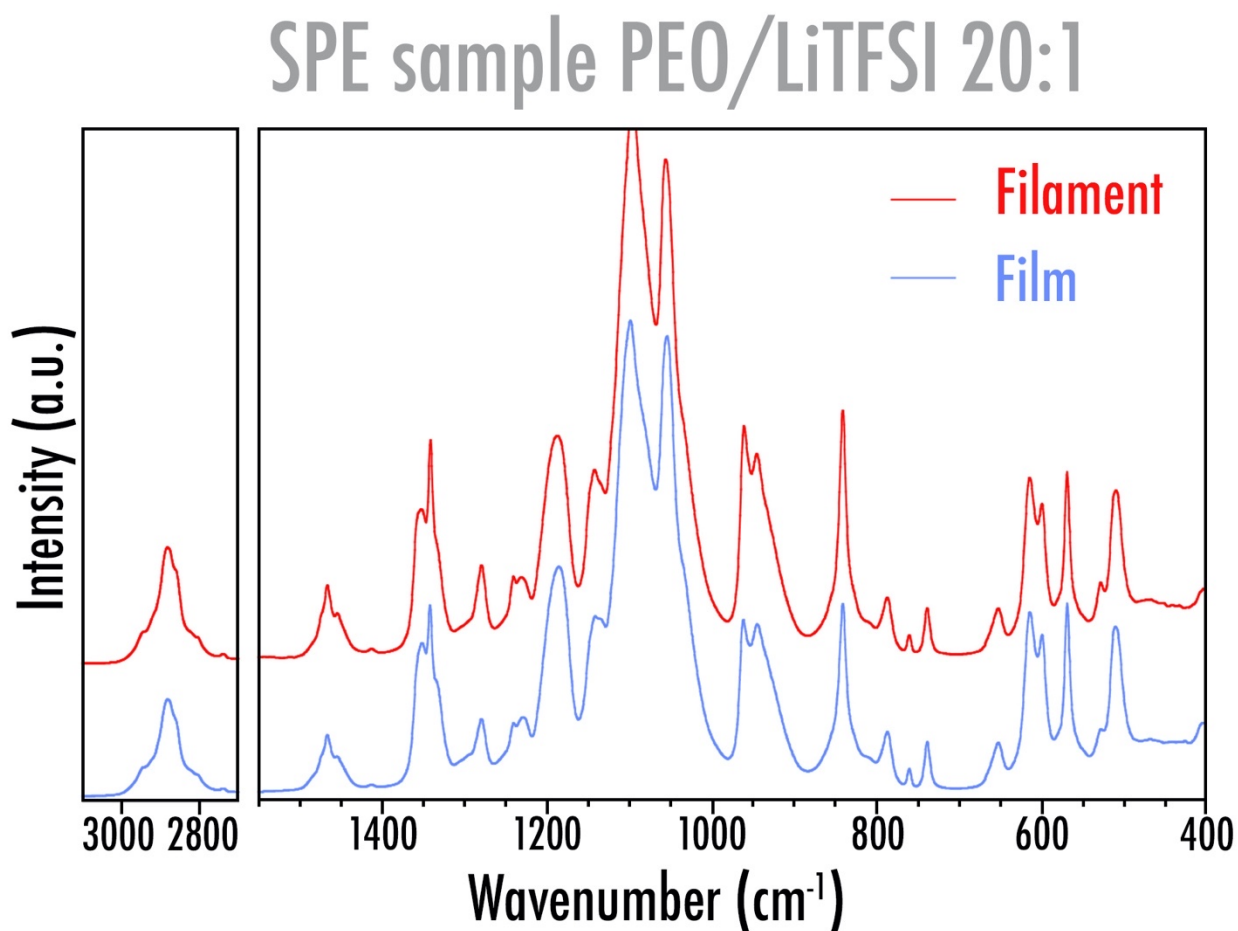


Figure 4.11. Infrared spectra of PEO/LiTFSI 20:1 filament and film samples in the $3100\text{--}2700\text{ cm}^{-1}$ and $1550\text{--}400\text{ cm}^{-1}$ (cf. Preface – III).

The global homogeneity of films as well as that of the produced composite SPE filament was then investigated by means of a FEI Quanta200F (Thermo Fisher Scientific, USA) scanning electron microscope under high vacuum. The secondary electron images were recorded with a 5 kV electron beam acceleration voltage. In a dry room, samples were soaked and cut into liquid nitrogen to perform cross-sectional observation. To prevent any water trace, tested samples were

transferred from the dry room to the microscope using a homemade vacuum transfer holder. As depicted in **Figure 4.12.a**, it is interesting to note that the filament microstructure is very compact with almost no porosity due to the extrusion process. This observation is totally different from what is depicted for the film showing spheres separated by a clearly visible porosity created during the solvent evaporation (**Figure 4.12.b**).

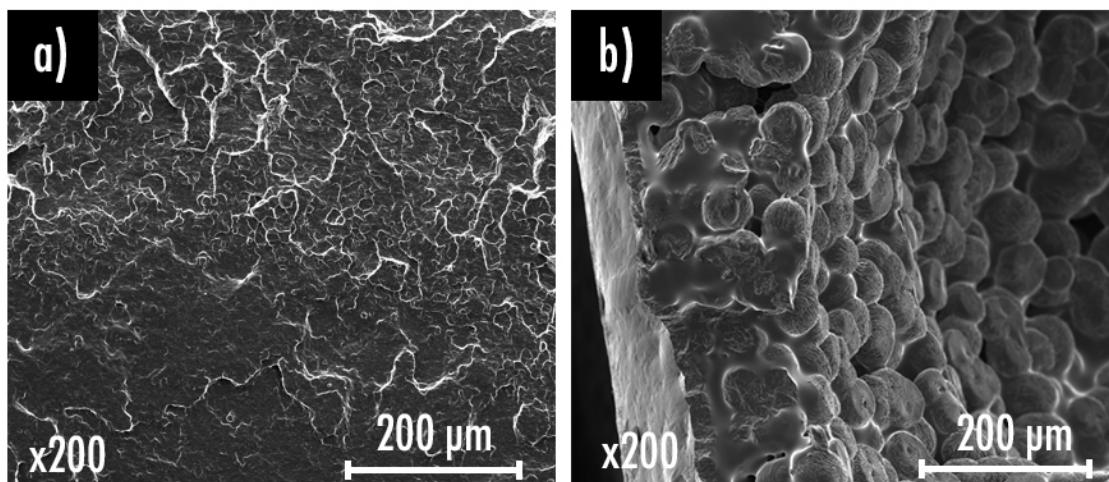


Figure 4.12. Secondary Electron SEM images depicting the PEO/LiTFSI 20:1 sample microstructure for the (a) filament and (b) film (cf. **Preface – III**).

4.4.2. Mechanical properties deduced via nano-indentation

Comparative nano-indentation experiments were carried within the scanning electron microscope under high vacuum by means of a MM3A-EM micromanipulator equipped with a force measurement system (FMS-EM) and a FMT-120 silicon indenter tip (Kleindiek Nanotechnik, Germany — **Figure 4.14.a**). Three film samples were tested, including the optimized PEO/LiTFSI 20:1, pure PEO (90 wt% PEO Mn~100,000 and 10 wt% PEO Mn~5,000,000) and pure PLA serving here as a reference. Beforehand, it is worth mentioning that each film was heated 50 °C above its respective melting temperature during 1 h and subsequently dried under vacuum during 24 h. Samples (about 2 mm thick) were then finally transferred from the dry room to the microscope using a homemade vacuum transfer holder to avoid any water trace.

The calibration of the device was completed using a calibration string with a spring constant of $9.16 \mu\text{N } \mu\text{m}^{-1}$. Experiments were then launched by controlling the rotation of the indenter at a specific rate ($8 \times 10^{-7} \text{ rad s}^{-1}$) upon loading and unloading. For each sample, 4 nano-indentations were performed on random positions to check the reproducibility and the corresponding force vs time curves were recorded. As depicted in **Figure 4.13**, the indenter tip was pressed into the sample (loading) at a controlled displacement rate. Subsequently, the force of the indenter was maintained constant during a dwell time. Finally, the indenter tip was removed from the sample (unloading) at the same rate.

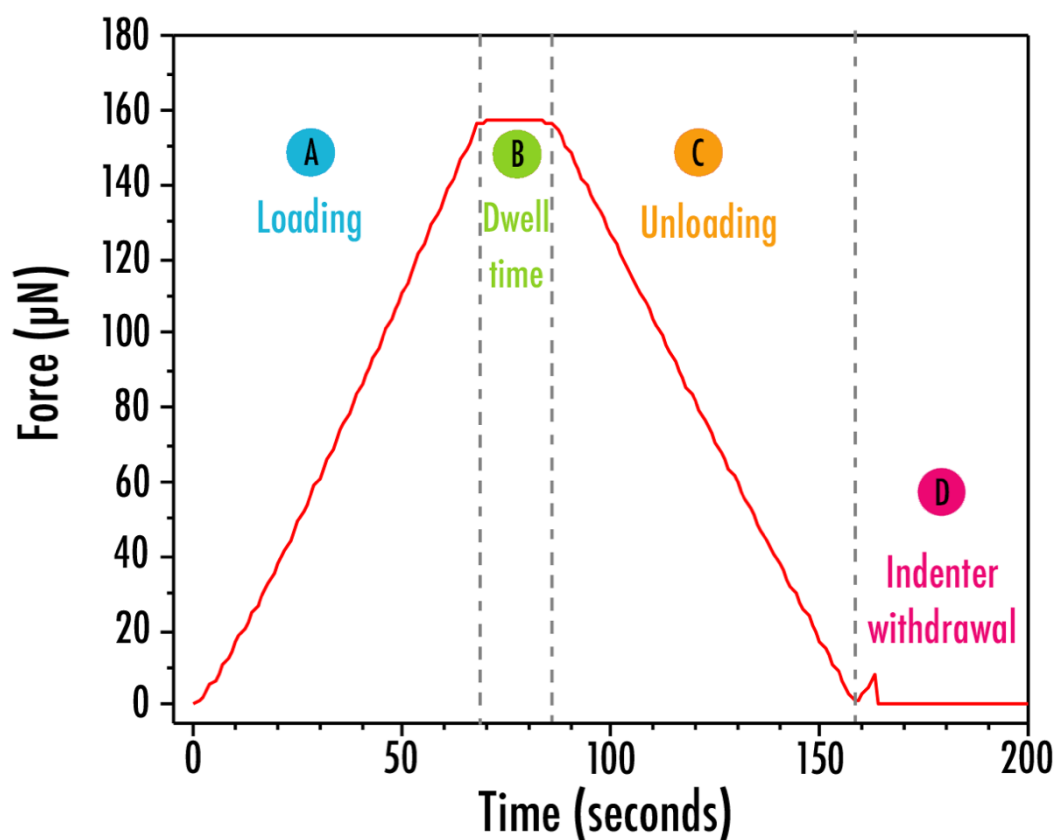


Figure 4.13. Classical force-time curve obtained from the nano-indentation experiment (cf. **Preface – III**).

From the nano-indentation experiments, mechanical properties of the materials such as the Young modulus can usually be calculated precisely as described in literature by Oliver and Pharr.²⁴ Here, due to the unconventional geometry of the employed indenter tip (**Figure 4.14.a**), such information could not be calculated accurately. Nonetheless, from the force vs time curves, a rough estimation of the stiffness was possible by studying the response to the indentation upon unloading for each sample (**Figure 4.14.b**).

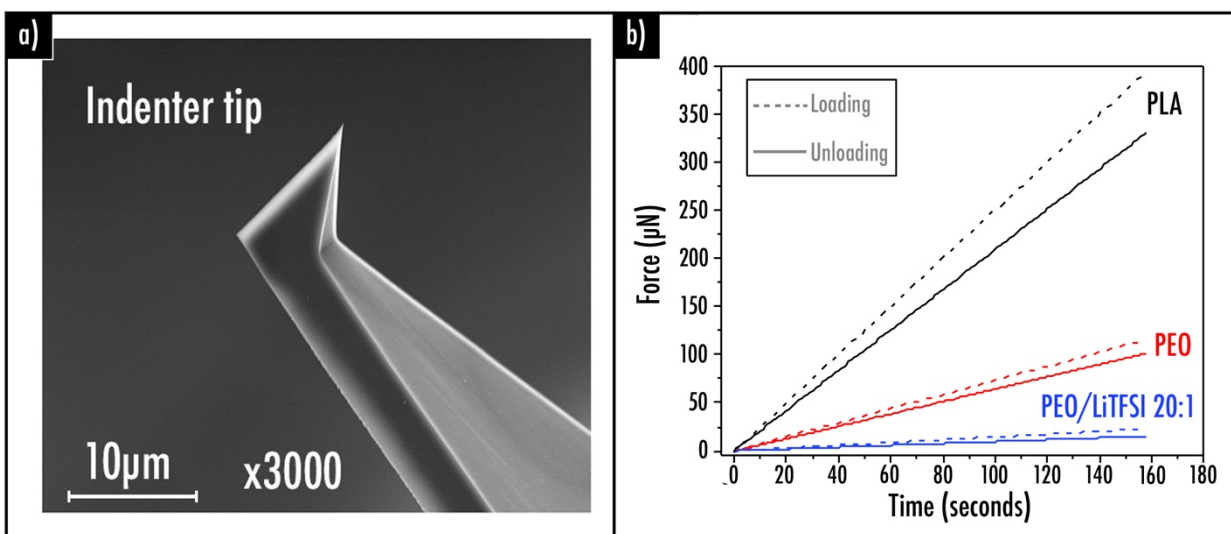


Figure 4.14. (a) Secondary electron SEM image depicting the unconventional indenter tip; (b) Response to the indentation upon loading and unloading for each sample (cf. **Preface – III**).

From the slope, rigidity of the pure PEO and PEO/LiTFSI 20:1 sample were thus estimated to be respectively about 3.5 and 22 times lower compared to pure PLA. Based on the premise that pure PLA, which is a classical 3D-printing polymer, exhibits a Young modulus value specified by the supplier of about 3 GPa, it was therefore estimated that pure PEO and PEO/LiTFSI 20:1 presents values about 850 MPa and 140 MPa respectively. These estimations appear to be in good agreement with values obtained via other techniques such as fluorescence (150 MPa for PEO Mn~100,000 and 1000 MPa for PEO Mn~5,000,000) and tensile tests (400 MPa for PEO Mn~100,000) as reported in literature.^{25, 26} Also, they are consistent with the fact that PEO and PEO/LiTFSI 20:1 are both qualitatively softer than PLA while manipulating the filament.

On the other hand, a peak attributed to the sample material adhesion to the indenter tip was also observed at the end of the unloading, until the tip was entirely withdrawn from the sample (**Figure 4.15**). This particular feature was particularly noticeable for the PEO/LiTFSI sample in comparison to the PLA and PEO exhibiting a subtler similar response. Thus, it clearly indicates the optimized PEO/LiTFSI sample is much stickier in comparison with the other pure PEO and pure PLA sample. Appearing as a logical follow-up, its printability-related issue will be discussed in the next section (cf. **4.4.3. FDM 3D-printing**).

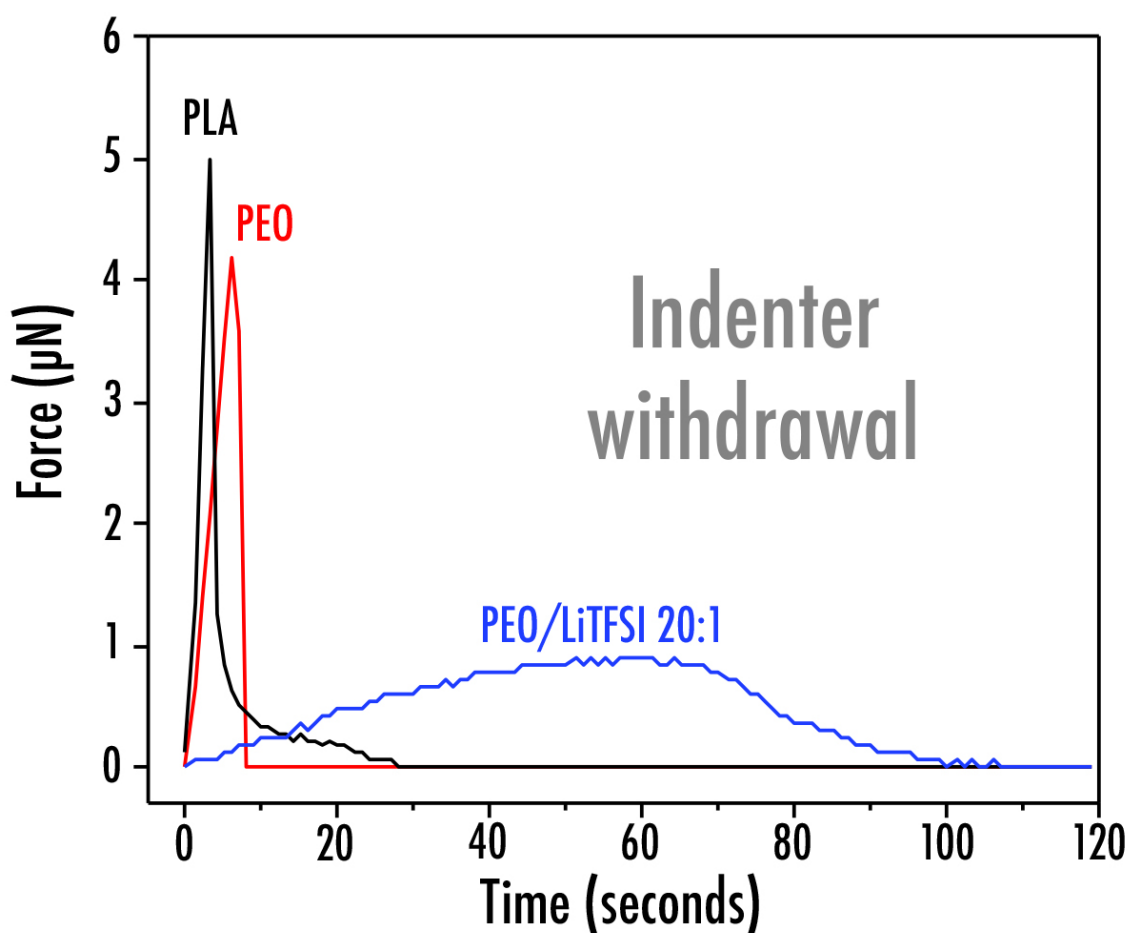


Figure 4.15. Force-time curves displaying the peaks attributed to the sample material adhesion to the indenter tip observed at the end of the unloading (indenter withdrawal) (cf. **Preface – III**).

4.4.3. FDM 3D-printing

4.4.3.1. Classical 3D-printer

Preliminary tests were performed using a commercial printer i3 Metal Motion (eMotionTech, France), with unchanged nozzle input (1.75 mm) and output (0.4 mm) diameters. Maximum resolution in the Z direction is estimated to be ≈ 200 μm . The afore-optimized SPE filament (PEO/LiTFSI 20:1) was used as material source for the printer (**Figure 4.10.b**).

Unfortunately, using this unmodified configuration (**Figure 4.16**), 3D-printing of the PEO/LiTFSI was impossible. Indeed, while a pure PEO filament (90 wt% PEO $M_n \sim 100,000$ and 10 wt% PEO $M_n \sim 5,000,000$) can be printed without any issue, the introduction of a lithium salt such as LiTFSI, acting as a plasticizer, alters considerably the mechanical properties of the filament, becoming much more soft, flexible and stickier, as previously observed via comparative nano-indentation (cf. **4.4.2. Mechanical properties deduced via nano-indentation**). Thus, from these experiments, it clearly seems that thermoplastic filament must exhibit a Young modulus above ≈ 850 MPa (corresponding to pure PEO) to be printable using an unmodified FDM configuration.

Commercial 3D-printer

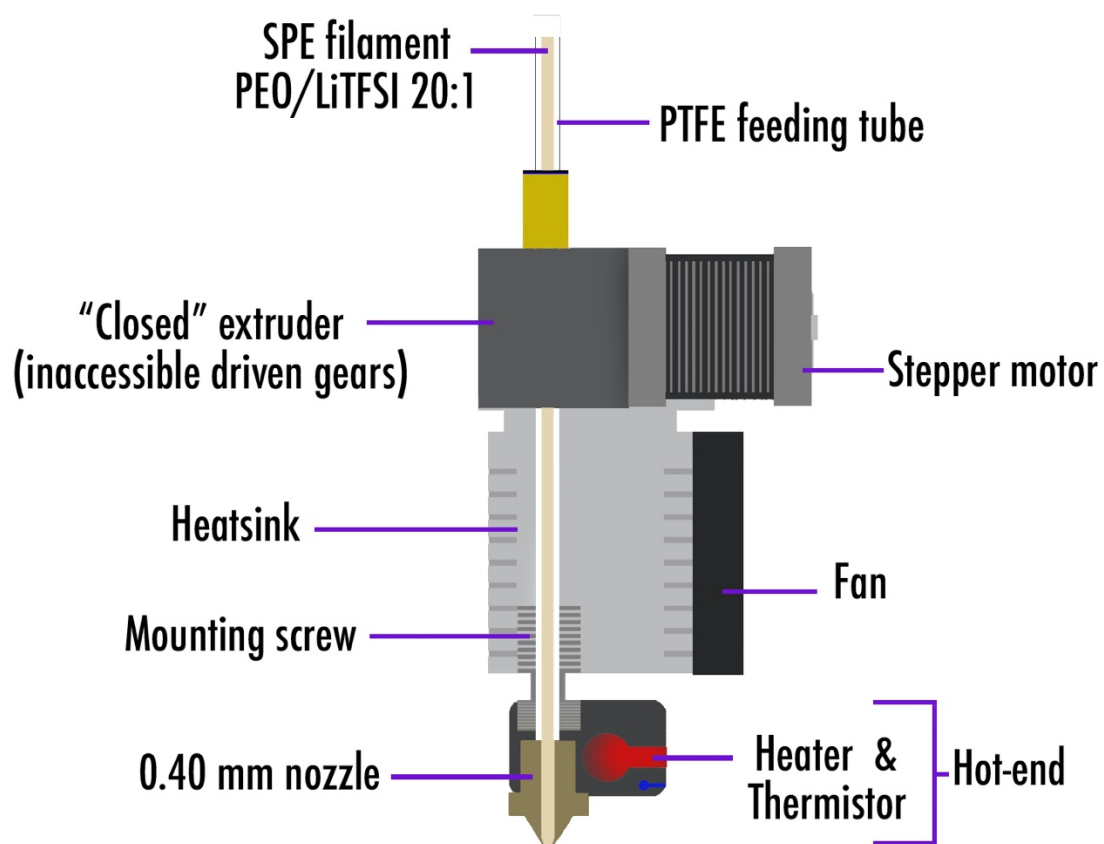


Figure 4.16. Scheme depicting the extruder part of the commercial FDM 3D-printer (cf. **Preface – III**).

4.4.3.2. Modified 3D-printer

As the printability of the optimized SPE filament (PEO/LiTFSI 20:1) was not achievable with a classical FDM 3D-printer, important machine modifications (**Figure 4.17**) were thus initiated.

Modified 3D-printer

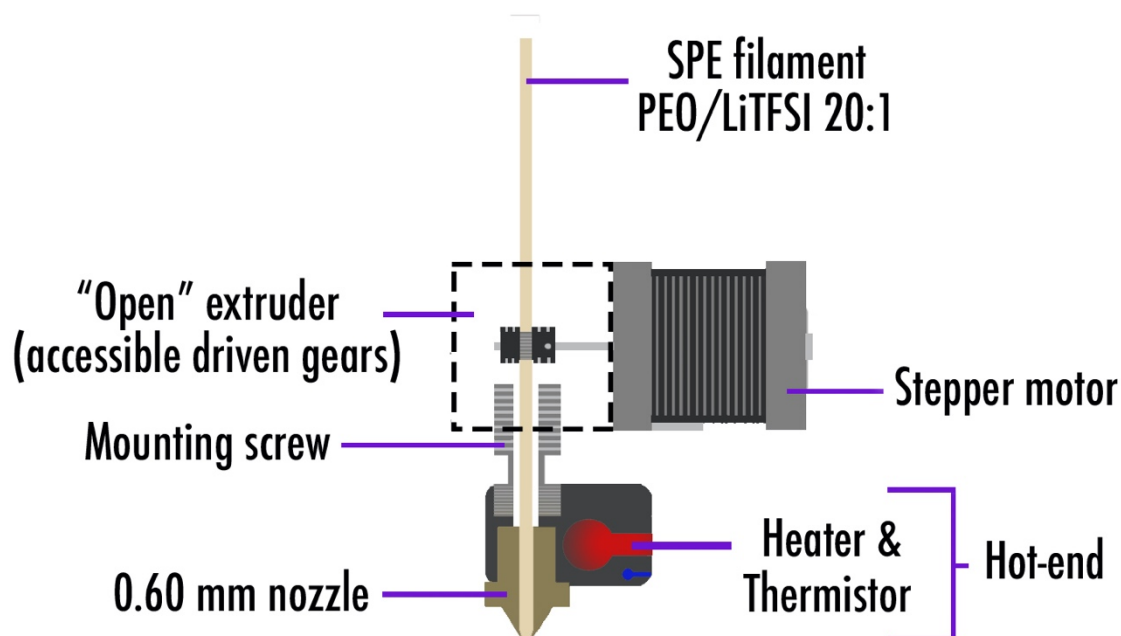


Figure 4.17. Scheme depicting the extruder part of the modified FDM 3D-printer (cf. **Preface – III**).

First of all, to counteract the minimum printing temperature limitation (set at 175 °C for the commercial FDM 3D-printer), the firmware (code controlling the main printing parameters of the 3D-printer) was modified and set to 75 °C. This modification was unavoidable as the PEO/LiTFSI 20:1 melting temperature appears at 41.4 °C (**Figure 4.5.a**). As a reminder, the printing temperature is a crucial parameter as the extruded thermoplastic material on the substrate must cool down straightaway and solidify. On the other hand, mechanical adjustments were implemented. The

original “closed” extruder was replaced with a direct drive “open” extruder. This modification is important as it allows the operator to see directly if the filament is brought correctly within the nozzle. Also, Bondtech Drive Wheels were added instead of the original gears in order to facilitate the filament introduction within the nozzle without deforming it. Finally, it was decided to remove the heatsink part with a view to get as close as possible the gears from the nozzle to avoid the filament buckling (cf. **3.2.1. Composite filament-related issues**). Indeed, considering the unmodified 3D-printer, main issue was that the force exerted on the filament by the gears was not transferred entirely to the filament part within the nozzle. Last but not least, a brand-new nozzle with a larger diameter output (0.6 mm) was installed to allow the filament printing in an easier way. The latter modified FDM machine was subsequently used to obtain a 3D-printed discs (3 mm thick and 12 mm diameter). While its printing was made possible by the machine alteration, it must be clearly emphasized that printability of this PEO/LiTFSI 20:1 filament still remains complex.

Finally, the good homogeneity of the resulting SPE 3D-printed disc (PEO/LiTFSI 20:1) was then ensured by performing further EIS measurement using a sandwich-type sample holder. Here, the conductivity behavior of the 3D-printed disc obtained from the PEO/LiTFSI filament was investigated in the same conditions described previously (cf. **4.2.2. Correlation between electrical and thermal characterization**). Conductivity values obtained by EIS ($2.18 \times 10^{-3} \text{ S cm}^{-1}$ at 90 °C and $9.28 \times 10^{-7} \text{ S cm}^{-1}$ at 20 °C) were really close to the ones observed for the film. Indeed, values almost perfectly fits within the conductivity zone above-defined by means of the lateral, sandwich and interdigitated-comb sample holders (**Figure 4.18**), thus confirming the good homogeneity of the SPE 3D-printed disc.

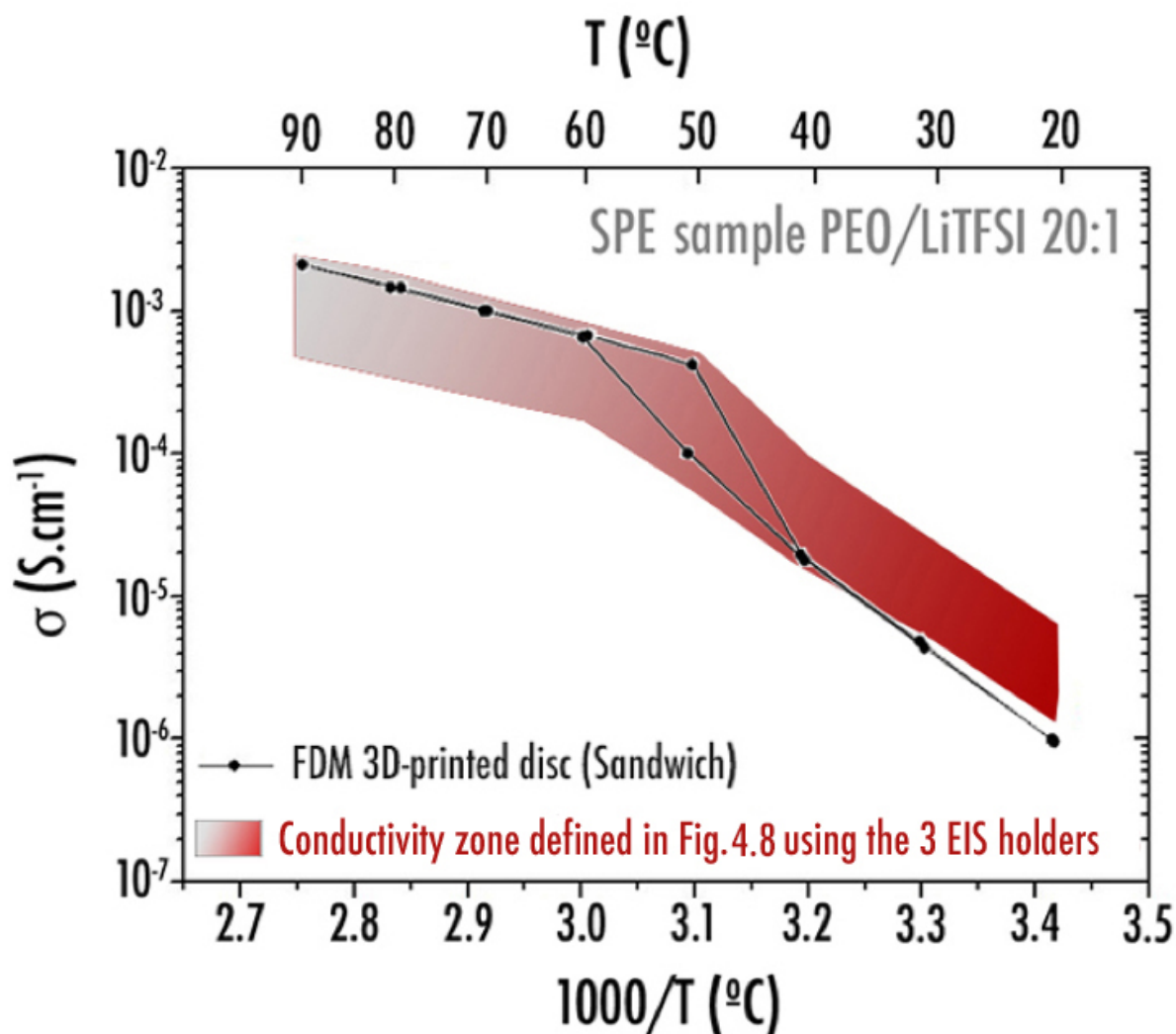


Figure 4.18. Arrhenius plot of the ionic conductivity for the 3D-printed disc (PEO/LiTFSI 20:1) and comparison with the conductivity zone (red) previously defined using the various sample holders (lateral, sandwich and interdigitated-comb) (cf. Preface – III).

4.4.4. Comparison with contemporary studies

Machine modifications of the FDM 3D-printer being very demanding, Ragonès et al.²⁷ rather decided to focus their research on the introduction of another polymer matrix (PLA) within the classical PEO/LiTFSI mixture to strengthen the filament mechanical aspect and printability behavior. Authors developed two SPE filaments composed of PLA/PEO/LiTFSI with SiO₂ or

Al_2O_3 ceramic fillers (wt% 59:20:20:1) and demonstrated their printability with a commercial FDM 3D-printer. Resulting printed samples depicted an ionic conductivity of $8 \times 10^{-5} \text{ S cm}^{-1}$ and $3 \times 10^{-5} \text{ S cm}^{-1}$ at 120°C respectively. These values are relatively low in comparison with what was depicted for the optimized PEO/LiTFSI 20:1 SPE sample in this PhD thesis (**Figure 4.18**). As portrayed by the authors,²⁷ this difference with neat PEO/LiTFSI SPE systems is explained by stronger lithium coordination by ester oxygens (carbonyl) of the PLA chains than by ether oxygens of PEO chains and the fact that the polymers were initially suspended in different solvents, which may lead to an incomplete miscibility. Interestingly, this latter hypothesis was corroborated during this PhD thesis as a clearly visible miscibility issue was perceived via SEM (**Figure 4.19**) for a film sample containing PEO (100.000 MW) and PLA (wt% 50:50), obtained after tape-casting (both polymers were here combined in a common solvent, DCM). Once solvent evaporation was completed, PLA was shown to exhibit a nodular structure, incorporated in a fibrous PEO matrix. Polymer identification was made possible by performing in-situ SEM. When temperature was increased above 60°C , PEO matrix was seen to completely melt, while PLA nodules remained unaffected. Such tendency completely matches the observations made from DSC for this sample (**Figure 4.20**). Indeed, sample was shown to exhibit thermal features corresponding to both polymers. PEO glass transition and melting temperature were observed at -41.1°C and 45.0°C (onset) respectively, while PLA glass transition and melting temperature were observed at higher temperatures of 63.3°C and 143.7°C (onset) respectively. In order to reach a compromise between conductivity and printability, future investigations may be concentrated on comb-block polymers such as the PLA/PEG-based SPE developed recently by Zaheer et al.²⁸ depicting a conductivity of $6.9 \times 10^{-5} \text{ S cm}^{-1}$ at ambient temperature and a wide electrochemical stability window up to 4.6 vs. Li/Li^+ .

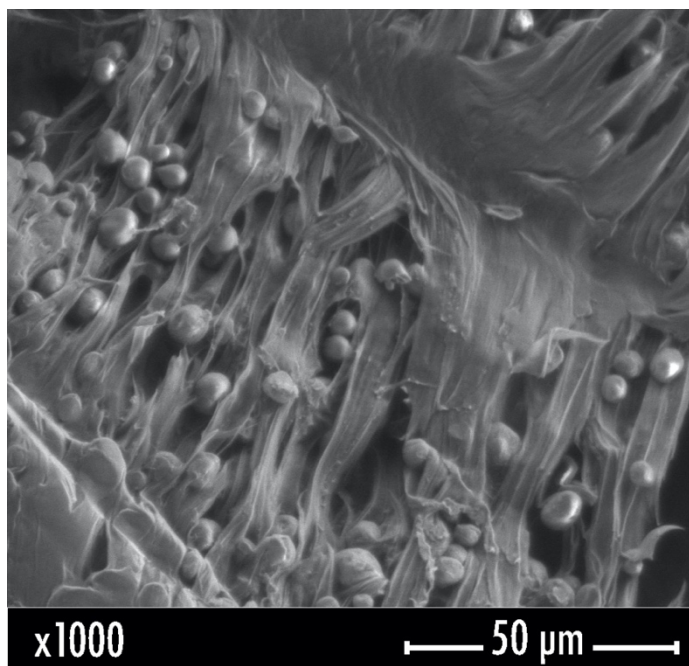


Figure 4.19. Secondary Electron SEM images (5kV) depicting the PEO/PLA wt% 50:50 film sample microstructure.

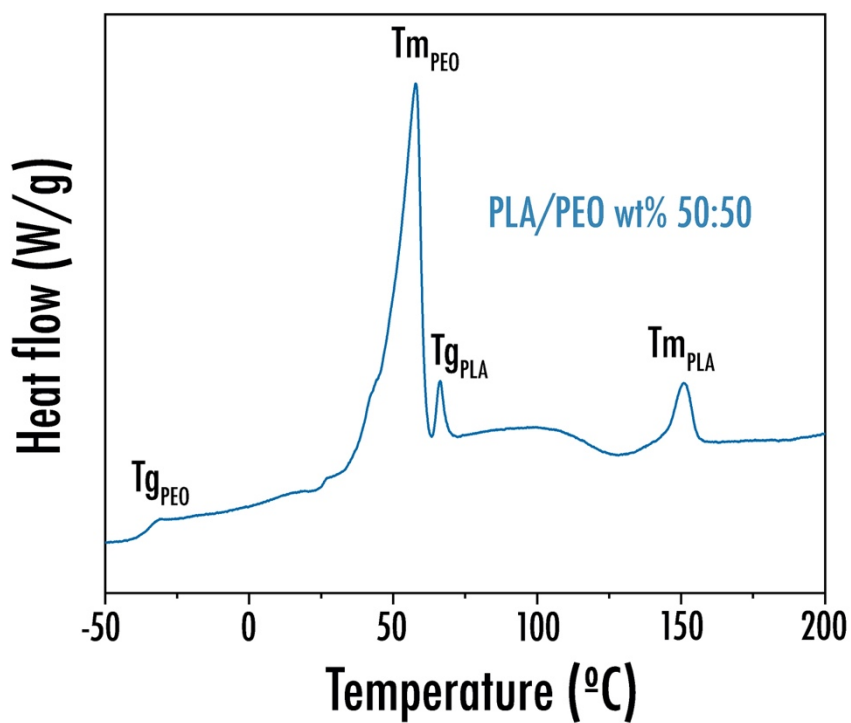


Figure 4.20. DSC curve for the prepared PLA/PEO (wt.% 50:50) film sample.

Conclusions

To conclude, in this chapter, a 3D printable PEO/LiTFSI filament was specially designed to be used as solid polymer electrolyte in a lithium-ion battery and to feed a FDM 3D-printer. For this purpose, optimization of the ionic conductivity was first accomplished by fine-tuning the O/Li⁺ ratio. Most promising film composition (O/Li⁺ = 20) was finally used for extrusion and 3D-printing. Important machine modifications were required to finally print a SPE 3 mm disc ($2.18 \times 10^{-3} \text{ S cm}^{-1}$ at 90 °C). Indeed, while the printability of the optimized PEO/LiTFSI 20:1 filament was demonstrated, printing still remains highly complex due to the flexibility and sticky behavior of this latter as clearly demonstrated during the nano-indentation experiments. This study clearly opens the way toward a fully printed solid state battery. Future studies may be focused on the introduction of a comb-block polymer with a view to confer some rigidity.²⁹ Also, another way to facilitate the printability could be the use of a modified FDM 3D using directly pellets or powder as material source instead of a filament.

Besides, using three different EIS sample holders (lateral, sandwich and interdigitated-comb), it was found that conductivity values are significantly different for a same sample. This behavior was reproducible and observed for each tested composition (PEO/LiTFSI). Lateral configuration displays the highest conductivities due to the polymer chains orientation along the substrate XY plane. Advantage of the interdigitated-comb sample holder is that sample dimensions (thickness) are not required to calculate the conductivity value, thus preventing from any eventual measurement errors. Nonetheless, it requires further investigations as lower conductivity values are obtained using this particular configuration. To confirm this behavior, upcoming research may also be extended to other polymers and salts. In future studies, authors might rather report a delimited conductivity-zone instead of a very specific value within the low temperature range (<90 °C).

References

1. Marcinek, M.; Syzdek, J.; Marczewski, M.; Piszcz, M.; Niedzicki, L.; Kalita, M.; Plewa-Marczewska, A.; Bitner, A.; Wieczorek, P.; Trzeciak, T.; Kasprzyk, M.; Lezak, P.; Zukowska, Z.; Zalewska, A.; Wieczorek, W., Electrolytes for Li-ion transport - Review (vol 276, pg 107, 2015). *Solid State Ionics* **2015**, 282, 95-95.
2. Wang, F.; Li, L.; Yang, X.; You, J.; Xu, Y.; Wang, H.; Ma, Y.; Gao, G., Influence of additives in a PVDF-based solid polymer electrolyte on conductivity and Li-ion battery performance. *Sustainable Energy & Fuels* **2018**, 2, (2), 492-498.
3. Abraham, K. M.; Jiang, Z.; Carroll, B., Highly conductive PEO-like polymer electrolytes. *Chemistry of Materials* **1997**, 9, (9), 1978-1988.
4. Gauthier, M.; Fauteux, D.; Vassort, G.; Belanger, A.; Duval, M.; Ricoux, P.; Chabagno, J. M.; Muller, D.; Rigaud, P.; Armand, M. B.; Deroo, D., Behavior of polymer electrolyte batteries at 80-100 degrees-C and near room-temperature. *Journal of Power Sources* **1985**, 14, (1-3), 23-26.
5. Mindemark, J.; Lacey, M. J.; Bowden, T.; Brandell, D., Beyond PEO-Alternative host materials for Li⁺-conducting solid polymer electrolytes. *Progress in Polymer Science* **2018**, 81, 114-143.
6. Croce, F.; Persi, L.; Scrosati, B.; Serraino-Fiory, F.; Plichta, E.; Hendrickson, M. A., Role of the ceramic fillers in enhancing the transport properties of composite polymer electrolytes. *Electrochimica Acta* **2001**, 46, (16), 2457-2461.
7. Croce, F.; Curini, R.; Martinelli, A.; Persi, L.; Ronci, F.; Scrosati, B.; Caminiti, R., Physical and chemical properties of nanocomposite polymer electrolytes. *Journal of Physical Chemistry B* **1999**, 103, (48), 10632-10638.
8. Liu, W.; Lee, S. W.; Lin, D. C.; Shi, F. F.; Wang, S.; Sendek, A. D.; Cui, Y., Enhancing ionic conductivity in composite polymer electrolytes with well-aligned ceramic nanowires. *Nature Energy* **2017**, 2, (5).
9. Mauger, A.; Julien, C. M.; Paoletta, A.; Armand, M.; Zaghib, K., A comprehensive review of lithium salts and beyond for rechargeable batteries: Progress and perspectives. *Materials Science & Engineering R-Reports* **2018**, 134, 1-21.

10. Rey, I.; Johansson, P.; Lindgren, J.; Lassègues, J. C.; Grondin, J.; Servant, L., Spectroscopic and Theoretical Study of $(\text{CF}_3\text{SO}_2)_2\text{N}^-$ (TFSI) and $(\text{CF}_3\text{SO}_2)_2\text{NH}$ (HTFSI). *The Journal of Physical Chemistry A* **1998**, 102, (19), 3249-3258.
11. Fergus, J. W., Ceramic and polymeric solid electrolytes for lithium-ion batteries. *Journal of Power Sources* **2010**, 195, (15), 4554-4569.
12. Hekselman; Kalita, M.; Plewa-Marczewska, A.; Zukowska, G. Z.; Sasim, E.; Wieczorek, W.; Siekierski, M., Effect of calix 6 pyrrole anion receptor addition on properties of PEO-based solid polymer electrolytes doped with LiTf and LiTfSI salts. *Electrochimica Acta* **2010**, 55, (4), 1298-1307.
13. Zhang, Q. Q.; Liu, K.; Ding, F.; Liu, X. J., Recent advances in solid polymer electrolytes for lithium batteries. *Nano Research* **2017**, 10, (12), 4139-4174.
14. Vallée, A. Effets associés à la nature des anions dans les électrolytes poly(oxyéthylène)-sel de lithium. Université de Montréal (Canada), 1994.
15. Vallee, A.; Besner, S.; Prudhomme, J., Comparative study of poly(ethylene oxide) electrolytes made with $\text{LiN}(\text{CF}_3\text{SO}_2)_2$, LiCF_3SO_3 and LiClO_4 - thermal-properties and conductivity behavior. *Electrochimica Acta* **1992**, 37, (9), 1579-1583.
16. Devaux, D., PhD Thesis, Characterization and optimization of block copolymers as electrolytes for lithium metal batteries. **2012**.
17. Lascaud, S.; Perrier, M.; Armand, M.; Prud'homme, J.; Kapfer, B.; Vallee, A.; Gauthier, M., Evidence for ion pairs and/or triple ions from transport measurements in mixed-alkali polyether electrolytes. *Electrochimica Acta* **1998**, 43, (10-11), 1407-1414.
18. Devaux, D.; Bouchet, R.; Gle, D.; Denoyel, R., Mechanism of ion transport in PEO/LiTFSI complexes: Effect of temperature, molecular weight and end groups. *Solid State Ionics* **2012**, 227, 119-127.
19. Ibrahim, M.; Claudel, J.; Kourtiche, D.; Nadi, M., Geometric parameters optimization of planar interdigitated electrodes for bioimpedance spectroscopy. *Journal of Electrical Bioimpedance* **2019**, 4, (1), 13-22.
20. Olthuis, W.; Streekstra, W.; Bergveld, P., Theoretical and experimental-determination of cell constants of planar-interdigitated electrolyte conductivity sensors. *Sensors and Actuators B-Chemical* **1995**, 24, (1-3), 252-256.

21. Golodnitsky, D.; Livshits, E.; Peled, E., Highly conductive oriented PEO-based polymer electrolytes. *Macromolecular Symposia* **2003**, 203, 27-45.
22. Armand, M. B., Polymer Electrolytes. *Annual Review of Materials Science* **1986**, 16, (1), 245-261.
23. Shi, J.; Vincent, C. A., The effect of molecular-weight on cation mobility in polymer electrolytes. *Solid State Ionics* **1993**, 60, (1-3), 11-17.
24. Oliver, W. C.; Pharr, G. M., An improved technique for determining hardness and elastic-modulus using load and displacement sensing indentation experiments. *Journal of Materials Research* **1992**, 7, (6), 1564-1583.
25. Jee, A.-Y.; Lee, H.; Lee, Y.; Lee, M., Determination of the elastic modulus of poly(ethylene oxide) using a photoisomerizing dye. *Chemical Physics* **2013**, 422, 246-250.
26. Ferretti, A.; Carreau, P. J.; Gerard, P., Rheological and mechanical properties of PEO/block copolymer blends. *Polymer Engineering and Science* **2005**, 45, (10), 1385-1394.
27. Ragonés, H.; Vinegrad, A.; Ardel, G.; Goor, M.; Kamir, Y.; Dorfman, M. M.; Gladkikh, A.; Golodnitsky, D., On the Road to a Multi-Coaxial-Cable Battery: Development of a Novel 3D-Printed Composite Solid Electrolyte. *Journal of the Electrochemical Society* **2019**, 167, (1).
28. Zaheer, M.; Xu, H.; Wang, B.; Li, L.; Deng, Y., An In Situ Polymerized Comb-Like PLA/PEG-based Solid Polymer Electrolyte for Lithium Metal Batteries. *Journal of the Electrochemical Society* **2019**, 167, (1).
29. Aldalur, I.; Martinez-Ibanez, M.; Piszcz, M.; Zhang, H.; Armanda, M., Self-Standing Highly Conductive Solid Electrolytes Based on Block Copolymers for Rechargeable All-Solid-State Lithium-Metal Batteries. *Batteries & Supercaps* **2018**, 1, (4), 149-159.

Chapter 5.

PP-based LIB 3D-printing via FDM and SLS

Chapter 5. PP-based LIB 3D-printing via FDM and SLS

5.1. Introduction.....	198
5.2. Polymer matrix: PLA vs. PP.....	199
5.3. PP-based positive electrode via SLS and FDM.....	199
5.3.1. Elaboration process.....	200
5.3.2. Printing of positive electrodes of the same composition.....	202
5.3.2.1. Electrical conductivity characterization	203
5.3.2.2. Electron microscopy	204
5.3.2.3. Electrochemical characterization	207
5.3.2.4. Mechanical characterization	209
5.3.3. Higher charge loading via FDM	210
5.3.3.1. Mechanical characterization	211
5.3.3.2. Electrical conductivity characterization	212
5.3.3.3. Electrochemical characterization	214
5.3.4. Future SLS and FDM independent electrodes optimization	215
5.3.4.1. SLS electrodes	215
5.3.4.2. FDM electrodes	216
5.3.5. Considering the complete LIB printability	218
Conclusions.....	219
References	221

5.1. Introduction

As depicted previously, **Chapters 2 and 3** were dedicated exclusively on the formulation and printing of PLA-based composite filaments corresponding to the electrodes and separator of a lithium-ion battery operating with a liquid electrolyte. Nonetheless, as it will be demonstrated in the next section, PLA polymer matrix is suspected to dissolve within the liquid electrolyte upon time. Hence, two options must be explored thoroughly in the future: 1) An optimization of the liquid electrolyte must be performed in order to enhance ionic conductivity while maintaining the PLA stability upon cycling; 2) Others polymer matrices must be considered instead of PLA. Recently, option n°1 had been considered by Reyes et al.¹ who concluded that a 1:1 (volume ratio) solution of propylene carbonate (PC) and ethyl methyl carbonate (EMC) with 1 M LiClO₄ might be used in future research as PLA film infused within the mixture depicted an ionic conductivity of $8.5 \times 10^{-5} \text{ S cm}^{-1}$ (20 °C) and retained its mechanical integrity while presenting an arguable significant volume change of 29%. In this context, it was rather decided to focus the last part of this PhD thesis on option n°2. Hence, instead of PLA, the development of a polypropylene (PP)-based positive electrode was initiated. In parallel with the FDM additive manufacturing technique, the ability of the SLS process was here also examined to 3D-print PP-based LIB components. This work being ongoing at the moment this PhD is written, only preliminary results (cf. **Preface - IV**) including requirements for printing materials, resolution, advantages and drawbacks of each technique to print PP electrodes will be presented in the following sections. As part of an international collaboration, SLS printing was performed by Professor Matti Haukka's group, located at the University of Jyväskylä, Finland.

5.2. Polymer matrix: PLA vs. PP

Due to its unique properties such as high mechanical strength, low toxicity and low melting/printing temperature in comparison with other offered options (cf. **2.1.2. Polymer choice**), PLA was previously chosen as polymer matrix for the composite filament formulation (cf. **Chapter 2 and 3**). Nonetheless, it lately appeared that PLA might be dissolved when soaked during a certain amount of time within the liquid electrolyte (1 M LiPF₆ in ethylene carbonate and diethyl carbonate — EC:DEC 1:1 weight ratio). Once placed in the liquid electrolyte mixture, PLA membrane absorbs large amount of electrolyte and swells due to the hydrophilic nature of PLA, thus creating a gel. This behavior is favored by the oxygen presence in PLA chains interacting with lithium cations. While this phenomenon may enhance the ionic conductivity and further electrochemical performances on the short term, degradation of the PLA composites membranes might lead to undesired phenomenon such as short-circuit on the long-term.

On the other hand, PP, usually used as polymer matrix within commercial separators,^{2,3} is known for being chemically inert within the liquid electrolyte. This behavior can be easily explained by its chains which does not contain any oxygen atoms. Hence, PP membranes do not swell when soaked in the liquid electrolyte and are expected to be more resistant than the PLA-based on the long term. In this context, the elaboration of a PP-based FDM filament for its use as a positive electrode within a LIB was initiated. In parallel with FDM, the ability of the SLS process was also studied to 3D-print PP-based LIB components.

5.3. PP-based positive electrode via SLS and FDM

A preliminary and comparative study specifically focused on the formulation of a positive electrode composed of polypropylene acting as polymer matrix, LiFePO₄ as active material, and carbon black (C45) or carbon nanofibers (CNF) as conductive additives was initiated. Polypropylene powder AdSint® PP flex (particle size: 70 μm) was provided by Advanc3d Materials, Germany. LiFePO₄ (LFP) (particle size: 1 μm) provided by Aleees was used as active material for the positive electrode of the lithium-ion battery. Carbon black Timcal Super 45 (C45) (particle size: 20 nm, 45 m² g⁻¹), carbon nanofibers (CNF), (D × L 100nm × 20-200 μm, 24 m² g⁻¹) and paraffinic oil used as plasticizer for PP were all purchased from Sigma-Aldrich, USA.

5.3.1. Elaboration process

First of all, the polypropylene powder was combined and mixed thoroughly in a mortar with the desired amount of LFP, C45, CNF and paraffinic oil, to prepare the composition depicted in **Table 5.1**.

Table 5.1. Summary of the prepared electrodes composition (cf. **Preface - IV**).

Further printed via SLS and/or FDM	Wt.% total composite PP/LFP/Plasticizer/Conductive additive	Vol.% total composite PP/LFP/Plasticizer/Conductive additive
SLS and FDM	70/26/0/4	85/13/0/2
FDM	45/45/0/10	66/27/0/7
FDM	*33/49/13/5	*48/29/13/3

* During the extrusion and printing processes, paraffinic oil acting here as a plasticizer is partially evaporated leading to an even higher percentage of charges considering the total composite electrode. For weight-volume conversion, materials densities were acquired by helium pycnometer.

Subsequently, in order to produce a standard 1.75 mm diameter FDM 3D-printing filament, a Filabot Original extruder supplied by Filabot Triex LLC, USA was fed with the afore-mentioned pre-mixed powder. The extruder temperature was set at the relatively high temperature of 250°C, thereby obtaining a satisfactory extrusion rate. The filament released from the extruder nozzle was subsequently rolled around a spool by using a Filabot spooler (Filabot Triex LLC, USA). The extruder was purged thoroughly with pure PP before extrusion of each sample. Electrode filaments were kept in appropriate storage conditions under low temperature and in confined environment with low humidity. 11 mm diameter positive electrode discs (200 µm and 1mm thick) and specimens ISO527-2 were finally printed via FDM (**Figure 5.1.a**) to perform further galvanostatic, electrochemical impedance spectroscopy and mechanical tests. Nozzle standard input and output diameters of respectively 1.75 mm and 0.4 mm were used. Best resolution in the Z direction is 0.20 mm for the first layer and 0.05 mm for the following. Nozzle temperature was set at 250°C. Fan settings was set to 100%. Bed temperature was set to 100 °C in order to enhance the adherence of the first printed layer. Prior to printing of each sample, nozzle was cleaned thoroughly by printing a 2 cm³ purge cube with the corresponding filament.

On the other hand, regarding the SLS process (**Figure 5.1.b**), the afore-mentioned homogeneous powder mixture corresponding to the desired composition was directly inserted to feed the SLS bed. A Sharebot SnowWhite SLS 3D printer was employed and relatively low energy consuming printing parameters were chosen to produce low-density electrodes (LASER power 100 % (of maximum of 14 W), LASER rate 64 000 (2560 mm s^{-1}); powder temperature $122 \text{ }^\circ\text{C}$; powder layer 0.25 mm; wait time 600 s; wait layer 12 s; warming layers 20; layer thickness 0.08 mm). Powder temperature was kept constant through the printing processes. The printed objects were carefully cleaned of all non-sintered powder with a brush before using them in experiments. While applying the defined settings, only very thick electrodes (3mm and 11 mm diameter) discs were possible to acquire in order to have mechanically resistant electrodes. Specimens ISO527-2 were also printed to perform mechanical tests.

This study here acting as a preliminary work, the extrusion (FDM) and printing parameters (FDM and SLS) were kept unchanged in the following sections. For both printing techniques, the same electrochemically-active material loading was first tested and then increased as high as possible.

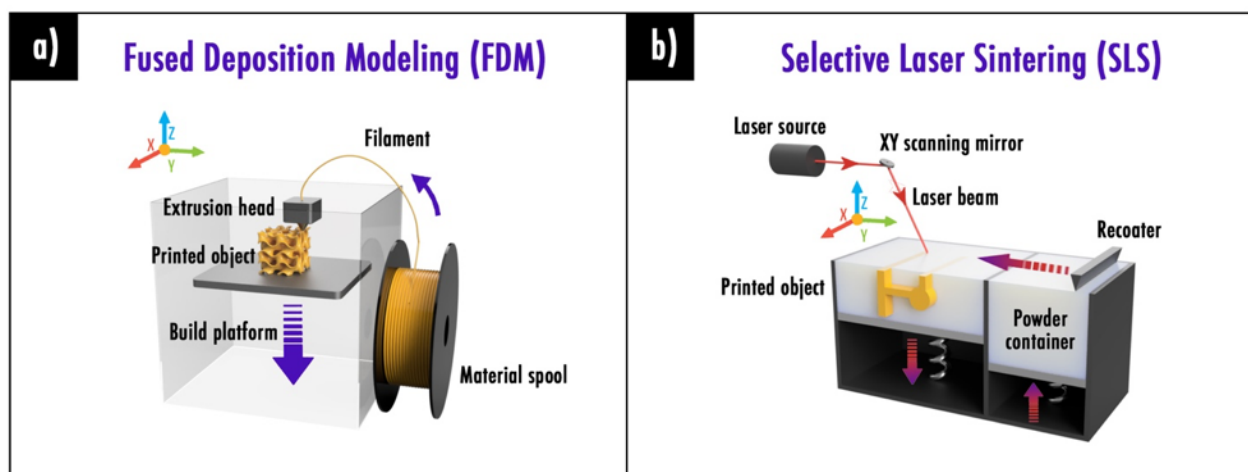


Figure 5.1. (a) Fused deposition modeling and (b) selective laser sintering 3D-printing scheme (cf. **Preface - IV**).

5.3.2. Printing of positive electrodes of the same composition

First part of this study was dedicated to the preparation of positive electrodes of the exact same composition through SLS and FDM. Positive electrode samples containing 26wt% LiFePO₄ as active material, 4wt% carbon black (C45) as conductive additives and 70wt% PP as polymer matrix were prepared. This specific composition was chosen as it corresponds to the highest loading of charges (active material + conductive additives) allowed by the SLS technique considering the aforementioned low energy printing parameters. Here, the loading of charges was maximized in order to enhance the electrochemical performances while still maintaining suitable mechanical properties for further handling and characterization. Experiencing a higher amount of charges was found to immediately result in major mechanical strength and printability issues.

On the other hand, a composite thermoplastic filament was prepared to feed the FDM printer. Hence, the afore-mentioned pre-mixed homogeneous powder was inserted into an extruder and a first PP/LFP/C45 filament was obtained. Due to the poor diameter consistency, the latter was pelletized and extruded again, resulting in a secondary filament with a much more reliable diameter (1.75 mm) as confirmed through SEM before printing. Via FDM printing, obtained electrodes were about 170 μm thick due to the first layer resolution limitation. Finally, it is important to mention that warping^{4, 5} tends to occur while printing polypropylene filaments. The material shrinkage, while 3D printing, causes the corners of the print to lift and detach from the build plate. To reduce this unfavorable effect with the PP/LiFePO₄/C45 composite, a heated bed set at 100°C and covered with adhesive tape was employed.

5.3.2.1. Electrical conductivity characterization

For both samples obtained by SLS and FDM with the exact same composition (26wt% LiFePO₄, 4wt% C45 and 70wt% PP), the influence of the AM technique on the electrode conductivity was investigated by electrochemical impedance spectroscopy (EIS). The exact same procedure than the one described previously (cf. 2.2.1.4.1. **Electrical conductivity**) was achieved. The corresponding impedance spectra were recorded from 20°C to 60°C. Nyquist and Bode plots portray typical behavior of an electronic conductor. Indeed, only Z' real part is depicted on the Nyquist plot whereas $|Z|$ magnitude is constant for all frequencies. For both tested samples, the electrical conductivity is increasing with temperature as exhibited in **Figure 5.2**, and homogeneous activation energy values equal to 0.101 eV (SLS) and 0.099 eV (FDM) are calculated.

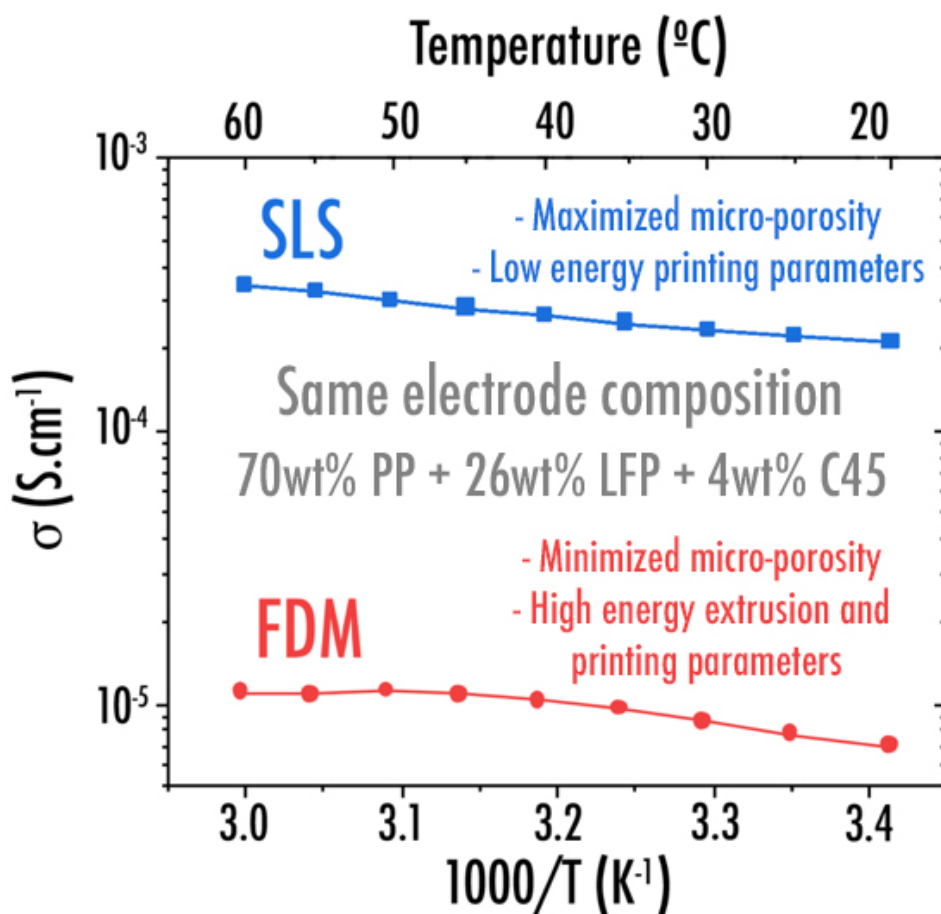


Figure 5.2. Arrhenius plots of the electrical conductivity for electrode of the same composition (70wt%PP + 26wt%LFP + 4wt%C45) printed via SLS and FDM (cf. Preface - IV).

From the results obtained, it can be clearly observed that depending on the printing technique, the electrodes depict very distinctive electrical performances. Here, electrode discs obtained by means of SLS, display electronic conductivity values about 30 times higher than the electrodes printed via FDM, on the whole recorded temperature range. Indeed, respectively at 20°C and 60°C, the SLS sample reveals a conductivity of 2.12×10^{-4} and 3.39×10^{-4} S cm⁻¹ while the FDM sample exhibits a much lower conductivity equals to 7.16×10^{-6} and 1.12×10^{-5} S cm⁻¹. Due to the printing technique itself as well as the LFP and PP insulating behavior, in addition to the relatively low quantity of conductive additives, these values still remain relatively low in comparison with what was depicted previously for the optimized PLA/LFP positive electrode film (cf. **2.2.2.2.1. Electrical conductivity**). Indeed, this latter, involving a much lower polymer amount (only 33%wt) exhibited a much higher electronic conductivity of 0.06 S cm⁻¹ at 50°C (cf. **Preface - II**). The incorporation of carbon additives such as C45 is here crucial to confer suitable electronical conductivity.

5.3.2.2. Electron microscopy

Similar to what was achieved previously for the PLA-based negative and positive electrode (cf. **Chapter 2**), the general homogeneity and the inner material (LFP and C45) dispersion within the PP matrix of the produced printed electrodes was examined by scanning electron microscope (5 kV) and transmission electron microscopy (200 kV). Prior TEM experiment, printed disc samples were cut and inserted in a resin following the exact same protocol described previously (cf. **2.2.1.4.2. Electrochemical characterization**). The conductivity difference observed between both samples in the previous section can be easily explained thanks to the images revealed by scanning electron microscopy and transmission electron microscopy depicting two completely different microstructures (**Figure 5.3**).

Same electrode composition 70wt% PP + 26wt% LFP + 4wt% C45

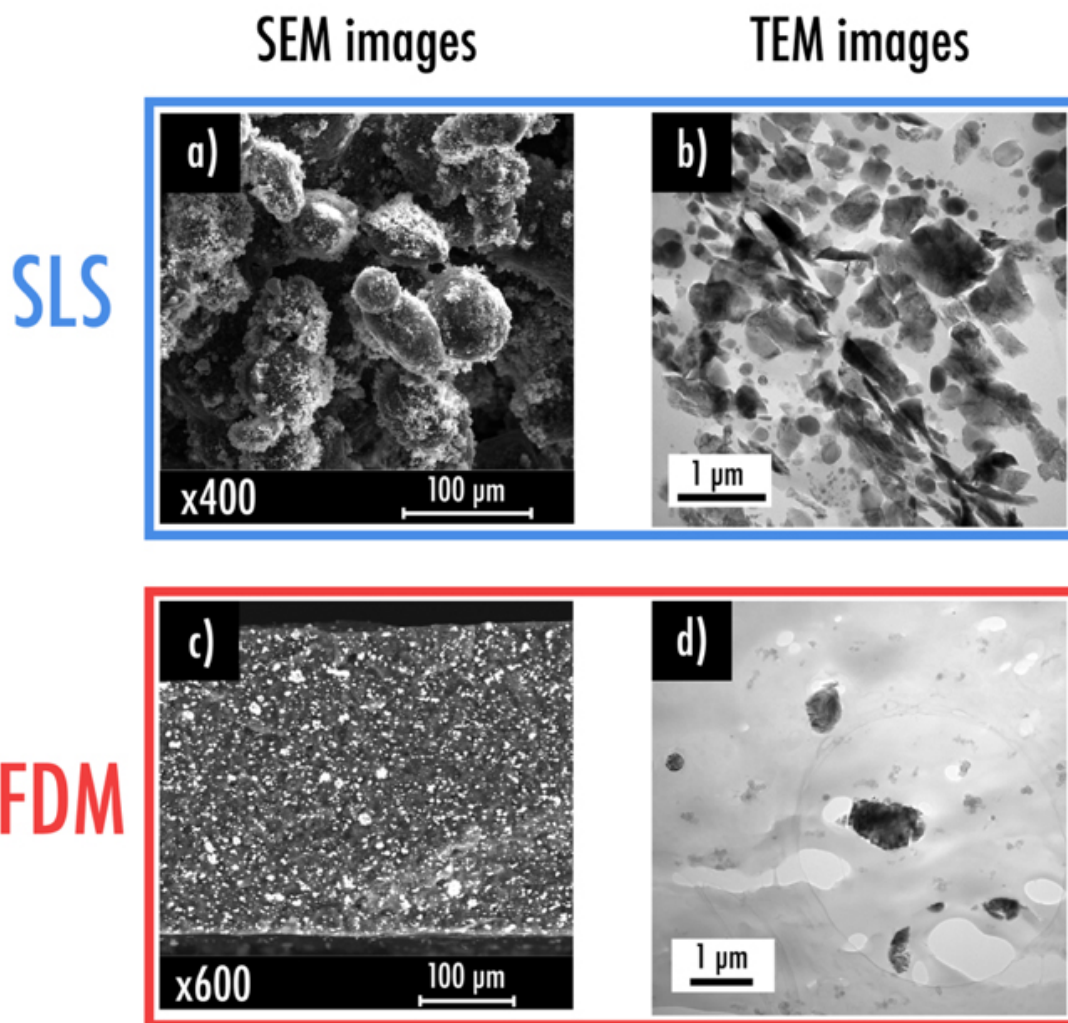


Figure 5.3. Cross-sectional images of the electrodes with the same composition (70wt%PP + 26wt%LFP + 4wt%C45) obtained via SLS or FDM: (a) Secondary electron SEM image of the SLS electrode in which spherical PP particles surfaces are covered with smaller charges particles consisting of LFP and C45; (b) TEM image of the SLS electrode where carbon black C45 (smaller grey particles) is homogeneously distributed between the LFP particles (bigger black particles) thus creating an efficient percolating network; (c) Backscattered SEM image of the FDM electrode in which LFP particles (white color) are isolated within the polymer matrix; (d) TEM image of the FDM electrode where carbon black C45 (smaller grey particles) and LFP (bigger black particles) are completely isolated within the nano-porous polymer matrix (cf. **Preface - IV**).

The SLS sample is composed of spherical PP polymer particles (70 μm) that were incompletely fused together on the surface during the sintering process (**Figure 5.3.a**). This was possible by fine-tuning the printing parameters in a low energy configuration. During the printing procedure, an important porosity with voids is created and a three-dimensional polymer network is clearly noticeable. Charges including the active material (LiFePO_4) and conductive additives particles (C45) are deposited in the surface of the PP spheres. Charges do not appear to be totally encapsulated within the PP matrix but are tightly attached to the incompletely melted surface. Thus, a percolating network composed of the C45 is created along all the microstructure and leads to the higher electrical conductivity values depicted via EIS. While this hypothesis cannot be confirmed via SEM as carbon black particles (20 nm) are not observable with this technique, it was confirmed by performing transmission electron microscopy (TEM) experiment as depicted in **Figure 5.3.b**. Indeed, C45 spherical particles (**Figure 5.4.a**) appear to be really well dispersed between the various LiFePO_4 particles. The latter are clearly identified thanks to their bigger size (1 μm) and crystalline olivine structure allowing the observation of the atomic arrangement (**Figure 5.4.b**).

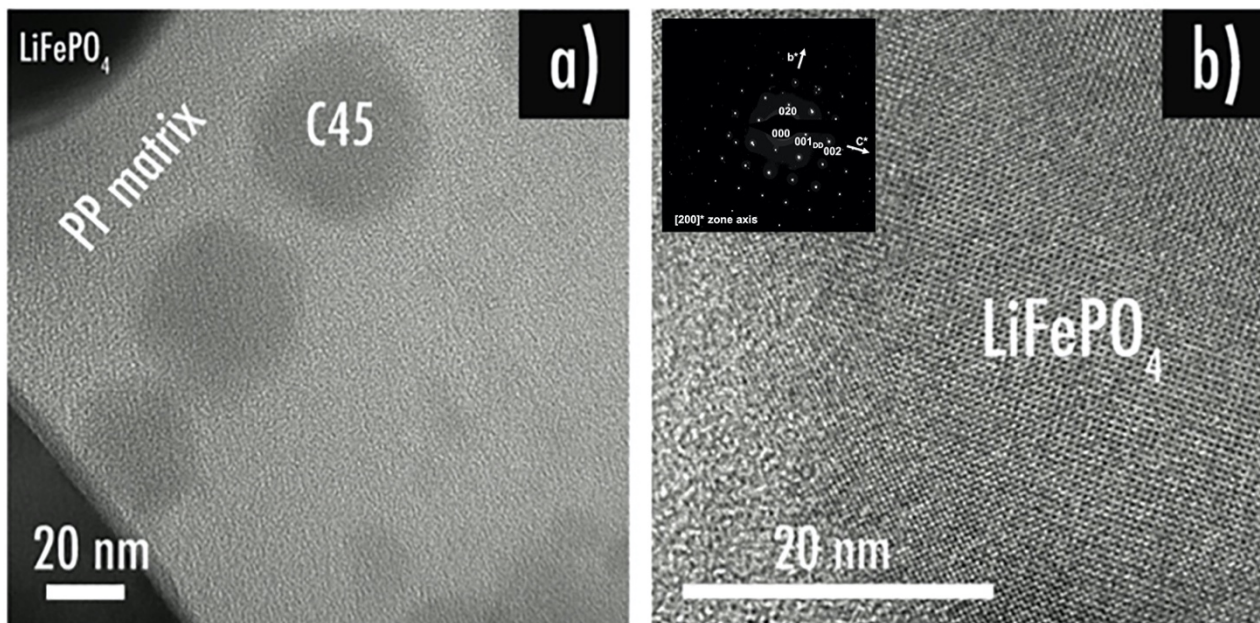


Figure 5.4. Cross-sectional TEM images of the SLS electrode: (a) carbon black C45 spherical particles are well dispersed between the LiFePO_4 particles; (b) olivine LiFePO_4 atomic arrangement. a^* zone axis Selected Area Electron Diffraction (SAED) pattern is displayed in inset (LFP: Pmnb ; $a=6.018\text{\AA}$, $b=10.34\text{\AA}$, $c=4.703\text{\AA}$) (cf. **Preface - IV**).

On the other hand, as expected, the FDM sample microstructure does not show any apparent micro-porosity (**Figure 5.3.c**). This can be explained by the relatively high extrusion and printing operating temperature (250°C). Backscattered SEM image (**Figure 5.3.c**) confirms that LiFePO₄ particles are evenly distributed in the polymer matrix. Nonetheless, it is important to emphasize that an important amount of these particles seems to be isolated within the polymer matrix. These active material particles being intimately related to the final electrochemical performances, it represents an important concern. Indeed, isolated active material particles within the polymer matrix will act as electrochemically dead-material within the final electrode. Likewise, by performing TEM experiments (**Figure 5.3.d**), it can be seen that the carbon black particles are also secluded within the PP matrix. Hence, it has obviously a detrimental effect on the percolating network and leads to the very low electrical conductivity values observed previously by EIS.

5.3.2.3. Electrochemical characterization

The electrochemical performances of the electrodes obtained by SLS and FDM were investigated. Swagelok-type cells were assembled following the afore-described exact same conditions (cf. **2.2.2.2.4. Electrochemical characterization**). Here also, 150 μL of 1 M LiPF₆ in ethylene carbonate and diethyl carbonate (EC:DEC 1:1 weight ratio) was used as liquid electrolyte (LP40, Merck KGaA, Germany). Subsequently, cells were galvanostatically charged (delithiation) and discharged (lithiation) at different current densities calculated per gram of active material, between 3.8 and 2.6 V (vs Li/Li⁺). The potential profiles versus specific capacity based on the active material, and specific capacity versus cycle number were studied thoroughly at various current densities (2.1, 4.2, 8.5, and 17 mA g⁻¹ of active material corresponding respectively to C/80, C/40, C/20 and C/10) as displayed in **Figure 5.5**.

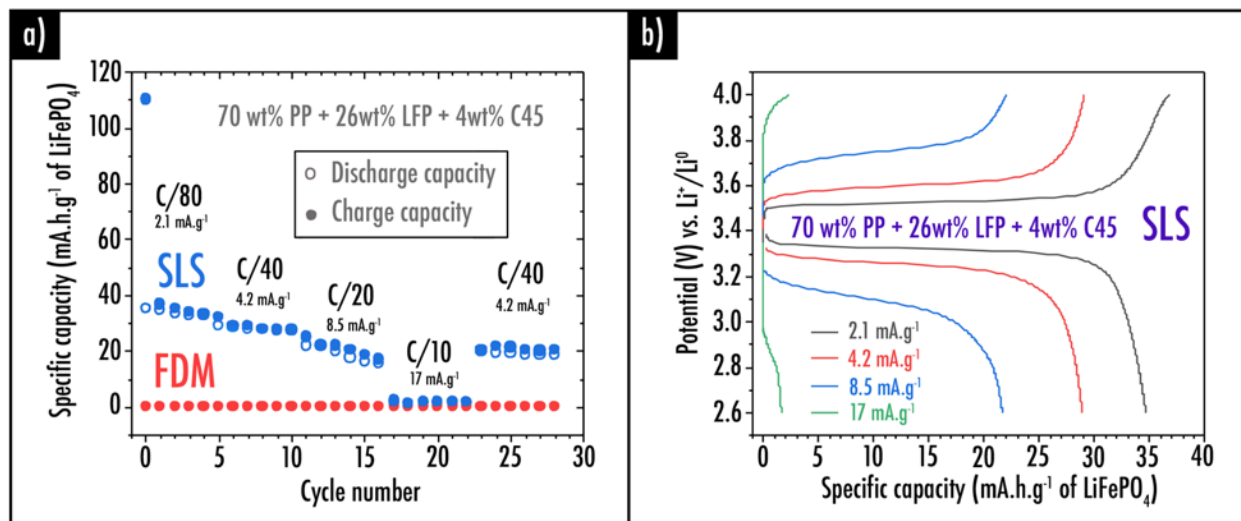


Figure 5.5. (a) Capacity retention plots at various current density for printed electrodes via SLS and FDM for composition containing 70wt%PP + 26wt%LFP + 4wt%C45; (b) Charge/discharge capacity profiles for the electrode printed via SLS (70wt%PP + 26wt%LFP + 4wt%C45) (cf. **Preface - IV**).

Due to its important micro-porosity and higher electronic conductivity, the SLS sample exhibits logically higher electrochemical performances. The latter depicts an important irreversible capacity during the first cycle of 74 mAh g⁻¹ of LiFePO₄ corresponding to a percentage loss of 65% at current density of 2.1 mA g⁻¹ and reversible capacity values of 35, 30, 20 and 2 mAh g⁻¹ of LiFePO₄ during 5 cycles at current density of 2.1, 4.2, 8.5, and 17 mA g⁻¹ respectively. When finally coming back at a lower current density of 8.5 mA g⁻¹, a good capacity retention was preserved. While the electrode depicts a promising and undeniable electrochemical response, it is important to note that values are still very far from the theoretical specific capacity of LFP (170 mAh g⁻¹). Moreover, considering that the total printed composite electrode is composed of only 26wt.% of active material (LFP), it means that the electrochemical performances reported per gram of total composite are much lower (reversible capacity of 9.1, 7.8, 5.2 and 0.5 mAh g⁻¹ of total composite at current density of 2.1, 4.2, 8.5, and 17 mA g⁻¹ respectively). On the other hand, the FDM sample, due to its absent micro-porosity and aforementioned isolated charges within the polymer matrix, depicts insignificant specific capacity values. The nano-porosity that was observed through TEM does not seem accessible by the lithium ions.

5.3.2.4. Mechanical characterization

Tensile strength experiments were finally performed on FDM and SLS printed specimens of composition (70%PP + 26%LFP + 4%C45), following the same characterization procedure described previously (cf. **2.2.1.3.1. Mechanical characterization and printability**). As depicted in **Table 5.2**, classical mechanical properties such as the Young's modulus, tensile strength and elongation at break were calculated from the stress-strain curves (**Figure 5.6**). Obtained values logically corroborate the previous observations done by microscopy (cf. **5.3.2.2. Electron microscopy**). Samples printed with both AM technologies exhibited a brittle behavior. Compared with pure PP, a drastically decrease of the elongation at break is observed of respectively 97 % for the SLS sample and 94% for FDM. This phenomenon can be explained by the addition of charges, known to decrease the elongation at break of a reinforced polymer. Regarding the Young's modulus and the tensile strength, it appears that both parameters corresponding to the SLS sample are lower than the ones obtained with FDM for the same composition. While the tendency observed for the FDM sample is classical (increase of the Young's modulus and decrease of the tensile strength in comparison with pure PP reference), the SLS sample with the exact same composition shows degraded properties due to its significant micro-porosity.

Table 5.2. Mechanical properties for printed electrodes of different composition (cf. **Preface - IV**).

Sample name and composition in wt%	Young's modulus (MPa)	Tensile strength (MPa)	Elongation at break (%)
Pure PP	1400 ± 100	25 ± 1	50 ± 10
SLS – 70%PP + 26%LFP + 4%C45	284 ± 38	2.55 ± 0.41	1.39 ± 0.13
FDM – 70%PP + 26%LFP + 4%C45	1468 ± 124	20.78 ± 1.28	2.87 ± 0.07

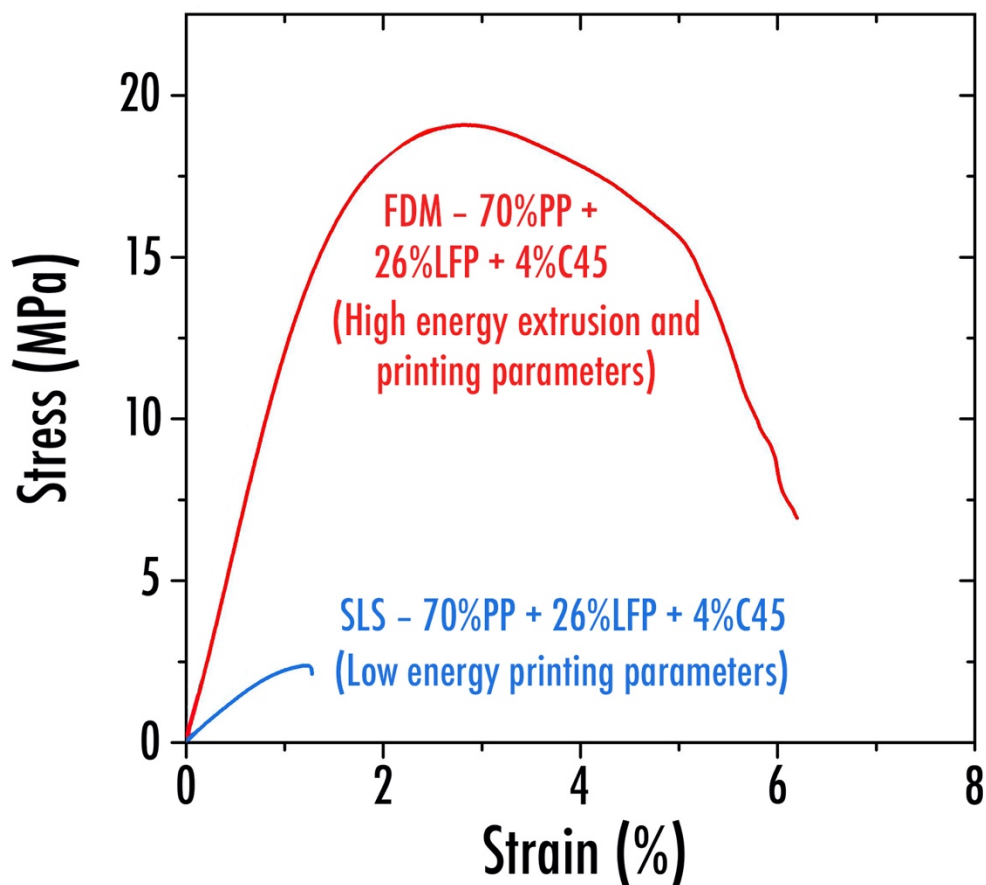


Figure 5.6. Strain-stress curves of the same electrode composition printed by SLS and FDM (cf. **Preface - IV**).

5.3.3. Higher charge loading via FDM

Distinct from what was observed previously using the SLS technique (maximum of 15 vol.% of charges allowed among the total composite with the aforementioned low energy printing parameters), it was possible via FDM (extrusion and printing parameters unchanged) to increase even more the amount of charges without affecting the filament printability. Indeed, as depicted previously (cf. **2.2.2.2.2. Printability and mechanical characterization**) in order to obtain enough mechanical performances to be printed, the total amount of charges (sum of active material and conductive additives) within the filament can reach up to 30 vol.%. This percentage can be further increased thanks to the introduction of an appropriate plasticizer, thus resulting in a final total amount of charges reaching up to 50 vol.%. Paraffinic oil, being traditionally used as

plasticizer for polypropylene,⁶ was here employed in order to enhance the charge loading within the total composite electrode filament and facilitate its printability. The summary of the electrode compositions produced via FDM and SLS is exhibited previously in **Table 5.1** (cf. **5.3.1. Elaboration process**). During both extrusion and printing processes, paraffinic oil is partially evaporated. Hence, this phenomenon leads to a higher percentage of charges when the printed electrode composition is considered.

5.3.3.1. Mechanical characterization

From the mechanical point of view, as expected, the addition of charges has an unfavorable outcome on the resulting mechanical strength of the printed electrodes (**Table 5.3** and **Figure 5.7**). An increase of the LFP weight content from 26% to 45% leads to a small evolution of the mechanical properties. In addition, a low decrease of the Young's modulus is observed while an increase should be obtained. All these observations (mechanical properties and previous SEM analysis) permit to conclude that the mechanical behavior is driven by the properties of the interface between the charges and the matrix. With the introduction of paraffin oil as plasticizer, Young's modulus and tensile strength tend to decrease while elongation at break increases in good agreement with literature.⁶ Although the resulting Young's modulus is relatively small, the subsequent filament is stiff enough to be printed.

Table 5.3. Mechanical properties for printed electrodes of different composition (cf. **Preface - IV**).

Sample name and composition in wt%	Young's modulus (MPa)	Tensile strength (MPa)	Elongation at break (%)
Pure PP	1400 ± 100	25 ± 1	50 ± 10
FDM – 70%PP + 26%LFP + 4%C45	1468 ± 124	20.78 ± 1.28	2.87 ± 0.07
FDM – 45%PP + 45%LFP + 10%C45	1435 ± 113	17.55 ± 2.50	2.88 ± 0.63
* FDM – 33%PP + 49%LFP + 13%Parrafinic oil + 5%C45	485 ± 48	8.17 ± 0.55	4.73 ± 0.66

* During the extrusion and printing processes, paraffinic oil acting here as a plasticizer is partially evaporated leading to an even higher percentage of charges considering the total composite electrode.

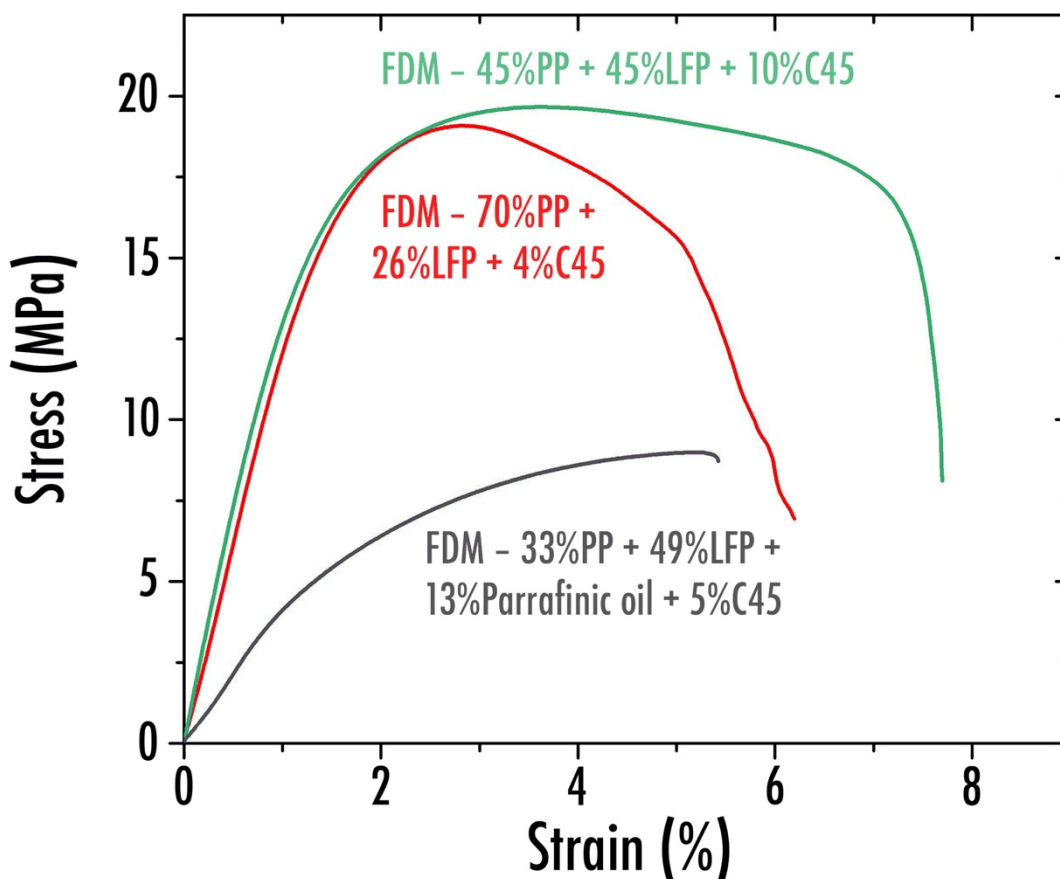


Figure 5.7. Strain-stress curves of the different electrode compositions printed via FDM (cf. Preface - IV).

5.3.3.2. Electrical conductivity characterization

As revealed in **Figure 5.8** depicting the Arrhenius plots of the electrical conductivity for each sample, C45 particles tend to be less isolated within the polymer matrix for FDM specimens containing a higher amount of charges, thus resulting in a more efficient percolating network conferring higher electronic conductivity values ($4.73 \times 10^{-5} \text{ S cm}^{-1}$ at 20°C for sample “FDM – 45%PP + 45%LFP + 10%C45” in comparison with $7.16 \times 10^{-6} \text{ S cm}^{-1}$ for the sample “FDM - 70%PP + 26%LFP + 4%C45” at the same temperature). Nonetheless, the addition of paraffinic oil, expected to create a micro-porosity through its evaporation during printing, does not seem to have an important and effective impact on the final electronic conductivity ($1.88 \times 10^{-5} \text{ S cm}^{-1}$ at 20°C for sample “33%PP + 49%LFP + 13%Parrafinic oil + 5%C45”). Values obtained are still much

lower than the one depicted for the “SLS - 70%PP + 26%LFP + 4%C45” sample ($2.12 \times 10^{-4} \text{ S cm}^{-1}$ at 20°C), thus meaning that while C45 additives are effectively used to improve the electronical conductivity, their final contribution within the FDM electrodes is not optimal. This difficulty to obtain an efficient percolating network within the FDM sample can be explained by the size of the C45 particles which is only about 20 nm as perceived previously through TEM (**Figure 5.4.a**). These latter are not all connected between each other, thus resulting in still relatively low conductivity. On the contrary, the introduction of bigger conductive particles would increase the probability to achieve an efficient percolating network. Hence, C45 additives appearing to be not appropriate for the non-porous FDM samples, it was decided to incorporate larger carbon nanofibers (CNF) about 20-200 μm long with a diameter of 100 nm. The exact same compositions were thus tested via FDM using CNF instead of C45. As expected, the introduction of CNF enhances the electronic conductivity values considerably, up to $1.60 \times 10^{-3} \text{ S cm}^{-1}$ at 20°C for sample “33%PP + 49%LFP + 13%Parrafinic oil + 5%CNF”.

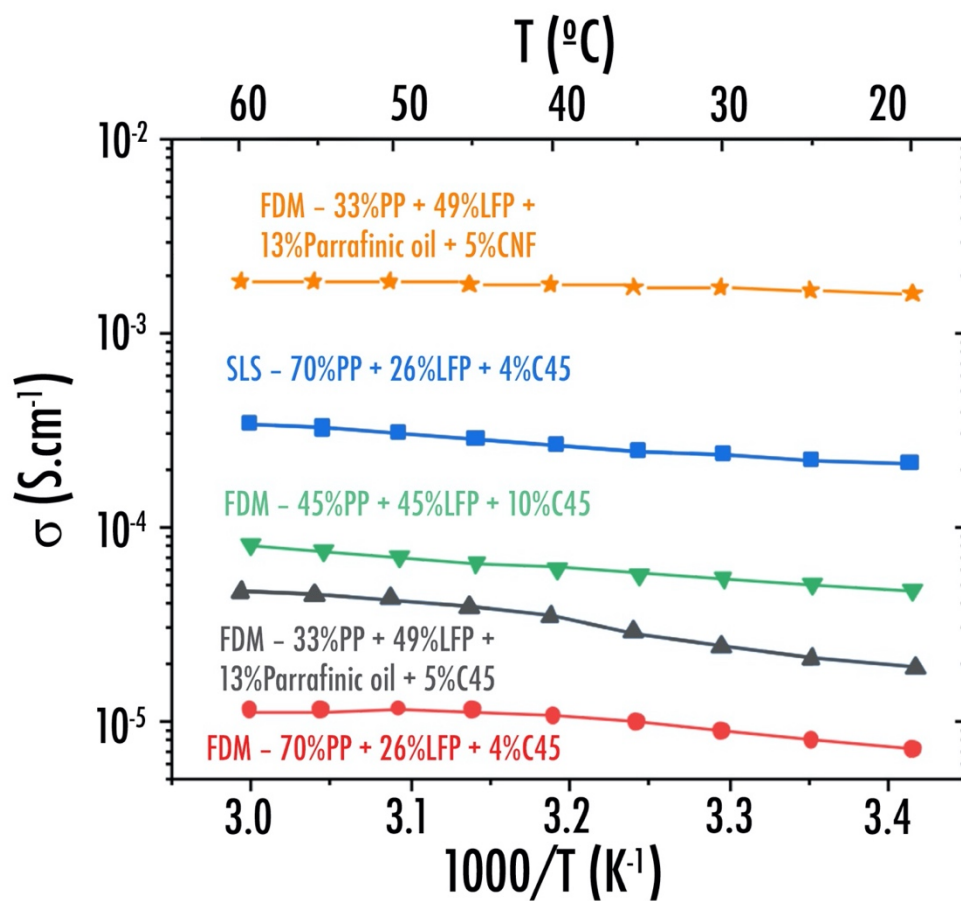


Figure 5.8. Arrhenius plots of the different electrode compositions printed by SLS and FDM (cf. **Preface - IV**).

5.3.3.3. Electrochemical characterization

Finally, investigations were focused on galvanostatic cycling to have a better understanding of the charges loading impact on the electrochemical performances. Same experimental conditions than the one described previously were set (cf. **5.3.2.3. Electrochemical characterization**). While samples comprising a higher loading of active material and conductive additives (“FDM – 45%PP + 45%LFP + 10%C45” and “FDM – 33%PP + 49%LFP + 13%Parrafinic oil + 5%CNF”) were expected to display highly enhanced performances, instead, insignificantly higher specific capacity values were barely attained in comparison with what was observed beforehand (**Figure 5.5**) for reference sample “FDM - 70%PP + 26%LFP + 4%C45”. These very poor performances can be justified by the lack of micro-porosity, caused in part by non-adequate printing parameters and little plasticizer evaporation, but also due to the chemical aversion of the liquid electrolyte with the PP polymer matrix. Indeed, it is well-known that within the electrolyte, Li^+ are solvated by around 4 EC molecules to form complexes.⁷ Upon cycling, under the applied electric field, these latter are driven through the liquid electrolyte from an electrode to the other. Li^+ desolvation process is thus required to allow these ions to enter correctly the active material. Previously, in **Chapter 2**, a polar polymer matrix (PLA) was employed, containing an electron withdrawing group C=O enabling to solvate Li^+ and having an affinity with the polarized molecules of EC. Hence, PLA was prone to absorb the liquid electrolyte, thus promoting samples ionic conductivity and electrochemical performances under cycling. However, here, the employed PP polymer matrix does not contain any polar groups thus conferring poor affinity with the polar molecules contained in the liquid electrolyte. The 3D-printed PP-based electrodes do not swell when soaked in the liquid electrolyte, resulting in poor ionic conductivity and specific capacity upon cycling.

5.3.4. Future SLS and FDM independent electrodes optimization

5.3.4.1. SLS electrodes

In the above sections, the preparation of the PP-based positive electrodes through SLS was performed while setting printing parameters in a “low energy configuration” in order to maximize the micro-porosity and favor the electrochemical properties (**Figure 5.9**). So far, due to the LASER power which was kept relatively low, the PP particles were sintered in such a way that only their surfaces were partially melted. Charges being evenly distributed on the PP particles surface, active material particles (LFP) were easily reachable by the liquid electrolyte favoring electrochemical performances under cycling while C45 created an efficient percolating network leading to good electronic conductivity of the electrode. Hence, as highlighted in the previous experiments, SLS seems to be a very promising technique to print highly micro-porous electrodes. Higher charges loadings and lower electrode thickness would require selecting appropriate printing parameters such as a higher LASER power, longer exposition time and higher local temperature to reach the best compromise between electrochemical and mechanical properties. In a future study, the impact of these parameters on the resulting electrode performances could be investigated.

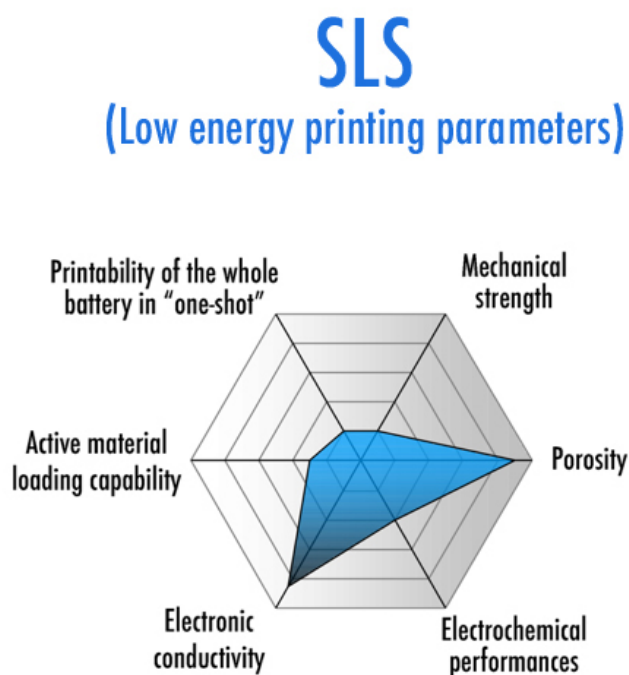


Figure 5.9. Summary of the advantages/drawbacks of SLS (considering a low energy printing parameters configuration) for the LIB printability (cf. **Preface - IV**).

5.3.4.2. FDM electrodes

On the other hand, the preparation of the positive electrodes through FDM was completed while setting parameters in a “high energy configuration” in order to ease the extrusion and printing processes and favor the mechanical properties (**Figure 5.10**). Unfortunately, even if the introduction of a high amount of charges was possible via FDM, the electronic conductivity and electrochemical performances under cycling were drastically limited due to the LFP and conductive particles isolation within the PP polymer matrix. While it was demonstrated in the **Chapter 2** for PLA-based electrodes that a micro-porosity could be created by introducing a plasticizer, paraffinic oil which was utilized here to plasticize PP does not appear to be effective enough. This behavior is different than what was observed previously (cf. **Chapter 2**) where the addition of PEGDME500 to plasticize PLA tends to create an important micro-porosity after extrusion and printing steps. Indeed, it was demonstrated that PEGDME500 partially evaporates during both steps but also upon time, thus creating a micro-porosity leading to an enhanced ionic conductivity and better electrochemical performances under galvanostatic cycling. Hence, future research may be dedicated to find the appropriate plasticizer for PP to create a significant micro-porosity capable to be filled with electrolyte or to find a plasticizer able to absorb electrolyte. Paraffinic oil employed here may inappropriately grease all the surfaces and interfaces, and be dissolved in the liquid electrolyte thus diminishing the resulting conductivities. The introduction of a polar polymer matrix coupled with the addition of ceramic nanoparticles such as SiO₂ or Al₂O₃ within the electrodes could be also investigated to enhance the electrolyte impregnation. Furthermore, surfactants containing EO units and long alkyl chains (Brij type) must be investigated in order to reduce the polarization. In parallel, an in-depth optimization of the extrusion and printing temperatures must be achieved in a future work in order to reach the best compromise between mechanical and electrochemical performances.

FDM

(High energy extrusion and printing parameters)

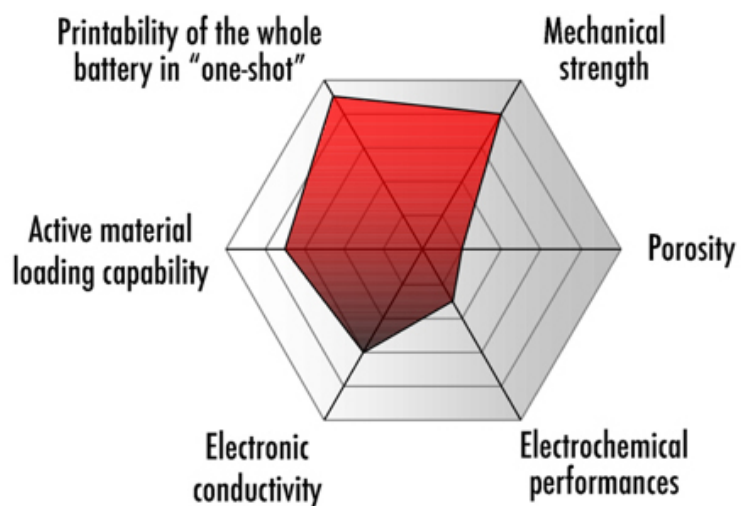


Figure 5.10. Summary of the advantages/drawbacks of FDM (in a high energy extrusion and printing parameters configuration) for the LIB printability (cf. **Preface - IV**).

5.3.5. Considering the complete LIB printability

The ultimate goal of this project being the printability of the complete lithium-ion battery in one single step, the multi-material printing abilities for both FDM and SLS techniques must be thoroughly compared.

As depicted previously, FDM printing already offers many different multi-material commercial options with a view to print complete LIB complex architectures in one single step (cf. **3.4.2. Multi-materials FDM printing**). In the meanwhile, so far, very few studies were reported in literature on LIB SLS 3D-printing precisely because this powder bed fusion printing technique does not allow to print the full battery in one single print (“one shot”). Indeed, printability of multi-material objects via SLS or SLM is not widely established for now.⁸ During SLS printing, the object is completely immersed within the material powder, thus it is technically not possible for now to print an object with six different kind of powder corresponding to each part of the battery (negative electrode, positive electrode, solid electrolyte, Cu and Al based current collectors and packaging) in one single print. The only alternative for now is to print each part separately and to assemble it afterwards. Hence, only planar or perfectly fitting printed parts can be considered. 3D complex interpenetrated architectures cannot be obtained via SLS for now. Unfortunately, this kind of architectures is expected to result in enhanced performances in terms of specific capacity and power as demonstrated beforehand (cf. **3D architectures impact on electrochemical performances**). The development and use of a hybrid printer configuration combining many AM techniques, such as FDM, SLS and LDM (among others) may be an interesting solution to reach efficient complex LIB interpenetrated 3D-architectures.

Conclusions

This last chapter of this PhD thesis was focused on the development of PP-based composite electrodes via FDM and SLS processes. PLA polymer matrix being suspected to dissolve within the liquid electrolyte upon time, PP was here employed to overcome this issue. The development of a polypropylene (PP)-based composite filament to be used as positive electrode in a LIB and feed a FDM printer was thus initiated. In parallel with the FDM additive manufacturing technique, the ability of the SLS process was here also examined to 3D-print PP-based LIB components. This study acting as a preliminary work, the extrusion (FDM) and printing parameters (FDM and SLS) were kept unchanged from the outset: high energy extrusion and printing parameters were set for the FDM technique while low energy printing parameters were fixed for SLS.

Considering these settings, it was demonstrated that resulting electrical, morphological, mechanical and electrochemical performances are significantly different for a similar electrode composition (26wt% LiFePO_4 as active material, 4wt% carbon black (C45) as conductive additives and 70wt% PP) printed via SLS or FDM. A clearly noticeable 3D polymer network was created with SLS in which an important porosity was witnessed. Interestingly, charges appeared to be deposited uniformly at the PP particles surface and did not appear to be entirely encapsulated within the PP matrix. Such an electrode resulted in an efficient percolating network that, composed of the C45 along the microstructure, leads to a promising electronical conductivity. Moreover, due to the great LFP accessibility for the liquid electrolyte, decent electrochemical performances were observed. These latter are nonetheless still highly limited by the low active material loading within the composite. Indeed, increasing the charge loading within the SLS electrode was shown to immediately result in poor mechanical properties. In parallel, considering the afore-mentioned printing parameters, FDM electrode sample of the same composition depicted a very dense microstructure with almost no porosity, leading to acceptable mechanical properties. Nonetheless, active material particles and conductive additives were shown to be completely encapsulated within the polymer matrix thus leading to very poor electrochemical and electrical performances.

On the other hand, the loading of charges within the FDM electrode was then maximized in order to enhance the electrochemical performances while still maintaining suitable mechanical properties for further handling and characterization. Higher loading of charges was made possible

through the introduction of paraffinic oil used as plasticizer for polypropylene. Unfortunately, the electronic conductivity and electrochemical performances under cycling were still significantly limited due to the remaining LFP and conductive particles isolation within the PP polymer matrix. Hence, future research should be devoted to find the appropriate plasticizer for PP to create a significant micro-porosity capable to be filled with electrolyte. The introduction of a polar polymer matrix coupled with the addition of ceramic nanoparticles such as SiO_2 or Al_2O_3 within the electrodes must also be investigated to improve the electrolyte impregnation. In parallel, a major optimization of the extrusion and printing temperatures must be accomplished in a future work to reach the best compromise between mechanical and electrochemical performances.

To conclude, from this comparative study, it is clear that neither FDM nor SLS should be eliminated hastily as both techniques present advantages and drawbacks for the LIB printability. Research routes must be kept opened for now on both techniques and especially on the development of innovative multi-materials and hybrid options that will, one day, pave the way towards an efficient LIB 3D-printing in one-single step.

References

1. Reyes, C.; Somogyi, R.; Niu, S.; Cruz, M. A.; Yang, F.; Catenacci, M. J.; Rhodes, C. P.; Wiley, B. J., Three-Dimensional Printing of a Complete Lithium Ion Battery with Fused Filament Fabrication. *ACS Applied Energy Materials* **2018**, 1, (10), 5268-5279.
2. Arora, P.; Zhang, Z. M., Battery separators. *Chemical Reviews* **2004**, 104, (10), 4419-4462.
3. Guan, H. Y.; Lian, F.; Ren, Y.; Wen, Y.; Pan, X. R.; Sun, J. L., Comparative study of different membranes as separators for rechargeable lithium-ion batteries. *International Journal of Minerals Metallurgy and Materials* **2013**, 20, (6), 598-603.
4. Wu, W. Z.; Geng, P.; Zhao, J.; Zhang, Y.; Rosen, D. W.; Zhang, H. B., Manufacture and thermal deformation analysis of semicrystalline polymer polyether ether ketone by 3D printing. *Materials Research Innovations* **2014**, 18, 12-16.
5. Ligon, S. C.; Liska, R.; Stampfl, J.; Gurr, M.; Mulhaupt, R., Polymers for 3D Printing and Customized Additive Manufacturing. *Chemical Reviews* **2017**, 117, (15), 10212-10290.
6. Wypych, G., Effect of plasticizers on properties of plasticized materials. In *Handbook of Plasticizers: Third Edition*, 2017; pp 209-219.
7. Cui, W.; Lansac, Y.; Lee, H.; Hong, S. T.; Jang, Y. H., Lithium ion solvation by ethylene carbonates in lithium-ion battery electrolytes, revisited by density functional theory with the hybrid solvation model and free energy correction in solution. *Physical Chemistry Chemical Physics* **2016**, 18, (34), 23607-23612.
8. Chivel, Y., New approach to multi-material processing in selective laser melting. *Laser Assisted Net Shape Engineering 9 International Conference on Photonic Technologies Proceedings of the Lane 2016* **2016**, 83, 891-898.

General conclusions and perspectives

General conclusions and perspectives

The aim of this PhD thesis was to demonstrate the printability of lithium-ion battery components by means of the Fused Deposition Modeling 3D-printing process. Combining the Laboratoire de Réactivité et Chimie des Solides (LRCS) and Laboratoire des Technologies Innovantes (LTI) expertise on energy storage and additive manufacturing techniques respectively, the development and optimization of FDM printable composite thermoplastic filaments was thus initiated.

First stage was dedicated to the development and optimization of PLA-based composite filaments, corresponding to each part of a liquid electrolyte LIB configuration. In order to maximize the electrochemical performances while still maintaining just enough mechanical strength for handling and printing, the active material (graphite for the negative electrode, and LiFePO_4 for the positive electrode) within the electrode filaments was increased as high as possible (up to 62.5 wt.%). The incorporation of such a high amount of charges was made possible thanks to the incorporation of an optimized amount of poly(ethylene glycol) dimethyl ether average $M_n \sim 500$ (PEGDME500) acting as plasticizer (100:40 PLA : PEGDME500 weight ratio). Electrodes optimization was subsequently performed through the addition of conductive additives improving the electronical conductivity. Similarly, for the current collector, the loading of Ag-Cu particles was maximized (up to 86.5 wt.%) to enhance the electronical conductivity. In parallel, a PLA-based separator filament was developed and optimized through the addition of SiO_2 nanoparticles (7 wt.%) improving the liquid electrolyte impregnation ($1.20 \times 10^{-4} \text{ S cm}^{-1}$ at 25°C after 10h immersion). For each composite filament developed along this thesis, the impact of granulometry on the final electrochemical and mechanical performances must be studied in detail in the future.

From the optimized electrodes and separator filament compositions, next step was devoted to the FDM 3D-printing of a complete LIB operating with a liquid electrolyte. Assembly from independent 3D-printed components (stacking), and direct printing of the complete LIB in a single step (one-shot), were demonstrated. Taking advantage of classical 3D-printing software (slicer) capabilities, separator infill patterns and density were introduced to improve the liquid electrolyte

impregnation and avoid short-circuits. An in-depth investigation is however required in the future to further optimize these infill parameters with the aim of diminishing the separator/electrolyte thickness. While electrochemical performances of the complete cells still remain relatively limited due to the printer resolution limitation (only 30 mAh g⁻¹ of active material at C/40 for the one-shot system), the complete LIB FDM 3D-printing proof of concept was demonstrated. In order to improve the overall LIB electrochemical performances, optimized current collector filament must be used to print the first layer subjected to the 200 μm thickness limitation. Hence, this will allow printability of thinner (down to 50 μm) and balanced electrodes on top of it. As emphasized in this PhD thesis, future investigations must be concentrated on multi-materials FDM printer options to allow the printability of three-dimensional complex LIB architectures (gyroid, interdigitated, cube) that were demonstrated to exhibit enhanced electrochemical performances in term of power compared to classical planar configuration.

On the other hand, as a safer alternative to the classical volatile and flammable organic solvent-based liquid electrolyte configuration, the printability of an all-solid-state LIB through FDM was initiated. The elaboration and optimization of a solid polymer electrolyte filament composed of PEO as polymer matrix and LiTFSI as lithium salt was achieved. The most electrochemically promising film composition (O/Li⁺ = 20) was finally used for extrusion and 3D-printing. After important machine modifications, a 3D-printed SPE disc exhibiting an ionic conductivity of $2.18 \times 10^{-3} \text{ S cm}^{-1}$ at 90 °C was obtained. While these results, here, clearly open the way toward a fully printed solid state battery, further investigations are still required. Particularly, these latter may be devoted to the introduction of comb-block polymers with a view to facilitate the printability without affecting the ionic conductivity. Besides, slightly apart from this LIB 3D-printing project, it is worth mentioning that using three different commercial EIS sample holders (lateral, sandwich and interdigitated-comb), conductivity values were found to be different for a same sample. Within the low temperature range (<90 °C), lateral configuration displayed the highest conductivities due to the polymer chains orientation along the substrate XY plane. This behavior was reproducible and observed for each SPE composition (PEO/LiTFSI) that were tested along this PhD thesis. Further investigations, highlighting the importance of the orientation of PEO chains, are required to really understand the origin of such discrepancies. In future studies, authors are rather encouraged to report a delimited conductivity-zone instead of a very specific value within the low temperature range (<90 °C).

Finally, acting as a perspective study, the last part of this PhD thesis was focused on the development of PP-based composite electrodes via FDM and SLS processes. In parallel, the ability of the SLS process to print LIB components was here also examined. By setting right from the outset, high energy extrusion and printing parameters for the FDM technique, and low energy printing parameters for SLS, the resulting electrical, morphological, mechanical and electrochemical performances were shown to be significantly different for a similar electrode composition. SLS sample depicted a high porosity, promising electronical and electrochemical performances, but was very brittle. On the contrary, FDM sample depicted low porosity, low electronical and electrochemical performances, but great mechanical strength. Through the addition of a plasticizer, the introduction of a much higher loading of active material was made possible through FDM. Future research should be devoted to find the appropriate plasticizer for PP to create a significant micro-porosity capable to be filled with electrolyte. A major optimization of the extrusion and printing temperatures is also required to reach the best compromise between mechanical and electrochemical performances.

In summary, in this PhD thesis, the development of homemade composite thermoplastic filaments and 3D-printing of a complete liquid-based lithium-ion battery was demonstrated by means of the Fused Deposition Modeling. Moreover, some optimizations have been proposed. Encouraged by the successful preliminary printing tests on solid polymer electrolyte, future investigations towards the multi-materials printability of all-solid-state lithium-ion batteries, based on the electrochemically-promising 3D complex architectures can be envisaged.

Abbreviations

ABS	Acrylonitrile-butadiene-styrene
AM	Additive manufacturing
ASTM	American Society for Testing and Materials
ATBC	Acetyl tributyl citrate
BN	Boron-nitride
C45	Carbon black Timcal Super 45
CAD	Computer-aided design
CB	Carbon black
CESH	Controlled environment sample holder
CMC	Carboxymethyl cellulose
CNF	Carbon nanofibers
CSP	Carbon black Super P
DCM	Dichloromethane
DEC	Diethyl carbonate
DIW	Direct Ink Writing
DLP	Digital light processing
DMC	Dimethyl carbonate
DSC	Differential scanning calorimetry
EBM	Electron beam melting
EC	Ethylene carbonate
EIS	Electrochemical Impedance Spectroscopy
EMC	Ethyl methyl carbonate
ETPTA	Ethoxylated trimethylolpropane triacrylate

FDM	Fused Deposition Modeling
GnP	Graphene nanoplatelets
GO	Graphene oxide
GPE	Gel polymer electrolyte
IR	Infrared
ITS	Intermediate temperature system
KB	Ketjen black
LAGP	$\text{Li}_{1.4}\text{Al}_{0.4}\text{Ge}_{1.6}(\text{PO}_4)_3$
LCO	LiCoO_2
LDM	Liquid Deposition Modeling
LFP	LiFePO_4
LGPS	$\text{Li}_{10}\text{GeP}_2\text{S}_{12}$
LIB	Lithium-ion battery
LiTFSI	Lithium bis(trifluoromethanesulfonyl)imide
LLTO	$\text{Li}_{0.33}\text{La}_{0.557}\text{TiO}_3$
LLZO	$\text{Li}_7\text{La}_3\text{Zr}_2\text{O}_{12}$
LMO	LiMn_2O_4
LSPSC	$\text{Li}_{9.54}\text{Si}_{1.74}\text{P}_{1.44}\text{S}_{11.7}\text{Cl}_{0.3}$
LT-LDM	Low temperature Liquid Deposition Modeling
LTO	$\text{Li}_4\text{Ti}_5\text{O}_{12}$
MWCNT	Multi-walled carbon nanotube
NCA	$\text{LiNi}_{0.8}\text{Co}_{0.15}\text{Al}_{0.05}\text{O}_2$
NMC	$\text{LiNi}_x\text{Mn}_y\text{Co}_z\text{O}_2$
NMP	N-methyl-2-pyrrolidone
NMR	Nuclear magnetic resonance spectroscopy

PAN	Polyacrylonitrile
PANI	Polyaniline
PC	Propylene carbonate
PCL	Polycaprolactone
PDMS	Polydimethylsiloxane
PE	Polyethylene
PEGDME500	Poly(ethylene glycol) dimethyl ether average Mn ~ 500
PEGDME2000	Poly(ethylene glycol) dimethyl ether average Mn ~ 2000
PETG	Polyethylene terephthalate glycol
PEO	Poly(ethylene oxide)
PLA	Polylactic acid
PolyC	Polycarbonate
PP	Polypropylene
PPYDBS	Dodecylbenzenesulfonate doped polypyrrole
PTFE	Polytetrafluoroethylene
PVA	Polyvinyl alcohol
PVDF	polyvinylidene fluoride
PVDF-co-HFP	Polyvinylidene fluoride-co-hexafluoropropylene
Pyr13TFSI	N-Propyl-N-methyl pyrrolidinium bis (trifluoromethanesulfonyl) imide
RT	Room temperature
SBR	Styrene-butadiene rubber
SEI	Solid electrolyte interphase
SEM	Scanning electron microscopy
SEM/EDS	Scanning electron microscopy with energy dispersive spectroscopy
SLA	Stereolithography apparatus

SLM	Selective laser melting
SLS	Selective laser sintering
SPE	Solid polymer electrolyte
T _c	Crystallization temperature
TEM	Transmission electron microscopy
T _g	Glass transition temperature
T _m	Melting temperature
UV	Ultraviolet
VC	Vinylene carbonate
VTF	Vogel-Tamman-Fulcher
X _c	Crystallinity percentage

**Résumé développé de la thèse
en Français**

(Summary in French)

Résumé développé de la thèse en Français
(Summary in French)

Résumé développé de la thèse en Français

(Summary in French)

La population mondiale actuelle étant estimée à 7,8 milliards de personnes au moment de la rédaction de cette thèse, l'approvisionnement d'énergies propres et durables et systèmes de stockage, pour répondre à la demande énergétique sans fin, est plus que jamais une préoccupation contemporaine majeure. Outre l'expansion des sources d'énergie renouvelables telles que l'énergie solaire, éolienne ou également l'hydroélectricité pour remplacer les combustibles fossiles traditionnels suscitant des préoccupations environnementales, les dispositifs de stockage d'énergie sont récemment apparus comme un obstacle décisif à surmonter. Capable de capter l'énergie produite à un moment donné pour la délivrer ultérieurement lorsque cela est nécessaire, la technologie la plus répandue, parmi les différentes options de stockage d'énergie actuelles, est la batterie lithium-ion. De nos jours, en raison de ses performances prometteuses en matière de densité d'énergie, de puissance et de durée de vie, il s'agit d'un composant au cœur de tous les dispositifs électroniques modernes : smartphones, ordinateurs portables, scooters électriques et véhicules électriques. Incontestablement devenue impérative dans notre vie de tous les jours, cette technologie particulière de batteries a récemment fait la une de l'actualité lorsque le prix Nobel de chimie 2019 a été décerné à trois chercheurs (Goodenough-Whittingham-Yoshino) pour leur travail pionnier. Alors que les batteries lithium-ion commerciales actuelles sont constituées de feuillets empilés (bidimensionnelles), des approches innovantes sont désormais nécessaires en vue de faciliter le développement d'architectures 3D complexes, permettant d'améliorer considérablement les performances électrochimiques en termes de puissance. En outre, l'élaboration de batteries flexibles, portables et personnalisables tout en maximisant le stockage d'énergie ainsi qu'en diminuant le volume et le poids doit être traitée.

La fabrication additive, également appelée impression 3D, apparaît comme une discipline révolutionnaire de pointe basée sur la préparation d'objets 3D par ajout de matière couche par couche. Cette technologie innovante permet précisément de mettre en œuvre l'optimisation topologique des dispositifs de stockage d'énergie. En effet, les composants de la batterie tels que les électrodes, le séparateur, l'électrolyte et les collecteurs de courant peuvent être élaborés de

n'importe quelle forme, permettant ainsi l'incorporation directe de la batterie dans l'objet tridimensionnel final. De plus, cette technique présente l'avantage de pouvoir construire des architectures d'électrodes complexes tridimensionnelles (3D). Ces dernières, très prometteuses, amélioreraient théoriquement de manière significative les performances de la batterie lithium-ion en termes de puissance et de capacité, la rendant ainsi particulièrement attrayante. Parmi les différents procédés de fabrication additive, le dépôt de filament fondu (FDM) apparaît comme une option prometteuse en vue d'obtenir une batterie lithium-ion complète sans avoir à effectuer de post-traitement.

Dans ce contexte, cette thèse a été effectuée sous la direction conjointe de deux laboratoires, respectivement spécialisés sur la formulation et la caractérisation de matériaux pour batteries lithium-ion et sur l'impression 3D et l'ingénierie mécanique :

- le Laboratoire de Réactivité et Chimie des Solides (LRCS), situé à l'Université Picardie Jules Verne à Amiens, France;
- le Laboratoire des Technologies Innovantes (LTI) situé à l'Université Picardie Jules Verne à Amiens, France.

Associant l'expertise des deux laboratoires, cette thèse de doctorat s'est alors concentrée sur l'élaboration de batteries lithium-ion par impression 3D utilisant le procédé dépôt de filament fondu.

La première étape de cette thèse a été consacrée au développement et à l'optimisation de filaments composites à base d'acide polylactique (PLA), correspondant à chaque partie d'une batterie lithium-ion utilisant une configuration à électrolyte liquide. Afin de maximiser les performances électrochimiques tout en conservant une résistance mécanique suffisante en vue de la manipulation et l'impression ultérieure, la quantité de matériau actif (graphite pour l'électrode négative et LiFePO_4 pour l'électrode positive) au sein des filaments d'électrodes a été augmentée le plus possible (jusqu'à 62,5 % en masse). L'incorporation d'une quantité aussi élevée de charges a été rendue possible grâce à l'incorporation de poly(éthylène glycol) diméthyléther $M_n \sim 500$

(PEGDME500), agissant comme plastifiant (rapport en masse optimisé 100:40 PLA:PEGDME500). Postérieurement, l'optimisation des électrodes a été réalisée par l'ajout d'additifs conducteurs améliorant la conductivité électronique. De même, pour le collecteur de courant, l'introduction de particules d'Ag-Cu a été maximisée (jusqu'à 86,5 % en masse) afin d'améliorer la conductivité électronique. En parallèle, un filament séparateur à base de PLA a été développé et optimisé par l'ajout de nanoparticules de SiO₂ (7 wt%) améliorant ainsi l'imprégnation de l'électrolyte liquide ($1,20 \times 10^{-4}$ S cm⁻¹ à 25 ° C après 10h d'immersion). Pour chaque filament composite développé au cours de cette thèse, l'impact de la granulométrie sur les performances électrochimiques et mécaniques finales devra faire l'objet d'une étude plus détaillée.

A partir des compositions de filaments optimisées pour les électrodes et le séparateur, l'étape suivante a été consacrée à l'impression 3D, par dépôt de filament fondu, d'une batterie lithium-ion complète fonctionnant avec un électrolyte liquide. L'assemblage à partir de composants indépendants imprimés en 3D (empilement) et l'impression directe de la batterie complète en une seule étape ont été démontrés. Tirant parti des capacités classiques du logiciel d'impression 3D (slicer), les motifs de remplissage et la densité du séparateur ont été introduits afin d'améliorer l'imprégnation de l'électrolyte liquide et d'éviter les courts-circuits. Une étude approfondie est toutefois nécessaire, à l'avenir, pour optimiser davantage ces paramètres. Alors que les performances électrochimiques des cellules complètes restent relativement limitées (seulement 30 mAh g⁻¹ de matériau actif à C/40 pour le système complet imprimé en une seule étape), la démonstration de faisabilité de l'impression 3D d'une batterie lithium-ion complète et fonctionnelle, par dépôt de filament fondu, a été démontrée. Dans le but d'améliorer les performances électrochimiques du dispositif final, une fois le filament de collecteur de courant optimisé, ce dernier devra être utilisé pour imprimer la première couche soumise à la limitation d'épaisseur de 200 μm, malheureusement intrinsèque au procédé FDM. Par conséquent, l'impression d'électrodes plus minces (jusqu'à 50 μm) permettant l'équilibrage de la batterie sera alors rendue possible. A l'issue de cette thèse, il est nécessaire que les futures recherches se concentrent sur les options d'imprimantes FDM multi-matériaux. Ces avancées permettront alors l'impression d'architectures de batteries tridimensionnelles complexes (gyroïdes, interdigités, cubes) dont les performances électrochimiques améliorées en termes de puissance par rapport à une configuration planaire classique ont été démontrées à l'aide de la simulation numérique. Des

modélisations plus avancées pourront être envisagées afin de prendre en compte les effets thermiques, à l'aide d'un couplage électrothermique, susceptibles de diminuer les performances d'une batterie.

D'autre part, en tant qu'alternative plus sûre à la configuration classique d'électrolyte liquide à base de solvants organiques volatils et inflammables, l'impression d'une batterie lithium-ion tout solide via le procédé FDM a été étudiée. L'élaboration et l'optimisation d'un filament d'électrolyte polymère solide composé de poly(oxyde d'éthylène) (PEO), comme matrice polymère, et de lithium bis(trifluoromethanesulfonyl)imide (LiTFSI), comme sel de lithium, ont été réalisées. La composition de film la plus prometteuse d'un point de vue électrochimique ($O/Li^+ = 20$) a finalement été utilisée pour les étapes consécutives d'extrusion et d'impression. Après d'importantes modifications apportées à l'imprimante, un disque imprimé d'électrolyte polymère solide présentant une conductivité ionique de $2,18 \times 10^{-3} \text{ S cm}^{-1}$ à 90 °C a été obtenu. Bien que ces résultats, ici, ouvrent clairement la voie à une batterie tout solide entièrement imprimée, d'autres investigations sont encore nécessaires. En particulier, ces dernières doivent être consacrées à l'introduction de copolymères en vue de faciliter l'impression sans pour autant affecter la conductivité ionique. En outre, il convient de mentionner qu'en utilisant trois porte-échantillons d'impédance commerciaux différents (latéral, sandwich et peignes-interdigités), les valeurs de conductivité se sont révélées significativement différentes pour un même échantillon. Ce comportement est reproductible et a été observé pour chaque composition d'électrolyte polymère solide (PEO / LiTFSI) testée pendant cette thèse. Des investigations additionnelles sont nécessaires pour bien comprendre l'origine de ces écarts. Dans les études futures, les auteurs sont donc encouragés à rapporter une zone de conductivité délimitée plutôt qu'une valeur très spécifique (dans la plage de basse température $<90 \text{ °C}$). Les recherches à venir devront être étendues à d'autres polymères.

Enfin, s'agissant d'une étude préliminaire s'inscrivant dans la perspective des recherches à mener, la dernière partie de cette thèse de doctorat a été axée sur le développement d'électrodes composites à base de polypropylène (PP) via les procédés de dépôt de filament fondu (FDM) et frittage sélectif par laser (SLS). Une telle matrice polymère a été utilisée à la place du PLA, car ce dernier est soupçonné de se dissoudre dans l'électrolyte liquide avec le temps. Par ailleurs, la

capacité du procédé SLS à imprimer des composants d'une batterie lithium-ion a également été examinée. En fixant dès le départ les paramètres d'extrusion et d'impression à haute énergie pour la technique FDM, et les paramètres d'impression à basse énergie pour SLS, les performances électriques, morphologiques, mécaniques et électrochimiques qui en résultent se sont révélées significativement différentes pour une composition d'électrode similaire. L'échantillon obtenu par SLS présente une porosité élevée, des performances électroniques et électrochimiques prometteuses, mais est très fragile. Au contraire, l'échantillon FDM présente une faible porosité, de faibles performances électroniques et électrochimiques, mais une grande résistance mécanique. Grâce à l'ajout d'un plastifiant, l'introduction d'une quantité beaucoup plus élevée de matière active a été rendue possible par FDM alors qu'elle n'est pas envisageable par la technologie SLS. Les recherches à venir doivent néanmoins être consacrées à trouver le plastifiant le plus approprié pour la matrice de PP en vue de créer une microporosité importante capable d'être remplie d'électrolyte liquide. Une optimisation importante des températures d'extrusion et d'impression est également nécessaire pour atteindre le meilleur compromis entre performances mécaniques et électrochimiques.

En résumé, le développement de filaments thermoplastiques composites sur mesure et l'impression 3D d'une batterie lithium-ion complète fonctionnelle utilisant un électrolyte liquide, ont été démontrés au moyen du procédé de dépôt de filament fondu. De plus, certaines optimisations ont été proposées. Encouragées par les tests d'impression prometteurs sur l'électrolyte polymère solide, les recherches futures s'orientent désormais vers l'impression multi-matériaux d'une batterie lithium-ion tout solide, basée sur les architectures 3D complexes (gyroïdes, interdigités, cubes) prometteuses d'un point de vue électrochimique.

Résumé

Alors que les batteries lithium-ion commerciales actuelles sont constituées de feuillets empilés (bidimensionnelles), des approches innovantes, telles que la fabrication additive, sont désormais nécessaires en vue de faciliter le développement d'architectures 3D complexes, permettant d'améliorer considérablement les performances électrochimiques en termes de puissance. Dans ce contexte, le but de cette thèse a été de démontrer l'impression 3D de composants d'une batterie lithium-ion au moyen du procédé de dépôt de filament fondu (FDM). La première étape a donc été consacrée au développement et à l'optimisation de filaments composites à base d'acide polylactique (PLA), correspondant à chaque partie (électrodes, séparateur et collecteur de courant) d'une batterie lithium-ion utilisant une configuration à électrolyte liquide. La quantité de matériau actif au sein des filaments d'électrodes a été augmentée le plus possible afin de maximiser les performances électrochimiques tout en conservant une résistance mécanique suffisante en vue de la manipulation et impression ultérieure. L'incorporation d'une quantité aussi élevée de charges a été rendue possible grâce à l'incorporation de poly(éthylène glycol) diméthyléther Mn ~ 500 (PEGDME500), agissant comme plastifiant. En parallèle, des filaments PLA/Ag-Cu et PLA/SiO₂, respectivement utilisés pour le collecteur de courant et le séparateur, ont été développés. A partir des compositions de filaments optimisées, l'assemblage à partir de composants indépendants imprimés en 3D (empilement) et l'impression directe de la batterie complète en une seule étape ont été démontrés. D'autre part, en tant qu'alternative plus sûre à la configuration classique d'électrolyte liquide à base de solvants organiques volatils et inflammables, l'élaboration et l'optimisation d'un filament d'électrolyte polymère solide, composé de poly(oxyde d'éthylène) (POE) et de lithium bis(trifluoromethanesulfonyl)imide (LiTFSI), pour une batterie lithium-ion tout solide, ont été réalisées. Enfin, s'agissant d'une étude préliminaire s'inscrivant dans la perspective des recherches à mener, la dernière partie de cette thèse de doctorat a été axée sur le développement d'électrodes composites à base de polypropylène (PP) via les procédés de FDM et de frittage sélectif par laser (SLS).

Mots clés : Batteries lithium-ion, Impression 3D, Fabrication additive, Polymères, Composites, Chimie des matériaux

Abstract

While current commercial lithium-ion batteries consist of stacked leaflets (2D planar design), innovative approaches, such as additive manufacturing, are now required to enable the development of 3D complex architectures reported to significantly improve the electrochemical performances in terms of power. In this context, the aim of this PhD thesis was to demonstrate the printability of lithium-ion battery components by means of the Fused Deposition Modeling (FDM) 3D-printing process. First stage was thus dedicated to the development and optimization of polylactic acid (PLA)-based composite filaments, corresponding to each part (electrodes, separator and current collector) of a liquid electrolyte lithium-ion battery (LIB) configuration. The active material within the electrode filaments was increased as high as possible to maximize the electrochemical performances while still maintaining just enough mechanical strength for handling and printing. The incorporation of such a high amount of charges was made possible thanks to the incorporation of an optimized amount of poly(ethylene glycol) dimethyl ether average Mn ~ 500 (PEGDME500), acting as plasticizer. In parallel, PLA/Ag-Cu current collector, and PLA/SiO₂ separator filaments were developed. From the optimized filament compositions, assembly from independent 3D-printed components (stacking), and direct printing of the complete LIB in a single step (one-shot), have been demonstrated. On the other hand, as a safer alternative to the classical volatile and flammable organic solvent-based liquid electrolyte configuration, the elaboration and optimization of a solid polymer electrolyte filament composed of poly(ethylene oxide) (PEO) as polymer matrix and lithium bis(trifluoromethanesulfonyl)imide (LiTFSI) as lithium salt, for an all-solid-state LIB, was achieved. Finally, acting as a perspective study, the last part of this PhD thesis was focused on the development of polypropylene (PP)-based composite electrodes via FDM and selective laser sintering (SLS).

Keywords: Lithium-ion batteries, 3D-printing, Additive manufacturing, Polymers, Composites, Materials Chemistry